OPTICAL AND OPTOELECTRONIC PROPERTIES OF SI NANOCRYSTALS EMBEDDED IN DIELECTRIC MATRIX

DING LIANG

School of Electrical and Electronic Engineering

A thesis submitted to Nanyang Technological University
in fulfillment of the requirement for the degree of
Doctor of Philosophy

2009

ACKNOWLEDGMENTS

This thesis arose from extensive collaborations. It is a great pleasure to take this opportunity to express my gratitude to all the people who have made contributions to the thesis.

First and foremost, I would like to thank my supervisor, Dr. Chen Tupei, for all his guidance, help, support, and encouragement throughout my Ph. D studies. As both an enthusiastic scientist and an academic professional, he took me into the fascinating world of nanoscience and nanotechnology with his knowledgeable mind and precious insight. This thesis could not be finished without his guidance, including insightful direction on experiments, suggestions on writing, and many scientific discussions. I am grateful that I have had the opportunity to learn from him. I believe I will benefit from the knowledge and experience I obtained while working with Dr. Chen in my whole life.

Mrs. Liu Yuchan and Dr. Ding Xingzhao from Singapore Institute of Manufacturing Technology also deserve my thanks. They helped me with the studies on the optical properties of silicon nanocrystals embedded in SiO_2, which are significantly important in my project. I would especially like thank Dr. Zhu Furong and Mrs. TAN Mei Chern from Institute of Materials Research & Engineering for their help with the photoluminescence measurements and the deposition of indium tin oxide film as the transparent electrode in the light emitting structures. Furthermore, I am deeply grateful to Dr. Tung Chih-Hang and Alastair David Trigg from Institute of Microelectronics for their help with transmission electron microscopic (TEM) measurements on my samples.

I am also indebted to Dr. Liu Yang and Dr. Ng Chi Yung for teaching me to use the probe station for electrical characterization of Si nanocrystals. As senior members in our group, they have offered me a lot of useful and insightful suggestions on my experiments throughout my research. I also benefited a lot from the discussions with them. I greatly enjoyed the time working with them and sincerely appreciate their help, guidance, and patience. Thanks also go to my fellow Ph. D students, Mr. Yang Ming and Mr. Wong Jen It, with whom I spent many hours having discussions on the experimental designing, result analyzing, and paper writing. Their technical assistances with my experiments and sample preparation are of great importance in my Ph. D research.

Furthermore, I would like to extend my warmest gratitude to all my colleagues at the Measurements Laboratory, Integrated System Research Lab, and Nanoelectronics Lab II. They have helped provide an enjoyable and supportive research environment, as well as creating a positive atmosphere for cooperation and creativity. It has been a pleasure to work in these labs. I am very grateful to all of you, through it is not possible to list everybody individually.

My parents provided me unwavering encouragement during my Ph. D study and research. Their continuous love and support throughout my education should be undoubtedly thanked. They made this thesis possible. The degree is meaningless if I could not share it with them.

Dedicated to my parents

TABLE OF CONTENTS

ACKNOWLEDGMENTS .... **I**

TABLE OF CONTENTS .... **IV**

SUMMARY .... **VIII**

LIST OF FIGURES .... **X**

LIST OF TABLES .... **XVIII**

NOMENCLATURES .... **XIX**

CHAPTER 1 INTRODUCTION **1**

1.1 Si Photonics **1**

1.2 Si Nanocrystals **3**

1.3 Objectives and Scope of Research **5**

1.4 Major Contributions of the Thesis **6**

1.5 Organization of the Thesis **9**

CHAPTER 2 LITERATURE REVIEW **12**

2.1 Introduction **12**

2.2 Synthesis of Si Nanocrystals **13**

2.2.1 Porous silicon 13

2.2.2 Chemical Vapor Deposition 14

2.2.3 Sputtering 15

2.2.4 Pulse Laser Deposition 16

2.2.5 Ion Implantation 18

2.2.6 What Is Important in the Fabrication of nc-Si? 19

2.3 Characterization of Dielectric Films Embedded with nc-Si **21**

2.3.1 X-ray Diffraction 21

2.3.2 X-ray Photoelectron Spectroscopy 22

2.3.3 Raman Spectroscopy 23

2.3.4 Secondary Ion Mass Spectroscopy 24

2.3.5 Transmission Electron Microscopy 25

2.3.6 Scanning Electron Microscopy 28

2.3.7 Atomic Force Microscopy 29

2.3.8 Spectroscopic Ellipsometry 30

2.3.9 Current-Voltage (*I-V*) Characteristics 31

2.3.10 Capacitance-Voltage (*C-V*) Characteristics 33

2.3.11 Other Characterization Techniques 35

2.4 Light Emission from Dielectric Films Embedded with nc-Si 35
2.4.1 Introduction: Direct and Indirect Transitions 35
2.4.2 Photoluminescence 37
2.4.3 Electroluminescence 44
2.4.4 Mechanisms of Light Emission 45
2.5 Possible Structures of Si-based light emitters 48
2.5.1 Raman Si Laser Based on SOI Rib Waveguide 48
2.5.2 Conventional p-n Junction LED Structure 49
2.5.3 MOS Structure with nc-Si Embedded in Oxide 50
2.6 Other Application of Si nanocrystals 52
2.6.1 Memory Devices 52
2.6.2 Solar Cells 55
2.7 Summary 58
CHAPTER 3 DIELECTRIC FUNCTION OF SI NANOCRYSTALS EMBEDDED IN A SILICON DIOXIDE MATRIX 60
3.1 Introduction 60
3.2 Ellipsometry 61
3.2.1 Basic Principles 62
3.2.2 Single-wavelength and Spectroscopic Ellipsometry 64
3.2.3 Dielectric Functions and Optical Constants 65
3.3 Dielectric Function of Dispersed nc-Si Embedded in SiO_2 66
3.3.1 Sample Fabrication 67
3.3.2 Characterization 67
3.3.3 Ellipsometry Measurement 69
3.3.4 Methodology 70
3.3.5 Results and Discussions 82
3.3.6 Analysis of Parameter Uncertainty 86
3.3.7 Bandgap Expansion 88
3.3.8 Dielectric Suppression 90
3.4 Depth Profile of Optical Constants of SiO_2 Film Containing nc-Si .. 91
3.4.1 Methodology 91
3.4.2 Results and Discussions 92
3.4.3 Conclusion 97
3.5 Thermal Annealing Effect on Dielectric Functions of nc-Si Embedded in SiO_2 97
3.5.1 Sample Fabrication and Experiments 97
3.5.2 Results and Discussions 99
3.5.3 Conclusion 103
3.6 Size Effect on Dielectric Functions of nc-Si Embedded in SiO_2 104
3.6.1 Sample Fabrication and Experiments 105

3.6.2 Results and Discussions 108
3.6.3 Conclusion 112

3.7 Dielectric Functions of Densely-stacked nc-Si Layer Embedded in SiO_2 112

3.7.1 Sample Fabrication and Experiments 113
3.7.2 Methodology 114
3.7.3 Results and Discussions 116
3.7.4 Conclusion 121

3.8 Summary 121

CHAPTER 4 PHOTOLUMINESCENCE OF SI NANOCRYSTALS EMBEDDED IN DIELECTRIC FILMS. 123

4.1 Introduction 123

4.2 PL from Si^+-implanted SiO_2 Films 125

4.2.1 Sample Fabrication and Experiments 125
4.2.2 Annealing Effect on PL Properties 126
4.2.3 Effect of Excess Si Concentration on PL Properties 138
4.2.4 Conclusion 145

4.3 PL from Si^+-implanted Si_3N_4 Films 146

4.3.1 Sample Fabrication and Experiments 146
4.3.2 Results and Discussions 147
4.3.3 Conclusion 151

4.4 PL from PECVD-Grown Si rich Si Oxide 152

4.4.1 Sample Fabrication and Experiments 152
4.4.2 Results and Discussions 154
4.4.3 Conclusion 157

4.5 Summary 158

CHAPTER 5 ELECTROLUMINESCENCE OF SI NANOCRYSTALS EMBEDDED IN DIELECTRIC FILMS. 159

5.1 Introduction 159

5.2 EL from Si^+-implanted SiO_2 Films 160

5.2.1 Sample Fabrication and Experiments 160
5.2.2 SRIM Result and Excess Si Distribution 163
5.2.3 EL Spectra 164
5.2.4 Influence of Implantation Recipe on EL 166
5.2.5 Relationship Between Current Transport and EL 170
5.2.6 EL Mechanisms 174
5.2.7 Annealing Effect on EL Properties 184
5.2.8 Comparison between EL and PL 188
5.2.9 Conclusion 191

5.3 EL from Si^+-implanted Si_3N_4 Films 192

5.3.1 Sample Fabrication and Experiments 193
5.3.2 EL Spectra 194
5.3.3 Annealing Effect on EL Properties 196
5.3.4 Comparison between EL and PL 198
5.3.5 Conclusion 200

5.4 Summary 201

CHAPTER 6 ELECTRICAL PROPERTIES OF SI NANOCRYSTALS EMBEDDED IN SIO2 FILMS 202

6.1 Introduction 202

6.2 Electrical Characterizations 203

6.2.1 Sample Fabrication and Experiments 203
6.2.2 Results and Discussion 205
6.2.3 Conclusion 213

6.3 Charging Mechanism 214

6.3.1 Sample Fabrication and Experiments 215
6.3.2 Results and Discussion 216
6.3.3 Conclusion 222

6.4 Summary 223

CHAPTER 7 CONCLUSION AND RECOMMENDATIONS 224

7.1 Conclusion 224

7.1.1 Dielectric Functions 224
7.1.2 PL Properties 225
7.1.3 EL Properties 226
7.1.4 Electrical Properties and Charging Mechanism 226

7.2 Recommendations 227

7.2.1 First-Principle Calculation 228
7.2.2 Si Nanocrystal Based Laser 228
7.2.3 Memory Devices Based on Si nanocrystals 229
7.2.4 Photon-Programmed Si nanocrystal Memory 229

List of Publications 231

BIBLIOGRAPHY 234

SUMMARY

It is the intent of this work to investigate the optical and optoelectronic properties of Si nanocrystals (nc-Si) embedded in dielectric matrix. Si nanocrystals embedded in dielectric films have been synthesized with the technique of Si ion implantation and plasma enhanced vapor deposition (PECVD). A comprehensive optical study has been performed with SE analysis based on the effective medium approximation (EMA) theories and proper optical dispersion model. The dielectric functions of nc-Si have been experimentally determined for the first time from the spectroscopic ellipsometric (SE) analysis. The bandgap and dielectric constant of nc-Si have been also obtained. Based on the optical constants of nc-Si obtained and EMA theories, the depth profiling of optical constants of SiO_2 film containing nc-Si have been determined, which is very important to device modeling. Thermal annealing effect on optical properties of nc-Si embedded in SiO_2 films has been studied also. The influence of nanocrystal size on the band gap and dielectric function has been investigated. Furthermore, a comprehensive study has been carried out on the dielectric function of dispersed nc-Si and densely-stacked nc-Si layer embedded in SiO_2 fabricated with the technique of ion implantation.

Strong room-temperature photoluminescence (PL) has been observed from SiO_2 thin films embedded with nc-Si. Thermal annealing effect on the PL properties of nc-Si embedded in SiO_2 has been investigated. It has been found that thermal annealing at 1100 ^{o}C exhibits PL related to the formation of nc-Si. Size-dependent PL emission has been realized through adjusting implantation recipes. The PL energy decreases with the increasing nanocrystal size in

accordance with the quantum confinement concepts. However, the size-dependent PL could not originate from the direct band to band transition of nc-Si. Based on the knowledge of band structure of nc-Si obtained in this work, the size-dependent PL band could be attributed to the indirect band-to-band transition of the nc-Si assisted by the Si-O vibration at the interface of nc-Si/SiO_2.

Visible and near infrared (IR) electroluminescence (EL) has been observed from a metal–oxide–semiconductor-like (MOS-like) structure with nc-Si embedded in the gate oxide. The nanocrystal distribution is found to play an important role in the EL. The influence of the applied voltage, the implantation dose, and implantation energy on the EL properties has been investigated. The current transport of the device follows a power law, and it is determined by the concentration and distribution of the nc-Si in the oxide. A linear relationship between the EL intensity and the current transport is observed. The current transport evolves with both the concentration and distribution of the nc-Si, and so does the EL.

For MOS capacitors with nc-Si embedded in the gate oxide, both the stress voltage and stress duration play important roles on the flatband voltage shift and the conductance peak, due to the charging and discharging effect of nc-Si. XPS analysis is used to study the charging mechanism of nc-Si embedded in SiO_2. The results indicate that the charging effect mostly takes place inside the nc-Si rather than at the nc-Si/SiO_2 interface.

LIST OF FIGURES

Figure 2.1 Schematic illustration of a typical LPCVD reactor. 15
Figure 2.2 Schematic of the deposition chamber and off-axis RF magnetron sputtering system.. 16
Figure 2.3 Schematic of typical PLD system [39]. 17
Figure 2.4 Schematic illustration of a typical ion implanter. 18
Figure 2.5 A schematic illustration of three most important factors of nc-Si fabrication for device applications [52]. 20
Figure 2.6 XPS spectra of Si-rich SiO_x ($x < 2$) formed by Si ion implantation into thermally grown SiO_2 for the (a) as implanted sample and (b) the sample annealed at 1000 °C for 20 min [63]. 23
Figure 2.7 Raman spectra of the SiO_2 embedded with nc-Si. The particle size of nc-Si is indicated on the related curves [71]. 24
Figure 2.8 Depth profiles of excess Si in the SiO_2 film obtained from SIMS and TRIM code calculation [80]. 25
Figure 2.9 Cross-sectional HRTEM image of a typical Si nanocrystals embedded in SiO_2 synthesized by Si ion implantation and subsequent high temperature annealing (a) with a single-twin structure; and (b) with a double-twin structure [60]. The implantation was carried out at the energy of 100 keV with the Si ion dose of 3×10^{17} cm^{-2}. 27
Figure 2.10 Cross-sectional HRTEM images of SiO_2 samples implanted with a constant Si ion dose of 10^{16} cm^{-2} at implantation energies ranging from 1 to 5 keV followed by thermal annealing at 950 °C for 30 min in N_2 ambient [81]. 27
Figure 2.11 Plan-view TEM images of nc-Si embedded in SiO_2 synthesized by rapid thermal CVD process (a) [84] and aerosol reaction (b) [51]. 27
Figure 2.12 SEM image of time dependency of the growth of Si nanocrystals [85]. 28
Figure 2.13 Tapping-mode AFM images of as-grown nc-Si taken with the scanning rate of (a) 1Hz; (b) 1, 2, and 4 Hz as indicated; (c) 1 Hz taken right after (b) [96]. 29
Figure 2.14 (a) Refractive index and extinction coefficient as a function of wavelength for different silicon materials [98]; (b) Dielectric function of embedded nc-Si with the size of 3.9 nm in SiO_2 matrix and c-Si sample as a function of energy [102]. 31
Figure 2.15 Current-voltage (*I-V*) characteristics of the MOS capacitors with nc-Si embedded in the gate oxide [106].. 32
Figure 2.16 Reversible drain current I_d measurements for both the samples (a) without nc-Si and (b) without nc-Si embedded in the gate oxide [107]. 32
Figure 2.17 Hysteresis effect observed in the *C-V* measurement of the MOS capacitor with nc-Si embedded in the gate oxide fabricated by Si ion implantation and thermal annealing [108]. 33

Figure 2.18 (a) Comparison of the *C-V* characteristics between two annealing temperature (850 ^{o}C and 1000 ^{o}C); (b) Flatband voltage shift as a function of both annealing temperature and annealing time [111]. 34
Figure 2.19 Schematic of the absorption of a photon in a direct bandgap (a) and indirect bandgap (b) semiconductor material................................ 36
Figure 2.20 (a) Schematic of direct band-to-band radiative transitions; (b) Schematic of indirect band-to-band radiative transitions............... 37
Figure 2.21 Typical PL spectra of porous Si sample with a porosity of 65%, in which the sample for the upper spectrum has the highest extent of oxidation [122].. 38
Figure 2.22 (a) PL spectra of 1 MeV Si^+-implanted silica glass to a fluence of 1×10^{17} ion/cm^2 (1) at liquid nitrogen temperature, (2) at room temperature, and (3) a fluence of 2×10^{17} ions/cm^2 at room temperature [123]; (b) PL spectra of a Si^+-implanted sample annealed in air at 900 ^{o}C for different annealing times [42]......... 39
Figure 2.23 (a) PL spectra of samples annealed for 1 h at 1100 °C in N_2, 5% H_2 in N_2 (FG), or Ar; (b) PL of the samples from (a) after H passivation (500 °C in FG for 1 h); (c) PL of the samples from (a) after 750 °C in N_2 for 1 h. The spectrum from the sample annealed in Ar in (a) has been multiplied by a factor of 10 for clarity [45].. 40
Figure 2.24 PL spectra of nc-Si showing a blueshift with the reduction of nanocrystal size [126]. 41
Figure 2.25 (a) PL decay curves of nc-Si measured a different wavelengths; (b) Normalized life time distribution derived from the experimental PL decay curves [129]. 42
Figure 2.26 (a) The decay rate of silicon nanocrystals at 750 nm varies with oxide thickness in good agreement with a calculation of the local density of optical states. The ensemble radiative decay rate (9.4±1.3 kHz) and quantum efficiencies for two samples are determined by a least squares fit to the linearized data (inset). (b) Measured total decay rate as function of LDOS at different wavelengths. (c) Quantum efficiency as function of wavelength suggesting that there is an optimal wavelength (nanocrystal size) for PL quantum efficiency [137]. 43
Figure 2.27 (a) Comparison between the PL and EL spectra of the device with a Si content of 42% in the SiO_x layer. The EL spectrum was measured with a voltage of 48 V and current density of 4 mA/cm^2; (b) emission microscopy image of the device annealed at 1100 ^{o}C for 1 h [145]. 44
Figure 2.28 (a) Current density as a function of applied voltage; (b) comparison between the EL and PL spectra of the device [121]...................... 45
Figure 2.29 Schematic of the system of nc-Si embedded in a dielectric matrix and possible radiative electron hole recombination...................... 46
Figure 2.30 Raman silicon laser proposed by Rong *et al.* (a) Schematic layout of the silicon waveguide laser cavity with optical coatings applied to the facets and p-i-n structure along the waveguide; (b) cross-section of the silicon Raman laser [178]. 49

Figure 2.31 Schematic of conventional p-n junction LED structure based on nc-Si [16]..50
Figure 2.32 Field-effect electroluminescence based on a MOSFET structure with nc-Si embedded in the gate oxide [181]................................51
Figure 2.33 (a) Schematic cross-section of Si nanocrystal-based memory structure; (b) band diagrams showing the functions of write and erase [108]..53
Figure 2.34 Transfer characteristics of the programmed and erased states under the programming/erase (P/E) operation of (a) FN/FN and (b) CHE/FN with the P/E time of 1 μs [190]......................................54
Figure 2.35 (a) Traditional photoexcitation; (b) an ideal picture of multiple exciton generation upon absorption of a single photon [197]........56
Figure 2.36 Schematic structure of (a) two-cell and (b) three-cell tandem solar cell with nc-Si embedded in SiO_2 [198].......................................57
Figure 3.1 Schematic illustration of an ellipsometric experiment, showing the polarized light reflected by the surface of the measured sample. ..63
Figure 3.2 Cross-sectional TEM image of nc-Si embedded in SiO_2 matrix. The sample was fabricated by Si ion implantation with the dose of 1×10^{17} cm^{-2} at 100 keV followed by annealing at 1000 ^oC at N_2 for 30 min. 68
Figure 3.3 XRD measurement of Si nanocrystals embedded in SiO_2 matrix and the pseudo-Voigt fit to the data...69
Figure 3.4 Volume fraction of excess Si in SiO_2 as a function of depth. 73
Figure 3.5 Multi-layer model used in the SE analysis. 75
Figure 3.6 The procedure to extract information of nc-Si embedded in SiO_2 from ellipsometric measurements. 81
Figure 3.7 The flow chart of the fitting program. 81
Figure 3.8 Best spectral fittings of ψ and Δ based on the Lorentz oscillator model and the four-term FB model with the approach described in the text...82
Figure 3.9 Real (ε_1) and imaginary (ε_2) parts of the complex dielectric functions of the nc-Si obtained from the spectral fitting based on the Lorentz oscillator model and the FB model. The dielectric function of bulk crystalline Si is also included for comparison.....85
Figure 3.10 Refractive index (n) and extinction coefficient (k) of the nc-Si and bulk crystalline Si as functions of wavelength..............................86
Figure 3.11 Plots of $(\alpha E)^\gamma$ versus photon energy (E) for both the nc-Si synthesized at 1000 ^oC and bulk crystalline silicon. (a) $\gamma = 1/2$; and (b) $\gamma =2$..89
Figure 3.12 The depth profile of optical constants of SiO_2 film containing Si nanocrystals synthesized with Si ion implantation. 93
Figure 3.13 Optical constants of the film structure as functions of wavelength at the depths of 20, 50, 90, and 120 nm. The optical constants of pure SiO_2 are also included for comparison..95
Figure 3.14 Depth profile of $\Delta n / n_{SiO_2}$ for various wavelengths. 96

Figure 3.15 Depth profile of extinction coefficient for various wavelengths. ... 96

Figure 3.16 Real (ε_r) and imaginary (ε_i) parts of the complex dielectric functions of both the nc-Si annealed for 0, 30, and 80 min at 1000 ºC and the bulk crystalline silicon as functions of photon energy. 102

Figure 3.17 Real (ε_r) and imaginary (ε_i) parts of the complex dielectric functions of both the nc-Si of as-implanted sample and annealed at 700 and 900 ºC, for 20 min and the bulk crystalline silicon as functions of photon energy. 103

Figure 3.18 XRD measurement of Si nanocrystals embedded in SiO_2 matrix and the pseudo-Voigt fit to the data for (a) sample 1 with nc-Si size of 4.6 nm; and (b) sample 2 with nc-Si size of 5.3 nm. 106

Figure 3.19 Volume fractions of nc-Si in SiO_2 as a function of depth for the five samples obtained from SRIM simulation. 107

Figure 3.20 Real (ε_1) and imaginary (ε_2) parts of the complex dielectric function of the nc-Si with various sizes obtained from the spectral fittings. The dielectric function of bulk crystalline silicon is also included for comparison. 109

Figure 3.21 Band gap expansion of nc-Si as a function of nc-Si size. 111

Figure 3.22 Cross-sectional TEM image of the densely-stacked Si nanocrystal layer embedded in SiO_2 thin film for sample *a*. 114

Figure 3.23 (a) Five-phase model used in the SE analysis. (b) Spectral fittings of Ψ and Δ for sample *a*. 116

Figure 3.24 Real (ε_1) and imaginary (ε_2) parts of the complex dielectric functions of the densely-stacked Si nanocrystal layer for sample *a*. For comparison, the dielectric functions of the continuous nc-Si thin film [98], the isolated nc-Si dispersed in a SiO_2 matrix, amorphous Si and bulk crystalline Si are also included in this figure. 118

Figure 3.25 Influence of annealing duration on the imaginary (ε_2) part of the complex dielectric functions of the densely-stacked Si nanocrystal layer. The annealing temperature is fixed at 1000 ^{o}C. 120

Figure 3.26 Influence of annealing temperature on the imaginary (ε_2) part of the densely-stacked Si nanocrystal layer. The annealing duration is 20 min. 120

Figure 4.1 Excitonic energy as a function of nc-Si diameter. Open circles correspond to the pseudopotential calculation result of Reboredo [226]; open squares correspond to the quasiparticle calculations results of Ogut [202]; and full triangles correspond to the experimental results of Wolkin [225]. 124

Figure 4.2 Energy gap of the nc-Si embedded in SiO_2 versus annealing temperature. The energy gap was extracted from the FB model in the SE analysis. 127

Figure 4.3 PL spectra of Si^{+}-implanted SiO_2 films at different temperatures. . 128

Figure 4.4 Decomposition of PL spectra for the samples of Si^{+}-implanted SiO_2

annealed at (a) 500 ^{o}C, (b) 600 ^{o}C, (c) 700 ^{o}C, (d) 850 ^{o}C, (e) 900 ^{o}C, (f) 1000 ^{o}C, and (g) 1100 ^{o}C for 20 min................................130
Figure 4.5 Integrated intensity of each PL band as a function of annealing temperature..131
Figure 4.6 Maximum integrated intensity for each PL band...........................136
Figure 4.7 PL spectra for the samples annealed at 1100 ^{o}C for (a) 20 min, (b) 40 min, and (c) 120 min. 137
Figure 4.8 Integrated PL intensity as a function of annealing time. The annealing temperature is 1100 ^{o}C...138
Figure 4.9 Normalized PL spectra for the following samples annealed at 1100 ^{o}C for 20 min: (a) 3×10^{16} ions/cm^2 at 120 keV, (b) 1×10^{17} ions/cm^2 at 100 keV, (c) multiple implantations with 5×10^{15} ions/cm^2 at 20 keV, 1×10^{16} ions/cm^2 at 40 keV, and 2×10^{16} ions/cm^2 at 80 keV, (d) 4×10^{16} at 10 keV, and (e) multiple implantations with 3×10^{15} ions/cm^2 at 1 keV, 8×10^{15} ions/cm^2 at 5 keV, and 4×10^{16} ions/cm^2 at 16 keV..140
Figure 4.10 Band gap and PL peak energy as functions of nc-Si diameter......140
Figure 4.11 Optical-absorption and photoluminescence spectra of Si nanocrystals embedded in SiO_2 for sample a and d. The PL spectra were measured using the sample fabricated on p-type Si substrate, and the absorption spectra were measured using the sample fabricated on fused silica glass...142
Figure 4.12 Integrated PL intensity as a function of annealing time for the different excess Si volume fractions from 3% to 30%. All the samples are annealed at 1100 ^{o}C in N_2.......................................143
Figure 4.13 PL peak energy and integrated PL intensity as functions of excess Si volume fraction. 144
Figure 4.14 Full width at half maximum (FWHM) of the PL peaks as a function of the excess Si concentration for the sample annealed at 1100 ^{o}C. 145
Figure 4.15 PL spectra of Si^+-implanted Si_3N_4 films annealed at different temperatures. 148
Figure 4.16 Intensity of the blue-violet and red PL band...............................149
Figure 4.17 The x value and atomic concentration of nitrogen in deposited films as functions of the N_2O/SiH_4 flow ratio γ. 154
Figure 4.18 Selected PL spectra of PECVD-grown SiO_x films after the annealing at 1100 ^{o}C for 1 h...155
Figure 4.19 Normalized PL spectra of PECVD-grown SiO_x films for the samples with the N_2O/SiH_4 flow ratio from 20 to 30. The inset shows the PL peak wavelength as a function of x value. 157
Figure 5.1 (a) Schematic illustration of the device structure; (b) Cross-sectional TEM image of nc-Si embedded in SiO_2 of sample 2a. 162
Figure 5.2 Distributions of nc-Si in the gate oxide obtained from SRIM simulations. 164
Figure 5.3 EL spectra for sample 5a under the gate voltage of -15, -11, and -8 V, respectively. The inset shows the *I-V* characteristics and the

integrated EL intensity as a function of current density. 166
Figure 5.4 Microphotograph of EL patterns under different gate voltages for sample 5a. (a) -8 V, (b) -11 V, and (c) -15 V. 166
Figure 5.5 Dependence of the current and the integrated EL intensity on the voltage as a function of the implanted Si ion dose (samples 5a, 5b, and 5c). The implantation energy is fixed at 5 keV . The inset shows the concentrations and distributions of the excess Si in the oxide thin film obtained from the SRIM simulations. 168
Figure 5.6 Dependence of the current and the integrated EL intensity on the voltage as a function of the implantation energy (samples 2a, 5a, and 8a). The implanted Si ion dose is fixed at 1×10^{16} cm^{-2}. The inset shows the concentrations and distributions of the excess Si in the oxide thin film obtained from the SRIM simulations. 170
Figure 5.7 α_0 and ζ as functions of implanted Si ion dose (a) or implantation energy (b). 172
Figure 5.8 Integrated EL intensity under the gate voltage of -15 V as a function of implanted Si ion dose (a) or implantation energy (b). The calculated EL intensity is based on the power law shown in Eq. (5.2). 174
Figure 5.9 Decomposition of the EL spectrum for sample 5a under the gate voltage of -15 V into the following four EL bands: ~460-nm, ~610-nm, ~740-nm, and ~1260-nm bands. 175
Figure 5.10 Evolution of peak wavelength of the EL spectra with gate voltage for sample 5a. 176
Figure 5.11 Gate-voltage dependence of the contribution of each EL band for sample 5a. 176
Figure 5.12 Influence of the implanted Si ion dose on the EL spectrum. The EL spectra shown in the figure are from samples 5a, 5b and 5c. 177
Figure 5.13 Influence of the implantation energy on the EL spectrum. The EL spectra shown in the figure are from samples 8a, 5a and 2a. 177
Figure 5.14 Contribution of each EL band as a function of the implanted Si ion dose. 178
Figure 5.15 Contribution of each EL band as a function of the implantation energy. 179
Figure 5.16 Energy band diagram illustrating electroluminescence from the ITO/SiO_2:Si^+/Al capacitor structure. E_c, E_v, and E_f refer to the conduction band, the valence band, and the Fermi level energy, respectively. Energy values are denoted in eV. 184
Figure 5.17 EL spectra for the as-implanted sample, and the samples annealed at 700 and 1100 ^oC for 20 min. 185
Figure 5.18 EL spectra for the as-implanted sample, and the samples annealed for 10 and 30 min at 1000 ^oC. 186
Figure 5.19 Integrated EL intensity as a function of annealing temperature. .. 188
Figure 5.20 Integrated EL intensity as a function of annealing duration. 188
Figure 5.21 PL spectra of the samples with a thicker oxide (~1000 nm) and synthesized with a higher implantation dose (1×10^{17} cm^{-2}) at the

energy of 100 keV. The samples were annealed at 1000 ^{o}C and 1100 ^{o}C for 30 min, respectively. 190

Figure 5.22 PL and EL spectra of the samples implanted with 4×10^{16} cm^{-2} Si ions at the energy of 10 keV. The samples are annealed at 1100 ^{o}C for 1 hour. 191

Figure 5.23 Distribution of the implanted Si in the Si nitride film obtained from SRIM simulation. 194

Figure 5.24 EL spectra from the Si^{+}-implanted Si nitride film annealed at 1100 ^{o}C under the gate voltage of -12, -15, and -17, and -20 V, respectively. The inset shows the *I-V* characteristics and the integrated EL intensity as a function of current density. 195

Figure 5.25 Microphotograph of EL patterns under different gate voltages for sample 5a. (a) -12 V, (b) -15 V, (c) -17 V, and (d) -20 V. 196

Figure 5.26 EL spectra from the sample of Si^{+}-implanted Si nitride film annealed at 1000 ^{o}C under the gate voltage of -12, -15, and -17, and -20 V, respectively. 197

Figure 5.27 EL spectra from the Si^{+}-implanted Si nitride films for the as-implanted sample, and the samples annealed at 1000 ^{o}C and 1100 ^{o}C for 1 h. 198

Figure 5.28 Comparison between normalized PL and EL spectra of Si^{+}-implanted Si nitride films at different annealing temperatures. 200

Figure 6.1 TEM image of the nc-Si embedded in a SiO_2 thin film. 204

Figure 6.2 *C-V* and *G-V* characteristics for the voltage sweeping from -5 V to +5 V and then from +5 V to – 5V. 205

Figure 6.3 Flatband voltage shift as a function of positive stress voltage. 206

Figure 6.4 Flatband voltage shift as a function of negative stress voltage. 207

Figure 6.5 Change in conductance peak (G_{max}) as a function of positive stress voltage. 208

Figure 6.6 Change in conductance peak (G_{max}) as a function of negative stress voltage. 209

Figure 6.7 Flatband voltage shift as a function of stress time under positive voltage. 210

Figure 6.8 *G-V* characteristics before and after dielectric breakdown of the gate oxide containing Si nanocrystals. The breakdown is caused by the positive stress at 14 V for 70 s. The inset shows the corresponding *I-V* characteristics before and after the breakdown. 211

Figure 6.9 *C-V* characteristics before and after dielectric breakdown of the gate oxide containing Si nanocrystals. The breakdown is caused by the positive stress at 14 V for 70 s. 213

Figure 6.10 Equivalent circuit of a single nc-Si and the conversion to a frequency-dependent capacitance $C_p^j(\omega)$ in parallel with a frequency-dependent conductance $G_p^j(\omega)$ 213

Figure 6.11 C 1s core level shift relative to the reference for the pure SiO_2 sample, the as-implanted sample and the sample annealed at 1100 °C for 20 min. 216

Figure 6.12 The decomposition of Si 2p spectra for the as-implanted sample (a) and the sample annealed at 1100 °C for 20 min (b). The unfilled triangles represent the difference between the measurement and the fitting. 218

Figure 6.13 Annealing-temperature effect on C 1s core level shift (a), the total concentration of the interfacial suboxides (b) and the nc-Si concentration (c). The annealing duration is fixed at 20 min....... 220

Figure 6.14 (a) The total concentration of the interfacial suboxides as a function of annealing time; and (b) the comparison between the nc-Si concentration and the C 1s core level shift as a function of annealing time. The annealing temperature is fixed at 1000 °C. . 222

LIST OF TABLES

TABLE 3.1. Values of the parameters A_i, E_i, Γ_i (i = 1, 2, 3, 4), $\varepsilon_1(\infty)$ of the Lorentz oscillator model for both bulk crystalline silicon and the nc-Si embedded in SiO_2. 83

TABLE 3.2. Values of the parameters A_i, B_i and C_i (i = 1, 2, 3, 4), $n(\infty)$ and E_g of the FB model for both bulk crystalline silicon and the nc-Si embedded in SiO_2.. 83

TABLE 3.3 Size, bandgap and static dielectric constant of nc-Si annealed for different durations. E_g^{exp} and ε_s^{exp} are the bandgap and the static dielectric constant of nc-Si obtained from the spectral fittings based on the four-term FB model, respectively. E_g^{cal} is the nc-Si bandgap obtained from the calculation with Eq. (3.35), while ε_s^{cal} is the nc-Si static dielectric constant obtained from the calculation with Eq. (3.36). 99

TABLE 3.4. Implantation energies and doses, maximum volume fractions of excess Si in SiO_2, and the nc-Si sizes for the 5 samples. 107

TABLE 3.5. Values of the parameters A_i, B_i, and C_i (i = 1, 2, 3, 4), $n(\infty)$ and E_g of the four-term FB model for the 5 samples. The corresponding values of bulk crystalline Si are also included. 110

TABLE 4.1 Summary of sample conditions for the SiO_x films prepared by PECVD. 153

TABLE 5.1 Summary of implantation recipes for the samples in the EL study. 162

NOMENCLATURES

AFM	Atomic Force Microscopy
CB	Coulomb Blockade
CHE	Channel-Hot-Electron
CMOS	Complimentary Metal-Oxide-Semiconductor
C-V	Capacitance-Voltage
CVD	Chemical vapor Deposition
DOS	Density Of States
DRAM	Dynamic Random Access Memory
EDS	Energy Dispersive x-ray Spectroscopy
EEPROM	Electrical Erasable Programmable Read-Only Memory
EFM	Electrostatic Force Microscopy
EL	Electroluminescence
EMA	Effective Medium Approximation
ESR	Electron Spin Resonance
FB	Forouhi-Bloomer
FN	Fowler-Nordheim
FTIR	Fourier Transform Infrared Spectroscopy
G-V	Conductance-Voltage
HRTEM	High Resolution Transmission Electron Microscopy
ITO	Indium Tin Oxide
I-V	Current-Voltage
LED	Light-emitting Diode
LPCVD	Low Pressure Chemical Vapor Deposition

MEG	Multiple Exciton Generation
MOS	Metal-Oxide-Semiconductor
MOSFET	Metal-Oxide-Semiconductor Field Effect Transistor
NBOHC	Non-Bridging Oxygen Hole Center
nc-Si	Si nanocrystals
NOV	Neutral Oxygen Vacancy
NVM	Non-Volatile Memory
PECVD	Plasma Enhanced Chemical Vapor Deposition
PL	Photoluminescence
PLD	Pulse Laser Deposition
PMT	Photomultiplier Tube
PSi	porous silicon
QC	Quantum Confinement
rf	Radio Frequency
RT	Room Temperature
sccm	Standard Cubic Centimeters per Minute
SE	Spectroscopic Ellipsometry
SEM	Scanning Electron Microscope
SET	Single Electron Tunneling
SIMS	Secondary Ion Mass Spectroscopy
SOI	Silicon On Insulator
SPM	Scanning Probe Microscopy
SRIM	Stopping and Range of Ions in Matter
SRO	Si-Rich Oxide
TEM	Transmission Electron Microscopy

UV	Ultraviolet
VHFCVD	Very High Frequency Chemical Vapor Deposition
VLSI	Very Large Scale Integration
WOB	Weak Oxygen Bond
XPS	X-ray Photoelectron Spectroscopy
XRD	X-ray Diffraction

CHAPTER 1 INTRODUCTION

This thesis presents a study on optical and optoelectronic properties of Si nanocrystals (nc-Si) embedded in dielectric films and their applications in photonic and non-volatile memory devices. This chapter introduces the background, motivation, and major contribution of this work. Details of this study are presented in the following chapters.

1.1 Si Photonics

The semiconductor technology has undergone a tremendous development over the past several decades. Silicon has become the most important semiconductor material in microelectronic industry, since the invention of the first bipolar transistor in 1949 [1]. Germanium had been the initial choice of material for semiconductor devices, but it was soon replaced by silicon because of its natural superiority over germanium. First, the 1.12 eV bandgap of Si makes it ideal for operation at room temperature, while the 0.67 eV bandgap of Ge results in a high leakage current. Second, the resistivity of Si is much higher than that of Ge and thus allows for fabrication of devices with high breakdown voltages. Finally, pure Si can be produced with a much lower cost than Ge. Nowadays, Si devices constitute over 95% of the market of semiconductor devices [2].

On the other hand, as electronic device dimensions increasingly become smaller and smaller, the traditional electrical interconnects that were used for chip-to-chip communication becomes increasingly impractical due to the heat

dissipation of the metal wires which threatens the reliability of both the device and the system. When the device dimensions decrease to the nanoscale, the device will suffer a lot from the traditional electrical interconnects due to its propagation delay, high power consuming, and low bandwidth [3]. Fortunately, optical interconnects would probably provide us with a promising alternative strategy for overcoming these challenges. Since chip-to-chip communication via optical interconnects requires an on-chip emitter and detector, an important challenge on the materials and the integration of photonic devices into main stream silicon process has triggered a new research subject, i.e., silicon photonics, recently.

Over the past few years, the emergence of the new concept, Si photonics, has greatly encouraged the intensive pursuit of more inexpensive and commercial technologies for fabricating light emitters and modulators with Si-based materials. Given that the Si light emitters, especially, lasers, are not commercially available, research in the field of Si photonics is still in an early stage. Silicon photonics is a research and development effort of manufacturing photonic and optoelectronic devices with the mainstream Complimentary Metal-Oxide-Semiconductor (CMOS) technology in the semiconductor industry. To the best of our knowledge, most of the photonics components fabricated with Si technology have been demonstrated, such as optical modulators [4, 5], switches [6, 7], detectors [8, 9], and low-loss waveguides [10, 11], for the purpose of research. The further step of Si photonics is to find a low-loss active medium that can be used for achieving optical gain and wave-guiding in order to pave the way for fabricating a Silicon laser. However, for light emitting diodes (LEDs), III-V compound materials are predominantly used due to their

direct bandgap, which have the larger possibility of radiative recombination of electrons and holes. Since Si processing technology is more developed and cheaper, it would be advantageous to use silicon in these photonic applications. It would also allow for direct integration of the optoelectronic devices and the very large scale integration (VLSI) circuit. However, bulk crystalline Si is a poor light emitter at room temperature, mainly due to its indirect bandgap, resulting in a low rate of radiative recombination. Si is an indirect bandgap material, in which light emission is a phonon-mediated process with low probability (spontaneous recombination lifetimes in the ms range). In standard bulk Si, competitive non-radiative recombination rates are much higher than the radiative ones and most of the excited electron-hole pairs recombine non-radiatively. This yields very low internal quantum efficiency ($\eta_i \approx 10^{-6}$) of luminescence for bulk crystalline Si. In addition, fast non-radiative processes such as Auger or free carrier absorption severely prevent population inversion for silicon optical transitions at the high pumping rates needed to achieve optical amplification.

1.2 Si Nanocrystals

During the nineties many strategies have been employed to overcome these material limitations for fabricating all-Si LEDs and silicon lasers. The most successful ones are based on the exploitation of low dimensional Si where Si is nanoscaled and hence the optical and electronic properties of free carriers are modified by quantum confinement effects. Of all the types of low dimensional silicon, porous Si (PSi) has received the most intensive research attention in the

early years of exploitation of nanoscaled Si. The discovery of the visible photoluminescence (PL) from PSi in 1990 [12] has triggered a large research effort in the field of porous Si and other Si nanostructures. It has been shown, as well, that luminescence wavelength can be tuned in a wide range and relatively high quantum efficiencies could be obtained, improving the prospect of using Si for LEDs.

However, it is not reliable to utilize porous silicon in optoelectronic devices because of its instability in light emission [13] structural fragility [14], and incompatibility with conventional IC technology [15]. Therefore, silicon nanocrystals (nc-Si) are considered to be the preferable strategy for overcoming these challenges. SiO_2 thin film embedded with nc-Si, which is actually a planar waveguide, is considered as a very promising candidate for such an active medium with the advantages of chemical stability and full compatibility with the CMOS process. Among the different techniques used to fabricate nc-Si, the ion implantation of silicon into a dielectric matrix, preferably SiO_2 films, followed by high temperature annealing, is deemed as one of the most promising candidates for producing electrical and chemical stable silicon nanocrystals. This technique allows for an accurate control of the depth distribution of nc-Si within the SiO_2 film and yields a smaller size (~ 2-~ 5 nm) and a narrow size distribution of the nc-Si. Most importantly, it also offers the advantage of being fully compatible with the main stream CMOS process. In this thesis, we therefore mainly work on nc-Si synthesized by Si ion implantation in order to investigate the optical and optoelectronic properties of Si nanocrystals embedded in dielectric films.

1.3 Objectives and Scope of Research

Si nanocrystals are crystalline clusters with sizes of 1 to 10 nanometers (nm) in diameter, generally consisting of ~10 to ~1000 silicon atoms. The optical, electronic, magnetic properties of nc-Si are significantly modified by quantum confinement (QC) effect, which was initially thought to be the main mechanism of strong luminescence from nc-Si. In this work, nc-Si embedded in dielectric matrix is synthesized by techniques of Si ion implantation and plasma enhanced chemical vapor deposition (PECVD). The main objective of this thesis is to investigate the optical and optoelectronic properties of the nc-Si embedded in dielectrics. The scope of research and approach in this thesis is as follows:

1. Synthesis of nc-Si embedded in dielectric matrix using Si ion implantation and PECVD. Various nanocrystal distributions in the dielectric films have been achieved by varying the implantation energy and implanted Si ion dose.
2. Characterization of dielectric films containing nc-Si using transmission electron microscopy (TEM), x-ray diffraction, secondary ion mass spectroscopy (SIMS), and x-ray photoelectron spectroscopy (XPS), spectroscopic ellipsometry (SE).
3. Experimental determination of the optical properties, including the optical constants and dielectric function, of Si nanocrystals embedded in a SiO_2 matrix. The optical properties of different nc-Si structures, i.e., isolated Si nanocrystals dispersed in SiO_2 and densely-stacked nc-Si layer embedded in SiO_2, are determined using SE analysis.

4. Depth profiling of optical constants of SiO2 films embedded with Si nanocrystals.
5. Investigation on the photoluminescence (PL) properties of silicon nanocrystals embedded in dielectric thin films, including SiO_2 and Si_3N_4. The study on the PL mechanism of dielectric films embedded with Si nanocrystals.
6. Fabrication of LEDs based on a metal-oxide-semiconductor-like (MOS-like) structure with nc-Si embedded in the dielectrics.
7. Investigation on the electroluminescence (EL) and electrical properties, including the current-voltage (*I-V*) capacitance-voltage (*C-V*), of the MOS-like LEDs containing nc-Si in the dielectrics.
8. Electrical characterization of MOS capacitors with Si nanocrystals embedded in the gate oxide, including *I-V*, *C-V*, and conductance-voltage (*G-V*), for the investigation of charging/discharging effect of the structure.
9. Investigation on the charging mechanism of Si nanocrystals embedded in SiO_2 by XPS analysis.

1.4 Major Contributions of the Thesis

In this thesis, a thorough investigation on the optical and optoelectronic properties of silicon nanocrystals embedded in dielectric matrix has been performed. Photoluminescence and electroluminescence of light emitters based on nc-Si have been characterized. The major contributions of this thesis are listed as follows:

1. Optical properties of Si nanocrystals embedded in SiO_2 matrix have been

studied with SE analysis.

1). Dielectric functions and optical constants of Si nanocrystals embedded in SiO_2 matrix have been experimentally determined in the photon energy range of 1-5 eV.
2). The bandgap expansion of Si nanocrystals embedded in SiO_2 due to the quantum size effect has been investigated.
3). Thermal annealing effect on the bandgap and dielectric function of silicon nanocrystals has been studied.
4). Depth profiling of optical constants of the SiO_2 film containing Si nanocrystals has been determined.
5). The dielectric function of densely-stacked Si nanocrystal layer has been determined, and the thermal annealing effect on the dielectric function of densely-stacked Si nanocrystal layer has been investigated.
6). Influence of nanocrystal size on the optical properties of Si nanocrystals has been investigated.

2. Photoluminescence of Si nanocrystals embedded in dielectric matrix has been studies.

1). PL of Si nanocrystals embedded in SiO_2 synthesized by Si ion implantation has been studied, and related mechanisms of PL have been proposed.
2). Thermal annealing effect on PL properties of Si nanocrystals embedded in SiO_2 synthesized by Si ion implantation has been investigated.
3). The influence of excess Si concentration on PL properties of Si nanocrystals embedded in SiO_2 synthesized by Si ion implantation has

been investigated.

4). Photoluminescence of Si nanocrystals embedded in Si_3N_4 has been studied, and related mechanisms of PL have been proposed.

5). Photoluminescence of Si rich SiO_x films synthesized by PECVD have been investigated, and the related mechanisms have been proposed.

3. Electroluminescence of the metal-oxide-semiconductor-like (MOS-like) structures with Si nanocrystals embedded in SiO_2 has been investigated.

1). MOS-like LED structures with Si nanocrystals embedded in the gate oxide have been fabricated.

2). Visible and infrared electroluminescence of silicon nanocrystals embedded in SiO_2 has been realized. The electroluminescence properties have been systematically studied, and the related mechanisms have been discussed.

3). The influence of nanocrystals distribution and thermal annealing on the EL properties of Si nanocrystals embedded in SiO_2 has been studied.

4). Blue-violet electroluminescence has been observed from the Si_3N_4 film embedded with silicon nanocrystals synthesized by ion implantation.

5). The thermal annealing effect on the EL properties of Si nanocrystals embedded in Si_3N_4 has been investigated.

4. Electrical properties of Si nanocrystals have been studied.

1). Influence of stress voltage and stress time on the flatband voltage shift of the MOS capacitor with Si nanocrystals embedded in the gate oxide has been investigated.

2). The electrical properties of the MOS capacitor with Si nanocrystals embedded in the gate oxide after dielectric breakdown has been studied.

3). Charging mechanism of Si nanocrystals embedded in SiO_2 film has been studied with X-ray photoelectron spectroscopy.

1.5 Organization of the Thesis

This thesis is mainly focused on the study of optical and optoelectronic properties of silicon nanocrystals embedded in SiO_2 and Si_3N_4 films and their applications in photonics devices. The organization of this thesis is as follows:

CHAPTER 1 provides a brief introduction to silicon photonics and silicon nanocrystals. The motivation of this study and the major contributions of this thesis are briefed in this chapter also.

In CHAPTER 2, a literature review on the research of silicon nanocrystals is presented. Various fabrication methods for synthesizing silicon nanocrystals embedded in dielectric films are described. In addition, the characterizations of the SiO_2 films embedded with silicon nanocrystals by optical and non-optical techniques are discussed in this chapter. Finally, the applications of silicon nanocrystals in light emitters and memory devices are introduced.

CHAPTER 3 gives out a comprehensive optical study of silicon nanocrystals embedded in SiO_2 matrix. A non-destructive method is developed to determine the optical constants and dielectric function of silicon nanocrystals embedded in SiO_2 synthesized by ion implantation using spectroscopic ellipsometry. In this

chapter, the influence of thermal annealing on the bandgap and dielectric function of silicon nanocrystals is studied. Besides, the quantum size effect on the band gap and dielectric function of silicon nanocrystals is investigated. Moreover, we have carried out a comparative study on the dielectric function of two types of nanostructured silicon, i.e., dispersed silicon nanocrystals and densely stacked Si nanocrystal layer embedded in SiO_2. In addition, the depth profiling of optical constant of SiO_2 films embedded with nc-Si has been determined, suggesting a potential in the application of active waveguides.

CHAPTER 4 mainly investigates on the photoluminescence properties of Si nanocrystals embedded in SiO_2. Various mechanisms attributed for the related photoluminescence bands are discussed. Thermal annealing effect on the photoluminescence properties is studied. The PL mechanisms are discussed. In this chapter, two methods, i.e., ion implantation and PECVD, are employed to synthesize Si nanocrystals embedded in SiO_2.

In CHAPTER 5, MOS-like LEDs are fabricated with silicon nanocrystals embedded in the dielectrics (i.e., SiO_2 and Si_3N_4) synthesized by ion implantation. Electroluminescence properties of the MOS-like LEDs are investigated. The EL mechanisms are discussed. Influence of thermal annealing on the EL properties of the system is studied.

CHAPTER 6 mainly investigates on the electrical properties of MOS capacitors with Si nanocrystals embedded in the gate oxide. Charging/discharging effect is studied by *I-V*, *C-V*, and *G-V* characteristics. The charging mechanism of Si nanocrystals is investigated by XPS analysis.

Finally, CHAPTER 7 summarizes the work carried out in this thesis. Recommendations for the future research are also presented in this chapter.

CHAPTER 2 LITERATURE REVIEW

2.1 Introduction

If an all-Si laser could be created, it would revolutionize the design of supercomputers and lead to new types of optoelectronics devices [16]. It has been widely accepted that the realization of an efficient Si light emitter will broaden the spectrum of products from Si semiconductor industry. This will be of the most important benefit to the direct integration of optoelectronic devices into microelectronic circuit with CMOS processing, which would greatly reduce the fabrication cost and yields of optoelectronic devices. Recently, Si nanocrystals have received intensive research interest due to their efficient light emitting properties that arise from quantum size effect as a direct result of their nanometer size. Nanocrystals or quantum dots are particles with the physical dimensions on the scale of a few nanometers and typically contain only a few thousand atoms or less. The resulting three-dimensional quantum confinement of carriers in nanocrystals gives rise to many optical and electrical properties that are dramatically altered from their bulk semiconductor counterparts, and thus presents some fascinating physical phenomena that would be useful in device applications.

There has been a steady progress in both theoretical and technological aspects of Si nanocrystals-based optoelectronic devices. Some researchers have demonstrated that infrared light can be emitted, wave-guided, detected, modulated and switched in silicon [17]. Efficient visible light emission from

nanoscaled Si has been reported to be possible in theoretical [18-21] and experimental aspects [12, 14, 22, 23]. SiO_2 and Si_3N_4 have been proven to be robust matrix providing good chemical and electrical passivation of Si nanocrystals. Therefore, in the second part of this chapter, we summarize the fabrication methods that are commonly used to synthesize nc-Si embedded in dielectric films, such as SiO_2 and Si_3N_4.

2.2 Synthesis of Si Nanocrystals

The fabrication of nanoscaled silicon started in 1956 when Uhlir [24] made porous Si (PSi) for the first time, by etching a *p*-type silicon wafer in a solution containing HF. In this thesis, we are focused on the fabrication of silicon nanocrystals embedded in dielectric films, the most promising potential candidate for the application of nc-Si based optoelectronic devices. There are several fabrication techniques to synthesis nc-Si embedded in SiO_2 films including chemical vapor deposition (CVD) [25-32], sputtering [33-35], pulse laser deposition (PLD) [36-40], and Si ion implantation into dielectric films [14, 41-43]. In this thesis, Si ion implantation followed by high temperature annealing and PECVD are employed to synthesize nc-Si embedded in dielectric films.

2.2.1 Porous silicon

Porous Si occupies a special place in the research of Si nanocrystals, since it was the first and still the most inexpensive material which has been studied as

nanostructured Si. The fabrication procedure of PSi is very flexible and uncontrollable. PSi is usually formed by electrochemical anodization of Si in an HF electrolyte. The choice for the substrate should naturally be *p*-type Si wafers, because the anodization reaction at the interface of Si/electrolyte requires the presence of holes [44]. A most important factor that need to be controlled in the fabrication is the porosity (i.e., the fraction of Si removed from the substrate) of PSi, because it significantly influences the size of nc-Si, which has significant effect on the electrical and optical properties of porous Si.

2.2.2 Chemical Vapor Deposition

Chemical vapor deposition (CVD) is a chemical process used to produce thin solid films on the surface of a substrate by thermal decomposition and/or reaction of gaseous compounds. In a typical CVD process, the wafer (substrate) is exposed to one or more volatile precursors, which react and/or decompose on the substrate surface to produce the desired deposit. Both low pressure chemical vapor deposition (LPCVD) [25-27] and plasma enhanced chemical vapor deposition (PECVD) [30-32] have been frequently used in the fabrication of Si nanocrystals. Figure 2.1 shows the schematic illustration of a typical LPCVD reactor. LPCVD are CVD processes at subatmospheric pressures. Reduced pressures tend to reduce unwanted gas-phase reactions and improve film uniformity across the wafer. LPCVD is typically performed on both sides of the substrate at the same time at ~800 ºC in a reactor. Silicon nanocrystals can be synthesized by controlling the early stages of low pressure chemical vapor deposition with pure SiH_4. In the PECVD technique, several reacting gases are

activated by electric energy to react on the substrate, thus forming a thin solid film. Silicon nanocrystal films can be prepared using very high frequency (VHF) PECVD from a N_2O:SiH_4 mixture. After the mixture turn into plasma under high pressure and energy, the Si ions will be doped in situ with SiO_x (x<2) film formation. The ratio of Si to O in the film as well as the microstructure of the film can be varied by controlling gas composition and plasma condition as well as substrate temperature.

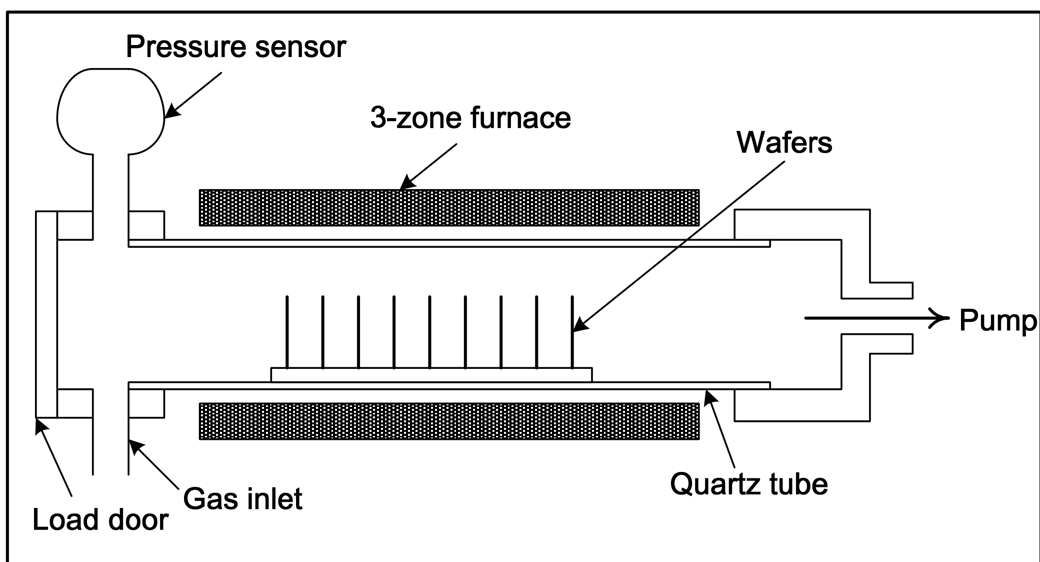

Figure 2.1 Schematic illustration of a typical LPCVD reactor.

2.2.3 Sputtering

Sputtering is achieved by bombarding a target with energetic ions, typically Ar^+. The schematic of a sputtering system is shown in Fig. 2.2. Co-sputtering is based on the simultaneous sputtering from two targets. This allows for production of alloyed composite materials which have a controlled composition. By independently varying the power applied to each magnetron in either balanced or unbalanced configurations, an entire spectrum of mixed

compositions and microstructures is possible. When Ar^+ gas is injected into the field formed by high voltage applied on the electrodes, they will be accelerated and collide on the cathode surface. Then atoms of cathode material will be sputtered out and deposited on the substrate surface forming an ultra-fine particle film. Silicon nanocrystals embedded in dielectric films can be prepared by co-sputtering with two electrodes, one with a silicon target and the other with quartz target [33-35]. Silicon nanocrystals can also be embedded in other dielectric films by replacing the quartz target with other dielectric materials of interest.

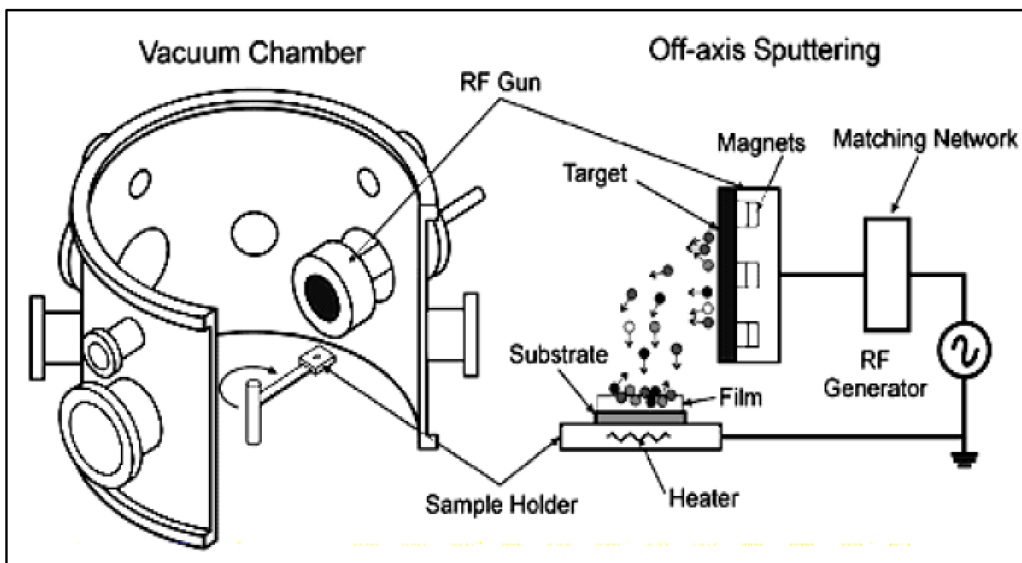

Figure 2.2 Schematic of the deposition chamber and off-axis RF magnetron sputtering system.

2.2.4 Pulse Laser Deposition

Strictly speaking, pulse laser deposition (PLD) is another type sputtering technique. A pulsed laser beam is focused onto the surface of a solid target. The strong absorption of the electromagnetic radiation by the solid surface leads to

rapid evaporation of the target materials. The evaporated materials consist of highly exited and ionized species. They presented themselves as a glowing plasma plume immediately in front of the target surface if the ablation is carried out in vacuum. Magnetron and plasma sputtering usually lead to energetic atoms and ions striking the substrate. This affects the films structure. In PLD, the ions and atoms are much less energetic, having less damage on the film microstructure. Figure 2.3 shows the schematic illustration of a typical PLD system that was used to synthesize silicon nanocrystals [39]. Indeed, PLD is so straightforward that only a few parameters, such as laser energy density and pulse repetition rate, need to be adjusted during the process. The distribution of Si nanocrystals synthesized by PLD can vary from 2 to 10 nanometers by changing the background gas species and pressures [40].

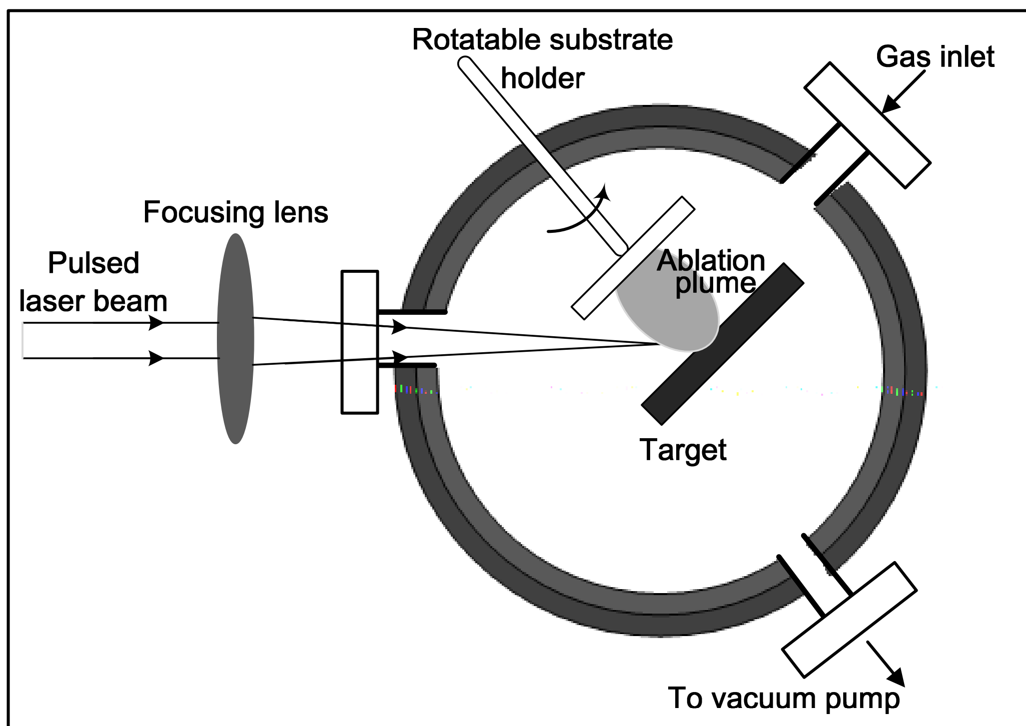

Figure 2.3 Schematic of typical PLD system [39].

2.2.5 Ion Implantation

Figure 2.4 presents the schematic illustration of a typical ion implanter. Ion implantation is a process conducted in a vacuum chamber at a very low pressure (10^4-10^5 Torr) in which charged energetic atoms are directly introduced into a substrate or dielectric films. In the standard fabrication process of the Si industry, ion implantation is mainly used to introduce dopant ions into the surface of silicon wafers. The superiority of ion implantation over diffusion doping method has made it steadily replace diffusion doping in an increasing number of applications.

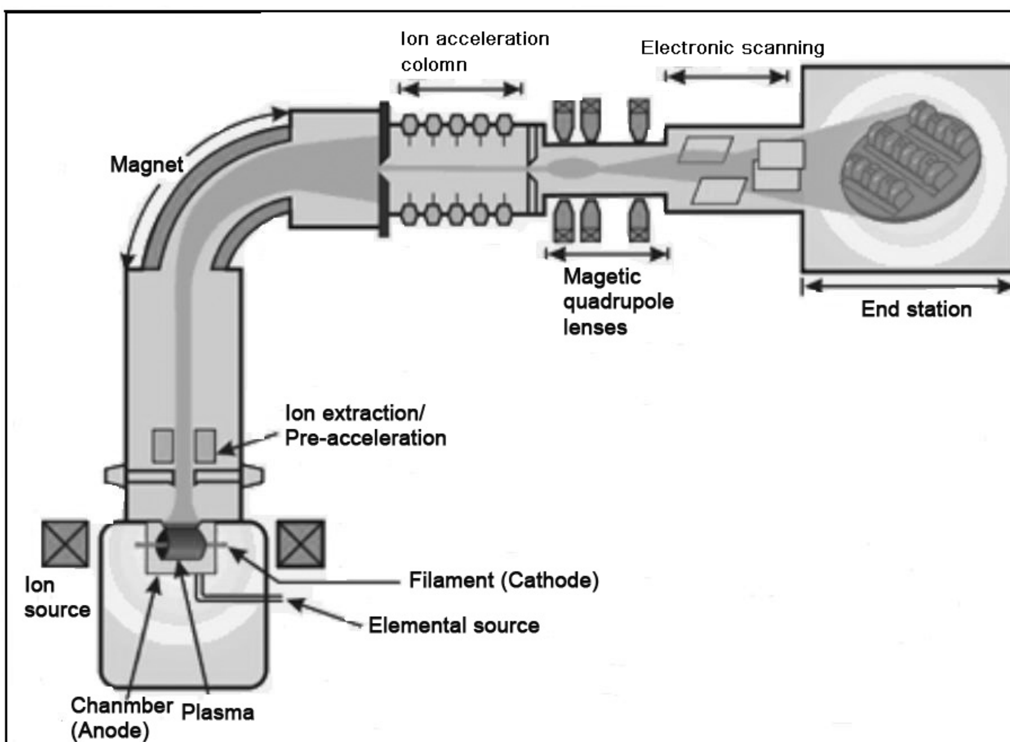

Figure 2.4 Schematic illustration of a typical ion implanter.

Ion implantation also offers many advantages in the fabrication of Si nanocrystals embedded in dielectric films. An ion implanter provides a high voltage accelerating particles to form a high-velocity beam of Si ions which can penetrate the surface of as-grown dielectric films. In a typical process, Si ions

are implanted into an as-grown SiO_2 or Si_3N_4 film. The concentration and depth distribution of nc-Si in the film are decided by the implantation energy and the implantation dose. By this technique, the distribution of excess Si can be controlled through adjusting the implantation energy and the dose of implanted Si ions. After Si ion implantation, nc-Si can be formed with a high temperature annealing typically above 1000 ^{o}C [14, 41-43]. N_2 is frequently used as the annealing ambient in the post-implantation annealing process. Other annealing ambient, such as Ar and N_2+H_2, have been also used for the investigation on the photoluminescence properties of nc-Si embedded in dielectric films [45]. Ion implantation allows for synthesis of nc-Si with a smaller size (~2-5 nm) and a narrow size distribution, which is a very import factor in device applications. A production-level implanter may cost from $1 to $2 million, and cost is its greatest disadvantage. However, the advantages of stability, flexibility and easy process control have far outweighed the disadvantage of cost. Therefore, we have employed the technique of Si ion implantation as the main method to fabricate nc-Si embedded in dielectric films in this study.

2.2.6 What Is Important in the Fabrication of nc-Si?

There are many other techniques that have been used to synthesize Si nanocrystals, such as reactive evaporation [46, 47], mechanical ball milling followed by spin-coating [48], and aerosol synthesis [49-51]. Each technique has its own advantages and disadvantages, though the purpose of all synthesizing methods is to achieve size-controlled Si nanocrystals. Except for the size of nc-Si, from the application point of view, researchers need to pay

special attention to the size distribution and depth distribution of nc-Si in dielectric films. As reported by Heitmann [52], the most important factors that may have significant impact on the potential device applications based on nc-Si are illustrated in Fig. 2.5. Methods mentioned above normally result in a relatively broad size distribution of synthesized nc-Si. Size control in these systems is usually realized by shrinking the entire size distribution by varying the ion implant energy and silicon within the SiO_2 matrix [41, 43] or by subsequent oxidation of nanocrystals [26, 53]. The resulting broad size distributions complicate the characterization of quantum confinement effects and are undesirable for potential applications. In the case of optical characterization, this problem can be partially resolved by resonant excitation which results in narrowing of the size distribution of silicon nanocrystals that are optically excited [54].

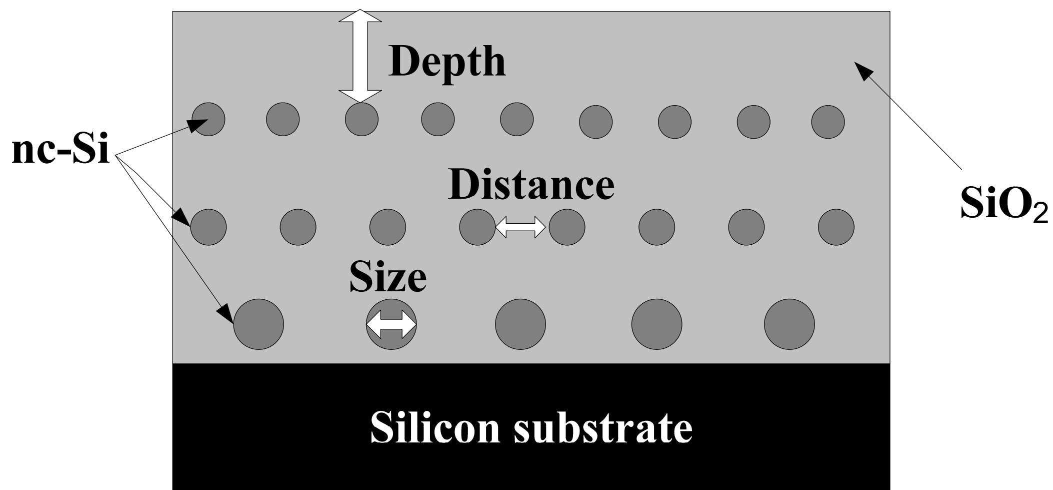

Figure 2.5 A schematic illustration of three most important factors of nc-Si fabrication for device applications [52].

2.3 Characterization of Dielectric Films Embedded with nc-Si

2.3.1 X-ray Diffraction

X-ray diffraction (XRD) is a powerful analytical technique which reveals information on the crystal structure, chemical composition, and physical properties of materials and thin films. It can be also used to estimate the size of the embedded nanocrystals inside the dielectric films [55-59]. The mean size of nc-Si embedded in a SiO_2 film can be estimated from the broadening of the Bragg peak in the XRD spectrum with the Scherer's equation

$$D = \frac{K\lambda}{\Delta\theta \cos(\theta_B)}, \qquad (2.1)$$

where D is the mean size of nc-Si, λ is the wavelength of the x-ray, θ_B is the Bragg angle, and $\Delta\theta$ is the full width of the half maximum (FWHM) of the Bragg peak, and K is a constant on order of unity whose exact value depends on the specific shape and size distribution of the crystalline clusters and on the specific crystallographic direction of the diffraction of the diffracting planes. K=0.9 within few percent is widely accepted for the calculation of average size of nc-Si embedded in dielectric matrix [56]. $\Delta\theta$ should be corrected for instrumental broadening with the equation

$$\Delta\theta^2 = \Delta\theta_{\mathrm{m}}^2 - \Delta\theta_{\mathrm{Si}}^2 \qquad (2.2)$$

where $\Delta\theta_{\mathrm{m}}$ is the measured FWHM of the peak, and $\Delta\theta_{\mathrm{Si}}$ is the FWHM of polycrystalline Si. Yerci has presented that ion implantation and subsequent annealing produces nc-Si with the size ranging from 3.7 to 7.4 nm embedded in

SiO_2 film [57]. This is in accordance with the results of transmission electron microscopy (TEM) conducted by Wang [60]. As a technique for determining the size of embedded nanocrystals, XRD has two superiorities over TEM. The first is that the averaging process for nanocrystal size determination is potentially more reliable than the results of TEM measurement because the diffraction signal from a large number of clusters is averaged over the x-ray-illuminated volume. Moreover, XRD allows for detection of amorphous precipitates as amorphous silicon also presents a characteristic x-ray diffraction pattern [59, 61].

2.3.2 X-ray Photoelectron Spectroscopy

X-ray photoelectron spectroscopy (XPS) is a surface analysis technique, with which samples are irradiated by monochromatic soft x-rays and characteristic kinetic and binding energies of emitted core electrons are measured. XPS can be employed to investigate the electronic and chemical structures of dielectric thin films embedded with nc-Si. Liu *et al.* has reported studies on the structure and chemical states of Si-rich SiO_x ($x < 2$) films by the technique of XPS [62, 63]. For nanoscale particles, it has been frequently reported that that the core levels measured with XPS shift with the reduction of particles size [64-68]. Figure 2.6 presents the XPS spectra for Si-rich SiO_x ($x < 2$) films and the Si 2p core level peaks. Various mechanisms have been proposed to explain the size-dependent core-level shift [64-67]. However, it was reported that the charging effect plays a more important role for the core-level shift in the system of nc-Si embedded in SiO_2 [67].

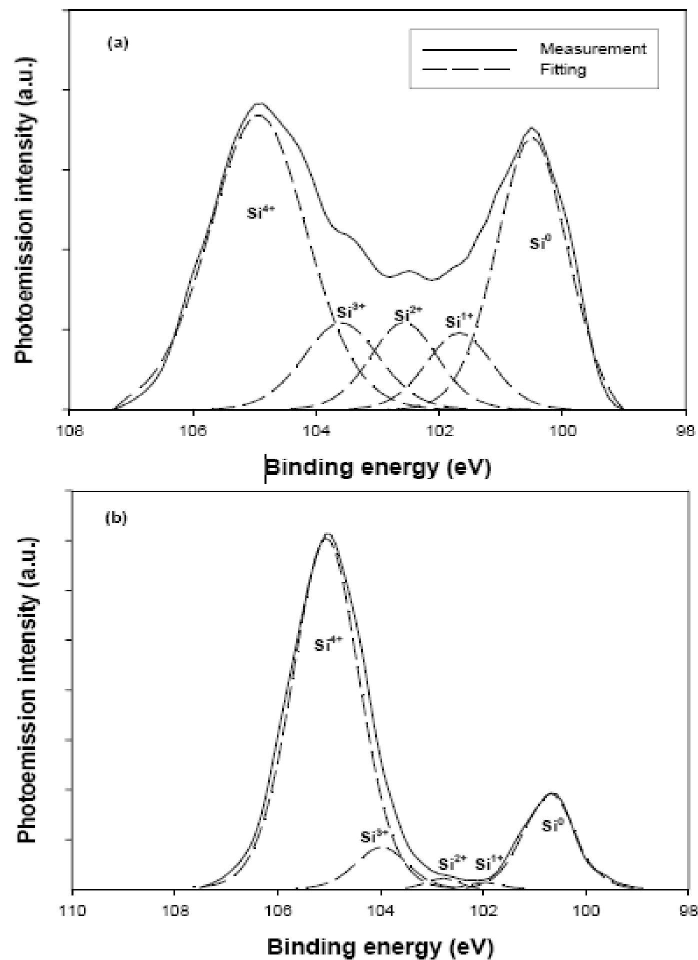

Figure 2.6 XPS spectra of Si-rich SiO_x ($x < 2$) formed by Si ion implantation into thermally grown SiO_2 for the (a) as implanted sample and (b) the sample annealed at 1000 ^{o}C for 20 min [63].

2.3.3 Raman Spectroscopy

Raman spectroscopy employs the Raman scattering or Raman effect, which is the inelastic scattering of a photon, for material analysis. Raman scattering has been demonstrated to be sensitive to the bonding of materials and the order/disorder of crystalline structures [58, 69-72]. Accordingly, Raman spectroscopy has been frequently used to characterize the material system of dielectric films embedded with nc-Si. Figure 2.7 shows Raman spectra of the SiO_2 embedded with nc-Si [71]. As a rough estimation for the crystallinity value,

i.e., the volume fraction of nc-Si and amorphous Si (*a*-Si) in the film, one can use a ration of t he integrated intensities for the signals related to nc-Si and *a*-Si, as shown in Fig. 2.7. Different models have been employed to interpret the Raman spectra of Si nanocrystals. A comparison study has been carried out on the models that have been widely used for the interpretation of Raman spectra of nc-Si [69].

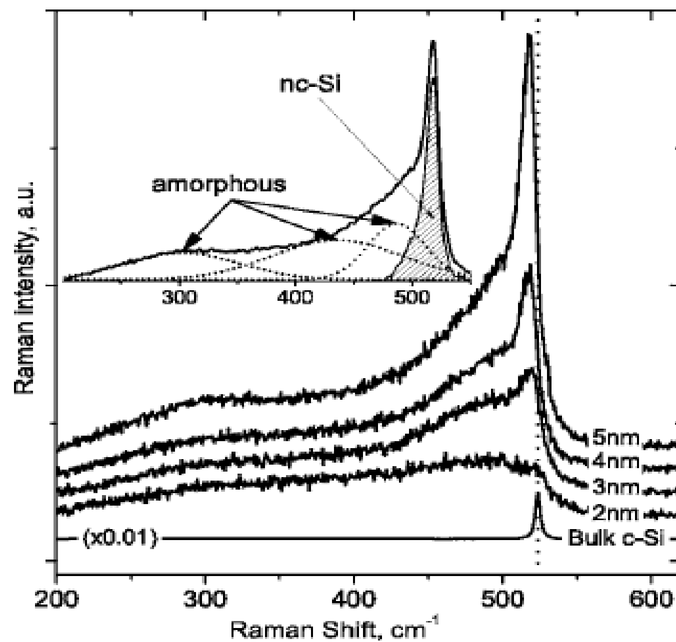

Figure 2.7 Raman spectra of the SiO_2 embedded with nc-Si. The particle size of nc-Si is indicated on the related curves [71].

2.3.4 Secondary Ion Mass Spectroscopy

Secondary ion mass spectroscopy (SIMS) is a technique to analyze the composition of thin solid films by sputtering the surface with a focused primary ion beam and analyzing ejected secondary ions. The secondary ions are measured with a mass spectrometer to determine the elemental, isotopic, or molecular composition of the surface. Researchers in the industry have frequently used SIMS to trace elements in solid materials, especially the doping

profiles in Si substrate [73]. It has been also widely used to determine the depth distribution of Si and Ge nanocrystals embedded in dielectric films [62, 68, 74-76] . As the operation of SIMS measurement is very expensive, researchers have frequently employed the simulation of stopping range of ions in matter (SRIM) to predict the depth profile of implanted Si ions in the SiO_2 or other dielectric films [77, 78]. It is a theoretical calculation based on a quantum mechanical treatment of ion-atom collisions for estimating the profile of implanted ions in a solid thin film [79] . As shown in Fig. 2.8, the consistency of the results between SIMS measurements and SRIM simulation indicates that SRIM can be used as a reliable tool to predict the distribution of nc-Si in the oxide [80].

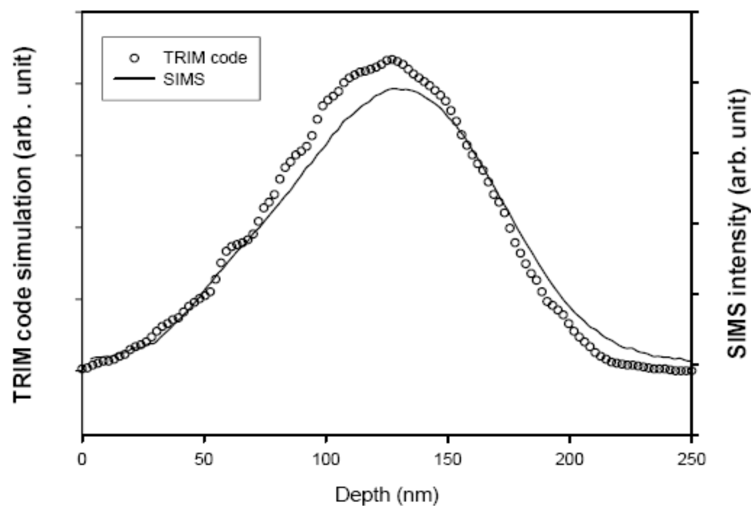

Figure 2.8 Depth profiles of excess Si in the SiO_2 film obtained from SIMS and TRIM code calculation [80].

2.3.5 Transmission Electron Microscopy

Transmission electron microscopy (TEM) is microscopy technique whereby a beam of electrons is transmitted through an ultra thin specimen, interacting with the specimen as it passes through. An image is formed from the electrons

transmitted through the specimen, magnified and focused by an objective lens and appears on an imaging screen. As for a state-of-the-art TEM facility, the incident electrons are with such a high energy (~100 – 200 keV) that the spatial resolution of the obtained image can be as small as 0.2 nm.

High resolution TEM (HRTEM) has been extensively used to study the formation of nc-Si, information on the nanocrystal size as well as the size distribution, and lattice structures [51, 60, 81-84].

Figure 2.9 shows a typical cross-sectional HRTEM image of a Si nanocrystal embedded in SiO_2 matrix fabricated by Si ion implantation at the implantation energy as high as 100 keV [60]. Wang *et al.* has carried out a study on the microstructural defects inside the nc-Si or around the interface using HRTEM [60, 83]. Bonafos *et al.* [81] has carried out cross-sectional TEM measurements for the samples with Si ions implanted into 10-nm SiO_2 films at low energies ranging from 1 to 5 keV, as shown in Fig. 2.10. Furthermore, plan-view TEM images have been also employed to investigate the formation and microstructure of Si nanocrystals embedded in SiO_2, as shown in Fig. 2.11.

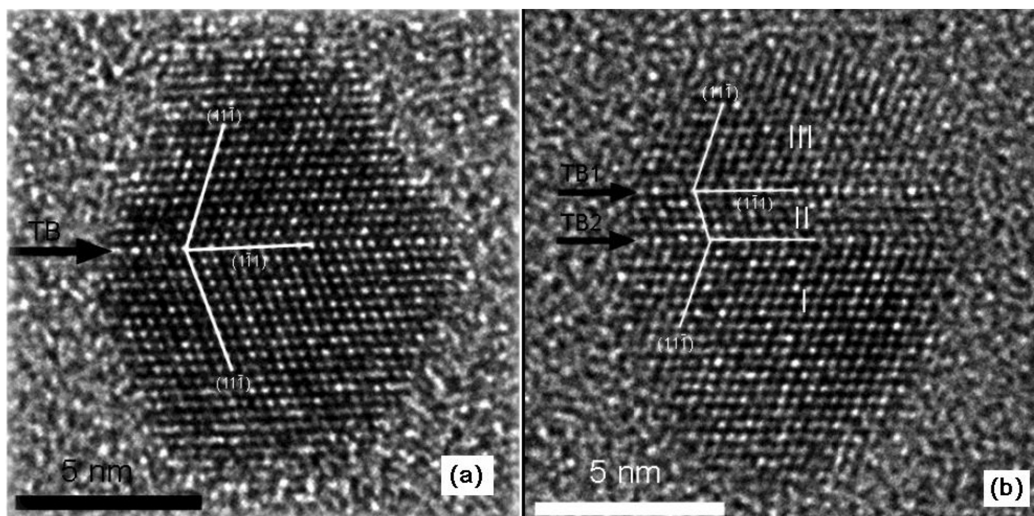

Figure 2.9 Cross-sectional HRTEM image of a typical Si nanocrystals embedded in SiO_2 synthesized by Si ion implantation and subsequent high temperature annealing (a) with a single-twin structure; and (b) with a double-twin structure [60]. The implantation was carried out at the energy of 100 keV with the Si ion dose of 3×10^{17} cm^{-2}.

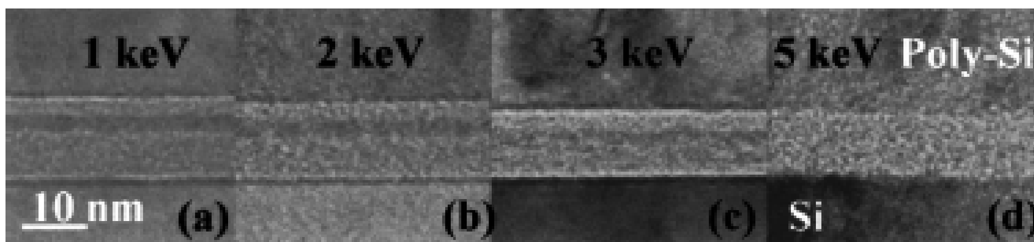

Figure 2.10 Cross-sectional HRTEM images of SiO_2 samples implanted with a constant Si ion dose of 10^{16} cm^{-2} at implantation energies ranging from 1 to 5 keV followed by thermal annealing at 950 °C for 30 min in N_2 ambient [81].

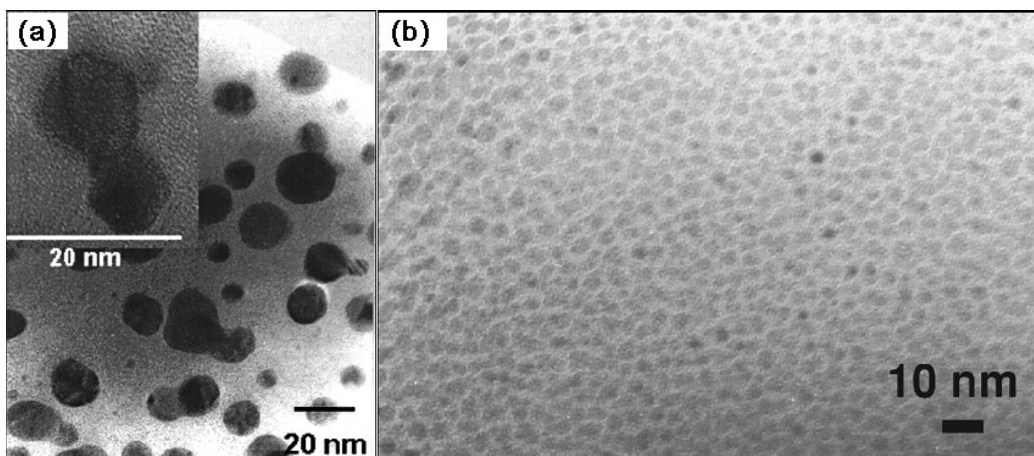

Figure 2.11 Plan-view TEM images of nc-Si embedded in SiO_2 synthesized by rapid thermal CVD process (a) [84] and aerosol reaction (b) [51].

2.3.6 Scanning Electron Microscopy

The scanning electron microscopy (SEM) is a type of electron microscopy that creates various images by focusing a high energy beam of electrons onto the surface of a sample and detecting signals from the interaction of the incident electron with the sample's surface. SEM has been frequently used to determine the size of number density of nc-Si [85-89]. Figure 2.12 presents typical TEM images of Si nanocrystals synthesized by photo chemical vapor deposition (photo-CVD) on a SiO_2/Si substrate, with each figure showing the size and the number density variation of nc-Si depending on the flow ratio of SiH_4 and H_2, and deposition time [85]. Si nanocrystals synthesized by low energy ion implantation and subsequent thermal annealing have been also observed with high resolution SEM [89].

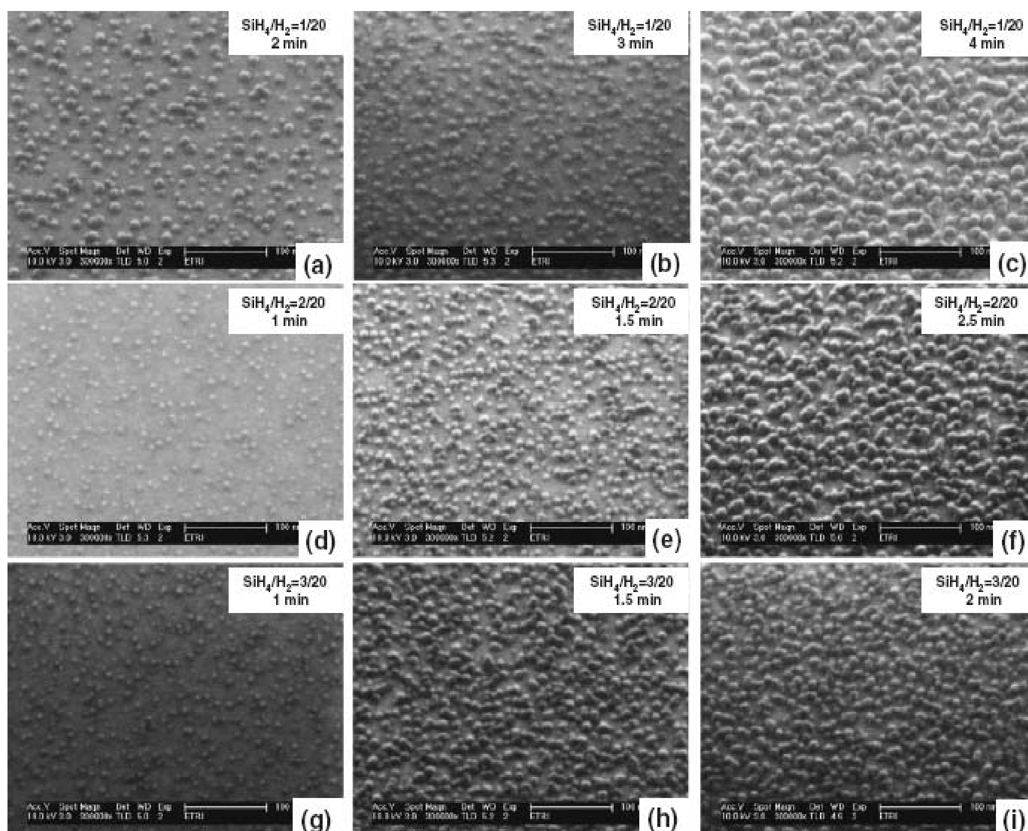

Figure 2.12 SEM image of time dependency of the growth of Si nanocrystals [85].

2.3.7 Atomic Force Microscopy

The atomic force microscopy (AFM) or scanning probe microscopy (SPM) is a very high-resolution type of scanning probe microscopy, with demonstrated resolution of fractions of a nanometer. There are three most common operation modes of AFM, including (a) contact [90, 91], (b) non-contact [92, 93], and (c) intermittent contact or tapping [94-96]. Contact mode operation is normally used to observe the topography. The capacitance of the sample from surface to bulk and the dc surface voltages can be measured under the non-contact operation mode. As for the tapping mode, the tip of the cantilever is intermittently touching the surface of the sample. Surface topography can also be measured with the tapping mode. As compared with the contact mode, the tapping mode can significantly reduce the damage on the surface during contacts between the tip and the surface of the sample. The tapping mode has been widely used to observe the topography of nc-Si deposited with CVD method. Figure 2.13 shows the tapping-mode image AFM image of as-grown nc-Si synthesized by very high frequency chemical vapor deposition (VHFCVD) pulsed plasma technique [96].

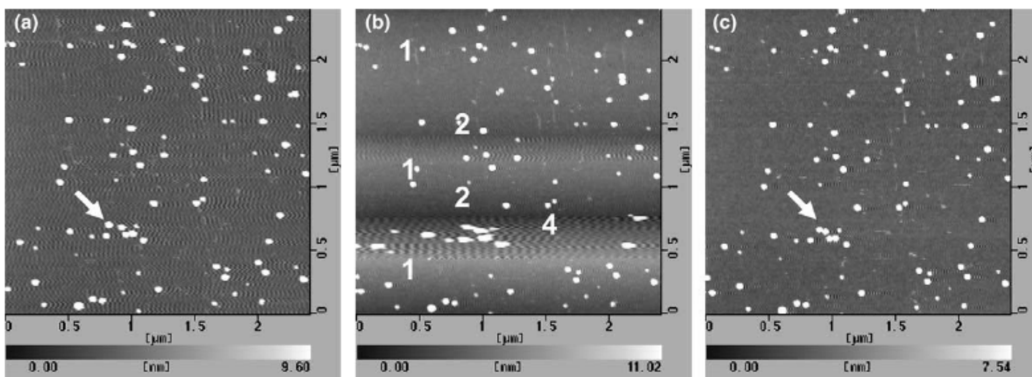

Figure 2.13 Tapping-mode AFM images of as-grown nc-Si taken with the scanning rate of (a) 1Hz; (b) 1, 2, and 4 Hz as indicated; (c) 1 Hz taken right after (b) [96].

2.3.8 Spectroscopic Ellipsometry

Spectroscopic ellipsometry (SE) is a versatile and powerful optical technique, which is non-destructive and contactless, for the investigation of the dielectric function or optical constants of thin films. Based on the analysis of the change of polarization of the reflected light, SE can yield information on the dielectric properties of layers that are thinner than the wavelength of the probing light itself, even down to a single atomic layer.

It is indispensible to know the optical constants of nc-Si for the application in the waveguides and light emitting layers. SE provides a useful tool for the investigation of optical constants of both continuous nc-Si layer and distributed nc-Si embedded in dielectric films. For the past decade, researchers have used SE to study the dielectric properties [74, 75, 97-101], including the optical constants (i.e., n is the refractive index, and k is the extinction coefficient) and dielectric functions. Optical constants of continuous nc-Si thin film deposited by pulsed CO_2 laser pyrolysis of silane has been studied by Amans *et al.* using ellipsometry [98], as shown in Fig. 2.14(a). With regard to the dispersed nc-Si embedded in amorphous SiO_2, the dielectric function of embedded nc-Si with the size of 3-5 nm have been determined using SE as reported in Ref. [102]. Figure 2.14(b) shows the dielectric function of the nc-Si embedded in SiO_2 synthesized by LPCVD [102]. Both the results of continuous nc-Si films and distributed nc-Si embedded in SiO_2 show a dielectric suppression as compared with bulk crystalline Si. This is consistent with the results that we have reported [74, 75].

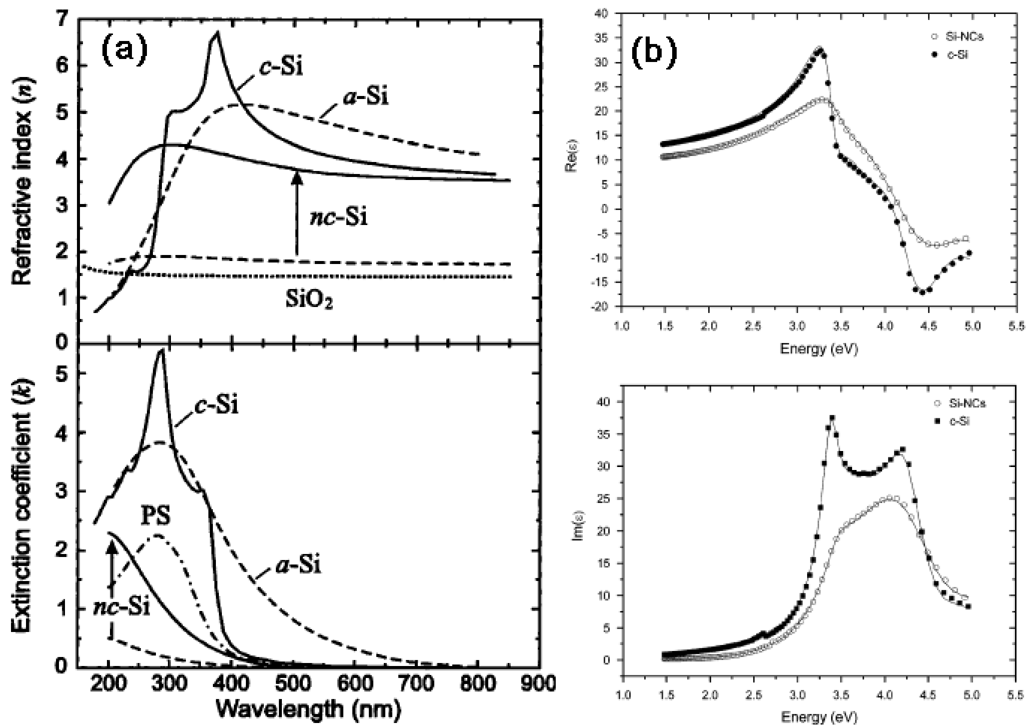

Figure 2.14 (a) Refractive index and extinction coefficient as a function of wavelength for different silicon materials [98]; (b) Dielectric function of embedded nc-Si with the size of 3.9 nm in SiO_2 matrix and c-Si sample as a function of energy [102].

2.3.9 Current-Voltage (*I-V*) Characteristics

The current transport mechanisms and charge trapping properties of nc-Si embedded in dielectric films have been generally studied by current-voltage (*I-V*) characterization. Despite the large number of works that have been carried out on the electrical properties of nc-Si, there are still many open questions remained about basic characteristics of non-volatile memory devices based on nc-Si. It has been frequently reported that the *I-V* characteristic of MOS capacitors with nc-Si embedded in the gate oxide presents hysteresis effect [103-105]. The hysteretic effect is due to the charging and discharging effect of nc-Si embedded in the oxide. By investigating on the *I-V* characteristics, Ng *et al.* have found that the introduction of nc-Si into the gate oxide leads to a

reduction in the onset voltage of Fowler-Nordheim (FN) tunneling, and the onset voltage decreases with the nc-Si concentration [106], as shown in Fig. 2.15.

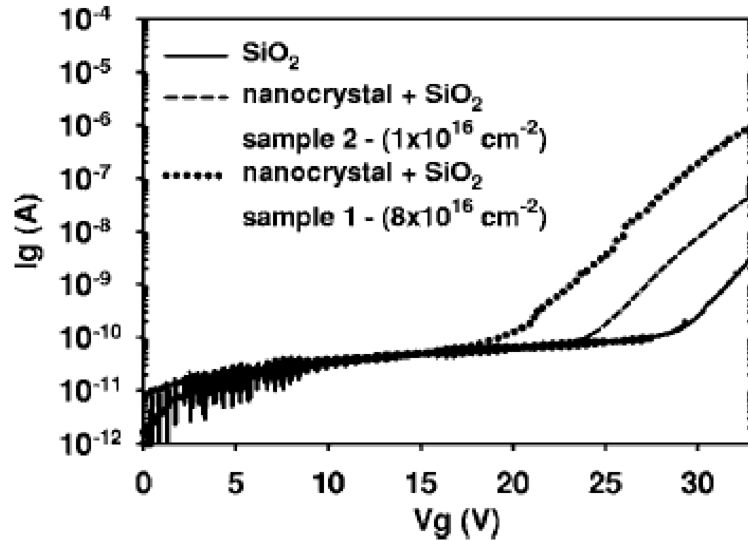

Figure 2.15 Current-voltage (*I-V*) characteristics of the MOS capacitors with nc-Si embedded in the gate oxide [106].

As for the MOSFET with nc-Si embedded in the gate oxide, a small hysteresis effect has been observed in the drain current (I_d) versus gate voltage (V_g) characteristics, as shown in Fig. 2.16 [107]. This is due to the shift of the flatband voltage because of the existence of nc-Si in the gate oxide where charging/discharging effect takes place.

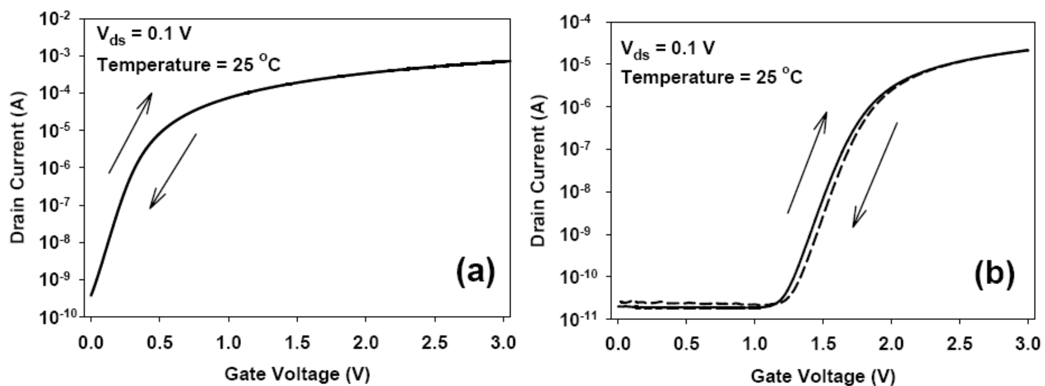

Figure 2.16 Reversible drain current I_d measurements for both the samples (a) without nc-Si and (b) without nc-Si embedded in the gate oxide [107].

2.3.10 Capacitance-Voltage (*C-V*) Characteristics

The capacitance-voltage (*C-V*) characteristic is very important for people to understand the operation conditions and the electrical behavior of MOS devices with nc-Si embedded in the gate oxide. The hysteresis effect can also be observed in the *C-V* measurement when sweeping from the accumulation region to the depletion region and afterwards from the depletion region to the accumulation region, as reported by many research groups [108-110]. The hysteresis effect represents a shift in the flatband voltage (V_{fb}) or the threshold voltage (V_{th}). Figure 2.17 shows the high-frequency *C-V* curve of the MOS capacitor with nc-Si embedded in SiO_2, from which a clear hysteresis effect has been observed [108].

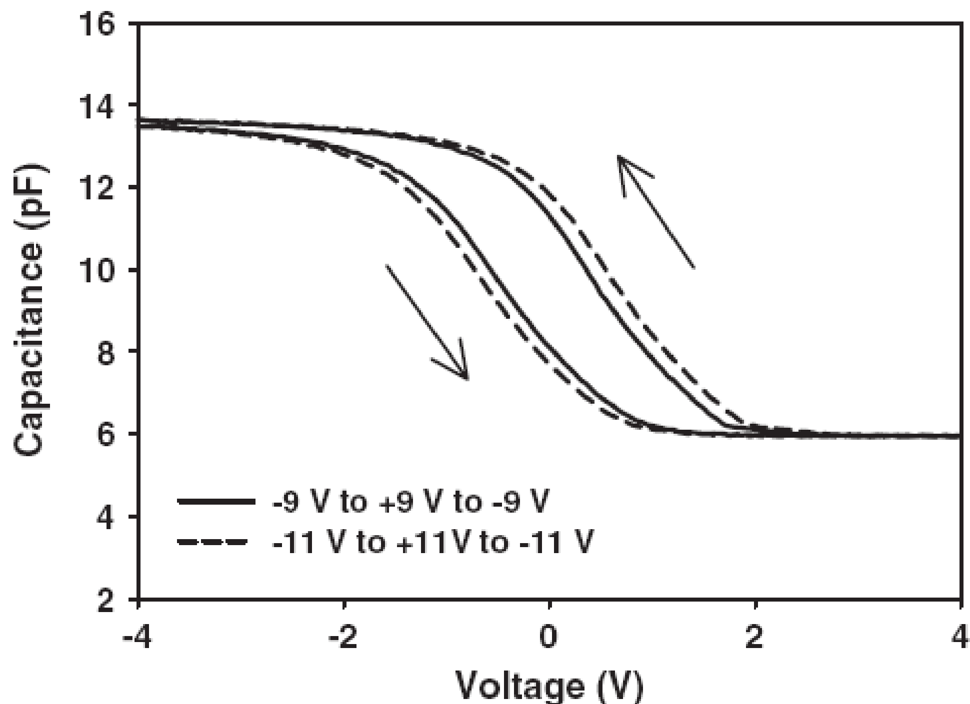

Figure 2.17 Hysteresis effect observed in the *C-V* measurement of the MOS capacitor with nc-Si embedded in the gate oxide fabricated by Si ion implantation and thermal annealing [108].

Ng *et al.* has reported a study on the thermal annealing effect on the flatband voltage as well as on the instability of the flatband voltage due to the remaining Si ions trough *C-V* measurements of a MOS capacitor with the gate oxide implanted with Si ions [111]. Figure 2.18 shows the effect of annealing on *C-V* characteristics and flatband voltage shift for the MOS capacitors with nc-Si embedded in the gate oxide synthesized by Si ion implantation [111].

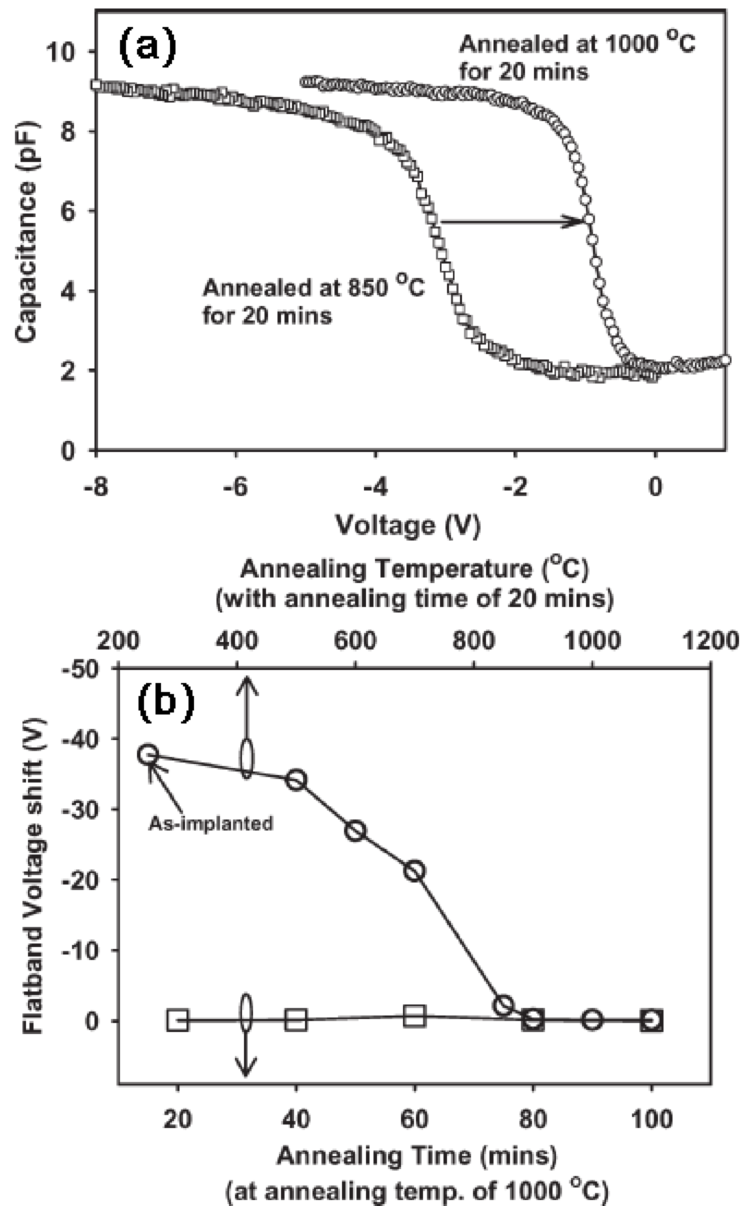

Figure 2.18 (a) Comparison of the *C-V* characteristics between two annealing temperature (850 ^{o}C and 1000 ^{o}C); (b) Flatband voltage shift as a function of both annealing temperature and annealing time [111].

2.3.11 Other Characterization Techniques

There are still many other characterization techniques, such as Energy dispersive x-ray spectroscopy (EDS) [26, 112], electron spin resonance (ESR) [42, 113], Fourier transform infrared spectroscopy (FTIR) [32, 112, 114], UV-visible absorbance [32, 112, 115, 116], and photoelectron spectroscopy [91], that people used to study the optical and electronic properties of Si nanocrystals. The material system with nc-Si embedded in dielectric matrix has so many unknown physical, chemical, optical, electrical, and structural properties to be discovered that one has to systematically correlate among the various results obtained by different characterization techniques. Only in this way can people understand the material system as comprehensive as possible.

2.4 Light Emission from Dielectric Films Embedded with nc-Si

2.4.1 Introduction: Direct and Indirect Transitions

Si is an indirect band gap material, thus the probability for a radiative transition is very low. This is reflected into the very long time for radiative recombinations. Due to these long radiative lifetimes, excited free carriers have large probabilities to find non-radiative recombination centers and to recombine non-radiatively. Minimum energy transitions are vertical in *k*-space for a direct bandgap semiconductor materials whereas indirect bandgap materials undergo a non-vertical transition as sketched in Fig. 2.19. In a direct bandgap material, any photon with energy equal to or larger than the energy bandgap (i.e., energy

difference between that of the valence band maximum and conduction band minimum) can participate in a direct transition and excite an electron from the top of the filled valence band to one of the states at the bottom of the conduction band. However, non-vertical absorptions in an indirect bandgap material occur via an intermediate virtual state, whereby photon absorption is accompanied by either the creation or annihilation of a phonon to achieve the momentum conservation. The indirect transition requires minimum photon energy of E_g+E_p to create an electron-hole pair and a phonon with the energy of E_p and the momentum of $\hbar(k_c-k_v)$. The alternative process is that a photon with the energy of E_g-E_p and a phonon with the energy of E_p and the momentum of $\hbar(k_c-k_v)$ are absorbed.

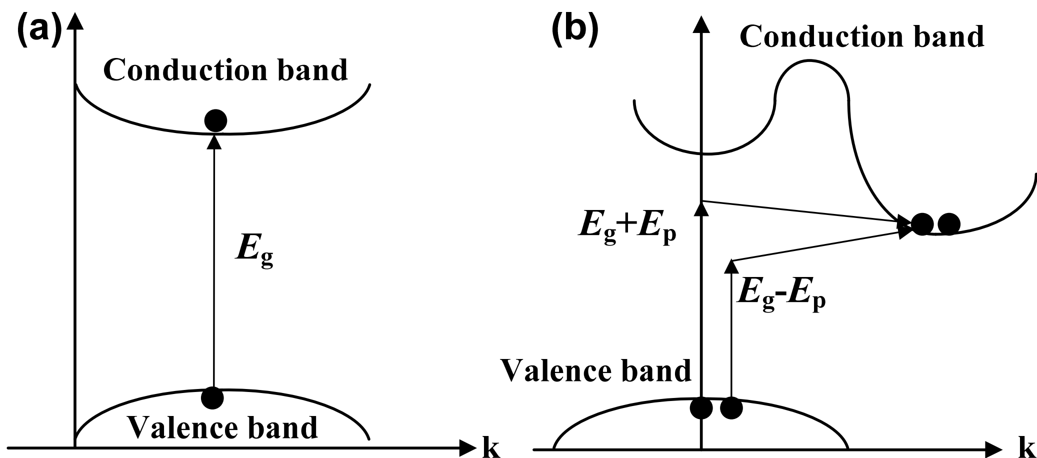

Figure 2.19 Schematic of the absorption of a photon in a direct bandgap (a) and indirect bandgap (b) semiconductor material.

In a perfect semiconductor, electron-hole pairs thermalise and accumulate at the conduction and valence band extremes. Fundamental radiative transitions in a semiconductor are those occurring at or near the band edges, namely, band-to-band or excitonic transitions. In a direct bandgap material,

momentum-conserving transitions connect states with the same k-value. Accordingly, the emitted photon has a low-energy threshold at $h\nu=E_g$, as sketched in Fig. 2.20(a). However, in an indirect bandgap semiconductor, since the momentum conservation requires electron-hole pairs to recombine radiatively only by phonon-assisted transitions, the probability of radiative transitions is smaller than that of competing non-radiative transitions. As shown in Fig. 2.20(b), indirect band-to-band radiative transitions could be realized by the assistant of phonon emission or absorption. However, the phonon emission is the most likely intermediate process, because the competing process with phonon emission emits a photon with the energy of $h\nu=E_g+E_p$ can readily be reabsorbed by the semiconductor.

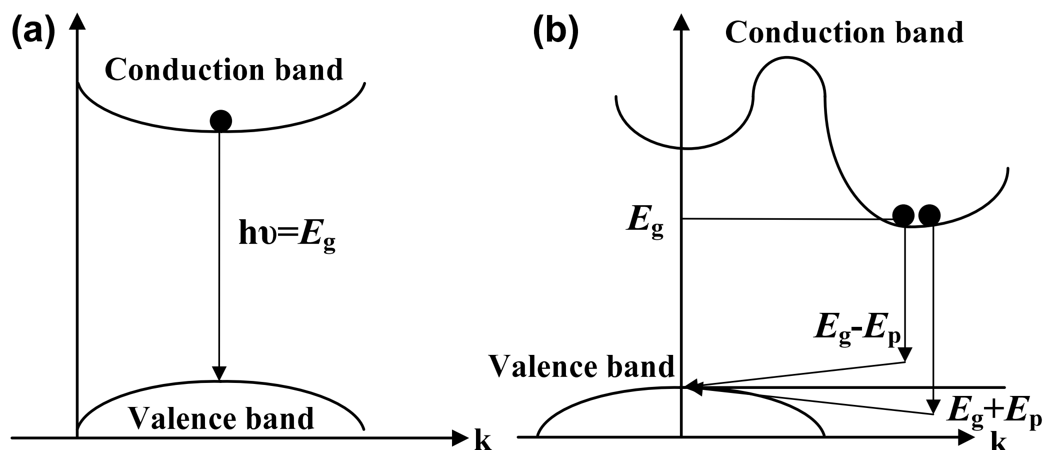

Figure 2.20 (a) Schematic of direct band-to-band radiative transitions; (b) Schematic of indirect band-to-band radiative transitions.

2.4.2 Photoluminescence

Although bulk Si is indirect semiconductor, it has been proven to be possible in the application of light generation if the size of crystal approaches to nanoscale. Efficient photoluminescence (PL) from porous Si and the material system

embedded with nc-Si has been frequently demonstrated over the past two decades [12, 14, 30, 33, 42, 113, 117-123]. Typical studies on luminescence properties of porous Si has been reviewed by Cullis [117]. In the early years of research on the nanoscaled Si, PL from porous Si has been studied most intensively [12, 122]. Figure 2.21 shows room temperature PL spectra of porous Si with 65% porosity. Two PL decay curves of porous Si with different extent of oxidation are shown in the insets. The luminescence decay is faster for the less oxidized sample, which is also less efficient.

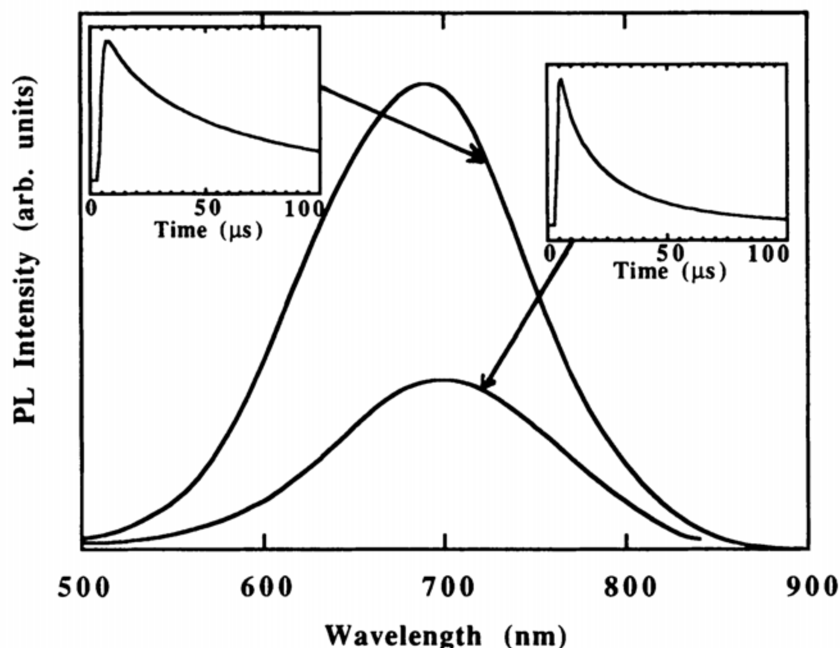

Figure 2.21 Typical PL spectra of porous Si sample with a porosity of 65%, in which the sample for the upper spectrum has the highest extent of oxidation [122].

PL properties of nc-Si embedded in SiO_2 film synthesized by Si ion implantation and subsequent annealing has been investigated intensively recently. Shimizu-Iwayama *et al.* found that a higher implantation dose leads to a bigger nanocrystal size, and thus a redshift in the PL spectrum due to the size effect could be observed with the increase of Si implantation dose [123], as

shown in Fig. 2.22(a). The result is consistent with that of another report on the size effect on PL [124]. Figure 2.22(b) shows the PL spectra as a function of annealing time at 900 ^{o}C [42]. It was found that the EL intensity increases with the annealing time without significant change in the PL peak position [42]. The unchanged PL peak position is due to the stable size of nc-Si embedded in the SiO_2 which is a result of the extremely low diffusion coefficient of Si in SiO_2. Similar results have been obtained in Ref. [125].

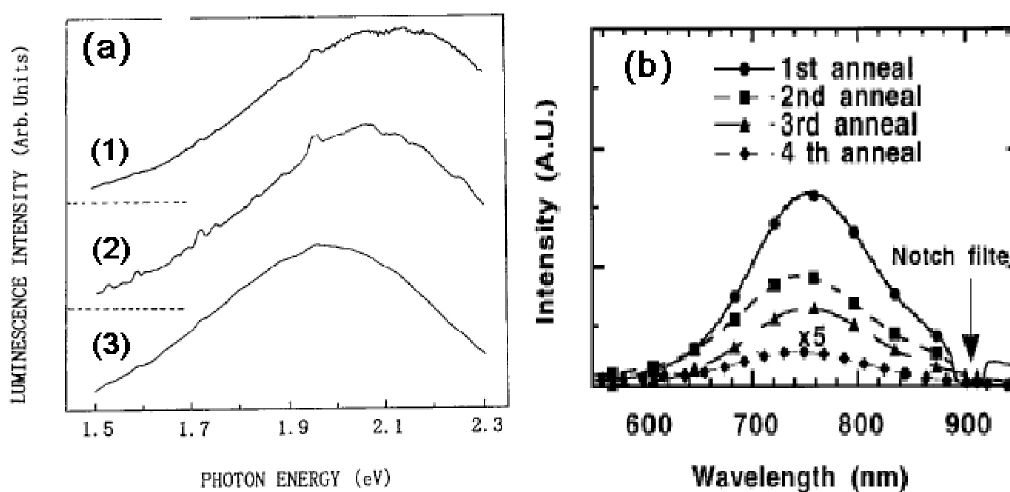

Figure 2.22 (a) PL spectra of 1 MeV Si^{+}-implanted silica glass to a fluence of 1×10^{17} ion/cm^2 (1) at liquid nitrogen temperature, (2) at room temperature, and (3) a fluence of 2×10^{17} ions/cm^2 at room temperature [123]; (b) PL spectra of a Si^{+}-implanted sample annealed in air at 900 ^{o}C for different annealing times [42].

Recently, there has been a report by Wilkinson *et al*. investigating on the effect of annealing environment on the PL of nc-Si embedded in silica [45]. The annealing ambient was found to affect the shape and intensity of PL spectra, which is an effect attributed to both variations in nanocrystal size and defect states at the nanocrystal/oxide interface. Figure 2.23 summarizes the results of Ref. [82] showing the effect of annealing ambient on the PL properties of silica embedded with nc-Si synthesized by Si ion implantation.

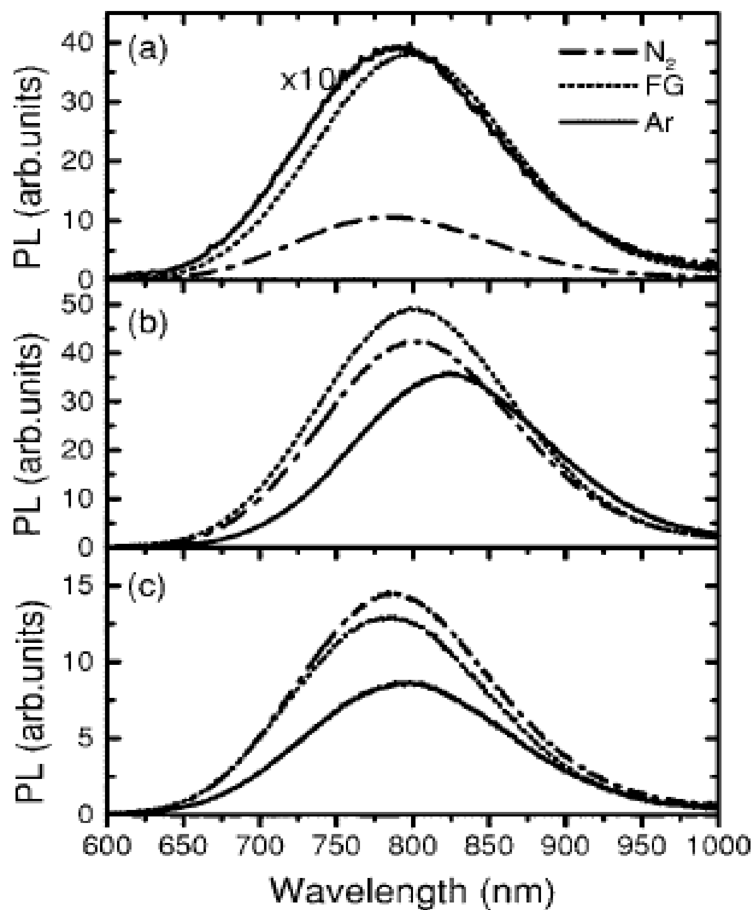

Figure 2.23 (a) PL spectra of samples annealed for 1 h at 1100 °C in N_2, 5% H_2 in N_2 (FG), or Ar; (b) PL of the samples from (a) after H passivation (500 °C in FG for 1 h); (c) PL of the samples from (a) after 750 °C in N_2 for 1 h. The spectrum from the sample annealed in Ar in (a) has been multiplied by a factor of 10 for clarity [45].

The effect of nanocrystal size on PL has been reported in Ref. [126]. The authors presented a simple and efficient method of synthesizing nc-Si in a specific depth of SiO_2 film and with a specific density of nanocrystals using reactive evaporation of SiO powders in O_2. A size-dependent blueshift of the PL spectra was observed, as shown in Fig. 2.24. The blueshift of the PL emission peak was considered to be attributed to the quantum confinement effect. Continuously tunable PL of nc-Si synthesized by Si ion implantation has also been observed [41], of which the results are consistent with that reported in Ref. [126]. Similar results have been reported for nc-Si embedded in silicon nitride

film [23].

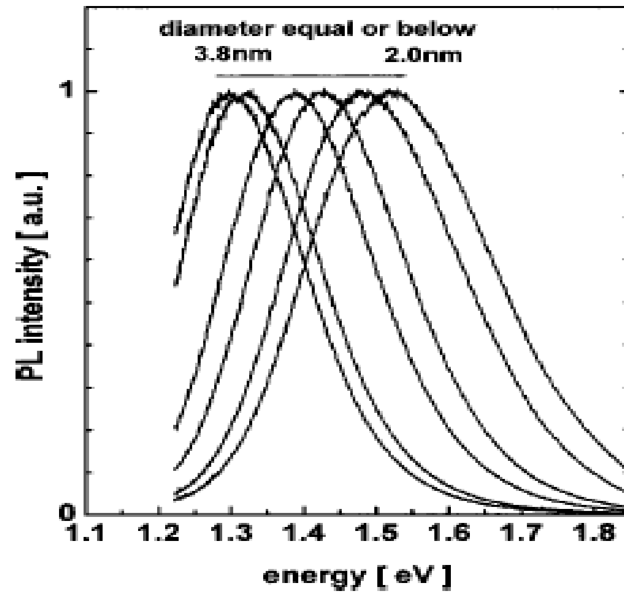

Figure 2.24 PL spectra of nc-Si showing a blueshift with the reduction of nanocrystal size [126].

Time-resolved luminescence studies on Si nanocrystals have been frequently reported [127-136]. Delerue *et al.* have proven that the PL decay behavior in an ensemble of nc-Si must be multiexponential based on time-resolve PL experiments and tight binding calculations of phonon-assisted optical transitions and can be interpreted as intrinsic properties of indirect bandgap nature of nc-Si [129]. The origin of the multiexponential PL decay of nc-Si has been debated for the last decade [128, 129, 136]. As shown in Fig. 2.25(a), longer wavelengths generally decay at a lower rate than do shorter wavelengths [129], which is in accordance with the result of Ref. [128]. Defining $G(\tau)$ as the probability of encountering a nc-Si with lifetime τ, the total PL intensity $I(t)$ can be given by

$$I(t) = I_0 \int_0^\infty \tau^{-1} G(\tau) \exp(-t/\tau) d\tau \qquad (2.2)$$

where I_0 is the PL intensity when t=0. The life time distributions determined

based on Eq. (2.2) are shown in Fig. 2.25(b). The result suggests that the multiexponential decay result from a variation of carrier localization where carries can escape from the nc-Si with different possibilities and recombine non-radiatively in the non-radiative recombination centers nearby. Other studies indicate that the decay behavior may also originate from the migration and trapping of excitons between nanocrystals with random sizes [128, 130].

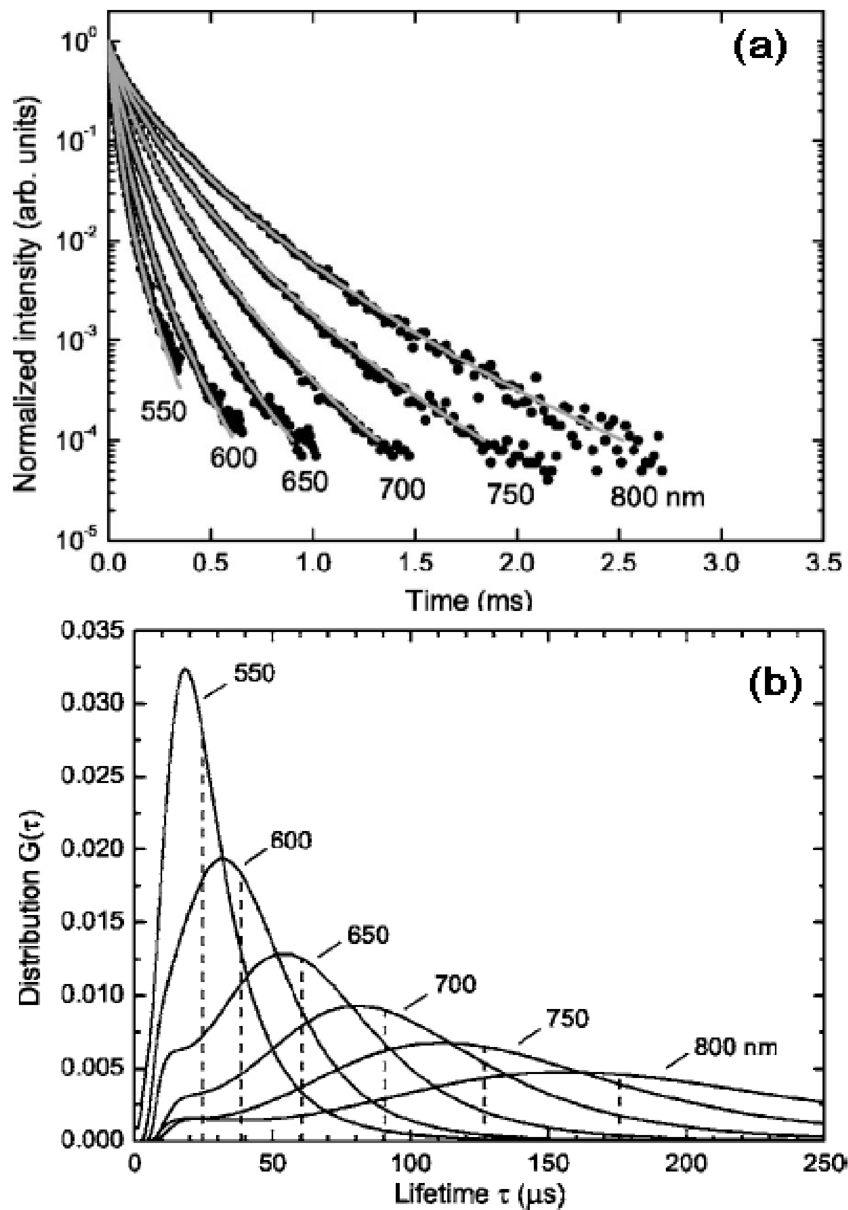

Figure 2.25 (a) PL decay curves of nc-Si measured a different wavelengths; (b) Normalized life time distribution derived from the experimental PL decay curves [129].

In the system of Si nanocrystals embedded in SiO_2 matrix, the measured PL decay rate can be described by

$$\Gamma = \Gamma_{rad}\rho + \Gamma_{nonrad} \tag{2.3}$$

where ρ is the local density of optical states of Si nanocrystals, Γ_{rad} is the radiative decay rate, and Γ_{nonrad} is the non-radiative decay rate which is dependent mainly on the passivation quality at the interface between Si nanocrystals and oxide [137]. Thus, the internal quantum efficiency (QE) can be expressed as $\eta = \Gamma_{rad}/(\Gamma_{rad} + \Gamma_{nonrad})$ [137]. Figure 2.26 shows the experimental and theoretical results of Walters *et. al* on the PL decay characteristics of Si nanocrystals in dense ensembles fabricated by ion implantation [137]. Based on the study of Walters *et. al* [137], an optimum internal quantum efficiency of ~60% can be obtained from Si nanocrystals that emit near 800 nm, as shown in Fig. 2.26(c).

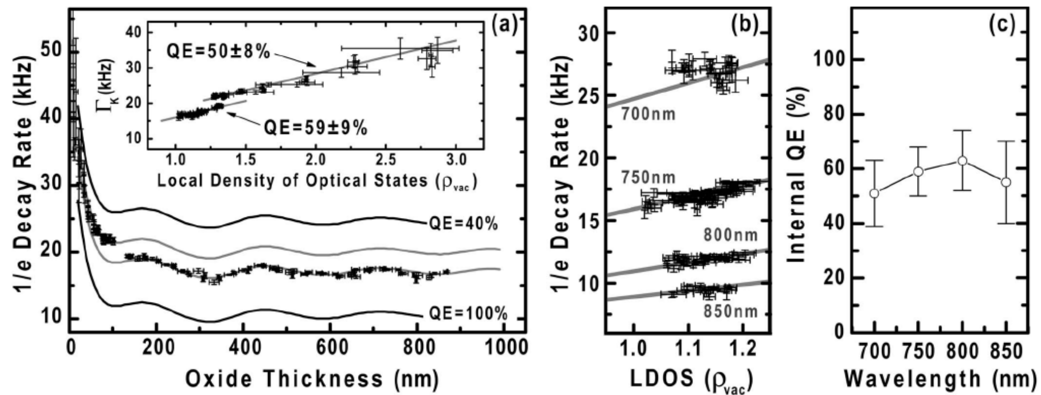

Figure 2.26 (a) The decay rate of silicon nanocrystals at 750 nm varies with oxide thickness in good agreement with a calculation of the local density of optical states. The ensemble radiative decay rate (9.4±1.3 kHz) and quantum efficiencies for two samples are determined by a least squares fit to the linearized data (inset). (b) Measured total decay rate as function of LDOS at different wavelengths. (c) Quantum efficiency as function of wavelength suggesting that there is an optimal wavelength (nanocrystal size) for PL quantum efficiency [137].

2.4.3 Electroluminescence

Over the past decade, intensive research has been carried out on the development of electroluminescence (EL) devices based on Si nanocrystals for the purpose of the realization of electrical driven Si-based lasers. Recently, visible electroluminescence from nanoscaled Si materials has been demonstrated [121, 138-155]. Even a possibility of electrically driven ultraviolet light emission from Si^+-implanted SiO_2 films was predicted [153]. Figure 2.27(a) shows the typical room-temperature PL and EL spectra measured in the device with nc-Si embedded in SiO_2 fabricated by PECVD, and Fig. 2.27(b) presents the microscopy image of the device with EL emission [145]. The EL peak spectrum presents two peaks: a weak one at 660 nm attributed to radiative defects in the oxide and a more intense one at 890nm that maybe related to the presence of nc-Si. Similar PL and EL results have been obtained in the study of Ref. [144].

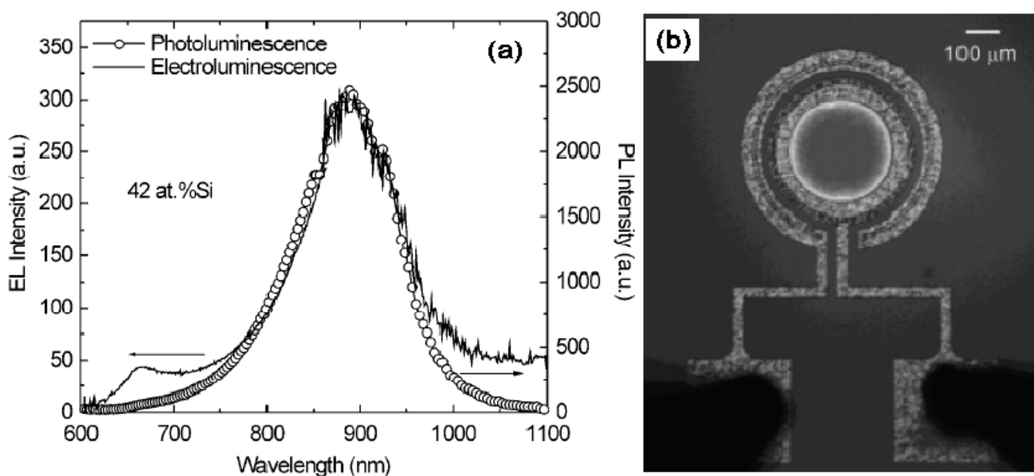

Figure 2.27 (a) Comparison between the PL and EL spectra of the device with a Si content of 42% in the SiO_x layer. The EL spectrum was measured with a voltage of 48 V and current density of 4 mA/cm^2; (b) emission microscopy image of the device annealed at 1100 ^oC for 1 h [145].

Recently, Cho *et al.* reported a study on the EL enhancement of nc-Si embedded in Si_3N_4 synthesized with PECVD [121] by adding a transparent doping SiC layer. Figure 2.28 presents the *I-V* characteristics and comparison between the EL and PL spectra of the device. Time decay studies on the EL spectra have also been carried out [147].

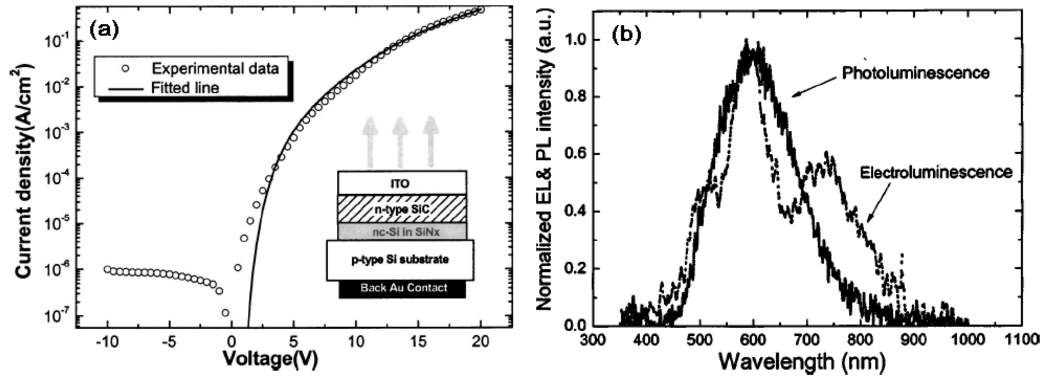

Figure 2.28 (a) Current density as a function of applied voltage; (b) comparison between the EL and PL spectra of the device [121].

2.4.4 Mechanisms of Light Emission

The mechanism of light emitting from nanoscaled silicon has been discussed extensively since the first discovery of photoluminescence from porous Si [12]. However, the origin of light emission from nc-Si is still unclear and controversial to date. Although many studies have shown that this PL is size-dependent in a variety of porous Si and other nc-Si systems, its origins remain only partially understood. In this section, the mechanisms of photon emission from the materials system of nc-Si will be discussed based on literature. Three possible mechanisms are demonstrated in the energy band diagram of nc-Si embedded in a dielectric matrix as shown in Fig 2.29, in which a simple sketch of nc-Si structure is included.

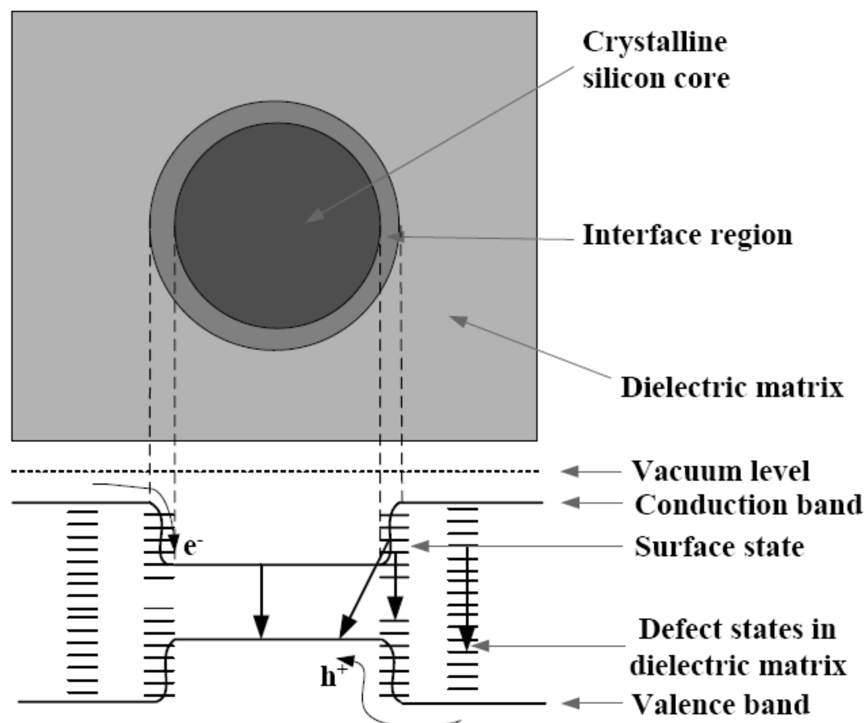

Figure 2.29 Schematic of the system of nc-Si embedded in a dielectric matrix and possible radiative electron hole recombination.

The most widely accepted theory is that excitonic emission due to quantum confinement effect is responsible for the light emission from nc-Si [12, 14, 23, 42, 120, 122, 124, 126, 156-160]. The Bohr radius of an exciton (excited electron-hole pair) in bulk silicon is 49 Å, so quantum confinement is likely to be a source of photon emission in structures with one or more dimensions smaller than this radius. The fundamental idea of quantum confinement effect relies in the expansion of optical bandgap as a result of the size reduction of Si nanocrystals. The expanded optical bandgap represents possible radiative recombination of electrons and holes and thus results a blueshift of emitting wavelength. When injected electrons and holes by electrical or optical stimulation are confined into an extremely small Si particle, the potential barrier formed around each silicon nanocrystal inhibits the diffusion of electrons and holes. This effect significantly increases the radiative recombination possibility.

Another factor that may contribute to the photo emissions is defect luminescence [22, 150, 161, 162]. This component can be diminished or removed with passivating techniques. It can also be distinguished by its rapid decay: in this indirect band gap semiconductor system, lifetimes on the order of 10 μs are expected for excitonic recombination, while defect-related luminescence has been determined to have a lifetime of less than 100 ns. Here the defects normally can be considered to be locating at the interface between nc-Si and the dielectric matrix [22, 125, 162, 163]. However, some other researchers support a defect-assisted recombination mechanism where luminescence is the result of the recombination of carriers trapped at radiative recombination centers that form in the defects in the dielectric matrix itself [150, 164].

As a conclusion, the mostly accepted mechanisms for light emitting from nc-Si can be divided into three considerations, including quantum confinement effect of nc-Si, presence of luminescent surface states in the interface between nc-Si and dielectric matrix and special defects causing photon emission in the dielectric matrix. These three proposed mechanisms can be summarized in Fig. 2.29. Many researchers believe that in most cases two or three of them together play important roles in the photon emission rather than only one of them contribute to light emitting [22, 30, 118, 134, 139, 161].

2.5 Possible Structures of Si-based light emitters

The recent observation of optical gain from Si nanocrystals [165-168] opens an opportunity to develop Si-based light emitting devices. However, the challenge remains to design a laser architecture that is compatible with Si technology. In this section, the most recent, reliable, and possible structures for Si light emitting devices are demonstrated and reviewed.

2.5.1 Raman Si Laser Based on SOI Rib Waveguide

Recently, a lot of research activities have been focused on light generation and amplification in Si waveguides [167, 169-172]. One approach to generate light emission and amplification in Si is Raman Effect [173-176] based on a silicon on insulator (SOI) rid waveguide. Raman Effect is a nonlinear optical effect that is used to induce light emission and amplification, which is also called 'stimulated Raman scattering'. This approach relies on the fact that Raman gain coefficient in silicon is rather strong, making it possible to achieve gain over length scales of an integrated waveguide. Rong *et al.* built a Si waveguide structure, in the shape of a ridge, surrounded by silica to guide the light with low losses, as shown in Fig. 2.30 [177-179]. With this design Rong *et al.* demonstrated a Si laser with continuous operation, a significant advance for the development of practical silicon lasers. Of course, the use of a nonlinear optics phenomenon means that optical pumping will always be required. However, the technique converts only a small fraction of the pump power to heat in the chip in contrast to optically pumped lasers that do not rely on nonlinear optical effects.

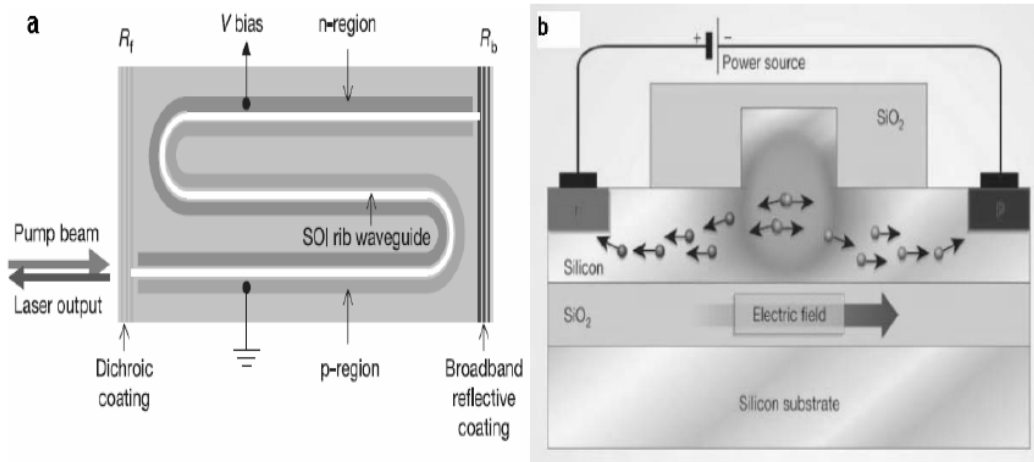

Figure 2.30 Raman silicon laser proposed by Rong *et al.* (a) Schematic layout of the silicon waveguide laser cavity with optical coatings applied to the facets and p-i-n structure along the waveguide; (b) cross-section of the silicon Raman laser [178].

2.5.2 Conventional p-n Junction LED Structure

Traditional semiconductor LEDs are formed from *p*-type and *n*-type semiconductors, which donate positively charged 'holes' and negatively charged electrons, respectively, when a voltage is applied across the structure [16, 140, 165]. The most obvious approach to form a silicon light emitting device is to emulate the two-terminal 'sandwich' structure of a conventional light-emitting diode (LED) as shown in Fig. 2.31. In this structure, recombination of an electron and hole, within the semiconductor, produces a photon and leads to the emission of light. If the efficiency of light emission is high enough and the whole structure is placed between two highly reflective mirrors, the LED can be turned into a miniature laser. In the conventional p-n junction structure, in order to ensure efficient tunneling of carriers through the matrix into the nanocrystals from both *n*-type and *p*-type contacts, the density of nanocrystals must be high enough. However, as this density increases, so does

the number of percolation paths between adjacent nanocrystals that allows carriers to leak through the whole structure as well as allowing them to escape from nanocrystals before they have a chance to recombine. Moreover, the voltages are required to supply electrical currents that are high enough to achieve efficient carrier injection in order to increases the occurrence of impact ionization, which causes the accumulation of defects and the eventual catastrophic deterioration of the nanocrystal embedded matrix.

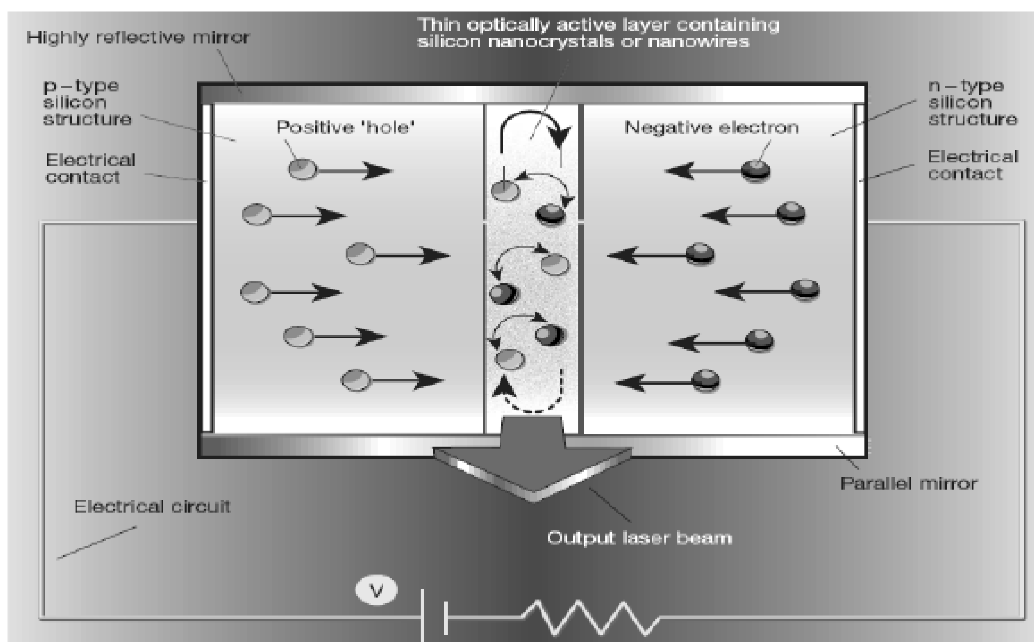

Figure 2.31 Schematic of conventional p-n junction LED structure based on nc-Si [16].

2.5.3 MOS Structure with nc-Si Embedded in Oxide

To overcome problems encountered in the conventional p-n junction structure, researchers have designed a three-terminal structure with Si nanocrystals embedded in the gate oxide of a conventional MOSFET [154, 180-182]. Electrons and holes are injected sequentially into the nanocrystals embedded in the oxide from the channel of the MOSFET by applying an alternating electric

field to the gate, as shown in Fig. 2.32 [181]. The sequential accumulation of electrons and then holes within these nanocrystals on each cycle thereby results in recombination and the emission of light. The key advantage of this approach is that the carriers are injected from only one side of the nanocrystal-embedded matrix. This relaxes constraints on the fabrication of these devices, because the carrier tunneling efficiency is governed only by the distance between the nanocrystals and the channel, and not by their density or the total matrix thickness. Furthermore, as the techniques needed to make ultra-thin tunneling oxides as well as all the other components of these devices are already commercially mature, the integration of nanocrystals with conventional Si-chip production should be straightforward. And because the fields necessary to produce light in these three-terminal devices is much lower than for two-terminal ones, issues of oxide degradation should be minimized, improving the prospects for their long-term operation.

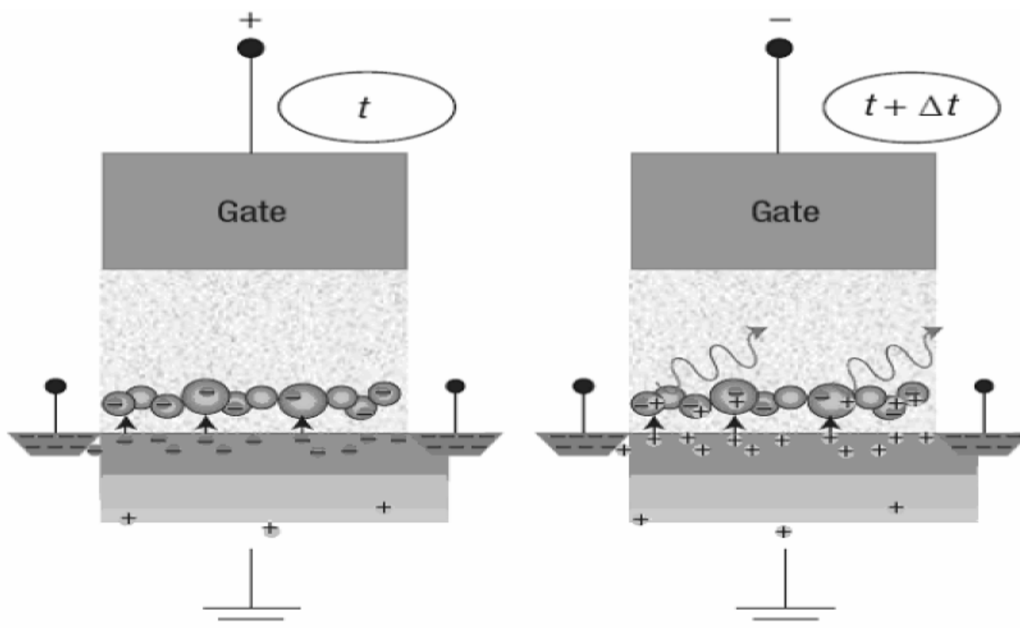

Figure 2.32 Field-effect electroluminescence based on a MOSFET structure with nc-Si embedded in the gate oxide [181].

2.6 Other Application of Si nanocrystals

Besides the applications in optoelectronic device (light emitters, waveguides), Si nanocrystals have come into the eyeshot of researchers for the possible application in non-volatile memory devices. Si nanocrystals embedded in dielectric films exhibit charging and discharging effect, which allow it to read, write and erase information stored in nc-Si [107, 108, 183-190]. Furthermore, recently Si nanocrystals have been paid increasing research attention due to the potential applications in photovoltaic devices [191-200].

2.6.1 Memory Devices

In a MOS structure with nc-Si embedded in the gate oxide, charging and discharging of nc-Si can be realized by applying different voltage polarities on the gate. Once the nc-Si is charged, flatband voltage will shift accordingly. If the nc-Si is discharged, flatband voltage will shift back to its initial value. This property of flatband voltage shift due to the charging and discharging of nc-Si can be used for the application in memory devices. As the memory application using conventional floating gate structure begin to reach it’s limitation in technology scaling, memory devices based on nc-Si embedded in dielectric films have great potential to overcome the current limitations. Figure 2.33

shows the cross-sectional schematic of a memory device with nc-Si embedded in the gate oxide and the band diagrams showing the functions of write and erase.

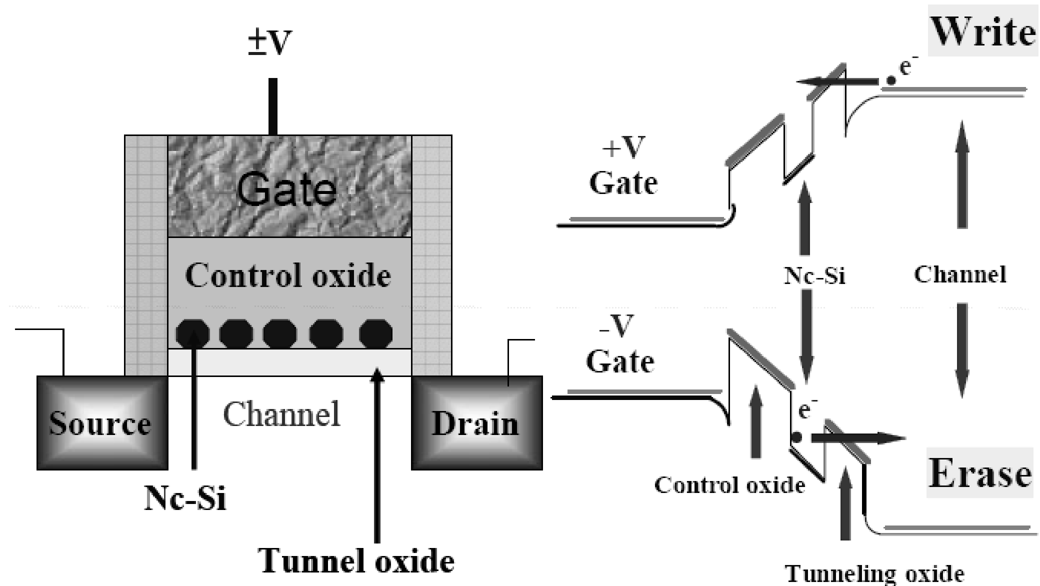

Figure 2.33 (a) Schematic cross-section of Si nanocrystal-based memory structure; (b) band diagrams showing the functions of write and erase [108].

This novel non-volatile memory (NVM) structure came with the idea of replacing the floating gate in conventional flash memory structure by discrete charge trapping centers such as isolated silicon nanocrystals [183, 185-187]. The reduction of the floating gate thickness leads to lower voltage operation and the use of ion implantation simplifies fabrication process. The Coulomb blockade effect of the nanocrystals makes the storage and operation of the memory device robust and fault-tolerant. Memory devices with embedded silicon nanocrystals fabricated using ion implantation exhibited superior data-retention characteristics as compared with conventional floating gate devices [107, 190]. Utilizing nanocrystals as the charge storage nodes enables the memory cell scaling even to a couple of tenths of nanometers. The goal of nc-Si memory is to achieve a programming speed as fast as dynamic random

access memory (DRAM) and the data retention characteristics as long as flash memory devices for possible replacement of DRAM and flash devices in the future. Si nanocrystal-based memory devices can be programmed by the injection of electrons into the nc-Si from the channel with either channel-hot-electron (CHE) injection or Fowler-Nordheim (FN) tunneling, but they are usually erased by FN tunneling regardless of the programming mechanisms [190]. Figure 2.34 shows a typical transfer characteristic of a Si nanocrystal-based memory device after programming and the erasing operation, showing the memory window (i.e., threshold voltage shift) between the *I-V* curves after the operation of programming and erasing.

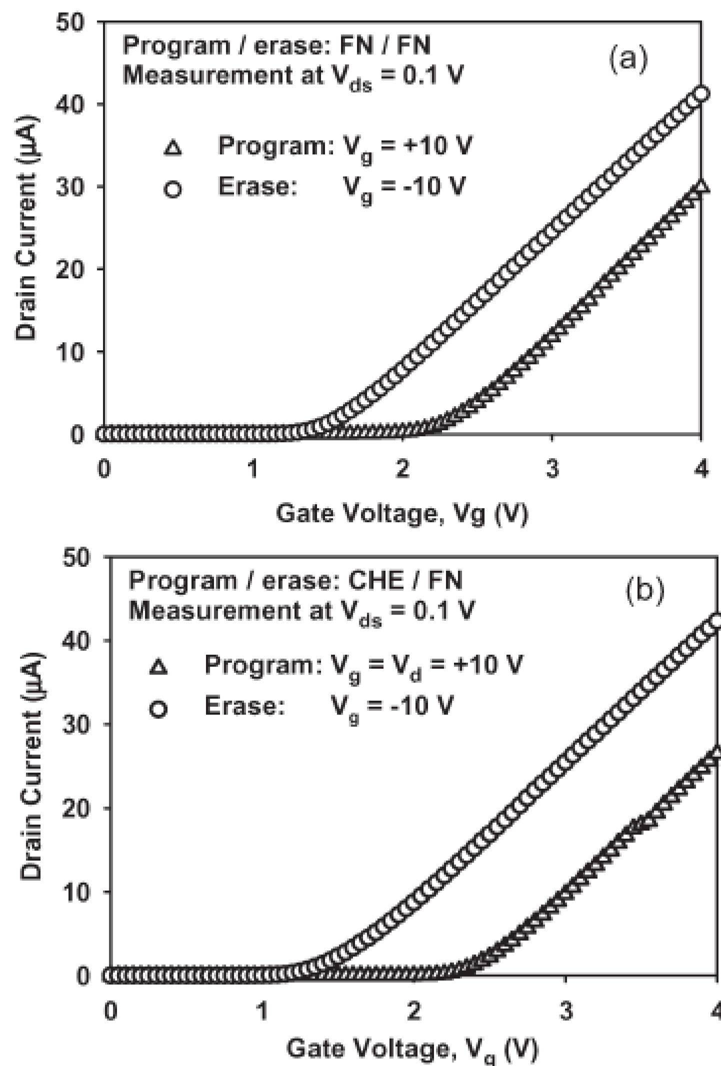

Figure 2.34 Transfer characteristics of the programmed and erased states under

the programming/erase (P/E) operation of (a) FN/FN and (b) CHE/FN with the P/E time of 1 μs [190].

The fully functional 4Mbit test chip of Si nanocrystal memory fabricated in Motorola in 2003 represents a major milestone in the search for successors to floating gate-based flash memories [201]. The realization of the first Si nanocrystal memory could lead to memories that are smaller, more reliable and more energy-efficient compared to the conventional floating gate-based flash memories.

2.6.2 Solar Cells

Some leading research groups in photovoltaic technology have recently reported that Si nanocrystals would present enticing ability to enhance the energy conversion efficiency of solar cells [193-198]. Theoretical calculations indicate that solar cells based on nanocrystals could convert 60% of solar irradiation into electricity [197]. Although a few research groups have theoretically and experimentally presented that Si nanocrystals possess the potential for fabricating solar cells with higher efficiency than that of conventional single junction solar cells, the research on nanocrystal-based solar cells is still in the early stage as most of the reported results were still based on the material characterization.

The main energy loss mechanisms in conventional p-n junction solar cells is the thermalization of electron-hole pairs generated by the absorption of high-energy photons through electron (hole) relaxation to conduction (valence) band edge

[198]. The research focus for today and the near future naturally falls into tackling problem of the energy loss caused by thermalization of electron-hole pairs generated by the absorption of short-wavelength photons. Si nanocrystals have been proposed to be a promising approach to make effective conversion of short-wavelength photons in solar spectrum to electrical energy. For the past half century, it has been a usual assumption that absorption of a single photon produces a single exciton (i.e., electron-hole pair) even if the photon energy is much greater than energy bandgap E_g of the material, like the situation shown in Fig. 2.35(a). However, recently Beard *et al.* have found that efficient multiple exciton generation (MEG) upon absorption of a single photon with energy larger than $2E_g$ in colloidal Si nanocrystals [197]. The ideal MEG process is illustrated in Fig. 2.35(b). In this regard, Si nanocrystals would provide a promising approach to make a more efficient use of short-wavelength photons in the solar irradiation. Current challenges for practical application of MEG are the effective dissociation of excitons into separated electrons and holes and extraction of charges from nanocrystals into an external circuit before Auger recombination occurs.

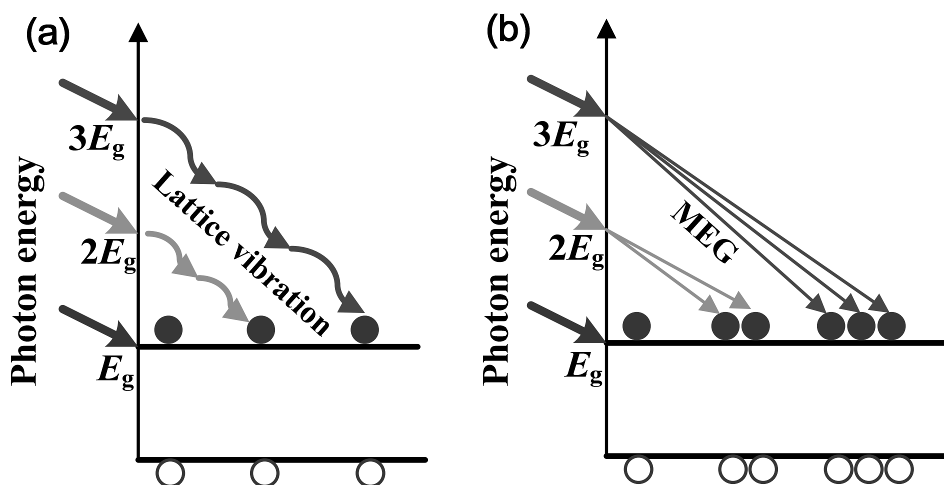

Figure 2.35 (a) Traditional photoexcitation; (b) an ideal picture of multiple

exciton generation upon absorption of a single photon [197].

The tandem solar cells with the nc-Si embedded in a matrix has been demonstrated [198]. Figure 2.36 shows the schematic structure of Si nanocrystal-based tandem solar cells. The top cell is connected to the bottom cell by an interband tunnel junction. The nanocrystals size and concentration in dielectric layers are two important factors to affect the efficiency of the solar cells. The nanocrystal size decides the band gap, which is the most concerned parameter in designing tandem solar cells. Another important factor would be the spacing between nanocrystals in the dielectric layer. To achieve high conductivity for the nanocrystal-based dielectric layer, Si nanocrystals should be separated by no more than 1-2 nm in the matrix of SiO_2. This spacing limit would be larger in the matrix of Si_3N_4 or SiC.

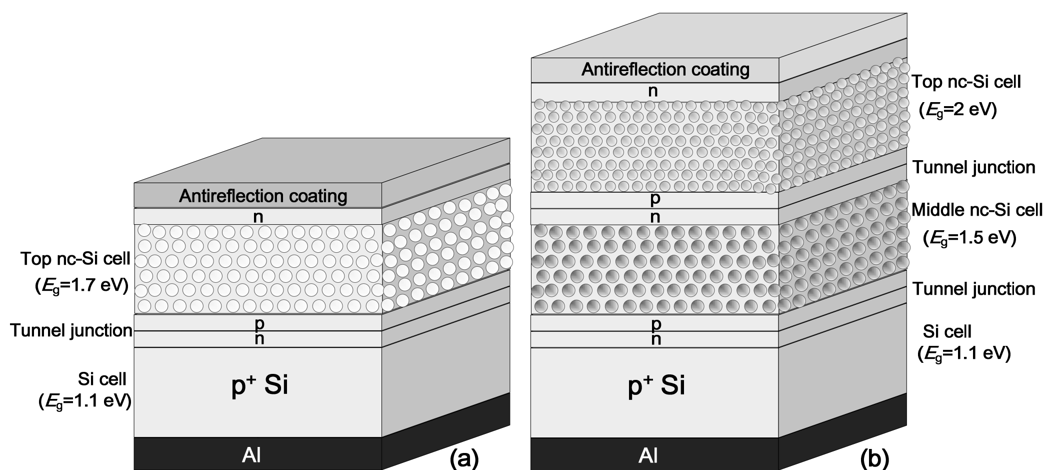

Figure 2.36 Schematic structure of (a) two-cell and (b) three-cell tandem solar cell with nc-Si embedded in SiO_2 [198].

2.7 Summary

This chapter has provided the reader with a description of fabricating method for the synthesis of Si nanocrystals. A review on the characterization techniques that were frequently used to study the optical and optoelectronic properties of nc-Si has been presented. Studies on the light emission properties of nc-Si and LED structures based on nc-Si previously reported by other researchers have been reviewed. Moreover, the applications of Si nanocrystals in memory devices and solar cells have been introduced in this chapter.

Although there have been many studies on Si nanocrystals since early years of the past decade, it is clear that there are still many areas in the research of nc-Si to be explored. How can one experimentally determine and model the dielectric function of nc-Si embedded in a SiO_2 film synthesized by Si ion implantation and subsequent annealing? How does the annealing influence the dielectric function and band gap of nc-Si embedded in SiO_2? How does the nanocrystal size influences the dielectric function and band gap of nc-Si embedded in SiO_2? What's the difference between the dielectric function of dispersed nc-Si and densely stacked nc-Si layer embedded in SiO_2? How does PL from SiO_2 embedded with nc-Si evolve with thermal annealing? Are the mechanisms of photoluminescence the same for SiO_2 embedded with nc-Si under different annealing temperatures? As regard to light emission, dose size really matter? What's the influence of implantation energy and dose on the electroluminescence? How do different matrixes affect the light emission properties? What's the relationship between PL and EL? Where does the

charging effect take place? What are other possible applications of nc-Si except for those have been reported? …

These issues will be discussed in the following chapters.

CHAPTER 3 DIELECTRIC FUNCTION OF SI NANOCRYSTALS EMBEDDED IN A SILICON DIOXIDE MATRIX

3.1 Introduction

In such material system of SiO_2 matrix embedded with Si nanocrystals, the dielectric function of isolated nc-Si should be different from those of bulk crystalline silicon due to the size effect, and should be also different from those of a continuous Si-nanocrystal film. Therefore, it would be interesting to examine the optical properties of isolated nc-Si embedded in SiO_2 matrix. Such a study is obviously important to the fundamental physics as it is concerned with a system of quantum dots isolated by a dielectric matrix, and it is also necessary to the optoelectronic and photonic applications of the nc-Si.

In spite of the fact that efficient PL and EL in Si nanocrystals embedded in SiO_2 matrix have been demonstrated, it remains necessary to accurately determine the dielectric function of embedded nc-Si in order to perform reliable device modeling for photonics applications of nc-Si. A lot of investigations on optical properties of nc-Si have been carried out by luminescence studies [12, 14, 30, 33, 42, 113, 118-123, 156, 157] and theoretical calculations [18-21, 159, 202, 203]. However, there have been few optical studies so far that can experimentally determine the dielectric function or optical constants of nc-Si embedded in a dielectric matrix in a wide range of photon energy. Especially, it is difficult to experimentally determine the optical properties of nc-Si embedded

in a dielectric matrix. Some experimental studies of the optical properties of a continued Si nanocrystal thin film [98] and SiO_2/nanocrystalline Si multilayers [204] have been reported recently. Nevertheless, a comprehensive experimental study of the optical properties in a wider photon energy range and a proper modeling to the optical properties are still lacking. Furthermore, very few studies have been focused on optical properties of nc-Si being prepared under different annealing conditions. Due to the reduced dimensionality, Si nanocrystals are expected to present size dependent dielectric function. However, only a few theoretical studies have been carried out on this significant issue [205-210]. In this chapter, a comprehensive study on the dielectric properties of nc-Si embedded in SiO_2 matrix by spectroscopic ellipsometry is presented. It is expected that the study presented in this chapter will enhance the current understanding on the dielectric properties of nc-Si embedded in dielectric matrix. The chapter begins with an introduction to the basic principles of ellipsometry, and is followed by a description of methodology, experiments, and interpretation and discussion on results.

3.2 Ellipsometry

In this section, the basic principles of ellipsometry are presented as well as its capacity in the material characterization. The optical fundamentals of ellipsometry are introduced, based on which we can describe the methodology that is used to determine the dielectric function of nc-Si embedded in SiO_2 in the following sections.

3.2.1 Basic Principles

Ellipsometry is a very sensitive surface and thin film measurement technique that uses polarized light. Ellipsometry measures the change in polarization state of light reflected from the surface of the measured sample. Fundamentally, ellipsometry refers just to the measurements of the polarization state of a light beam. However, ellipsometric measurements are usually performed in order to describe an optical material system that modifies the polarization state of a light beam. The exact nature of the polarization modification is determined by the properties of the measured sample (i.e., thickness, dielectric function or complex refractive index). Although optical techniques are inherently diffraction limited, ellipsometry exploits phase information and the polarization state of light, and can achieve angstrom resolution.

Linearly polarized light falls onto the sample and is reflected from the surface of the measured sample. The reflected light passes a polarizer, which is called analyzer, and falls into the detector. The measured values (ellipsometric angles) are expressed ψ and Δ, which are related to the ratio of Fresnel reflection coefficient R_p and R_s for p and s polarized components (the s component is oscillating perpendicular to the plane of incidence and parallel to the sample surface, and the p component is oscillating parallel to the plane of incidence), respectively, which is described by the fundamental equation of ellipsometry:

$$\rho = R_p / R_s = \tan(\psi)\exp(i\Delta) \tag{3.1}$$

where $\tan(\psi)$ denotes the amplitude ratio upon reflection, and Δ is the phase shift. For any angle of incidence greater than 0º and less than 90º, p-polarized

light and *s*-polarized light will be reflected differently. Because ellipsometry measures the ratio of two values, it can be highly accurate and very reproducible. Because the ratio is a complex number, it also contains “phase” information, which makes the measurement very sensitive. In ellipsometric experiment, it is common to use the so-called *p* and *s* directions as two orthogonal basis vectors used to express beam polarization states, as shown in Fig. 3.1. This figure illustrates the general idea of ellipsometric polarized light beam system.

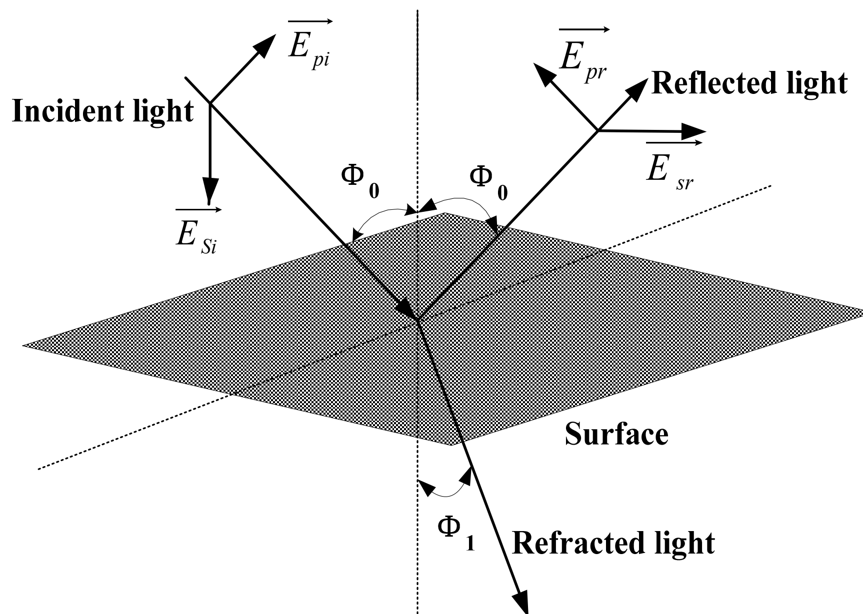

Figure 3.1 Schematic illustration of an ellipsometric experiment, showing the polarized light reflected by the surface of the measured sample.

Ellipsometry is an indirect method, i.e. in general the measured Ψ and Δ cannot be converted directly into the dielectric function or optical constants of the sample. Normally, a model analysis must be performed. Direct inversion of Ψ and Δ is only possible in very simple cases of isotropic, homogeneous and infinitely thick films. In all other cases a layer model must be established, which considers the optical constants (refractive index or dielectric function tensor)

and thickness parameters of all individual layers of the sample including the correct layer sequence. Using an iterative procedure (least-squares minimization) unknown optical constants and/or thickness parameters are varied, and Ψ and Δ values are calculated using the Fresnel equations. The calculated Ψ and Δ values, which match the experimental data best, provide the dielectric function and thickness parameters of the sample.

3.2.2 Single-wavelength and Spectroscopic Ellipsometry

Single-wavelength ellipsometry employs a monochromatic light source. This is usually a laser in the visible spectral region, for instance, a HeNe laser with the wavelength of 632.8 nm. Therefore, single-wavelength ellipsometry is also called laser ellipsometry. The advantage of laser ellipsometry is that laser beams can be focused on an extremely small spot size, and thus the incident spot has a very high power density. Therefore, laser ellipsometry can be used for imaging by using a CCD camera as a detector. However, the experimental output is restricted to one set of Ψ and Δ values per measurement. Spectroscopic ellipsometry (SE) employs broad band light sources, which cover a certain spectral range in the infrared, visible or ultraviolet spectral region. With dielectric functions or complex refractive index in the corresponding spectral region obtained, one can extract a large number of fundamental physical properties of the measured samples. Spectroscopic ellipsometry in the near infrared, visible up to ultraviolet spectral region studies the refractive index in the transparency or below-band-gap region and electronic properties, for instance, band-to-band transitions or excitons. In this study, spectroscopic

ellipsometry will be used to study the dielectric function and optical constants of nc-Si embedded in SiO_2.

3.2.3 Dielectric Functions and Optical Constants

As ellipsometry investigated on the interaction of polarized light with the surface of a material, it is the first step that we should know the optical function of material. The optical function of a material describes how it responds to an electromagnetic field (i.e., a beam of light). When a beam of light propagates through a material, it is polarized by the material on an atomic scale by pilling up electrons on some atoms and depleting them from others. The polarization vector ($\vec{P}$) is related to the electric field ($\vec{E}$) described by the equation

$$\vec{P} = \chi \varepsilon_0 \vec{E} \tag{3.2}$$

where χ is the electric susceptibility of the material and ε_0 is the dielectric constant of vacuum. The displacement field ($\vec{D}$) can be written as the sum of electric filed ($\vec{E}$) and polarization filed ($\vec{P}$) by

$$\vec{D} = (1+\chi)\varepsilon_0 \vec{E} \tag{3.3}$$

where the quantity $(1+\chi)$ is referred to as its dielectric constant (ε) described by

$$\varepsilon = 1 + \chi \,. \tag{3.4}$$

As the dielectric constant is a complex quantity, it can be expressed as the sum of real and imaginary parts.

$$\varepsilon = \varepsilon_1 + i\varepsilon_2 . \tag{3.5}$$

ε can also be expressed in terms of its complex refractive index (N)

$$\varepsilon = N^2 = (n + ik)^2 \tag{3.6}$$

where n and k are called optical constants together, in which n is the refractive index and k is called extinction coefficient. Therefore, the real and imaginary parts of dielectric constant can be re-written as

$$\varepsilon_1 = n^2 - k^2 \tag{3.7}$$

and

$$\varepsilon_2 = 2nk . \tag{3.8}$$

For a particular material, the dielectric constant is usually a complicated function of photon energy, thus it is a superimposed dispersion phenomena occurring at multiple frequencies. Therefore, when we consider the dielectric constant in a particular range of photon energy, it can be called dielectric function $\varepsilon(E)$. Similarly, $n(E)$ and $k(E)$ are referred to as the dispersion of refractive index and extinction coefficient, respectively. In this chapter, $n(E)$ and $k(E)$ of nc-Si are described. Afterwards, the real and imaginary part of dielectric function can be obtained through Eq. (3.7) and (3.8).

3.3 Dielectric Function of Dispersed nc-Si Embedded in SiO_2

In this section, the dielectric functions of dispersed nc-Si embedded in SiO_2 matrix in the photon energy range of 1.1-5.0 eV are determined with

spectroscopic ellipsometry (SE). The dielectric functions of nc-Si are modeled with the Lorentz oscillator model [211] and the Forouhi-Bloomer (FB) formulism [212]. The modeling based on the Lorentz oscillator model gives the information related to electron transitions, while the FB modeling yields the energy band gap of the nc-Si. A strong dielectric suppression and a large bandgap expansion are observed for the nc-Si.

3.3.1 Sample Fabrication

The nc-Si embedded in a SiO_2 matrix was synthesized by Si ion implantation with a dose of 1×10^{17} cm^{-2} at energy of 100 keV into a 550-nm-thick SiO_2 film thermally grown on a *p*-type Si substrate. A thermal annealing at 1000 ^{o}C for 30 minutes in nitrogen gas was carried out for the formation of Si nanocrystals.

3.3.2 Characterization

1. Transmission electron microscopy (TEM)

In order to prepare suitable TEM specimens, the samples with nc-Si embedded in SiO_2 were cut into small discs with the diameter of 5 mm. The discs were dimpled and polished for both sides. Afterwards, they were milled by argon plasma at 5 keV and a thinning angle of 14° at room temperature. Finally, microstructures of the samples were characterized using a transmission electron microscope equipped with an energy dispersive X-ray spectroscope. Figure 3.2 is the cross-sectional TEM micrograph showing the crystalline structure of nc-Si embedded in a SiO_2 matrix. Although only amorphous SiO_2 is visible in

the most of the image, the circle area is the crystalline lattice structure, demonstrating the existence of Si nanocrystals with the diameter of ~4.5 nm.

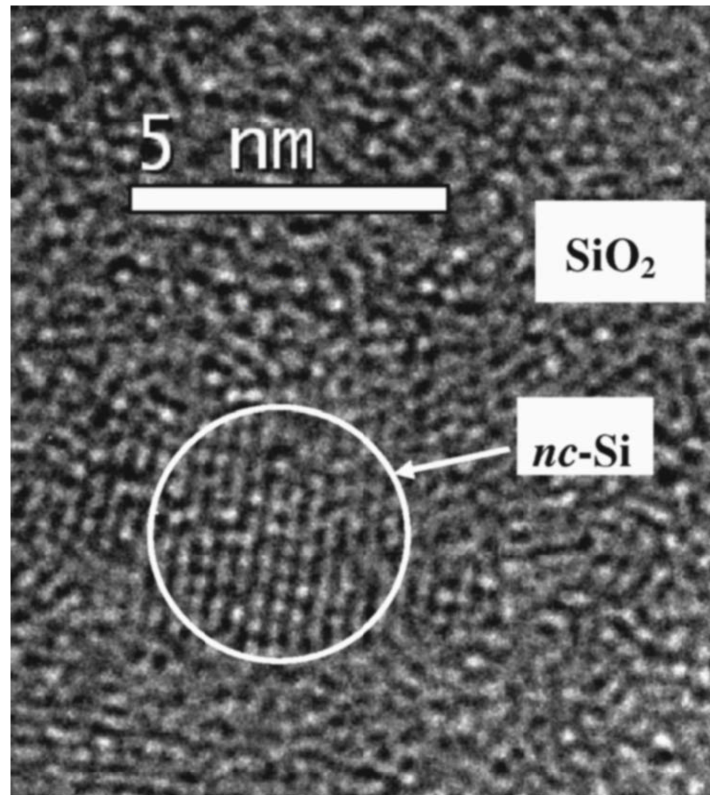

Figure 3.2 Cross-sectional TEM image of nc-Si embedded in SiO_2 matrix. The sample was fabricated by Si ion implantation with the dose of 1×10^{17} cm^{-2} at 100 keV followed by annealing at 1000 ^oC at N_2 for 30 min.

2. X-ray Diffraction (XRD)

The average size of Si nanocrystals can be determined from the broadening of the Bragg peak in the XRD spectrum after correction for instrumental broadening using Scherrer's equation, i.e., Eq (2.1). The XRD measurements were conducted at a fixed low incident angle of 0.5^o in order to eliminate the single from Si substrate. The diffractometer uses Cu Kα line (λ=0.1541 nm) as the x-ray source. Figure 3.3 shows the XRD measurement for nc-Si embedded in SiO_2 matrix and Pseudo-Voigt fit to the data, and the mean nc-Si size obtained is ~4.2 nm. Since the nanocrystal size estimation based on XRD Bragg

peak is limited by diffracting volume, this method does not allow detecting nanocrystals smaller than 2 nm. Thus, the average nanocrystal size may be slightly overestimated. However, this technique has been found to give overall agreement with the size extracted from TEM measurement within the experimental uncertainties of both techniques. Therefore, we use the Bragg peak of XRD spectrum to estimate the average size of nc-Si in this thesis.

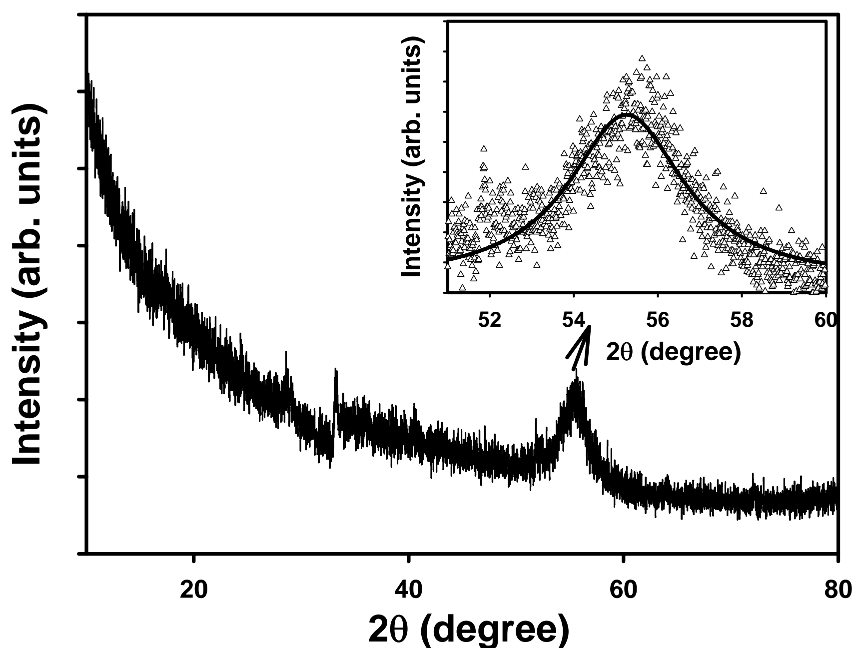

Figure 3.3 XRD measurement of Si nanocrystals embedded in SiO_2 matrix and the pseudo-Voigt fit to the data.

3.3.3 Ellipsometry Measurement

A spectroscopic ellipsometer (J. A. Woolam Co. VASE) is used to measure the ellipsometric angles Ψ and Δ in the wavelength range of 250 to 1100 nm with the incidence angle of 75 ^{o}C. In this system, there are several important optical components that should be addressed. Xe or Hg-Xe arc lamps are usually used because they have light irradiance in the UV and near IR region, which are

critical in the ellipsometric measurement. UV and IR optical fibers are used for the light transport in the specific transmission regions, coupling the light beam from the monochromator to the polarizer. A chopper is used to modulate the light intensity for the subsequent synchronous detection. A calcite Glan-Taylor polarizer is used as the most important optical component to convert light with any polarization into linearly polarized light. The analyzer in the system is Si and InGaAs photodetectors, which is insensitive to the polarization state and light intensity.

3.3.4 Methodology

A method is developed to extract optical information (dielectric functions and optical constants) of dispersed nc-Si embedded in SiO_2 from the measured results with spectroscopic ellipsometry studies. Effective medium approximation (EMA) theory together with a proper optical dispersion relationship has been used to determine the dielectric functions of dispersed nc-Si embedded in the SiO_2 matrix synthesized under different annealing temperatures. The methodology and principles are as follows.

1. Effective Medium Approximation (EMA)

Composite materials are often involved in ellipsometry studies. To investigate a mixture material system of two or three materials, many effective medium theories have been developed to model the optical constant of such mixture material structures. The simplest EMA is to linearly interpolate between the constituent optical constants, as expressed below [211]:

$$\varepsilon = f_a\varepsilon_a + f_b\varepsilon_b + f_c\varepsilon_c \tag{3.9}$$

where ε is the effective complex dielectric function of the mixture, f_a, f_b, and f_c are the volume fractions (ranging from 0 to 1) of each constituent material, and ε_a, ε_b, and ε_c are the complex dielectric functions of the constituent materials. The volume fractions must be total unity. Eq. (3.9) is valid for three-constituent EMA model and for two-constituent EMA model if f_c is fixed at zero. The linear interpolation EMA is not highly accurate, but is often used for graded layers to reduce calculation time.

The Maxwell-Garnett and Bruggemann EMAs are the most common models, and can be used to model a wide range of mixing effects such as surface and interfacial roughness. The Maxwell-Garnett EMA is derived assuming spherical inclusions of one or two material(s) (denoted materials "b" and "c") exist in a host matrix of the second material (denoted material "a") [211]:

$$\frac{\varepsilon-\varepsilon_a}{\varepsilon+2\varepsilon_a}=f_b\frac{\varepsilon_b-\varepsilon_a}{\varepsilon_b+2\varepsilon_a}+f_c\frac{\varepsilon_c-\varepsilon_a}{\varepsilon_c+2\varepsilon_a}. \tag{3.10}$$

This equation must be solved for the effective complex dielectric function ε given the volume fractions of two of the constituents f_b and f_c (f_a is assumed to equal $1-f_b-f_c$) and the dielectric functions of all the three materials. Equation (3.10) is valid for a three-constituent Maxwell-Garnett EMA, and the two-constituent case may be obtained by fixing f_c at zero. In our case, the peak volume fraction of implanted Si atoms is only ~18%. Thus the two-constituent Maxwell-Garnett model is most suitable for our study.

The Bruggemann EMA (sometimes referred to as the coherent potential approximation) makes the self-consistent choice of the host material complex

dielectric function equaling the final effective complex dielectric function of the multi-constituent material. The Bruggemann EMA requires the numerical solution of the following equation, valid for three constituents, or for two constituents with f_c fixed at zero [211]:

$$f_a \frac{\varepsilon_a - \varepsilon}{\varepsilon_a + 2\varepsilon} + f_b \frac{\varepsilon_b - \varepsilon}{\varepsilon_b + 2\varepsilon} + f_c \frac{\varepsilon_c - \varepsilon}{\varepsilon_c + 2\varepsilon} = 0 . \tag{3.11}$$

This equation can be quite difficult to solve correctly, particularly for three constituent EMA models. It is a complex equation and will yield an infinite number of solutions, such that one must correctly choose the appropriate solution branch.

2. Multilayer model for spectral fitting

The nc-Si distribution in the SiO_2 thin film is determined from secondary ion mass spectroscopy (SIMS) measurement. The SIMS intensity $I(x)$ due to the excess Si in the Si^+-implanted region at a given depth x can be obtained by deducing the Si SIMS single of the pure SiO_2 region from the measured total Si SIMS signal (which is from both the excess Si and the SiO_2) at the depth. The amount of excess Si at depth x should be proportional to the intensity $I(x)$. The volume fraction of excess Si $f(x)$ of the nc-Si embedded in SiO_2 at depth x can be expressed as [75]:

$$f(x) = \frac{QI(x)}{N_{Si} \int_0^{d_{\max}} I(x) dx} \tag{3.12}$$

where Q is the dose of implanted Si ions with the unit of cm^{-2}, $I(x)$ is the SIMS intensity of the excess Si with the unit of cm^{-3} under the dynamic mode of SIMS

operation, d_{max} is the largest depth in SiO_2 where excess Si occupies, and N_{Si} is the atom concentration of bulk crystalline silicon. In this study Q is equal to 1×10^{17} cm^{-2}, and N_{Si} is 5×10^{22} cm^{-3}.

The volume fraction of the nc-Si in the SiO_2 calculated from the SIMS measurement as a function of the depth is shown in Fig. 3.4. As can be seen in this figure, the nc-Si distributes from the surface of the SiO_2 film to a depth of 250 nm and there is almost no nc-Si in the SiO_2 film beyond a depth of 250 nm. Therefore the thin film system can be divided into two layers, namely, the first layer (0≤depth≤250 nm) with nc-Si distributing in SiO_2, and the second layer (depth>250 nm), which is just a basically pure SiO_2 layer without nc-Si.

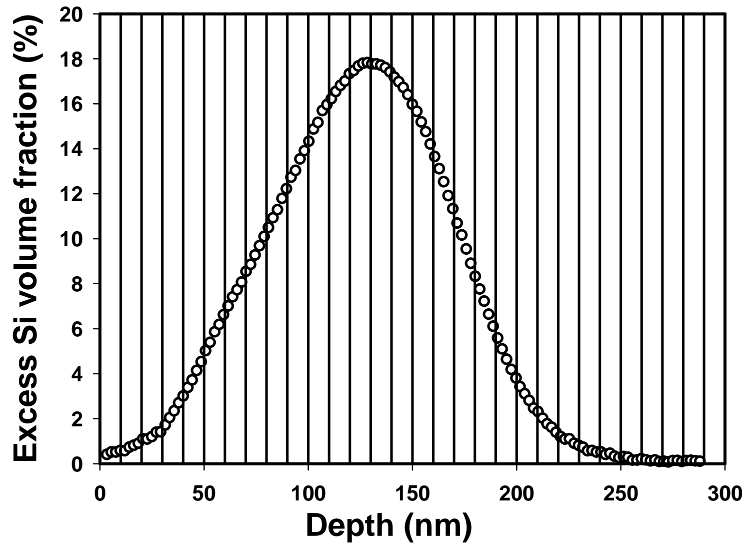

Figure 3.4 Volume fraction of excess Si in SiO_2 as a function of depth.

In the first layer, the optical properties vary with the depth as the volume fraction of the nc-Si varies with depth. In order to model the optical properties of the first layer, it is divided into n sublayers with equal thickness d_0 (n=25 and d_0=10 nm in this study). Each sublayer has an nc-Si volume fraction (f_i, i =1,

2,…, *n*) which can be calculated from the SIMS measurement, and the nc-Si volume fraction is considered to be constant within each sub-layer. Each sub-layer has its own effective dielectric function ε_i (i = 1, 2,…, *n*) due to its own nc-Si volume fraction. As such, the optical system in the SE analysis can be described with the multilayer model shown in Fig. 3.5. Each sublayer can be optically schematized as an effective medium, in which the SiO_2 is the host matrix while the nc-Si is an inclusion embedded in the SiO_2 matrix, represented by the Maxwell-Garnett EMA. As the volume fraction (f_i) and ε_{SiO_2} are known, the effective complex dielectric function ε_i (and thus the effective complex refractive index N_i) for the ith sub-layer (i=1, 2,..., m) can be expressed in terms of ε_{nc-Si} (or the refractive index and extinction coefficient of nc-Si) with an appropriate EMA as discussed in the first part of section 3.3.4.

Therefore, in the SE analysis, the ellipsometric angles (Ψ and Δ) can be expressed as functions of the dielectric functions of the nc-Si, although these functions cannot be displayed with analytical formulas due to their complexity. Based on these functions, a spectral fitting to the experimental data of Ψ and Δ can yield the optical constants of the nc-Si at various wavelengths.

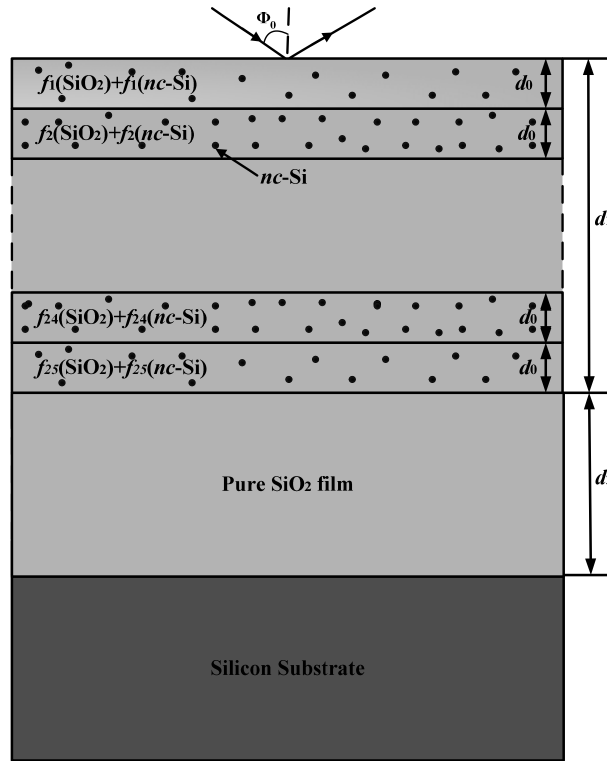

Figure 3.5 Multi-layer model used in the SE analysis.

3. Optical fundamentals

It is assumed that polarized light is reflected from an air/multilayer/substrate system, as shown in Fig. 3.5. For the total system, the ratio ρ of the complex reflection coefficients for the p and s polarizations is given by $\rho = R_p / R_s = \tan(\psi)\exp(i\Delta)$, where Ψ and Δ are the ellipsometric angles. Ψ is the angle whose tangent gives the ratio of the amplitude attenuation or magnification upon reflection for the p and s polarizations, respectively. Δ gives the difference between the phase shifts experienced upon reflection by the p and s polarizations. The complex reflection coefficient R_a (a $=p$, s) is given by [211]:

$$R_a = \frac{r_{01}^a + R_{12}^a X_1}{1 + r_{01}^a R_{12}^a X_1}, \tag{3.14}$$

where
$$X_1 = \exp(-i\frac{4\pi}{\lambda} N_1 d_1 \cos\phi_1), \tag{3.15}$$

$$R_{12}^a = \frac{r_{12}^a + R_{23}^a X_2}{1 + r_{12}^a R_{23}^a X_2} \tag{3.16}$$

$$X_2 = \exp(-i\frac{4\pi}{\lambda} N_2 d_2 \cos\phi_2), \tag{3.17}$$

$$\vdots$$

$$R_{(n-1)n}^a = \frac{r_{(n-1)n}^a + R_{n(n+1)}^a X_n}{1 + r_{(n-1)n}^a R_{n(n+1)}^a X_n}, \tag{3.18}$$

$$X_n = \exp(-i\frac{4\pi}{\lambda} N_n d_n \cos\phi_n), \tag{3.19}$$

$$R_{n(n+1)}^a = \frac{r_{n(n+1)}^a + r_{(n+1)(n+2)}^a X_{n+1}}{1 + r_{n(n+1)}^a r_{(n+1)(n+2)}^a X_{n+1}}, \tag{3.20}$$

$$X_{n+1} = \exp(-i\frac{4\pi}{\lambda} N_{n+1} d_{n+1} \cos\phi_{n+1}), \tag{3.21}$$

$$r_{(n-1)n}^s = \frac{N_{n-1}\cos\phi_{n-1} - N_n \cos\phi_n}{N_{n-1}\cos\phi_{n-1} + N_n \cos\phi_n}, \tag{3.22}$$

$$r_{(n-1)n}^p = \frac{N_n \cos\phi_{n-1} - N_{n-1}\cos\phi_n}{N_n \cos\phi_{n-1} + N_{n-1}\cos\phi_n}. \tag{3.23}$$

The angles ϕ_1, ϕ_2,…, ϕ_n, ϕ_{n+1} between the directions of propagation of the plane waves in media 0 (i.e., air) , 1 to *n* (i.e., sublayers containing nc-Si) , *n*+1 (i.e., pure SiO_2) and *n*+2 (i.e., Si substrate) are related by Snell's law [211]:

$$N_0 \sin\phi_0 = N_1 \sin\phi_1 = ... = N_n \sin\phi_n . \tag{3.24}$$

In the above equations, N_i (i= 0, 1, …, n+1, n+2) is the complex refractive index of the ith medium (the ith phase) ($N_i = n_i + ik_i$, n is the refractive index; k is the extinction coefficient); λ is the free-space wavelength of light; r_{ij}^{a}(i, j = 0, 1, 2,…, n+1) is the Fresnel complex-amplitude reflection coefficient for a (a=p, s) polarization at the interface of ith sublayer and j^{th} sublayer; d_i is the thickness of the ith sublayer. The depth profile of Si volume fraction is necessary for extracting the information of nc-Si embedded in SiO_2 matrix, and it is obtained from the SIMS measurements shown in Fig. 3.5. Each sublayer can be represented by the two-constituent Maxwell-Garnett model in which f_c is set to be 0 in Eq. (3.10):

$$\frac{\varepsilon_i - \varepsilon_{SiO_2}}{\varepsilon_i + 2\varepsilon_{SiO_2}} = \frac{\varepsilon_{nc-Si} - \varepsilon_{SiO_2}}{\varepsilon_{nc-Si} + 2\varepsilon_{SiO_2}} f_i \tag{3.25}$$

where ε_i (=N_i^2 where N_i is the complex refractive index of the ith sublayer) is the effective complex dielectric function of the ith sublayer, ε_{SiO_2} is the dielectric function of the SiO_2 film, ε_{nc-Si} $(= (n_{nc-Si} + ik_{nc-Si})^2$ where n_{nc-Si} and k_{nc-Si} are the refractive index and extinction coefficient of the nc-Si, respectively) is the complex dielectric function of the nc-Si, and f_i is the volume fraction of nc-Si in the ith sub-layer. As a whole material system, the

functional dependence of Ψ and Δ on the system parameters can be symbolically written as

$$\psi = f_1(f_{i(i=1,2,..,n)}, d_{i(i=1,2,..,n)}, d_{SiO_2}, n_{Si}, k_{Si}, n_{SiO_2}, k_{SiO_2}, \phi_0), \quad (3.26)$$

and

$$\Delta = f_2(f_{i(i=1,2,..,n)}, d_{i(i=1,2,..,n)}, d_{SiO_2}, n_{Si}, k_{Si}, n_{SiO_2}, k_{SiO_2}, \phi_0). \quad (3.27)$$

In Eq. (3.26) and Eq. (3.27), the nc-Si volume fraction and thickness of each layer, the thickness of SiO_2, and optical constants of bulk silicon and SiO_2 are already known. Thus, only the information of nc-Si (refractive index and extinction coefficient or dielectric functions) is unknown in the two equations. In fact, the above two equations are extremely complicated, and cannot be displayed with analytical formulas. Based on these functions, a spectral fitting to the experimental data of Ψ and Δ can yield the dielectric functions and optical constants of nc-Si at various wavelengths.

4. Dispersion models

In the spectral fitting, an appropriate optical dispersion model should be used to describe the spectral dependence of dielectric functions and optical constants of the nc-Si. In the present work, two optical dispersion models, the Lorentz oscillator model [211] and the four-term Forouhi-Bloomer (FB) model [212] are used to carry out the spectral fitting.

It is found that a combination of four Lorentz oscillators with different resonant energies is necessary to describe the spectral dependence of optical properties of

the nc-Si embedded in SiO_2 over the wavelength range of 250 to 1100 nm. The Lorentz oscillator model can be expressed as [211]:

$$\varepsilon(E) = \varepsilon(\infty) + \sum_{i=1}^{4} \frac{A_i}{E_i^2 - E^2 - i\Gamma_i E} \tag{3.28}$$

where $\varepsilon(\infty)$ refers to the dielectric constant at very large photon energies, A_i is the amplitude of the ith oscillator with the unit of $(eV)^2$, Γ_i is the damping factor of the ith oscillator with the unit of eV, and E_i is the resonant energy with the unit of eV.

Besides the Lorentz oscillator model, the four-term FB model is found to be another choice to get a reasonable spectral fitting. It should be pointed out that the FB model can yield not only the information of optical constants and dielectric functions but also the bandgap of the isolated nc-Si embedded in the SiO_2 matrix. The information of the nc-Si bandgap is very important because a bandgap expansion (if any) is a direct evidence of the quantum confinement effect. Based on the four-term FB model, the optical constants including the refractive index and extinction coefficient of the nc-Si are given by [212]:

$$k(E) = \left(\sum_{i=1}^{4} \frac{A_i}{E^2 - B_i E + C_i} \right) \left(E - E_g \right)^2, \tag{3.29}$$

$$n(E) = n(\infty) + \sum_{i=1}^{4} \frac{B_{0_i} E + C_{0_i}}{E^2 - B_i E + C_i}, \tag{3.30}$$

where

$$B_{0_i} = \frac{A_i}{Q_i} \left(-\frac{B_i^2}{2} + E_g B_i - E_g{}^2 + C_i \right), \tag{3.21}$$

$$C_{0_i} = \frac{A_i}{Q_i}\left((E_g^2 + C_i)\frac{B_i}{2} - 2E_g C_i \right), \tag{3.22}$$

$$Q_i = \frac{1}{2}(4C_i - B_i^{\ 2})^{\frac{1}{2}}, \tag{3.33}$$

where A_i, B_i and C_i (i=1, 2, 3, and 4) are some parameters related to electron transition, $n(\infty)$ is the refractive index when photon energy $E \rightarrow \infty$, and E_g is the energy bandgap of the nc-Si.

The spectral fitting is carried out by freely varying the parameters of the models to minimize the following mean-square error (MSE) [211]:

$$MSE = \frac{1}{2N - M}\sum_{i=1}^{N}\left[\left(\frac{\psi_i^{cal} - \psi_i^{\exp}}{\sigma\psi_i^{\exp}} \right)^2 + \left(\frac{\Delta_i^{cal} - \Delta_i^{\exp}}{\sigma\Delta_i^{\exp}} \right)^2 \right], \tag{3.34}$$

where N is the number of data points in the spectra, M is the number of variable parameters in the model, σ is the standard deviations on the experimental data points, $\psi^{\exp}$ and $\Delta^{\exp}$ are the measured values of the ψ and Δ while ψ^{cal} and Δ^{cal} are the corresponding calculated values .

In summary, the process to extract information of nc-Si embedded in SiO_2 matrix from ellipsometric measurements are concluded in Fig. 3.6, and the flowchart of fitting program is shown in Fig. 3.7.

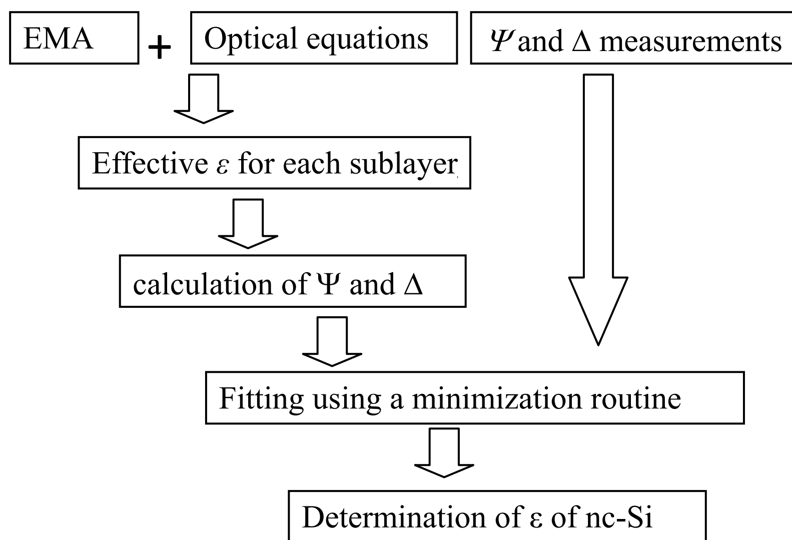

Figure 3.6 The procedure to extract information of nc-Si embedded in SiO_2 from ellipsometric measurements.

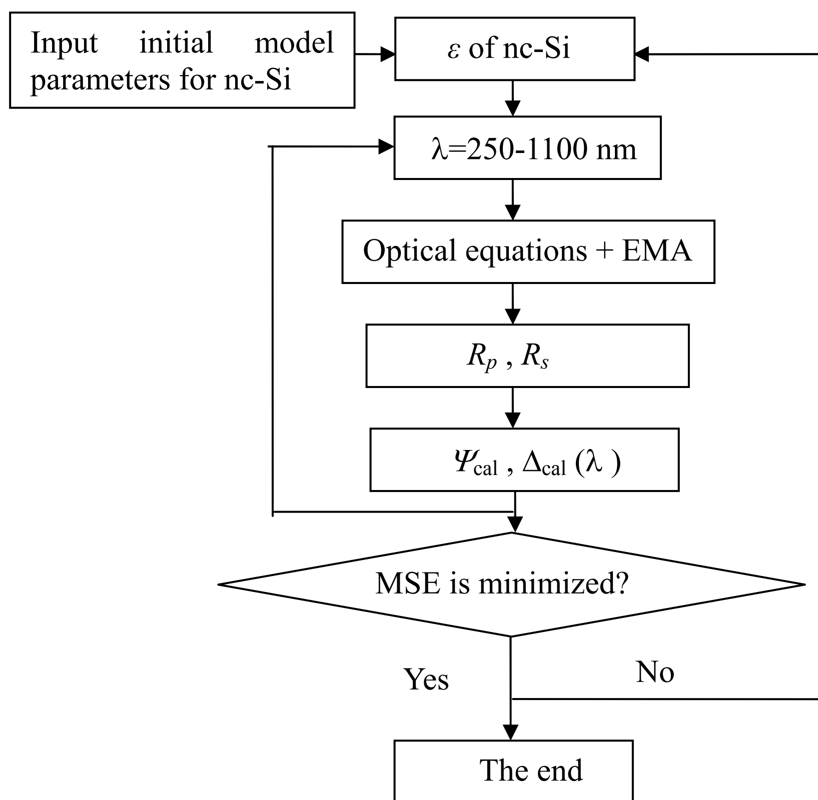

Figure 3.7 The flow chart of the fitting program.

3.3.5 Results and Discussions

For an efficient spectral fitting, the initial values of parameters of the two models are taken equal to that of bulk crystalline silicon listed in TABLE 3.1 and TABLE 3.2. An excellent spectral fitting based on the above approach in a wide wavelength range from 250 to 1100 nm has been obtained, as shown in Fig. 3.8, in which the best-fit spectra based on the FB model and Lorentz oscillator model are both included. As can be seen in this figure, all the complicated spectra features of both Ψ and Δ are fitted excellently.

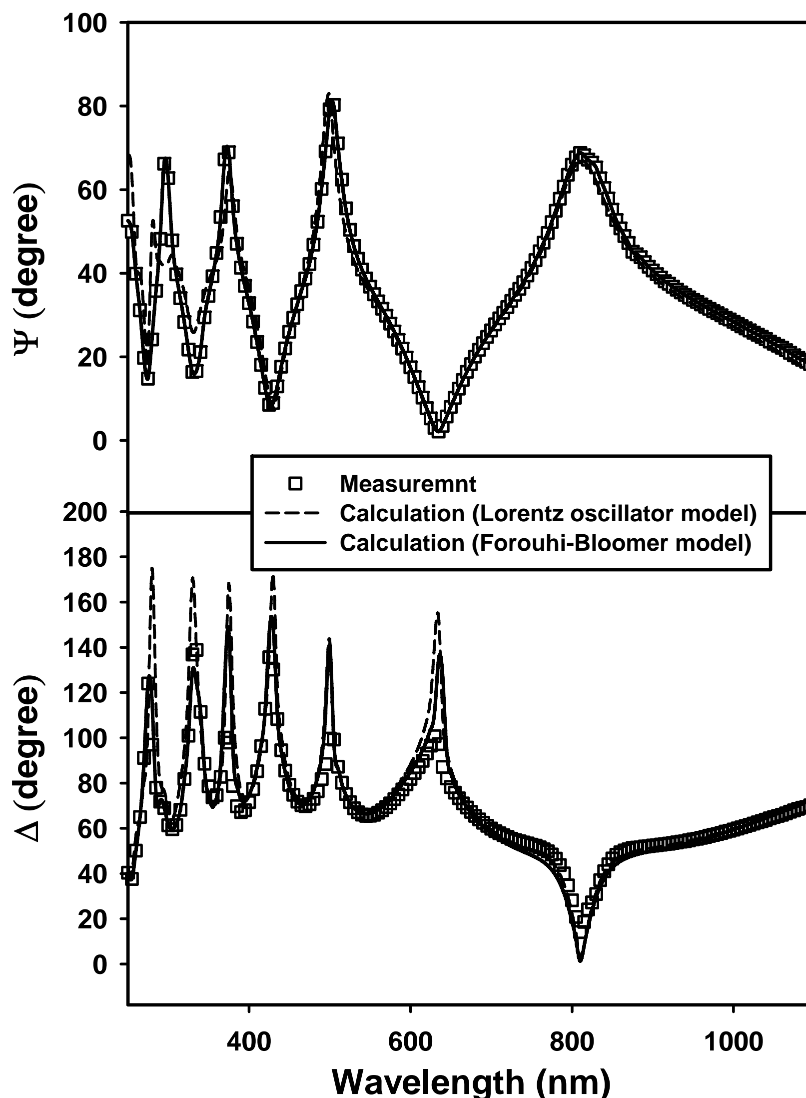

Figure 3.8 Best spectral fittings of ψ and Δ based on the Lorentz oscillator model and the four-term FB model with the approach described in the text.

TABLE 3.1. Values of the parameters A_i, E_i, Γ_i (i = 1, 2, 3, 4), $\varepsilon_1(\infty)$ of the Lorentz oscillator model for both bulk crystalline silicon and the nc-Si embedded in SiO_2.

	A_i	E_i (eV)	Γ_i (eV^2)	$\varepsilon_1(\infty)$
Bulk crystalline silicon	10.1124	3.4423	0.1407	3.803
	45.9013	3.7005	0.4823	
	92.2078	4.3172	0.5289	
	11.5679	5.3233	0.3823	
Si nanocrystals embedded in SiO_2	30.8123	3.5560	0.4313	6.209
	13.7089	4.0151	0.3681	
	5.4209	4.0529	0.2242	
	10.3012	5.1614	0.8173	

TABLE 3.2. Values of the parameters A_i, B_i and C_i (i = 1, 2, 3, 4), $n(\infty)$ and E_g of the FB model for both bulk crystalline silicon and the nc-Si embedded in SiO_2.

	A_i	B_i (eV)	C_i (eV^2)	$n(\infty)$	E_g (eV)
Bulk crystalline silicon	0.0036	6.8811	11.8486	2.3688	1.12
	0.014	7.401	13.7473		
	0.0683	8.634	18.7952		
	0.0496	10.2339	26.5029		
Si nanocrystals embedded in SiO_2	0.0538	7.1119	12.7176	2.8237	1.7369
	0.0056	8.0157	16.0797		
	0.0603	8.0300	18.7101		
	0.0003	10.3227	33.6447		

Using the values of the parameters of the nc-Si shown in TABLE 3.1 and TABLE 3.2, the complex dielectric functions and the optical constants of the nc-Si are calculated with Eq. (3.28) for the Lorentz oscillator model or Eq. (3.29) and (3.30) for the FB model. The dielectric function and optical constants of the nc-Si are shown in Fig. 3.9 and Fig. 3.10, respectively, in which the results calculated with the above two optical dispersion models are both included. The dielectric function and the optical constants of bulk crystalline Si are also included in the two figures for comparison. As can be seen in Fig. 3.9

and Fig. 3.10, the overall spectral features of optical properties of nc-Si are similar to that of bulk crystalline Si. However, the nc-Si shows a significant reduction in the dielectric function and optical constants as compared with bulk crystalline Si. This is also indicated by the parameters of Lorentz oscillator modeling for the dielectric functions of nc-Si. In general, the dielectric functions of bulk crystalline Si show main peaks at the transition energies E_1 (~3.4 eV), E_2 (~3.7 eV), E_3 (~4.3 eV), and E_4 (~5.3 eV) as its critical points as listed in TABLE 3.1. However, in the case of nc-Si, the spectral peaks below 4 eV, i.e., the two lower- frequency transition peaks, undergo slight blue shifts in E_1 (~3.6 eV) and E_2 (~4.0 eV), while the two higher-frequency transition peaks show slight red shift in E_3 (~4.1 eV) and E_4 (~5.2 eV). These peak positions are almost in coincidence with the corresponding values of $B_i/2$ (i = 1, 2, 3, and 4) of the four-term FB model. This good agreement in the peak energy positions between the two models underlines the validity of the present study. The fact of the blue shift of low transition energies and the red shift of high transition energies could be considered as a trend that the different transition energies tend to combine as the size of Si becomes nanoscale. Such consideration can be confirmed by the studies of Amans [98] and Lee [204], in which the dielectric function and optical constants of Si nanocrystals have only single peak in the spectral ranges of interest. The tendency of transition energies to combine is possibly due to the large broadening and significant weakening of strength of some oscillators. The trend of single-peak structure is also reported by Rossow [213] and Nguyen [214] , for porous silicon and nc-Si Si layer, respectively.

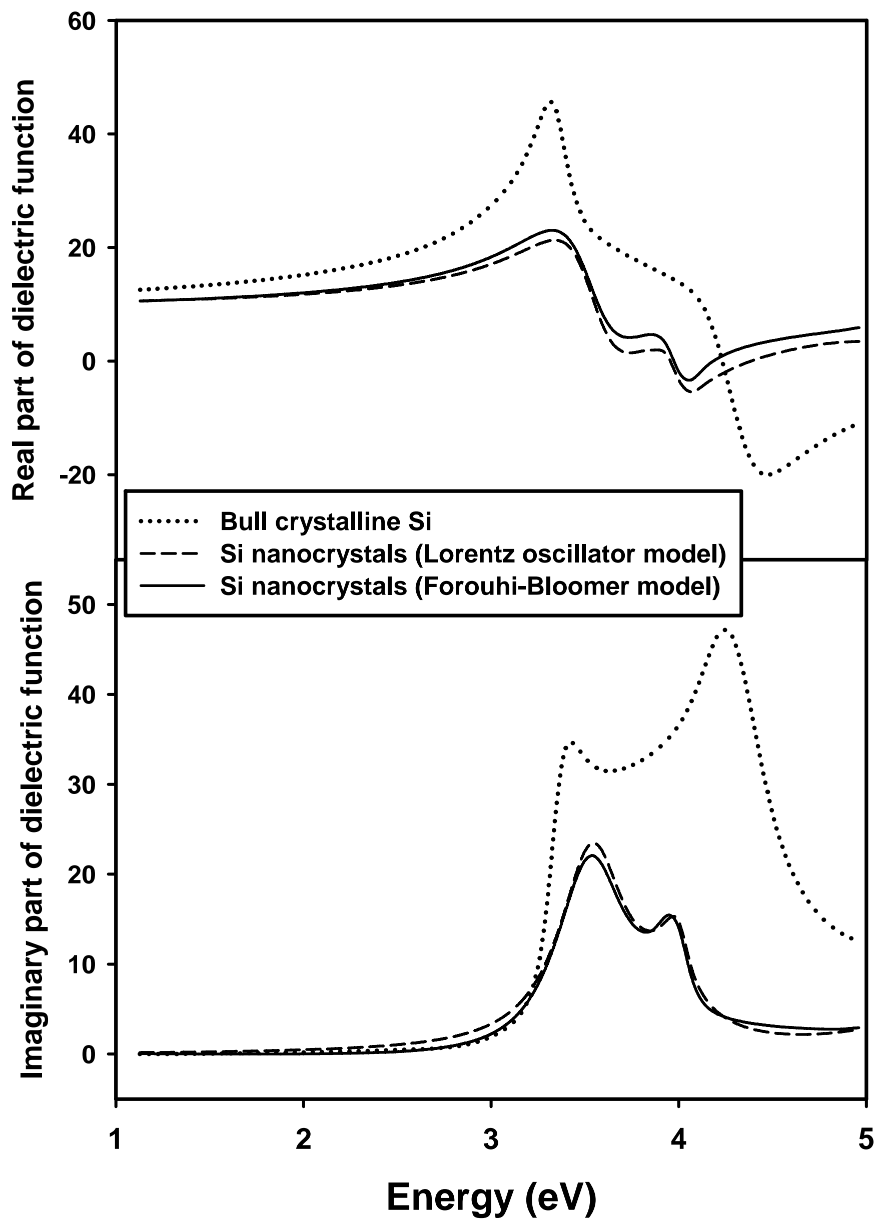

Figure 3.9 Real (ε_1) and imaginary (ε_2) parts of the complex dielectric functions of the nc-Si obtained from the spectral fitting based on the Lorentz oscillator model and the FB model. The dielectric function of bulk crystalline Si is also included for comparison.

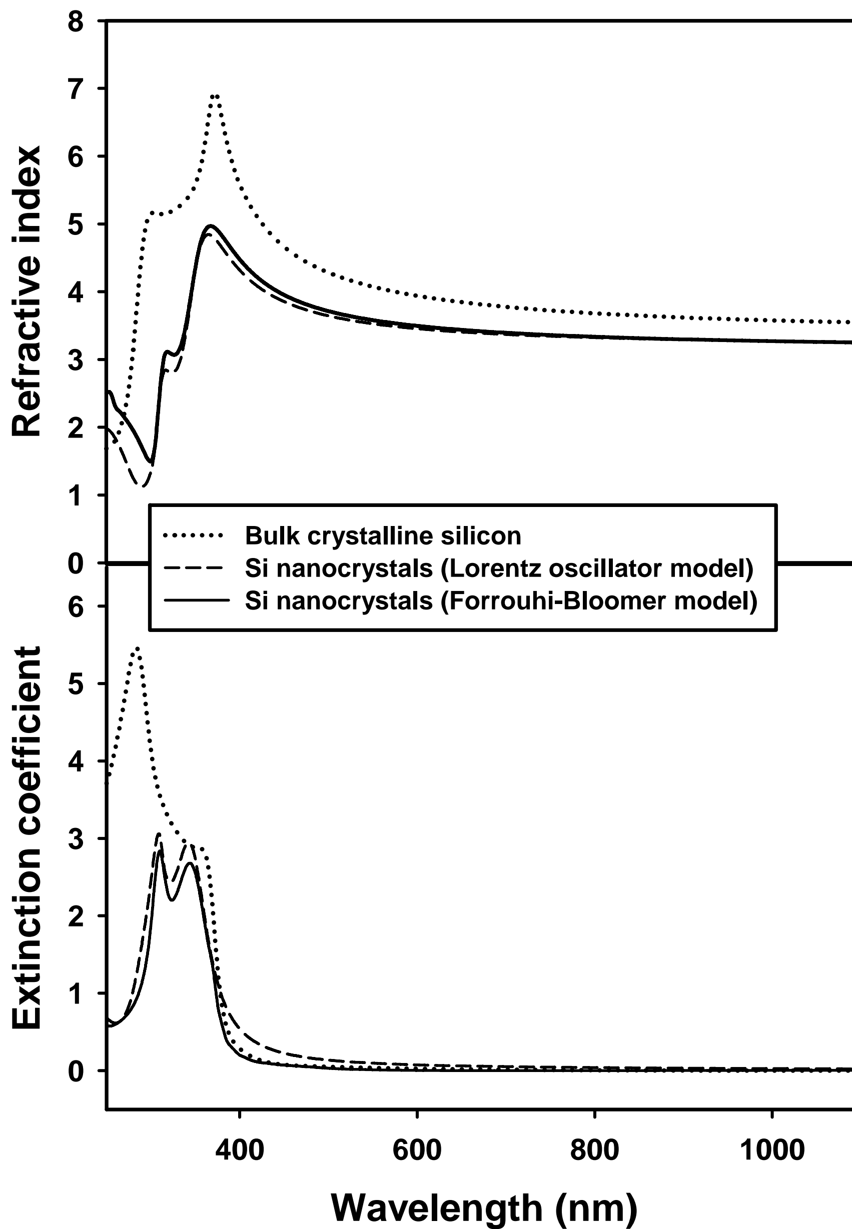

Figure 3.10 Refractive index (*n*) and extinction coefficient (*k*) of the nc-Si and bulk crystalline Si as functions of wavelength.

3.3.6 Analysis of Parameter Uncertainty

Although we have got excellent fitting spectra, it is important to analyze the uncertainty in physical parameters. The fitting procedure involves many parameters that are needed in dispersion models. Typically, in analyzing the SE data, we forcefully vary one parameter while allowing the others to be

adjustable to a best fit by fitting routine. In this study, the uncertainties of fitting parameters are obtained by allowing the fit quality indicator MSE to vary up to 0.1.

As can be seen from our best-fit spectra, the modeled $\Psi(\lambda)$ and $\Delta(\lambda)$ spectra with both dispersions simulate well the measured spectra. With the parameter given in TABLE 3.1 and TABLE 3.2, the obtained MSE is 0.041 and 0.012, respectively. In the SE analysis, starting with the different initial values, the fitting program can result with different parameters. This means that the parameters that can satisfy the SE fitting are not unique. Thus it is necessary to discuss the parameter uncertainty in the SE analysis. In the study, we found that $\Psi(\lambda)$ and $\Delta(\lambda)$ can be well fitted with an MSE value of up to 0.1. Therefore, in this thesis, the uncertainty of each parameter is obtained by allowing the MES value to vary in the range of 0 to 0.1. It should be pointed out that the number of digits of parameter we obtained in the fitting is not an indication of the parameter accuracy. In parameters obtained in the SE analysis, we pay most attention to the nc-Si band gap extracted in the FB model. Therefore, in our study, we mainly discuss the uncertainty of nc-Si band gap obtained from SE analysis. The uncertainty of the nc-Si band gap obtained from the FB model is found to be less than 2%. The uncertainty of other parameters, such as A_i, B_i, and C_i, are dependent on the energy position of each transition peak. For example, the uncertainties for A_i, B_i, and C_i are less than 2% when i = 2 and 3, but for i = 1 and 4, the uncertainties are approaching to 5%. The uncertainty of $n(\infty)$ is calculated to be under 5%. However, in the Lorentz oscillator model, the uncertainties for all the parameters are found to be ~10%. Therefore, we found that FB model can describe the dielectric functions of nc-Si more precisely. In

the following sections, the dielectric functions of nc-Si are modeled by the four-term FB dispersion equations.

3.3.7 Bandgap Expansion

On the other hand, based on the plot of $(\alpha E)^{\gamma}$ versus E where α is the absorption coefficient of the nc-Si and E is the photon energy, one can examine whether the nc-Si is a direct (γ=2) or indirect (γ=1/2) band gap semiconductor [215]. As an example, Fig. 3.11(a) shows the Tauc plot (γ=1/2) of nc-Si annealed at 1000 ^{o}C for 20 min, and the plot for bulk crystalline silicon is also included for comparison. With γ=1/2, a linear relationship in the photon energy range near the absorption edge is observed for both the nc-Si and bulk crystalline Si, as shown in Fig. 3.11(a). In contrast, as shown in Fig. 3.11(b), the linearity is much poorer when γ= 2 for both nc-Si and bulk crystalline silicon. This suggests that the nc-Si has an indirect band gap structure. As mentioned previously, the nc-Si embedded in SiO_2 has a bandgap expansion of ~0.6 eV as compared to bulk crystalline Si. The bandgap expansion is consistent with the blueshift of the plot of $(\alpha E)^{1/2}$ *vs.* E (where α is the absorption coefficient and E is the photon energy), as shown in Fig. 3.11(a). The bandgap of the nc-Si obtained by extrapolating the linear portion of the plot is 1.73 eV, which is almost the same as the value (1.74 eV) given in TABLE 3.2. The bandgap obtained in this work is in very good agreement with the first-principle calculation of the optical gap of Si nanocrystals based on quantum confinement [202]. A fit to the calculation shown in Fig. 3 of Ref. [202] yields

$$E_g(D) = E_{g0} + C / D^n \quad (3.35)$$

where D is the nanocrystal size in nm, $E_g(D)$ is the bandgap in eV, of the nanocrystal, $E_{g0} = 1.12$ eV is the bandgap of bulk crystalline Si, C=3.9, and n=1.22. For the nc-Si size of 4.2 nm of this study, Eq. (3.35) gives a bandgap of 1.79 eV, which is very close to the bandgap values mentioned above.

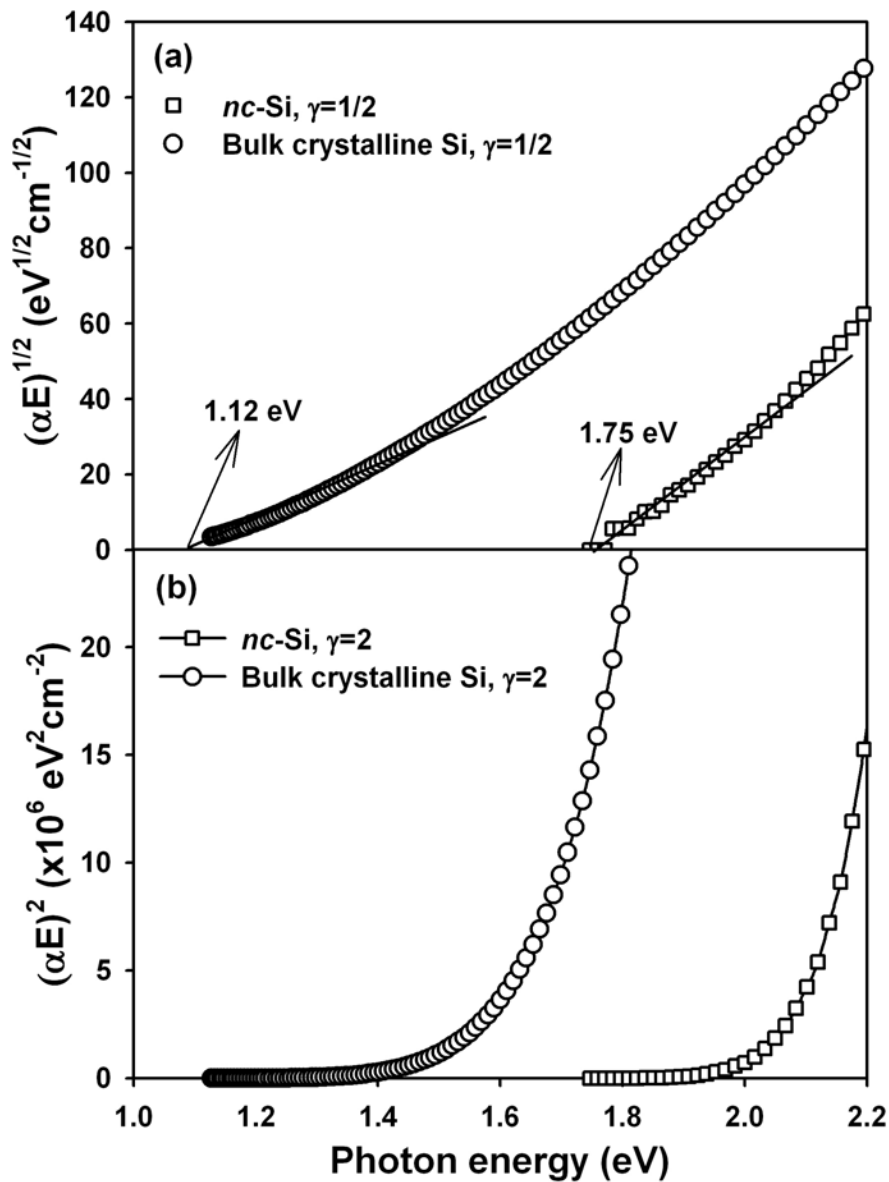

Figure 3.11 Plots of $(\alpha E)^{\gamma}$ versus photon energy (E) for both the nc-Si synthesized at 1000 ^{o}C and bulk crystalline silicon. (a) γ = 1/2; and (b) γ =2.

3.3.8 Dielectric Suppression

It has been well established that reduction of the static dielectric constant becomes significant as the size of the quantum confined physical systems, such as quantum dots and wires, approaches the nano-metric range [205, 216-218]. However, the origin of the reduction in static dielectric constant with the size is still not fully understood. It is often attributed to the opening of the gap which should lower the polarizability, but it is also shown that the reduction is due to the breaking of polarizable bonds at the surface and is not due to the opening of the bandgap induced by the confinement [219].

Nevertheless, the reduction in the static dielectric constant is also observed in the present study. The static dielectric constant of the dispersed nc-Si embedded in SiO_2 matrix is found to be 9.7, which is obtained from the calculation with the four-term FB model by setting the photon energy to zero. Taking the screening effect by the medium into account, Wang *et al.* pointed out that the static dielectric constant of the nc-Si as a function of the nanocrystal size could be expressed as follow:

$$\varepsilon_r(D) = 1 + \frac{\varepsilon_r(\infty) - 1}{1 + \left(\frac{6.9}{R}\right)^{1.37}} \tag{3.36}$$

where $\varepsilon_r(\infty)$ is the static dielectric constant of bulk crystalline silicon, and R is the radius of nc-Si with the unit of angstrom [205]. Based on Eq. (3.36), where $\varepsilon_r(D)$ and $\varepsilon_r(\infty)$ are 9.7 and 11.4 respectively, the diameter of nc-Si is found to be ~ 4.5 nm, which is very close to the XRD result (the mean size is ~ 4.2 nm) mentioned early.

3.4 Depth Profile of Optical Constants of SiO_2 Film Containing nc-Si

In optoelectronic device applications of nc-Si, it is necessary to determine the depth profiles of optical constants of SiO_2 films containing Si nanocrystals in order to perform reliable device modeling. Thanks to the work that we have done in the above section on the determination of the optical constants and dielectric functions of Si nanocrystals embedded in SiO_2 matrix, it is now convenient to calculate the optical constants of each sub-layer based on EMA theory. Therefore, the depth profiles of optical constants of the film can be determined. Here we take the sample implanted at 100 keV with the dose of 1×10^{17} cm^{-2} annealed at 1000 ºC for 20 min as an example.

3.4.1 Methodology

Deduced from Eq. (3.6) and Eq. (3.25), the refractive index n_i and extinction coefficient k_i for the ith (i=1, 2,…, 25) sub-layer can be expressed as follows:

$$n_i = n_{SiO2}\left[\frac{\sqrt{(A^2+B^2)(C^2+D^2)}+(AC+BD)}{2(C^2+D^2)}\right]^{1/2}, \quad (3.37)$$

and

$$k_i = n_{SiO2}\left[\frac{\sqrt{(A^2+B^2)(C^2+D^2)}-(AC+BD)}{2(C^2+D^2)}\right]^{1/2}, \quad (3.38)$$

where

$$A = (1 + 2f_i)(n_{nc-Si}^2 - k_{nc-Si}^2) + 2(1 - f_i)n_{SiO_2}^2 , \tag{3.39}$$

$$B = 2(1 + 2f_i)n_{nc-Si}k_{nc-Si} , \tag{3.40}$$

$$C = (1 - f_i)(n_{nc-Si}^2 - k_{nc-Si}^2) + (2 + f_i)n_{SiO_2}^2 , \tag{3.41}$$

$$D = 2(1 - f_i)n_{nc-Si}k_{nc-Si} , \tag{3.42}$$

In the above equations, $n_{\text{nc-Si}}$ and $k_{\text{nc-Si}}$ are the mean refractive index and extinction coefficient of the nc-Si, and n_{SiO2} is the refractive index of SiO_2. Note that all the parameters are dependent of wavelength. By using the nc-Si optical constants obtained in Section 3.3, the refractive index n_i and extinction coefficient k_i for the ith (i = 1,2,…25) sub-layer can be calculated with Eq. (3.37) and Eq. (3.38), and thus the depth profiles of optical constants (n and k) for SiO_2 thin film containing Si nanocrystals are obtained.

3.4.2 Results and Discussions

Figure 3.12 shows the three-dimensional view of refractive index and extinction coefficient as functions of both depth and wavelength. As shown in this figure, the peaks of both the refractive index and extinction coefficient are located at the depth of ~120 nm, and in the region deeper than 250 nm, the optical constants are basically the same as that of SiO_2. It can be expected that such a structure containing nc-Si in SiO_2 film with a proper nc-Si distribution has a graded refractive-index profile which can offer light-trapping ability and thus the possibility of waveguiding. For a clear demonstration of the light-trapping

ability of this structure, we re-plot the figure in a two-dimensional style as shown in Fig. 3.13.

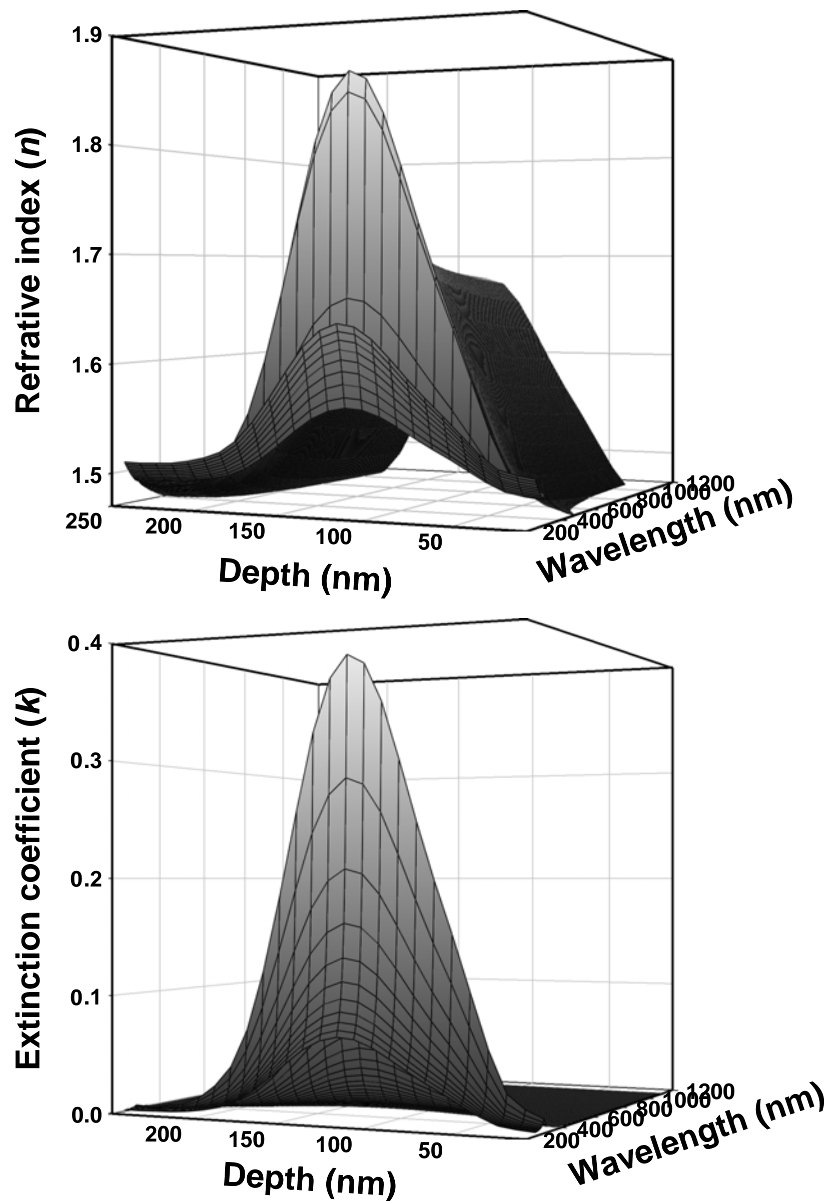

Figure 3.12 The depth profile of optical constants of SiO_2 film containing Si nanocrystals synthesized with Si ion implantation.

Figure 3.13 shows the spectral dependence of refractive index and extinction coefficient at the depth of 20, 50, 90, and 120 nm. For comparison, the optical constants of pure SiO_2 are also included in the figure. As can be seen in this figure, for any wavelength both the refractive index and extinction coefficient

increase with the depth. However, they decrease when the depth > ~120 nm (for simplicity, the optical constants beyond the depth of 120 nm are not shown in Fig. 3.13). The sharp change of the optical constants in the wavelength range of 250–350 nm is due to the spectral features of the nc-Si optical constants in this wavelength range. Figure 3.14 shows the depth dependence of $\Delta n / n_{SiO_2}$ (where Δn is the difference between the refractive index at a given depth and that of pure SiO_2) for the wavelengths of 250, 300,350,400, 600 and 900 nm. As shown in this figure, for all the wavelengths, the maximum refractive index is located at the depth of about 120 nm due to the maximum nc-Si concentration at this depth, and the refractive indices are basically the same as that of SiO_2 in the region deeper than 250 nm. It is clear that the maximum change of refractive index due to the existence of nc-Si occurs at the wavelength of ~350 nm. This is because of the peak structure of nc-Si refractive index at the wavelength of about 350 nm, as can be seen from Fig. 3.10. For the wavelengths longer than 350 nm, the changes of refractive index due to the nc-Si decrease with wavelength because of the decrease in the nc-Si refractive index with wavelength. Figure 3.15 shows the depth profile of extinction coefficient for the same wavelengths as in Fig. 3.14. As can be seen in this figure, for short wavelengths (<~400 nm), absorption occurs only in the region of 0<depth<250 nm with the strongest absorption at the depth of ~120 nm. However, for long wavelengths (>~400 nm), there is almost no absorption everywhere including in the region of 0<depth<250 nm. Therefore, it can be concluded from Fig. 3.14 and Fig. 3.15 that for long wavelengths (>~400 nm) there is a large refractive index but almost no absorption in the region of 0<depth<250 nm. This suggests that the thin film structure has the capability of waveguiding with very low

optical loss in the visible to infrared range.

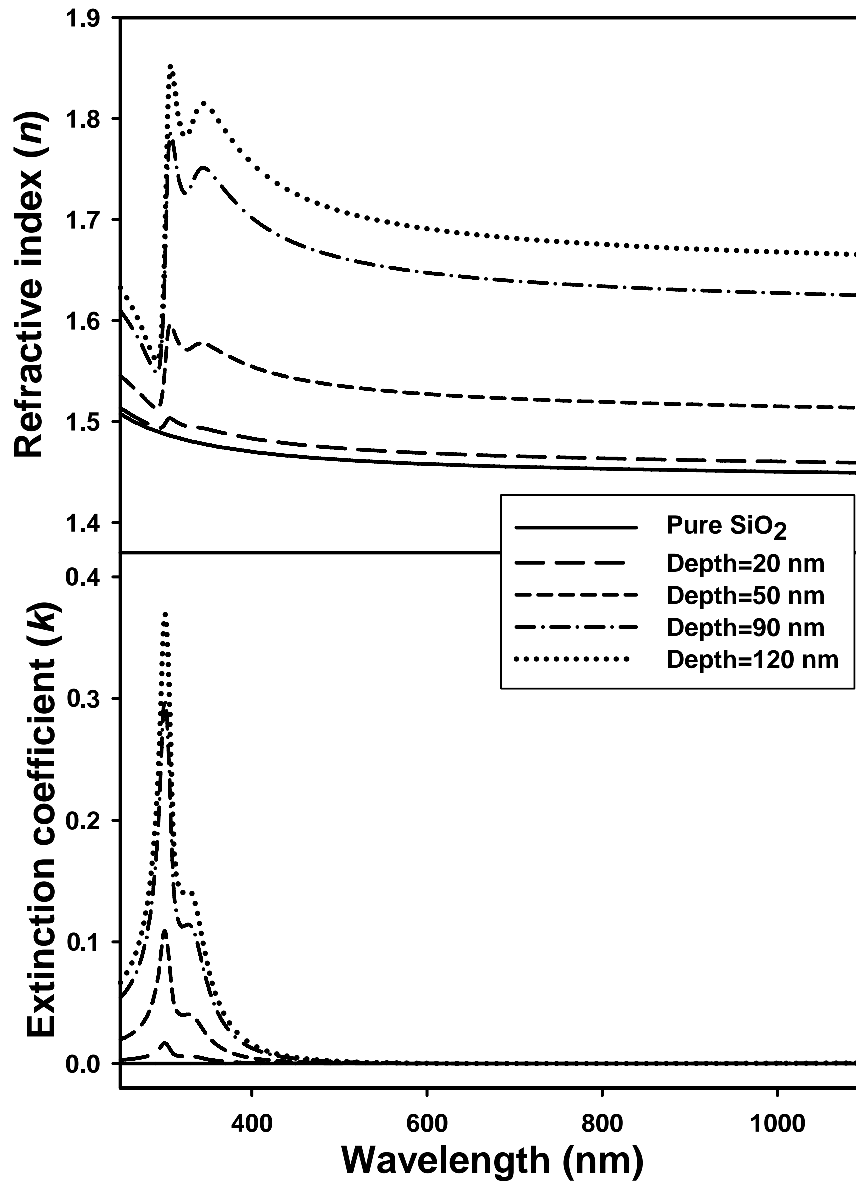

Figure 3.13 Optical constants of the film structure as functions of wavelength at the depths of 20, 50, 90, and 120 nm. The optical constants of pure SiO_2 are also included for comparison.

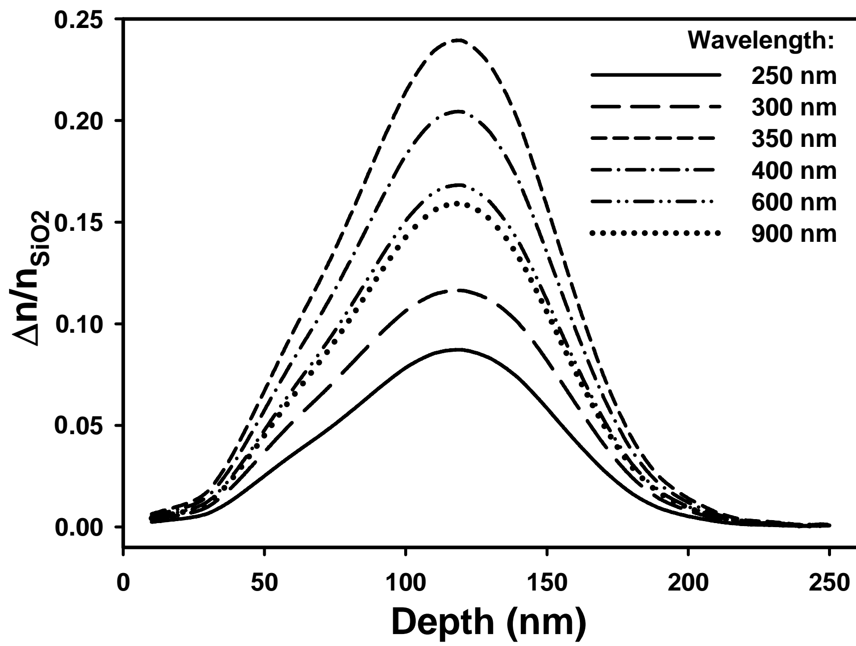

Figure 3.14 Depth profile of $\Delta n / n_{\mathrm{SiO_2}}$ for various wavelengths.

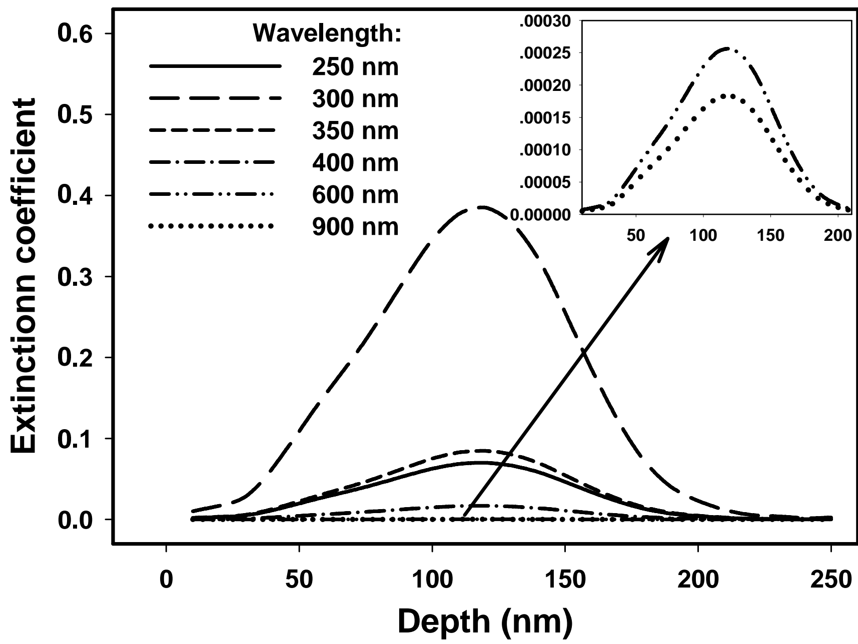

Figure 3.15 Depth profile of extinction coefficient for various wavelengths.

3.4.3 Conclusion

Based on the optical constants of nc-Si those have been obtained in Section 3.3 and the EMA theory, the optical constants of the film at a given depth are formulated, and thus the depth profiles of the optical constants of the SiO_2 film containing nc-Si synthesized with Si ion implantation are obtained. The result also suggests that the structure has a very low optical loss in the visible to infrared spectral range, and offers light-trapping ability and thus the possibility of wave guiding.

3.5 Thermal Annealing Effect on Dielectric Functions of nc-Si Embedded in SiO_2

Very few studies have been focused on dielectric functions of dispersed nc-Si embedded in SiO_2 being prepared with Si ion implantation under different annealing conditions. In this study, we present a comprehensive optical study on nc-Si embedded in SiO_2 matrix with SE in the photon energy range of 1.1–5 eV. The effects of post-implantation thermal annealing on both the bandgap and the dielectric functions of the nc-Si have been investigated.

3.5.1 Sample Fabrication and Experiments

500-nm-think SiO_2 thin films were grown on *p*-type silicon substrates with (100) orientation by thermal oxidation in dry oxygen at 950 ºC. A dose of 1×10^{17}

atoms/cm^2 Si ions were then implanted into SiO_2 films at the energy of 100 keV. Post-implantation thermal annealing was carried out in nitrogen ambient at various temperatures for different annealing times. For simplicity, here only the results of annealing at 1000 ºC for various annealing durations ranging from 0 to 100 min (0, 20, 30, 40, 60, 80 and 100 min) and the results of annealing for 20 min at different temperatures (500, 700, 850, 900 and 1000 ºC) are presented.

The average size of nc-Si was determined from the broadening of the Bragg peak in XRD measurement. The nc-Si size obtained was from ~3.3 nm for the as-implanted sample to ~4.5 nm for the samples annealed at 1000 ºC for different durations, and from ~3.3 nm for the as-implanted sample to ~4.6 nm for the samples annealed for 20 min at different annealing temperatures. The nc-Si sizes for various annealing conditions obtained from the XRD measurements are shown in TABLE 3.3. A very small increase in the nc-Si size with annealing time and temperature is observed. The slow nc-Si size evolution with thermal annealing is similar to the results of Ref. [125], which reported that the nc-Si size increases slightly from 2.5 nm after 1 min annealing to 3 nm after annealing for 16 hours at the temperature of 1100 ^{o}C. This slow evolution in the size is due to the very low diffusion coefficient (10^{-16}–10^{-18} cm/s) of Si in SiO_2 film [220-222].

The SE measurements were carried out in the wavelength range of 250 and 1100 nm with a step of 5 nm, and the incidence angle was set to 75º. The profile of excess Si in the SiO_2 thin films was measured with SIMS. The implanted Si distributes from the surface to the depth of ~250 nm, and the subsequent

annealing does not change the profile significantly because of the extremely low diffusion coefficient of Si in SiO_2 films.

TABLE 3.3 Size, bandgap and static dielectric constant of nc-Si annealed for different durations. E_g^{exp} and ε_s^{exp} are the bandgap and the static dielectric constant of nc-Si obtained from the spectral fittings based on the four-term FB model, respectively. E_g^{cal} is the nc-Si bandgap obtained from the calculation with Eq. (3.35), while ε_s^{cal} is the nc-Si static dielectric constant obtained from the calculation with Eq. (3.36).

Annealing conditions	Size (nm)	E_g^{cal} (eV)	E_g^{exp}(eV)	ε_s^{cal}	ε_s^{exp}
As-implanted	3.3±0.4	2.03±0.15	1.78	8.98±0.34	8.82
1000 ºC for 20 min	4.6±0.2	1.73±0.03	1.74	9.72±0.08	9.67
1000 ºC for 30 min	4.2±0.2	1.79±0.05	1.74	9.54±0.10	9.52
1000 ºC for 40 min	4.5±0.2	1.74±0.04	1.74	9.68±0.09	9.73
1000 ºC for 30 min	4.3±0.2	1.78±0.04	1.75	9.59±0.10	9.73
1000 ºC for 30 min	4.5±0.2	1.74±0.04	1.74	9.68±0.10	9.61
1000 ºC for 30 min	4.5±0.2	1.74±0.04	1.72	9.68±0.10	9.73
500 ºC for 20 min	3.3±0.4	2.03±0.15	1.78	8.98±0.34	8.82
700 ºC for 20 min	3.1±0.4	2.10±0.16	1.84	8.82±0.32	8.78
850 ºC for 20 min	3.9±0.2	1.86±0.07	1.76	9.38±0.12	9.29
900 ºC for 20 min	4.1±0.2	1.82±0.06	1.76	9.46±0.11	9.41

3.5.2 Results and Discussions

Based on the method discussed in Section 3.3.4, the dielectric functions of nc-Si have been obtained based on the best spectral fitting. The nc-Si bandgap (E_g) obtained from the spectral fittings for various annealing durations is given in TABLE 3.3. The nc-Si shows a large expansion in the bandgap as compared to the bulk crystalline Si. The nc-Si bandgap obtained in this work is in very good agreement with the values calculated with Eq. (3.35) which is obtained from the fitting result of the first-principle calculation of the nc-Si optical gap based on

quantum confinement. For comparison, the bandgap of nc-Si calculated with Eq. (3.35) is presented in TABLE 3.3. The very good agreement shown in TABLE 3.3 strongly suggests that the bandgap expansion is a result of quantum size effect.

As examples, the dielectric functions of nc-Si obtained after 0 (non-annealing), 30 and 80 min of annealing are shown in Fig. 3.16. The dielectric function of bulk crystalline Si are is included in the figure for comparison. Obviously, the nc-Si exhibits a significant reduction in the dielectric functions with respect to bulk crystalline silicon. It is observed that the dielectric-function spectra of the nc-Si of different annealing durations except the non-annealing sample are very similar. This is not surprising, and it can be explained in terms of quantum size effect on the dielectric functions [74, 205]. As shown in TABLE 3.3, except the non-annealing sample which shows the nc-Si size of ~3.3 nm, all other samples with different annealing durations have almost the same nc-Si size (~4.5nm). In general, the dielectric function of bulk crystalline Si shows main peaks at the transition energies E_1 (~3.4 eV) and E_2 (~4.3 eV) as its critical points. As for the case of nc-Si formed after high temperature annealing, the dielectric spectra show a slight blue shift in the main transition energy E_1 (~3.6 eV) position, and a slight red shift in E_2 (~4.0 eV) position. However, in the case of as-implanted (i.e., non-annealing) sample, the dielectric functions of nc-Si show only a single peak in the experimental photon-energy range, possibly because of larger broadenings of E_1 and E_2 bandgaps due to a significant change of surface area to volume ratio when the size of nc-Si is being close to 3 nm.

In order to investigate the annealing temperature effect on dielectric functions of nc-Si, the samples annealed for 20 min at various temperatures (500, 700,

800, 850, 900 and 1000 ºC) were also studied with spectroscopic ellipsometry. For simplicity, the dielectric functions of nc-Si for the as-implanted sample and the samples annealed 700 and 900 ºC are shown in Fig. 3.17. As can be seen in TABLE 3.3, the average size of nc-Si for 500 ºC annealing sample is approximately the same as that of the as-implanted sample. When the annealing temperature goes up greater than 500 ºC, say, 700, 900 and 1000 ºC, the dielectric functions and optical constants will have a distinct change due to the slightly increasing size with annealing, as shown in Fig. 3.17. This indicates that a high temperature annealing greater than 500 ºC is needed for the evolution of nc-Si size.

On the other hand, the static dielectric constant ($\varepsilon_{static}^{\exp}$) of nc-Si is obtained by setting the photon energy to zero in the FB model, and the result is also given in TABLE 3.3. Thanks to the extensive studies on the nano-structured Si, the fact that the suppression of dielectric constant becomes significant when the nanocrystal size approaches to the nano-metric range is nowadays unquestionable.

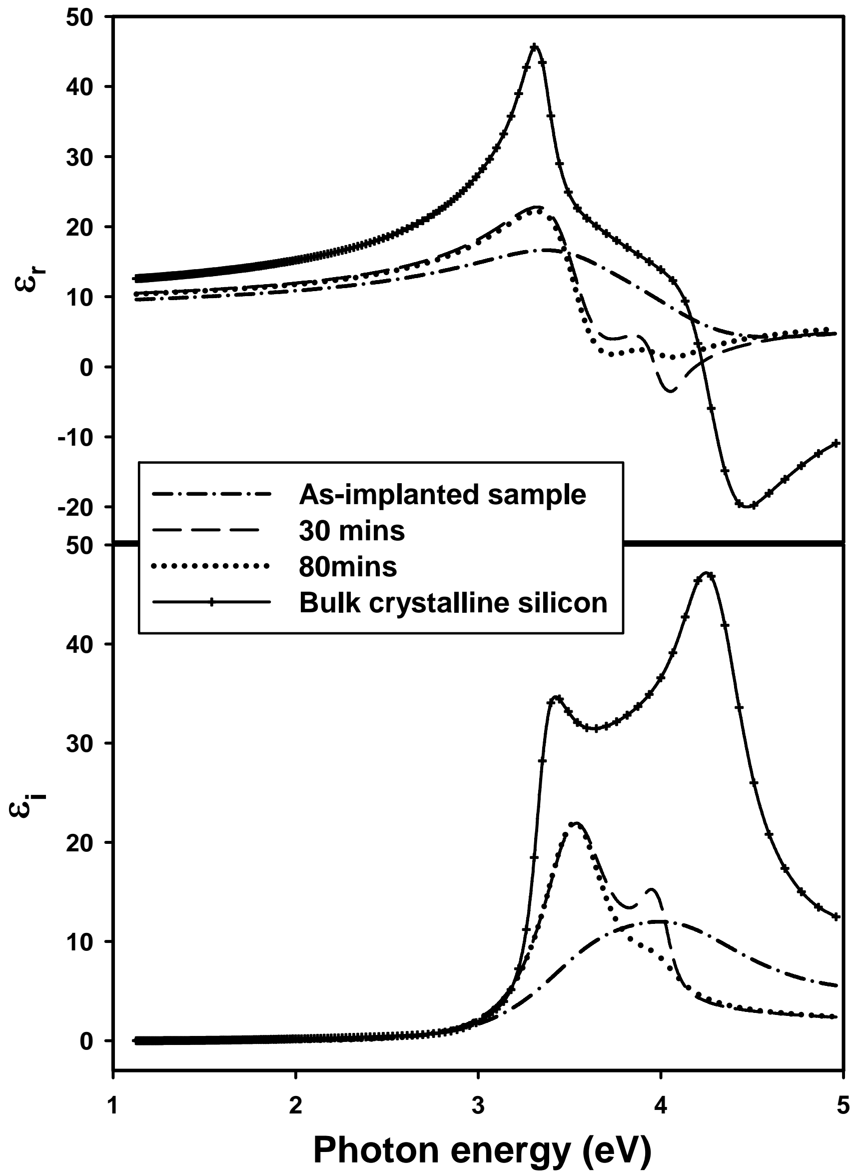

Figure 3.16 Real (ε_r) and imaginary (ε_i) parts of the complex dielectric functions of both the nc-Si annealed for 0, 30, and 80 min at 1000 ºC and the bulk crystalline silicon as functions of photon energy.

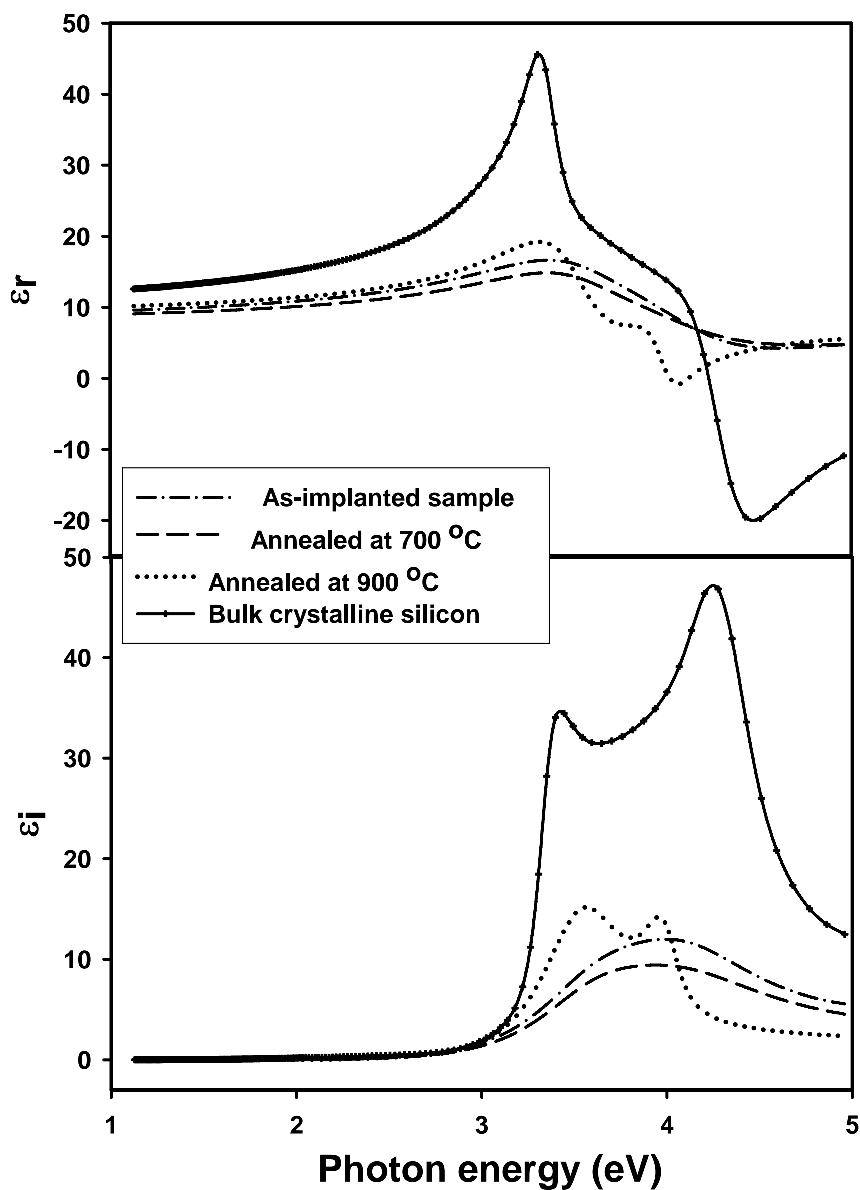

Figure 3.17 Real (ε_r) and imaginary (ε_i) parts of the complex dielectric functions of both the nc-Si of as-implanted sample and annealed at 700 and 900 ºC, for 20 min and the bulk crystalline silicon as functions of photon energy.

3.5.3 Conclusion

In conclusion, we have investigated the thermal annealing effect on dielectric functions and bandgap of Si nanocrystals embedded in SiO_2 matrix by spectroscopic ellipsometry. In the SE analysis, a multilayer optical model which

takes into account the nc-Si distributions in the SiO_2 film, the Maxwell-Garnett effective medium approximation and the four-term Forouhi-Bloomer optical dispersion relation are used. The dielectric functions of nc-Si for different annealing durations show a significant suppression as compared to bulk crystalline silicon, which is attributed to the quantum size effect. The nc-Si of as-implanted (i.e., non-annealing) sample presents only one peak in the dielectric spectra, while the annealed ones have two critical points in the range of 1-5 eV. The nc-Si for various annealing durations shows a large bandgap expansion of ~0.6 eV, which is in good agreement with the theoretical calculation based on quantum confinement. The bandgap of the nc-Si for the non-annealing condition (i.e., as-implanted) is 1.78 eV while it is 1.72 eV for the annealing at 1000 ºC for 100 min. The slight decrease in the bandgap is attributed to the slight increase in the nc-Si size with annealing.

3.6 Size Effect on Dielectric Functions of nc-Si Embedded in SiO_2

Experimental determination on the dielectric functions of nc-Si embedded in SiO_2 has been presented so far. However, few experimental investigations on the size effect on optical properties of nc-Si embedded in SiO_2 matrix have been reported. In this section, nc-Si with different sizes ranging from 4.6 nm to 7.8 nm embedded in SiO_2 are synthesized with various implantation recipes (i.e., different implantation energies and doses). The influence of nanocrystal size on dielectric functions of the nc-Si is investigated with spectroscopic ellipsometry.

3.6.1 Sample Fabrication and Experiments

Wafers used in this study were *p*-type Si(100) with resistivity of 20-30 Ω cm. SiO_2 films with thickness of 550 nm were grown on the Si substrate by wet oxidation at 1000 ^oC. Afterwards, a high dosage of Si ions (10^{16}-10^{17} atoms/cm^2) were implanted into the SiO_2 films at various energies ranging from 100 to 3 keV (100 keV, 50 keV, 18 keV, 5 keV, and 3 keV) at room temperature, and the samples are denoted as sample 1, sample 2,…, and sample 5, respectively. Implantations were conducted at 7° off axis to reduce channeling effect. Silicon nanocrystals were formed after high temperature annealing at 1000 ^oC for 20 min in N_2 ambient. The average size of nc-Si was determined from the broadening of Bragg peak in the XRD spectrum. TABLE 3.3 gives the sizes of nc-Si for all the samples (i. e., samples 1 to 5) under the investigation in this study. Spectroscopic ellipsometry (SE) measurement was carried out with a spectroscopic ellipsometer (J. A. Woollam Co., Inc.) in the wavelength range of 250–1100 nm with a step of 5 nm, and the incident angle was set at 75°.

As the operation of SIMS measurement is very expensive for a large number of samples, the excess Si distribution in the SiO_2 thin film is obtained from the stopping and range of ions in matter (SRIM) simulation in this study. The volume fractions of excess Si in the SiO_2 are calculated using Eq. (3.12). Figure 3.19 shows the depth profiles of the volume fraction of excess Si in SiO_2 for the five samples obtained from SRIM simulations. The peak volume fractions of excess Si for the samples are also included in TABLE 3.4.

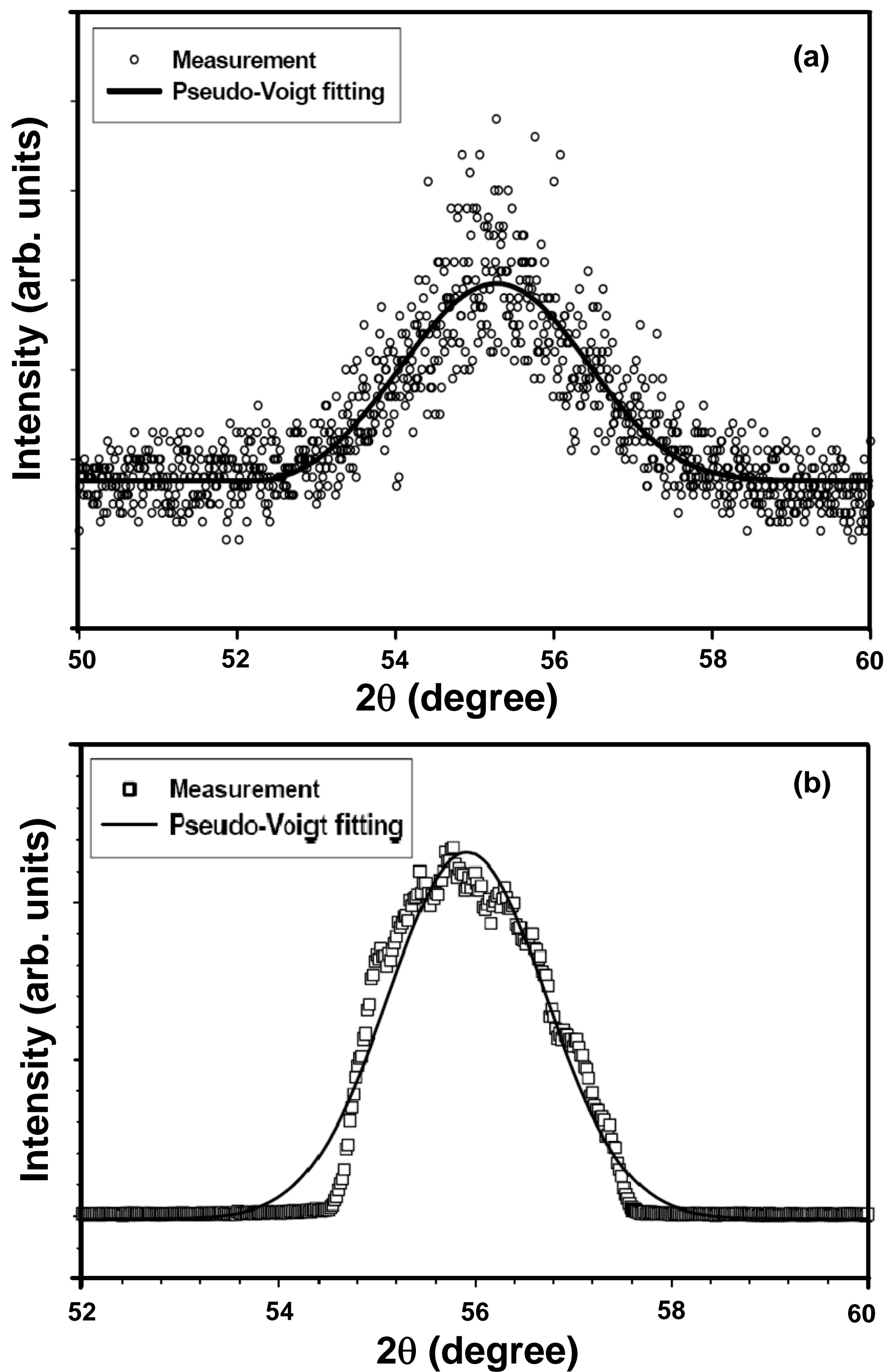

Figure 3.18 XRD measurement of Si nanocrystals embedded in SiO_2 matrix and the pseudo-Voigt fit to the data for (a) sample 1 with nc-Si size of 4.6 nm; and (b) sample 2 with nc-Si size of 5.3 nm.

TABLE 3.4. Implantation energies and doses, maximum volume fractions of excess Si in SiO_2, and the nc-Si sizes for the 5 samples.

	Implantation Energy (keV)	Dosage (ions/cm^2)	Peak volume fraction of excess Si	Size of nc-Si (nm)
Sample 1	100	1×10^{17}	17%	4.6
Sample 2	50	8×10^{16}	28%	5.3
Sample 3	18	5×10^{16}	40%	5.8
Sample 4	5	5×10^{16}	60%	6.3
Sample 5	3	5×10^{16}	93%	7.6

In this study, the four-term FB model is employed to obtain a reasonable fitting in the photon energy range of 1–5 eV. Increase in the number of the FB model terms can improve the fitting. However, the improvement is not significant, indicating that the four terms used in the FB model are the major contributors, while the computation time is increased significantly.

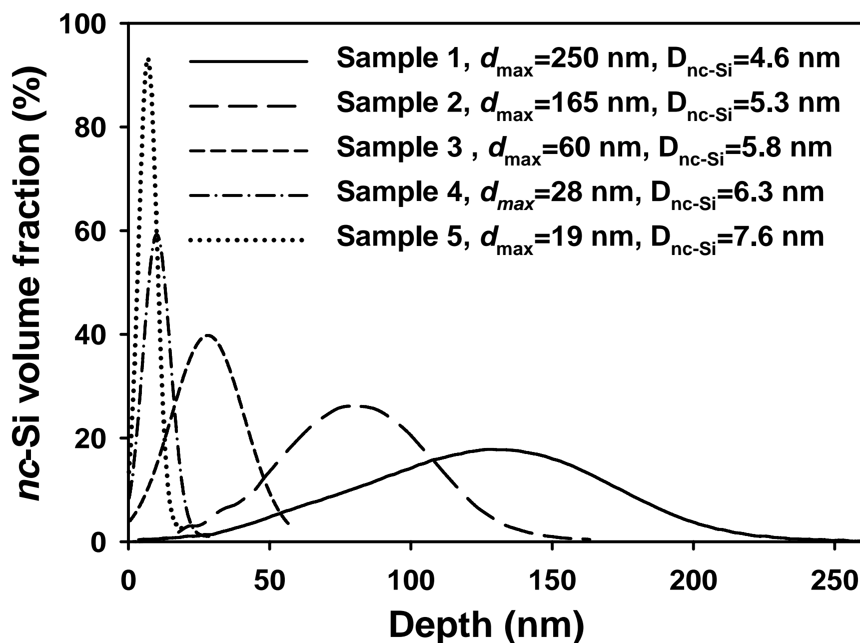

Figure 3.19 Volume fractions of nc-Si in SiO_2 as a function of depth for the five samples obtained from SRIM simulation.

As can be seen in TABLE 3.4, the size of nc-Si varies with the implantation recipe (i.e., the implantation energy and dose). This is actually a result of the variation in the concentration of excess Si in SiO_2. The excess Si with a higher concentration should tend to aggregate more easily and form nc-Si with a larger size during the high temperature annealing. As the concentration of excess Si in SiO_2 is determined by the implantation recipe (i.e., energy and dose), the nc-Si size can thus be varied in terms of the variation in the implantation energy and/or implantation dose. With this way we are able to synthesize the five samples with various nc-Si sizes.

3.6.2 Results and Discussions

Using the methodology described in Section 3.3.4, we have obtained the dielectric functions of the nc-Si with various sizes embedded in SiO_2 for the five samples, and they are shown in Fig 3.20. The dielectric functions of bulk crystalline Si are also included in the figure for comparison. The parameters including A_i, B_i, C_i (i=1, 2, 3, and 4), $n(\infty)$ and E_g of the four-term FB model for the nc-Si with various sizes are given in TABLE 3.5. For comparison, the corresponding parameters of bulk crystalline Si are also included in the table.

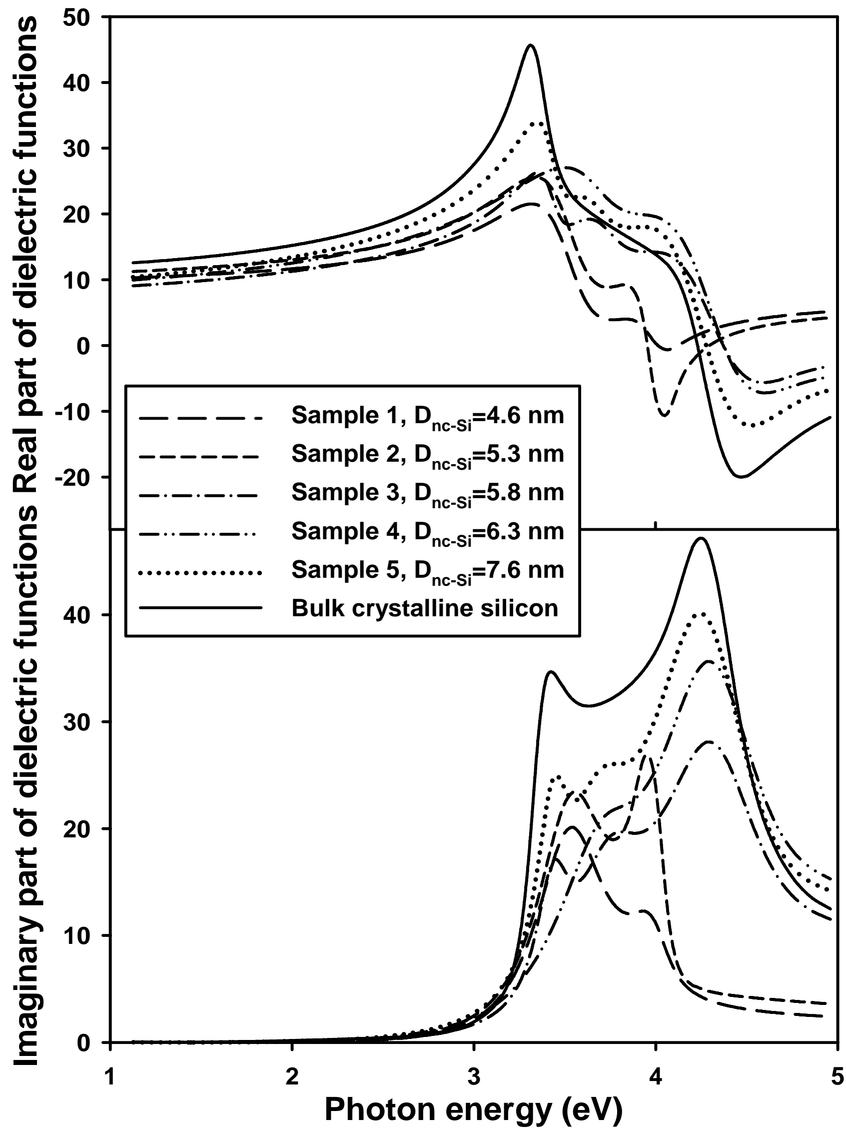

Figure 3.20 Real (ε_1) and imaginary (ε_2) parts of the complex dielectric function of the nc-Si with various sizes obtained from the spectral fittings. The dielectric function of bulk crystalline silicon is also included for comparison.

TABLE 3.5. Values of the parameters A_i, B_i, and C_i (i = 1, 2, 3, 4), $n(\infty)$ and E_g of the four-term FB model for the 5 samples. The corresponding values of bulk crystalline Si are also included.

	nc-Si size (nm)	A_i	B_i (eV)	C_i (eV^2)	$n(\infty)$	E_g (eV)
Sample 1	4.6	0.0534	7.1121	12.7223	2.8143	1.7371
		0.0057	8.0148	16.0834		
		0.0605	8.0312	18.7121		
		0.0003	11.3674	33.6447		
Sample 2	5.3	0.0458	7.1119	12.7176	2.8237	1.6864
		0.0089	8.0157	16.0797		
		0.0843	8.3300	18.7101		
		0.0113	10.3227	33.6447		
Sample 3	5.8	0.0043	6.8850	11.8641	2.0179	1.6312
		0.0154	7.5102	14.1610		
		0.0652	8.7143	19.1612		
		0.1854	10.5212	29.2021		
Sample 4	6.3	0.0145	7.0851	12.7275	2.0211	1.5312
		0.0146	7.4057	13.7881		
		0.0653	8.7143	19.1601		
		0.2154	10.5312	29.2021		
Sample 5	7.8	0.0041	6.8854	11.8654	1.9498	1.4503
		0.0149	7.4013	13.7545		
		0.0767	8.6341	18.8134		
		0.2117	10.6517	29.8456		
Bulk crystalline silicon	/	0.0036	6.8811	11.8486	2.3688	1.12
		0.014	7.4013	13.7473		
		0.0683	8.6348	18.7952		
		0.0496	10.2339	26.5029		

TABLE 3.5 clearly shows that the nc-Si exhibits a large expansion in the band gap as compared to that of the bulk crystalline Si and the band gap of the nc-Si increases when the nc-Si size is reduced. For example, for the nc-Si with a size of 4.6 nm (sample 1), it has a band gap of 1.74 eV which is significantly larger than the band gap (1.1 eV) of the bulk crystalline silicon. The band gap expansion is the most direct evidence of quantum confinement effect of nc-Si.

The band gap expansion of nc-Si and its dependence on the nanocrystal size have been demonstrated by some theoretical calculations of the band gap of nc-Si [202, 205]. The bandgap expansion obtained from the first-principle calculation of the optical gap of silicon nanocrystal based on quantum confinement reported in Ref. [202] can be expressed with Eq. (3.35). A calculation of the band gap expansion with Eq. (3.35) is shown in Fig. 3.21, and the calculation is also compared with the band gap expansions obtained from the SE analysis discussed above. A good agreement in the comparison can be seen in Fig. 3.21. This suggests that the band gap expansion is due to the quantum confinement and thus the dielectric functions and optical constants of the nc-Si obtained in this study should be related to the quantum confinement also.

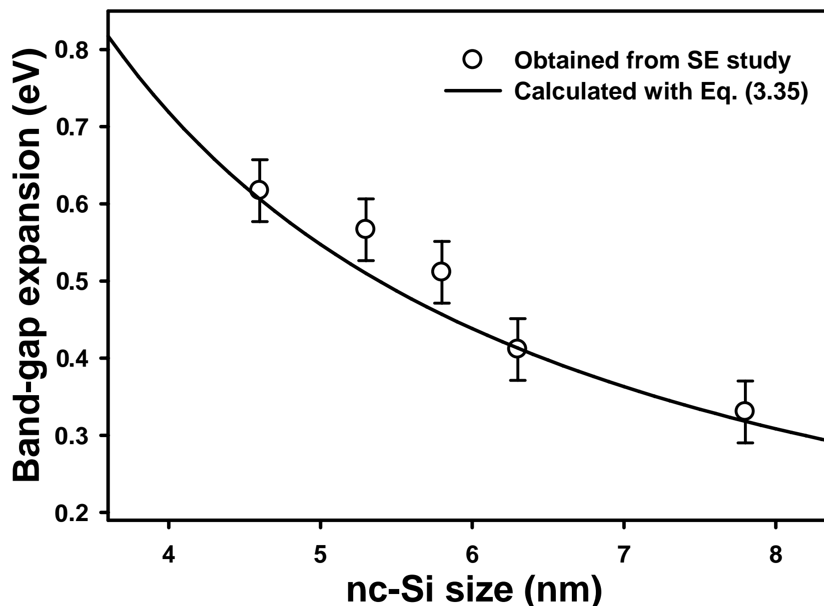

Figure 3.21 Band gap expansion of nc-Si as a function of nc-Si size.

3.6.3 Conclusion

Si nanocrystals with different sizes ranging from 4.6 nm to 7.8 nm embedded in SiO_2 have been synthesized with various implantation recipes (i.e., different implantation energies and doses). Dielectric functions of the nc-Si have been studied in the photon energy range of 1.1 - 5 eV with spectroscopic ellipsometry based on Maxwell-Garnett effective medium approximation and the four-term FB optical dispersion model. The band gap of the nc-Si embedded in SiO_2 is also obtained from the SE analysis. The influence of nanocrystal size on the optical properties of the nc-Si has been investigated. A strong dependence of the dielectric functions and optical constants on the nc-Si size is observed. For the imaginary part of the dielectric function, the magnitude of the main peaks at the transition energies E_1 and E_2 exhibits a large reduction and a significant redshift in E_2 depending on the nc-Si size. A band gap expansion is observed when the nc-Si size is reduced. The band gap expansion with the reduction of nc-Si size is in good agreement with the prediction of first-principle calculations based on quantum confinement.

3.7 Dielectric Functions of Densely-stacked nc-Si Layer Embedded in SiO_2

With this Si^+-implantation technique, isolated Si nanocrystals dispersed in a SiO_2 matrix [42, 124, 160] or densely-stacked Si nanocrystal layers [81, 106, 223, 224] embedded in SiO_2 can be formed depending on the implantation recipe. The former could be used for Si optoelectronic applications while the latter could be used in memory devices. Very few studies on the dielectric

functions of the densely-stacked Si nanocrystal layer synthesized by ion implantation have been reported so far. The optical properties of the densely-stacked nanocrystal layer should be different from that of both the isolated nc-Si and the continuous nc-Si film. It is necessary to investigate the optical properties of the densely-stacked nanocrystal layer because of the importance of such nanoscale structure in both fundamental physics and applications. In practice, the Si ion implantation into a thin SiO_2 film with a high dose (typically in the range of $\sim 10^{16}$-$\sim 10^{17}$ cm^{-2}) at a very-low energy (≤ 2 keV) can form such densely-stacked nanocrystal layers embedded in SiO_2 [81, 106, 223, 224]. In this study, the dielectric function of the densely-stacked Si nanocrystal layer embedded in SiO_2 has been determined by SE fittings, and the influence of thermal annealing on the dielectric function has been investigated also.

3.7.1 Sample Fabrication and Experiments

30-nm SiO_2 thin films were thermally grown in dry oxygen at 950 ^oC on a *p*-type Si (100) wafer. Si ions with a dose of 8×10^{16} cm^{-2} were then implanted into the SiO_2 thin films at 1 keV. Postimplantation thermal annealing was carried out in N_2 at various annealing temperatures for different durations. The mean size of nc-Si was estimated from full width at half-maximum (FWHM) of the Bragg in the X-ray diffraction (XRD) measurement. The average size of nanocrystals was estimated to be ~3-4 nm. It was found that the nc-Si size changes little with annealing. This observation is consistent with those reported in literatures [125, 223]. The cross sectional transmission electron microscopy

(TEM) measurement reveals the existence of a densely-stacked Si nanocrystal layer with a thickness of ~16 nm embedded in SiO_2, as shown in Fig. 3.21. The sample is annealed at 1000 ^{o}C for 20 min (i.e., sample *a*). To determine the optical properties of the densely-stacked Si nanocrystal layer, SE measurements were carried out in the wavelength range of 250–1100 nm with a step of 5 nm, and the incident angle was set at 75°.

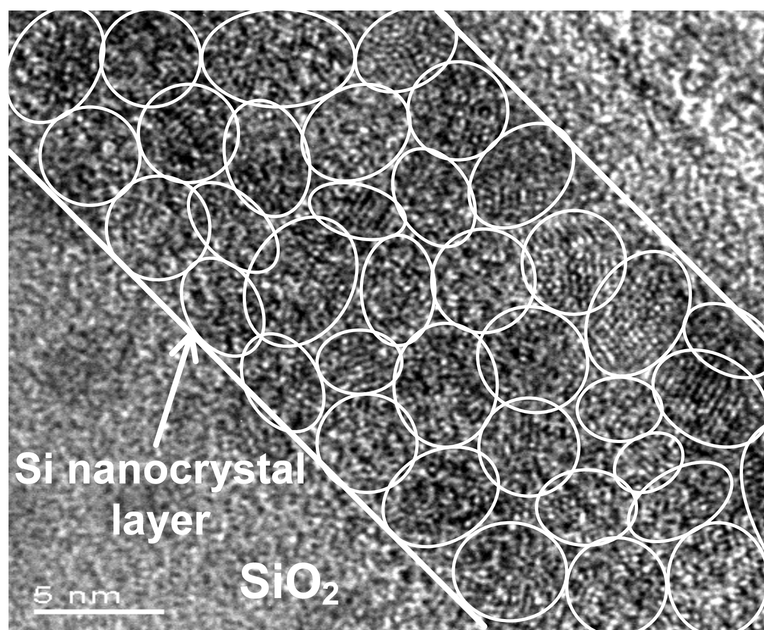

Figure 3.22 Cross-sectional TEM image of the densely-stacked Si nanocrystal layer embedded in SiO_2 thin film for sample *a*.

3.7.2 Methodology

For the SE analysis, an appropriate optical model is required. As a densely-stacked Si nanocrystal layer is formed in the SiO_2 thin film, the model developed for the isolated nc-Si embedded in a SiO_2 matrix that has been developed in the above sections is inadequate for this study. In the present study, a single layer of densely-stacked nc-Si is embedded in the SiO_2 thin film as revealed by the TEM image shown in Fig. 3.21, and the situation is different

from that of the isolated nc-Si dispersed in a SiO_2 matrix. Obviously, this densely-stacked nc-Si layer should be treated as a phase in the ellipsometric analysis. Therefore, a five-phase model, namely air/SiO_2 layer/densely-stacked nc-Si layer/SiO_2layer/Si substrate, which is shown in Fig. 3.22 (a), was employed to carry out the SE fittings in the present study. Note that in this model, the ellipsometric angles (Ψ and Δ) are functions of the thicknesses and dielectric functions of all the layers. Excellent fittings with meaningful outputs have been achieved with this model. Note that no optical dispersion model was required for the SE fittings with the model. As an example, Fig. 3.22(b) shows the spectral fitting of Ψ and Δ for sample *a* (i.e., the sample annealed at 1000 ^{o}C for 20 min). As can be seen in this figure, all the complicated spectral features of both Ψ and Δ can be fitted excellently, indicating that the model shown in Fig. 3.18(a) is effective.

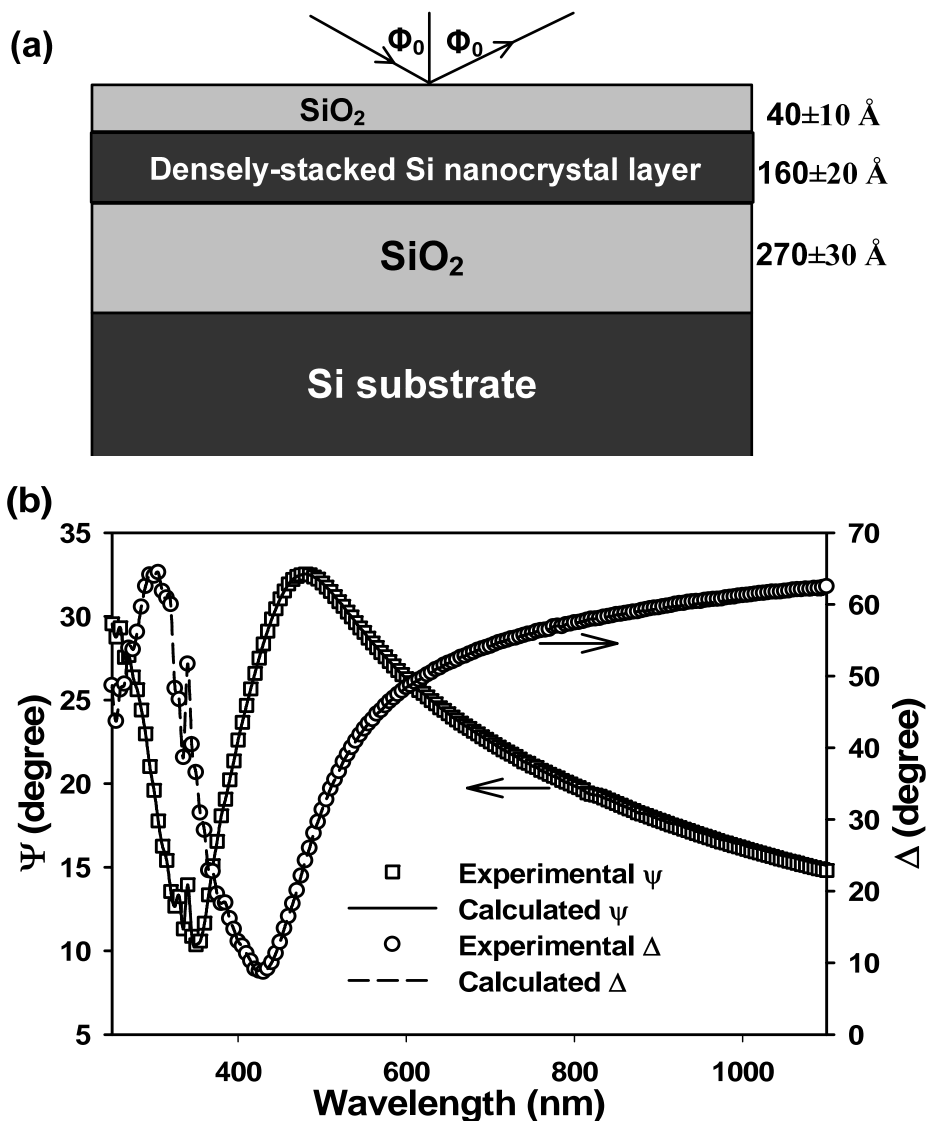

Figure 3.23 (a) Five-phase model used in the SE analysis. (b) Spectral fittings of Ψ and Δ for sample *a*.

3.7.3 Results and Discussions

Figure 3.24 shows the dielectric functions of the densely-stacked Si nanocrystal layer for sample *a*. For comparison, the dielectric functions of other Si materials are also included in Fig. 3.23. As can be seen in the figure, the dielectric spectra of the densely-stacked Si nanocrystal layer are similar to that of amorphous Si but different from those of both bulk crystalline Si and the isolated nc-Si whose

dielectric functions have been investigated in Section 3.3. For the imaginary part of dielectric functions, the densely-stacked Si nanocrystal layer and amorphous Si show a single broadened peak; in contrast, bulk crystalline Si and the isolated nc-Si exhibit a two-peak structure. The peak structures in the dielectric spectra are believed to originate from singularities in the joint density of states (DOS). Essentially, the DOS in the amorphous state is a broadened version of crystalline state, which leads to a single broad peak in the dielectric spectra of amorphous semiconductors. Therefore, the single peak structure may suggest that the nanocrystal layer is in an amorphous state to certain extent. On the other hand, the nanocrystal layer also shows significant reductions in the amplitude of dielectric functions as compared with bulk crystalline Si and amorphous Si, which is related to the size effect of the nanocrystals.

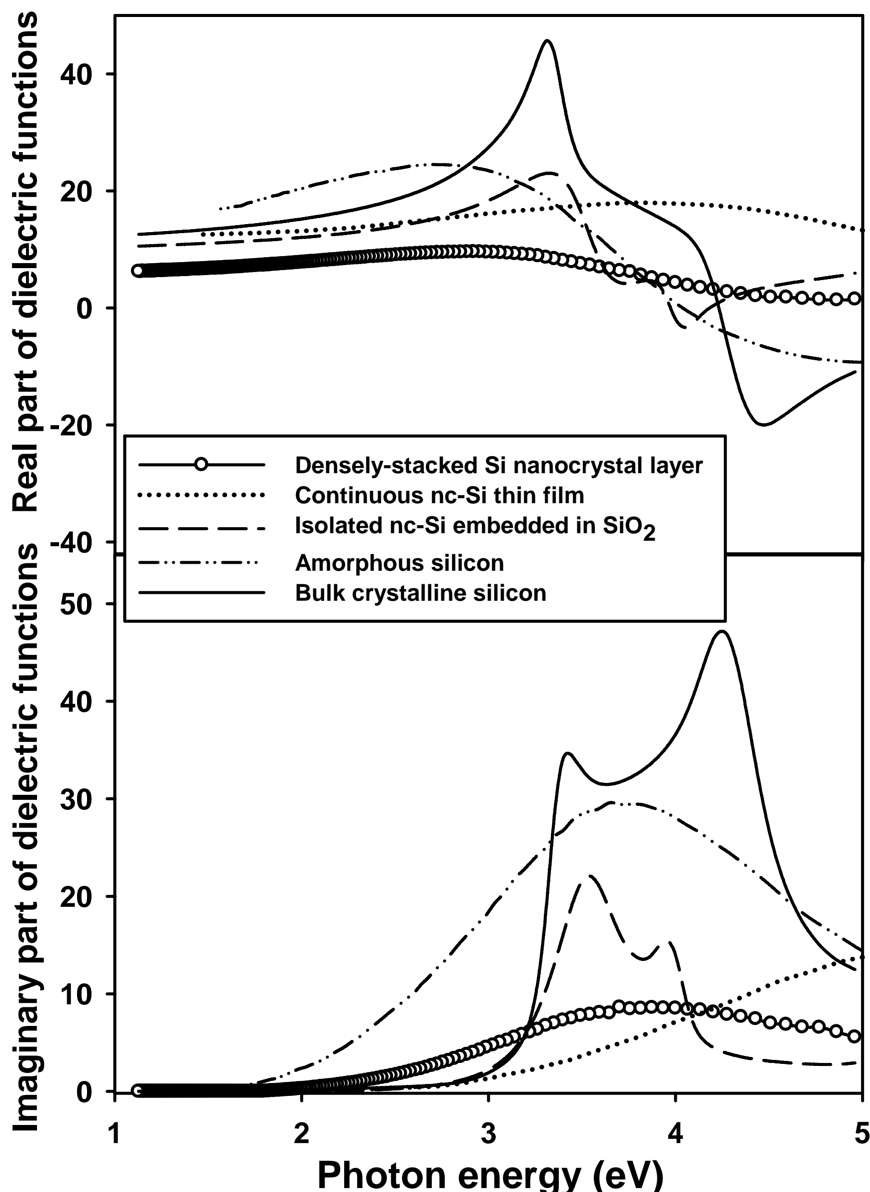

Figure 3.24 Real (ε_1) and imaginary (ε_2) parts of the complex dielectric functions of the densely-stacked Si nanocrystal layer for sample *a*. For comparison, the dielectric functions of the continuous nc-Si thin film [98], the isolated nc-Si dispersed in a SiO_2 matrix, amorphous Si and bulk crystalline Si are also included in this figure.

Furthermore, we observed a significant influence of the annealing on the dielectric functions of the densely-stacked Si nanocrystal layer. Figure 3.25 shows the imaginary part of dielectric functions of the densely-stacked silicon nanocrystal layer synthesized at a fixed annealing temperature of 1000 ^{o}C for different annealing durations. The dielectric function changes with the

annealing duration, showing a trend towards bulk crystalline Si. Firstly, the dielectric function increases with the annealing duration. Secondly, the dielectric function exhibits a clear two-peak structure when the annealing duration is 30 min, and the structure is further enhanced when the annealing duration is 80 min. The structure is analogue to that of bulk Si which has two peaks at the transition energies E_1 (~3.4 eV) and E_2 (~4.3 eV) as its critical points. E_1 of the nanocrystal layer is about the same as that of bulk crystalline Si, and it changes very little with the annealing duration. However, E_2 of the nanocrystal layer is slightly lower than that of bulk Si, but it shows a small blue-shift towards that of bulk Si with the increase in annealing duration. However, it should be pointed out that extending the annealing duration should not result a dielectric function that is approaching that of bulk crystalline Si because of the quantum size effect of the nc-Si and the difference in the structure between the two materials. A similar annealing effect on the dielectric functions is also observed from the experiment of various annealing temperatures. Figure 3.26 shows the evolution of the dielectric functions with annealing temperature for the fixed annealing duration of 20 minutes. One can observe from Fig. 3.25 together with Fig. 3.23 that for the annealing duration of 20 min, only a single broad peak in the dielectric spectra exists when the annealing temperature is 1000 ^{o}C or lower, but a two-peak structure emerges when the annealing temperature is 1100 ^{o}C. Therefore, it is clear that thermal annealing promotes the evolution of the dielectric functions towards that of bulk crystalline Si. The mechanism for the annealing effect is not known yet, but one may attribute it to the crystallization and or the growth of the nanocrystals caused by the annealing.

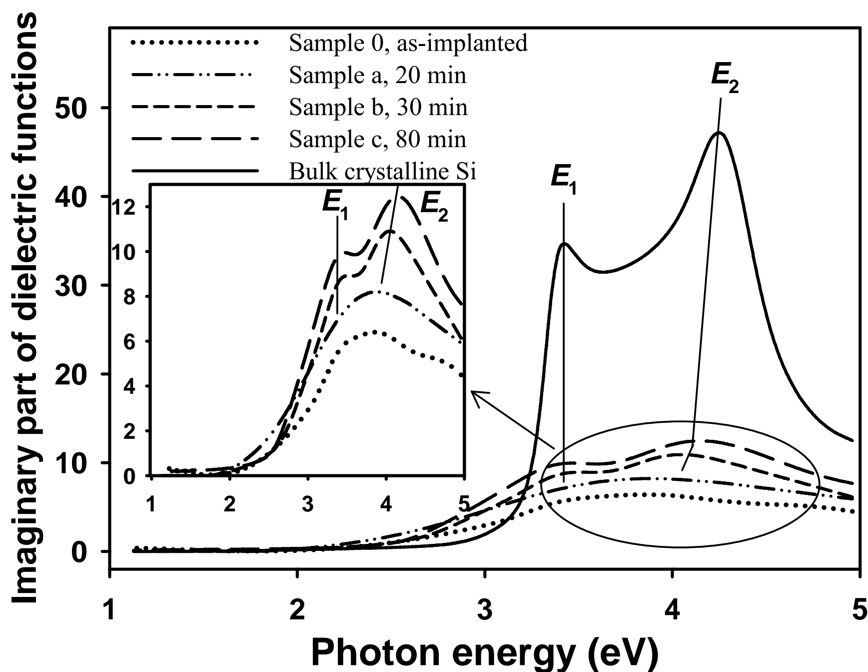

Figure 3.25 Influence of annealing duration on the imaginary (ε_2) part of the complex dielectric functions of the densely-stacked Si nanocrystal layer. The annealing temperature is fixed at 1000 ^{o}C.

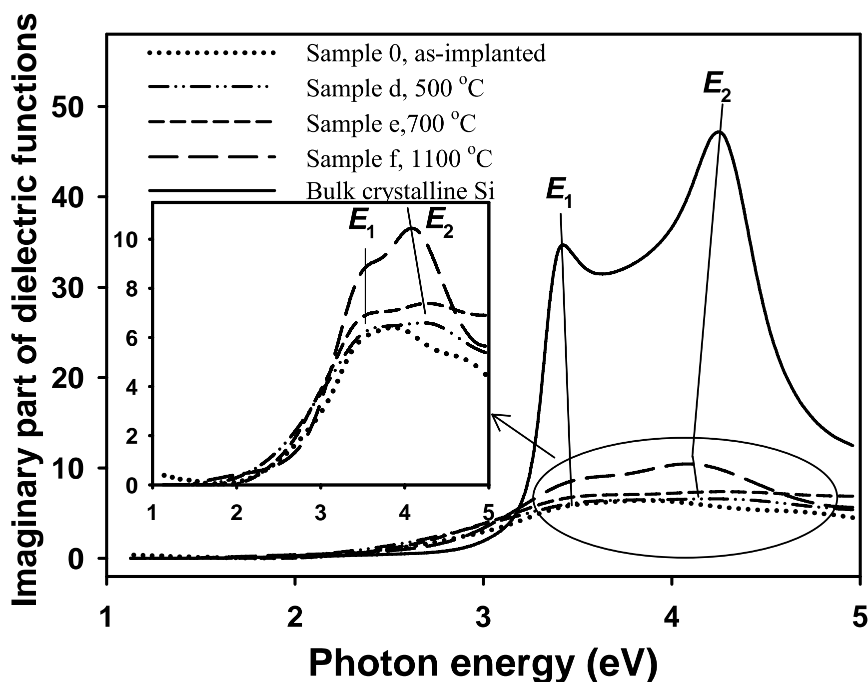

Figure 3.26 Influence of annealing temperature on the imaginary (ε_2) part of the densely-stacked Si nanocrystal layer. The annealing duration is 20 min.

3.7.4 Conclusion

The dielectric functions of the densely-stacked Si nanocrystal layer embedded in SiO_2 have been determined with spectroscopic ellipsometry. It is observed that thermal annealing has a strong influence on the dielectric functions. For the fixed annealing temperature of 1000 ^{o}C, if the annealing duration is 20 min or shorter, the dielectric functions are similar to that of amorphous Si, showing a single broad peak in the dielectric spectra; however, a two-peak structure, which is analogue to that of bulk crystalline Si, emerges when the annealing duration is 30 min or longer. For the fixed annealing duration of 20 min, if the annealing temperature is 1000 ^{o}C or lower, the dielectric functions are similar to that of amorphous Si, but the two-peak structure emerges when the annealing temperature is 1100 ^{o}C. In conclusion, thermal annealing promotes the evolution of the dielectric functions from the amorphous state towards crystalline state.

3.8 Summary

In this chapter, a non-destructive approach has been developed to determine the dielectric function of Si nanocrystals (nc-Si) embedded in a SiO_2 matrix with spectroscopic ellipsometry (SE) based on the Maxwell-Garnett effective medium approximation (EMA). Dielectric function, optical constants (i.e., refractive index and extinction coefficient), and absorption coefficient of the nc-Si embedded in SiO_2 have been obtained in the photon energy range of 1.1-5.0 eV. The annealing effect on the static dielectric constant and dielectric

function is studied. In addition, the size dependency on the dielectric properties of nc-Si is investigated. Dielectric functions of another type of Si nanocrystal structure (i.e., densely-stacked nc-Si layer) synthesized by Si ion implantation have been determined and compared with that of other Si materials. Finally, the depth profiling of optical constant of SiO_2 films embedded with nc-Si has been determined, suggesting a potential in the application of active waveguides.

CHAPTER 4 PHOTOLUMINESCENCE OF SI NANOCRYSTALS EMBEDDED IN DIELECTRIC FILMS

4.1 Introduction

Although efficient room-temperature photoluminescence (PL) from dielectric films embedded with nc-Si synthesized by ion implantation technique has been reported by many research groups, the mechanism of PL from such materials is still under debate. For example, for the system synthesized with Si ion implantation, the visible-light (in particular the red-light) luminescence has been found to be strongly size-dependent. [14, 23, 42, 120, 122, 124, 126, 156-160, 225]. They attributed the PL to the quantum-confined excitons in Si nanocrystals. There have been both theoretical and experimental reports that support the theory of quantum-confined excitons which are responsible for the size-dependent PL from Si nanocrystals. Figure 4.1 shows the calculated excitonic energy (corresponding to the lowest-energy-allowed exciton) as a function of the nc-Si diameter [202, 226], comparing the results with the experimental data of Wolkin [225]. Although, there are some discrepancies in the value of the excitonic energy among different studies, the trend is almost the same that the excitonic energy increases with the decreasing size of nc-Si and thus the PL emission peak energy increases.

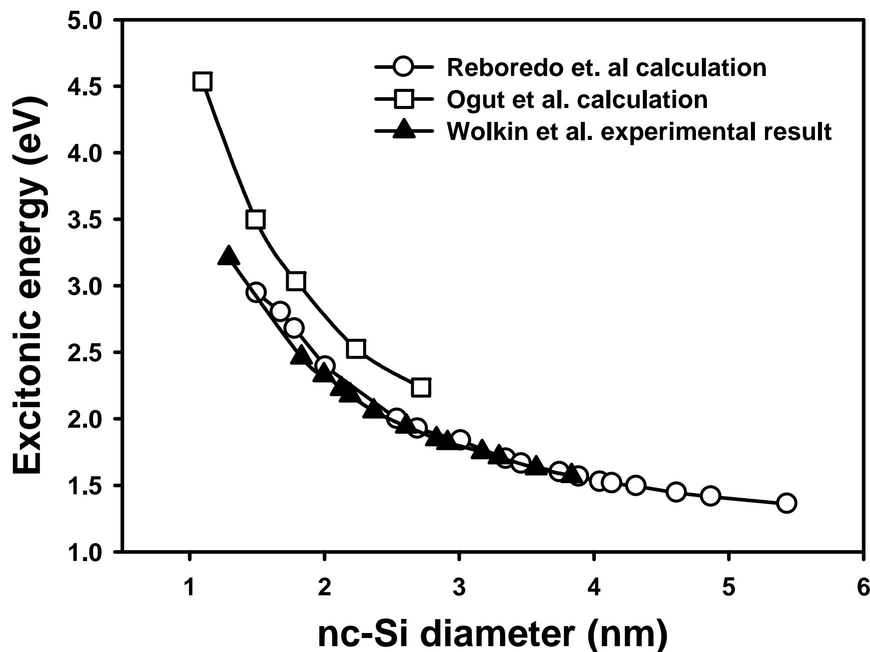

Figure 4.1 Excitonic energy as a function of nc-Si diameter. Open circles correspond to the pseudopotential calculation result of Reboredo [226]; open squares correspond to the quasiparticle calculations results of Ogut [202]; and full triangles correspond to the experimental results of Wolkin [225].

However, many other researchers found that the short-wavelength luminescence was related to the presence of the oxygen vacancies in the Si^+-implanted dielectric matrix [22, 150, 161, 162, 227]. Thanks to the large amount of previous studies, it is certain that there are multiple mechanisms responsible for the visible luminescence. However, to the best of our knowledge, few investigations have been carried out to examine the evolution of photoluminescence mechanisms with thermal annealing. On the other hand, to assert that the light emission is due to the defects or quantum confinement effect, the information of band structure including the optical band gap of nc-Si is necessary. Many theoretical calculations on the band gap and optical properties of silicon nanocrystals have been reported [18-21, 159, 202, 203, 205, 208-210, 228, 229], but there are very few experimental studies concerning the size effect on the band gap and the relationship between the bandgap and PL

properties. The main goal of this chapter is to investigate the PL properties of Si nanocrystals embedded in dielectric films and correlate light emission from the material with the nc-Si sizes and theirs band gaps. The evolution of PL of Si^+-implanted SiO_2 thin films under different annealing conditions is to be investigated. Based on the information of the nc-Si band structure obtained from spectroscopy ellipsometric (SE) analysis, the evolution of PL mechanisms with the annealing will be examined. PL from Si^+-implanted Si_3N_4 films will be also studied. Si nanocrystals embedded in SiO_2 are also fabricated by PECVD, and the PL properties will be investigated.

4.2 PL from Si^+-implanted SiO_2 Films

In this section, we will investigate the PL properties of Si^+-implanted SiO_2 films. In detail, 1) the evolution of PL properties and mechanisms with thermal annealing is investigated; and 2) the effect of excess Si concentration on the nanocrystal size and the PL properties is studied; and 3) The mechanism of each PL band is discussed.

4.2.1 Sample Fabrication and Experiments

550-nm SiO_2 films were grown on *p*-type Si wafers with (100) orientation by thermal oxidation in dry oxygen. A dose of 1×10^{17} cm^{-2} of Si ions were implanted into the SiO_2 films at the energy of 100 keV at room temperature. Afterwards, postimplantation thermal annealing was carried out in nitrogen

ambient at various temperatures ranging from 500 to 1100 ^{o}C (500, 600, 700, 850, 900, 1000, 1100 ^{o}C) for 20 min. No significant change in the nc-Si size under different annealing temperatures was observed from the x-ray diffraction (XRD) measurement. This could be due to the very low diffusion coefficient of Si in SiO_2 films [125], and/or the relatively short annealing duration. Both the XRD and TEM measurements show the formation of nc-Si with a mean size of ~4.5 nm embedded in the SiO_2 matrix. Other samples containing nc-Si with different sizes were fabricated using different implantation recipes. The implantation details of the six samples are given in the following: (a) 3×10^{16} ions/cm^2 at 120 keV, (b) 1×10^{17} ions/cm^2 at 100 keV, (c) multiple implantations with 5×10^{15} ions/cm^2 at 20 keV, 1×10^{16} ions/cm^2 at 40 keV, and 2×10^{16} ions/cm^2 at 80 keV, (d) 4×10^{16} at 10 keV, and (e) multiple implantations with 3×10^{15} ions/cm^2 at 1 keV, 8×10^{15} ions/cm^2 at 5 keV, and 4×10^{16} ions/cm^2 at 16 keV. The PL spectra of the samples were measured using the 325-nm line of a He-Cd laser as the excitation source.

4.2.2 Annealing Effect on PL Properties

In this study, we mainly investigate the sample implanted at 100 keV with 1×10^{17} cm^{-2}. In the study of different annealing temperatures, the samples were annealed for 20 min, and the annealing temperature varied from 500 to 1100 ^{o}C as given above. For the study on the effect of different annealing times on the PL spectra, the annealing temperature were fixed at 1100 ^{o}C, and the annealing time varied from 20 to 150 min.

1. Evolution of PL spectra versus annealing temperature

The band gaps of nc-Si synthesized at various annealing temperatures were obtained from the SE analysis. It can be observed in Fig. 4.2 that the nc-Si band gap, which is related to the optical transition, is not significantly affected by the annealing. As discussed early in Section 3.3.6, the Tauc plots indicate that nc-Si with the size of ~4.5 nm has an indirect band gap structure. Furthermore, we found that the Tauc plots are very similar for the sample with different annealings. Therefore, one can conclude that the annealing does not change the band structure and band gap of nc-Si.

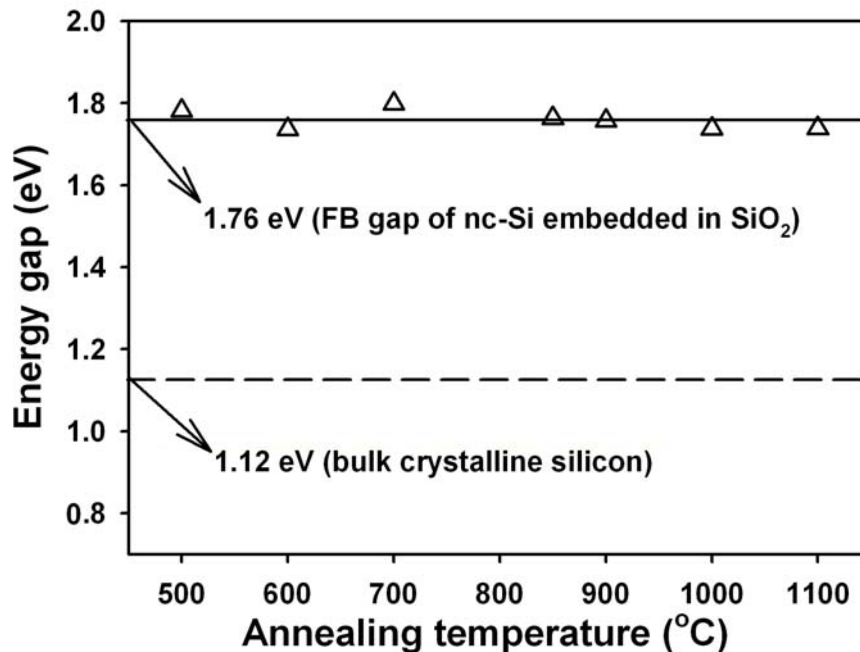

Figure 4.2 Energy gap of the nc-Si embedded in SiO_2 versus annealing temperature. The energy gap was extracted from the FB model in the SE analysis.

Visible light emission from our samples was observed with the excitation wavelength of 325 nm at room temperature. All the samples show a very broad PL spectrum, suggesting that it may be composed of several different PL bands. Figure 4.3 shows the PL spectra for the samples annealed at various

temperatures ranging from 500 to 1100 ^{o}C. The PL spectrum changes significantly when the annealing temperature increases from 500 to 1100 ^{o}C. It is found that the PL spectra of the samples annealed at 500, 600, and 700 ^{o}C have a similar shape while the PL spectra of the annealing at above 700 ^{o}C show some different traits. Particularly, the PL peak intensity of the sample annealed at 1100 ^{o}C is almost 30 times stronger than that of the samples annealed at the temperatures below 1100 ^{o}C.

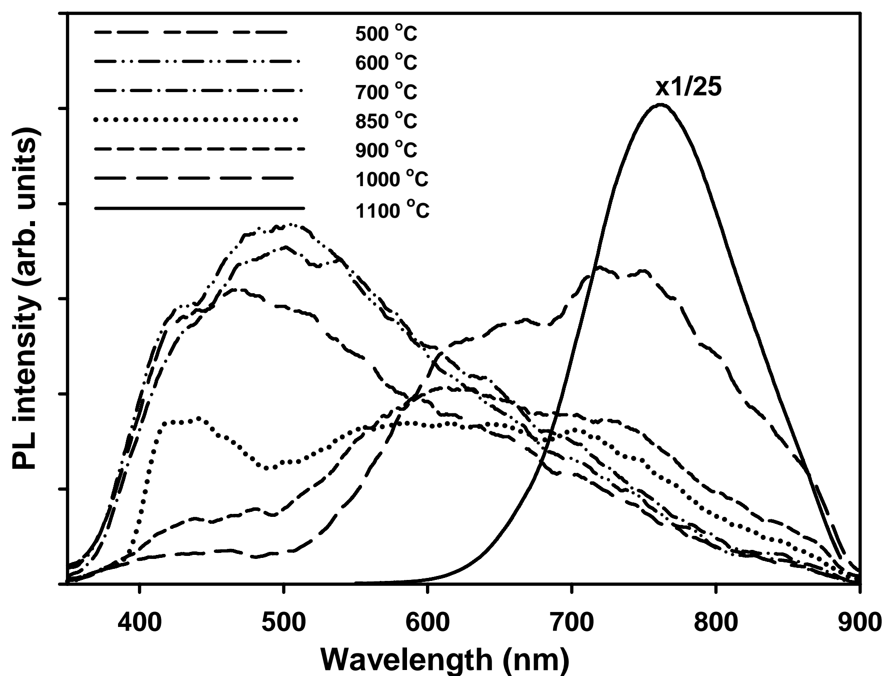

Figure 4.3 PL spectra of Si^{+}-implanted SiO_2 films at different temperatures.

It is found that the PL spectra of all the samples can be well represented by six Gaussian-shaped peaks centered at the wavelengths of ~415, ~460, ~520, ~610, ~760, and ~845 nm, respectively, which have been frequently reported and widely accepted in the literature [227, 230-237]. The full widths at half maximum (FWHM) of the 6 bands are ~50, ~64, ~125, ~149, ~118, and ~50 nm, respectively. The FWHMs of the 6 PL bands do not show a significant change with the annealing temperature. The decomposition of the PL spectra

into the 6 Gaussian-shaped peaks is shown in Fig. 4.4. Figure 4.5 shows the annealing-temperature dependence of the integrated PL intensity for each band. As can be observed in this figure, the ~415-, ~460-, and ~520-nm PL bands have a similar behavior, i.e., the integrated intensity first increases slightly and then decreases dramatically with the increase of the annealing temperature. The integrated intensity for the ~415-, ~460-, and ~520-nm bands reaches a maximum at 700, 600 and 700 ^{o}C, respectively. The above three bands almost disappear when the annealing temperature exceeds 900 ^{o}C. The ~610-nm band always exists for annealing temperatures up to 1000 ^{o}C, and no significant change in the intensity is observed with increasing the annealing temperature. In contrast, the integrated PL intensity of both the ~760- and ~845-nm bands continuously increases with the annealing temperature. Their integrated intensities increase slightly with the annealing temperature up to 1000 ^{o}C and then experience a dramatic increase by approximately 30 times when the annealing temperature reaches 1100 ^{o}C.

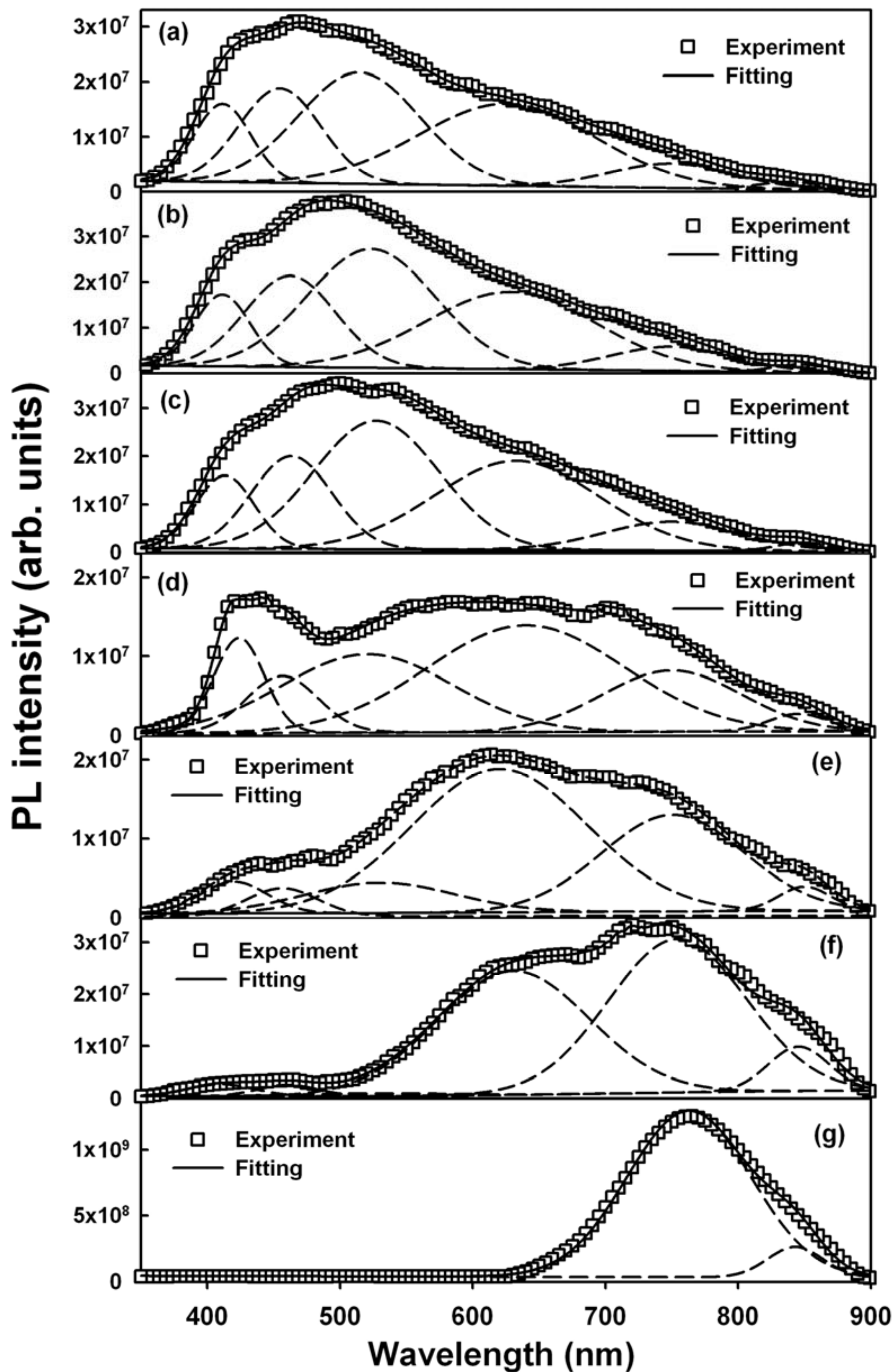

Figure 4.4 Decomposition of PL spectra for the samples of Si^{+}-implanted SiO_2 annealed at (a) 500 °C, (b) 600 °C, (c) 700 °C, (d) 850 °C, (e) 900 °C, (f) 1000 °C, and (g) 1100 °C for 20 min.

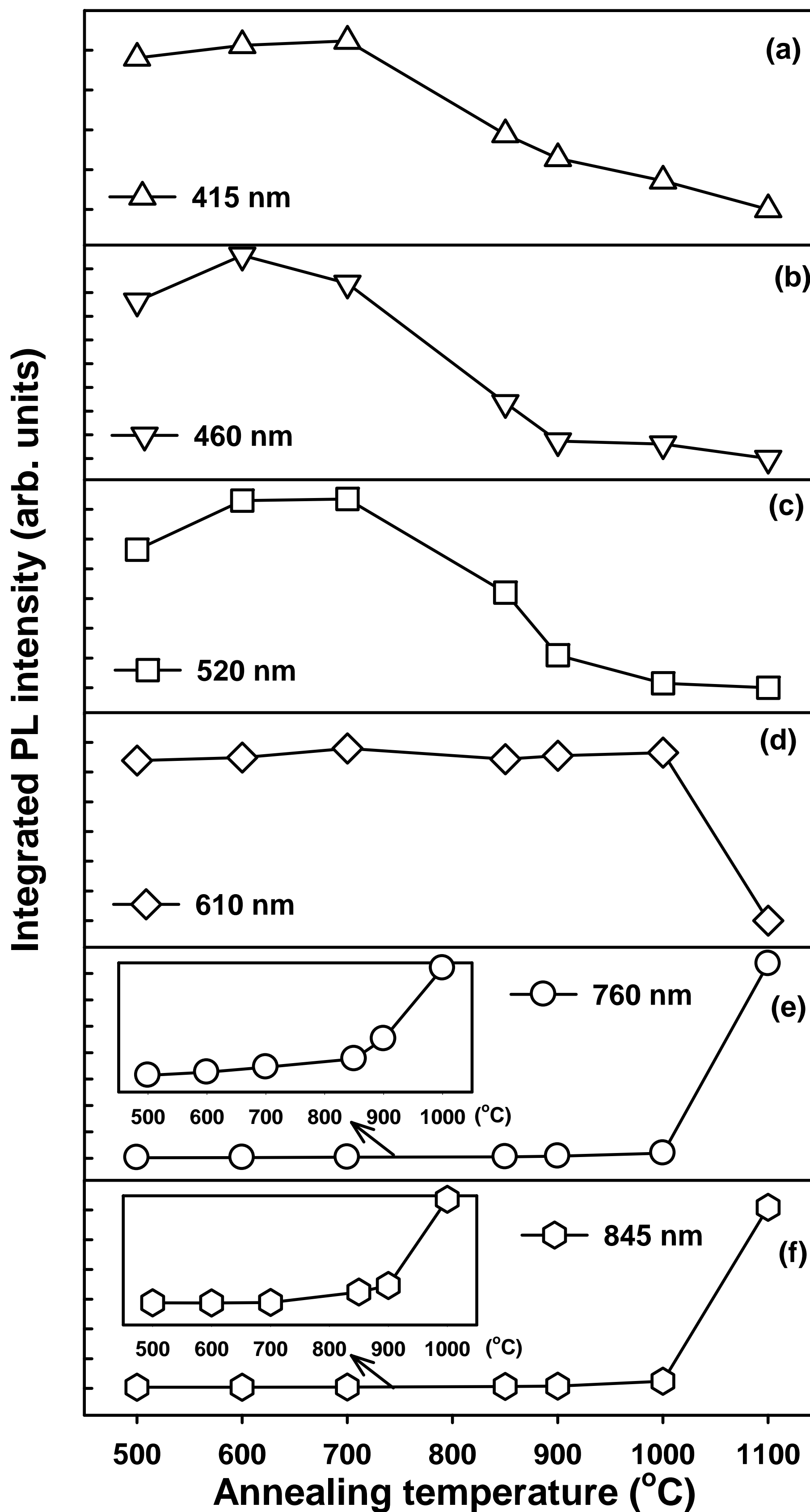

Figure 4.5 Integrated intensity of each PL band as a function of annealing temperature.

As discussed early, the annealing in the temperature range of 500–1100 ^{o}C does not change both the indirect band structure and the band gap of the nc-Si, as shown in Fig. 4.2. This contrasts with the very large changes in the PL discussed above. Therefore, one may conclude that not all the PL bands observed in this study originate from the quantum confinement effect of the nc-Si and some PL bands can be ascribed to the oxide matrix. It is well known that various defects in the oxide matrix can serve as visible luminescent centers. In the following discussions, the PL bands at ~415, ~460, ~520 and ~610 nm are attributed to the defects in the oxide matrix [18, 21, 227, 230-232]. As for the disappearance or steep decrease of these four PL bands when the annealing temperature is approaching 1100 ^{o}C, a possible explanation is that the high annealing temperature leads to the elimination of most of the luminescent defects in the oxide.

The 415-nm (~3 eV) PL band can be attributed to the weak oxygen bond (WOB) defects in silicon oxide [230-232]. The WOB defects are generated in the Si^+-implanted SiO_2 layers after a suitable thermal annealing. Oxygen vacancies are induced by the displacement of oxygen caused by the Si^+ implantation into a SiO_2 network, and the oxygen interstitials, which are considered as the precursors of the WOB defects, are created concurrently. The reaction can be represented by $O_3 \equiv \text{Si-O-Si} \equiv O_3 \rightarrow O_3 \equiv \text{Si-Si} \equiv O_3 + O_{\text{interstitial}}$. The oxygen interstitials will change into the WOB defects immediately after annealing, as described by the reaction $O_{\text{interstitial}} + O_{\text{interstitial}} \rightarrow \text{O-O}$, which is a reversible reaction subject to an excessive thermal annealing energy. The reverse reaction is indicated by the decrease of the 415-nm PL band with the

increase of annealing temperature when the temperature is higher than 700 ^{o}C. The ~460-nm (~2.7 eV) PL band has been observed from pure silica glass [238] and Si-rich silicon oxides [18, 21, 227]. The ~460-nm PL band was shown to be associated with the neutral oxygen vacancy (NOV) defect represented by $O_3 \equiv \text{Si-Si} \equiv O_3$ [227, 230, 233]. The NOV defect could be observed in ion-implanted or radiation-damaged SiO_2 networks. As for the Si^+-implanted SiO_2 film, the NOV defects are actually generated in the same process as for the WOB defects, as described above. Therefore, it is not surprising that the ~415- (WOB) and ~460-nm (NOV) PL bands have a very similar dependence on the annealing temperature. The origin of the ~520-nm band is thought to be associated with the $E_\delta^{'}$ defect [230, 239]. In Si^+-implanted SiO_2, $E_\delta^{'}$ defects can be generated by both extrinsic ion-implantation-induced dissociation process [230, 231] and intrinsic UV photon absorption during the PL measurement [240]. The generation of $E_\delta^{'}$ defects caused by ion-implantation is a transformation of an NOV defect to a $E_\delta^{'}$ center, as described by $O_3 \equiv \text{Si-Si} \equiv O_3 \rightarrow O_3 \equiv \text{Si} \bullet^{+} \text{Si} \equiv O_3 + e^{-}$ [230, 239]. As can be seen in Fig. 4.5, the WOB-related 415-nm band, the NOV-related ~460-nm band, and the $E_\delta^{'}$-related 520-nm band are observed in the same temperature range, and they have a similar dependence on annealing temperature. This indicates that the extrinsic ion-implantation-induced dissociation process plays an important role in the generation of $E_\delta^{'}$ defects. Another radiative defect, the non-bridging oxygen hole center (NBOHC) which has been observed in both pure silica glass and ion-irradiated SiO_2 [231, 234-237], could be responsible for the ~610-nm (~2.0 eV) PL band observed in this study. As shown in Fig. 4.5(d), the intensity

of the ~610-nm band changes little when the annealing temperature is increased until 1000 ^{o}C, indicating that the NBOHC defects are stable during the thermal annealing when the annealing temperature is below 1100 ^{o}C. However, the steep decrease in the intensity of the ~610-nmPL band for the annealing at 1100 ^{o}C suggests that the NBOHC defects have been largely reduced at this annealing temperature.

In contrast to the above PL bands, the ~760- and ~845-nm PL bands both show a drastic increase in the peak intensity when the annealing temperature is 1100 ^{o}C, suggesting that these two bands have luminescence mechanisms different from the defects in the oxide matrix discussed above. As the peak energy (~1.63 eV) of the ~760-nm band is close to the FB gap (~1.76 eV) of the nc-Si, one may easily link this PL band to the quantum confinement (QC) effect. Indeed, the QC effect has been frequently used to explain the PL from nc-Si, although there are many debates. However, the difference of ~0.13 eV (i.e., the Stokes shift) between the energy of the ~760-nm PL peak and the band gap has prompted us to rethink the QC mechanism for the ~760-nm band. As discussed above, the nc-Si embedded in the SiO_2 matrix has an indirect band structure. The probability of direct transitions is extremely low because of the indirect band structure. On the other hand, the role of the nc-Si/SiO_2 interface should not be overlooked in such a system in which the nanocrystals are embedded in the oxide matrix. It is interesting to note that the Stokes shift is about the same as the energy (~0.13 eV) of the Si-O vibration with a stretching frequency of ~1083 cm^{-1} in the system of nc-Si embedded in SiO_2 [62]. This could imply the important role of the phonons associated with the nc-Si/SiO_2 interface in the light emission of the ~760-nm band. The important role of the nc-Si/SiO_2

interface was highlighted in a previous study which showed that the coupling of the confined excitons and the Si-O stretch vibrations dominates the PL process in nc-Si embedded in SiO_2 [241]. Considering both the energy and momentum conservations and the indirect band structure of the nc-Si, we therefore are inclined to believe that the Si-O vibration at the nc-Si/SiO_2 interface provides the means required for both the energy dissipation due to the energy conservation requirement and the momentum conservation in the PL process. In other words, the ~760-nm band can be attributed to the band-to-band transition of the nc-Si assisted by the emission of a phonon which is actually the Si-O vibration at the nc-Si/SiO_2 interface. Figure 4.6 shows the maximum intensity of each PL band. It can be seen that the intensity of the ~760-nm band is more than 30 times stronger than that of the ~415, ~460, ~530, ~610 nm PL bands. For Si^+-implanted SiO_2, the 1100 ^oC annealing could lead to both ultra-fine nc-Si and the desirable nc-Si/SiO_2 interface such that the probability of the indirect exciton recombination assisted by the Si-O vibration is large leading to a strong light emission at ~760 nm.

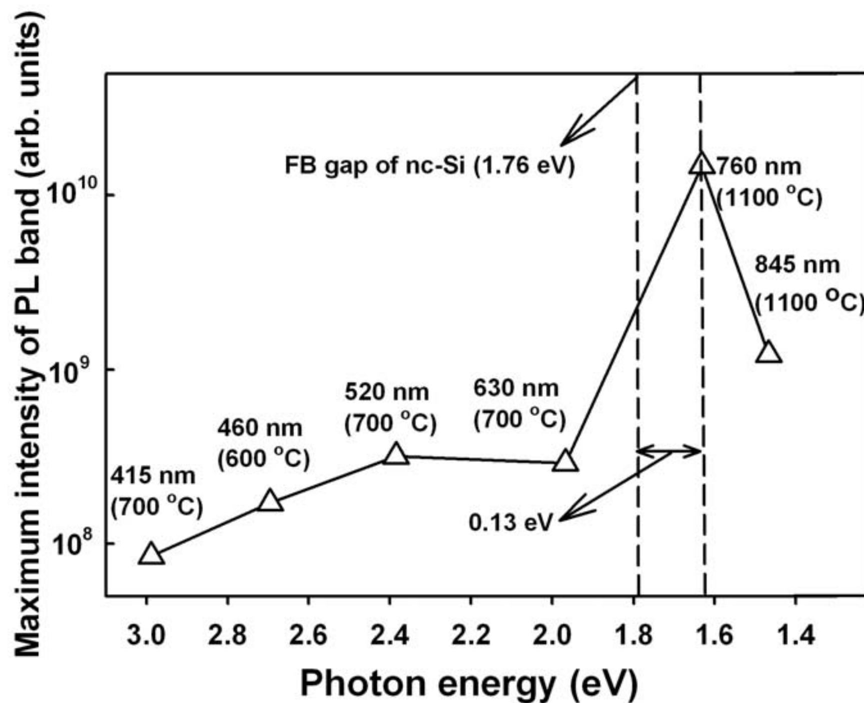

Figure 4.6 Maximum integrated intensity for each PL band.

As for the 845-nm band, it probably originates from the localized luminescent centers at the nc-Si/SiO_2 interface. In the study of Allan *et.al*, the 845-nm (~1.5-eV) PL was attributed to the luminescent surface state of nc-Si [242]. This argument was later supported by Zhuravlev *et.al* who also observed the 1.5-eV PL band from Si^+-implanted SiO_2 after high temperature treatment [243].

2. Evolution of PL spectra versus annealing time

To study the effect of annealing time on the PL spectra, we choose the annealing temperature when the PL intensity reaches its maximum in the range of our study, i.e., 1100 °C. For example, PL spectra for the samples annealed at 1100 °C for 20, 40, and 120 min are presented in Fig. 4.7. As clearly seen in the figure, the PL peak position does not change with the annealing time, but only the intensity increases with the annealing time. Figure 4.8 shows the integrated PL intensity as a function of annealing time. As can be seen in this figure, the PL intensity follows two distinct regimes with the increasing annealing time. It

first increases rapidly with the increasing annealing time when the annealing time is shorter than 60 min, and then increases more slowly till its saturation after a certain annealing time. This behavior is consistent with the findings that have been reported elsewhere [220, 244].

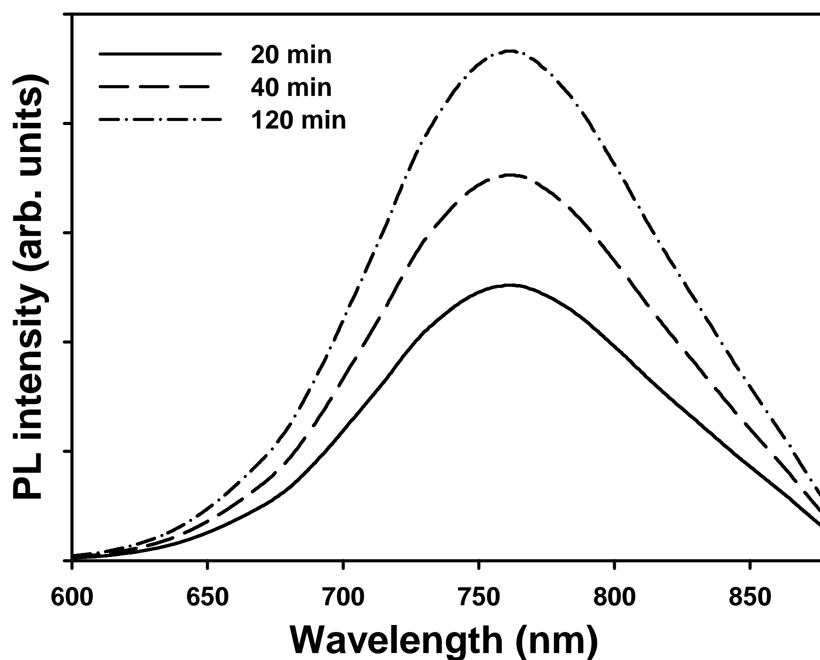

Figure 4.7 PL spectra for the samples annealed at 1100 ^{o}C for (a) 20 min, (b) 40 min, and (c) 120 min.

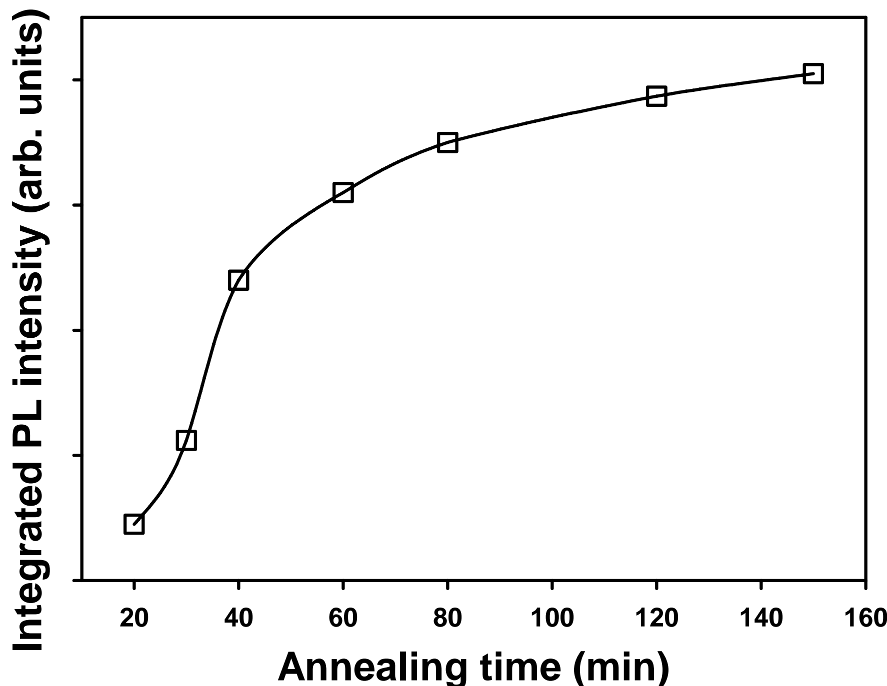

Figure 4.8 Integrated PL intensity as a function of annealing time. The annealing temperature is 1100 ^{o}C.

4.2.3 Effect of Excess Si Concentration on PL Properties

To further confirm the origin of the main PL peak for the sample annealed at 1100 ^{o}C which is attributed to the band-to-band transition of the nc-Si assisted by the Si-O vibration at the nc-Si/SiO_2 interface, we have fabricated four samples with different nc-Si size using Si ion implantation and subsequent annealing. The implantation details of the five samples are given in the following: (a) 3×10^{16} cm^{-2} at 120 keV, (b) 1×10^{17} cm^{-2} at 100 keV, (c) multiple implantations with 5×10^{15} cm^{-2} at 20 keV, 1×10^{16} cm^{-2} at 40 keV, and 2×10^{16} cm^{-2} at 80 keV, (d) 4×10^{16} cm^{-2} at 10 keV, and (e) multiple implantations with 3×10^{15} cm^{-2} at 1 keV, 8×10^{15} cm^{-2} at 5 keV, and 4×10^{16} cm^{-2} at 16 keV. After implantation, the samples were annealed at 1100 ^{o}C for 20 min in the atmosphere of N_2 to induce nanocrystallization. XRD measurements show the

average nc-Si sizes for the four samples are ~4 nm, ~4.5 nm, ~4.9 nm, 6.0 nm, and 7.2 nm, respectively. This result can be explained by the concentration of excess Si in SiO_2. The average volume fractions of excess Si over the regions containing the nc-Si were calculated to be 3%, 8%, 11%, 15%, and 30%, respectively. Excess Si with a higher concentration in SiO_2 forms a larger nanocrystal size after a high annealing temperature. The band gaps of the six samples obtained from the SE study are 1.85 eV, 1.76 eV, 1.70 eV, 1.56 eV, and 1.47 eV, respectively. The room temperature PL spectra were taken using the same excitation source as mentioned previously. The PL of the four samples is similar in their spectrum shapes, but the position of the main PL peak is different for different samples, as shown in Fig. 4.9. The main peaks of the four samples are located at ~720 nm (1.72 eV), ~760 nm (1.63 eV), ~785 nm (1.58 eV), ~870 nm (1.43), and ~925 nm (1.34 eV), respectively. This means that the PL peak shifts to a lower energy when the concentration of excess Si increases, which is consistent with the result reported in Ref. [245]. For all the five samples, the difference between the energy gap and the energy of the corresponding main PL peak is always 0.13±0.01 eV, as shown in Fig. 4.10. This energy difference is actually equal to the Si-O vibration energy. Although both the band gap and the PL peak energy changes with the nc-Si size, the energy difference remains unchanged. This strongly supports the suggestion that the main PL peaks of the samples annealed at 1100 ^{o}C are due to the band-to-band transition of the nc-Si assisted by the Si-O vibration at the nc-Si/SiO_2 interface.

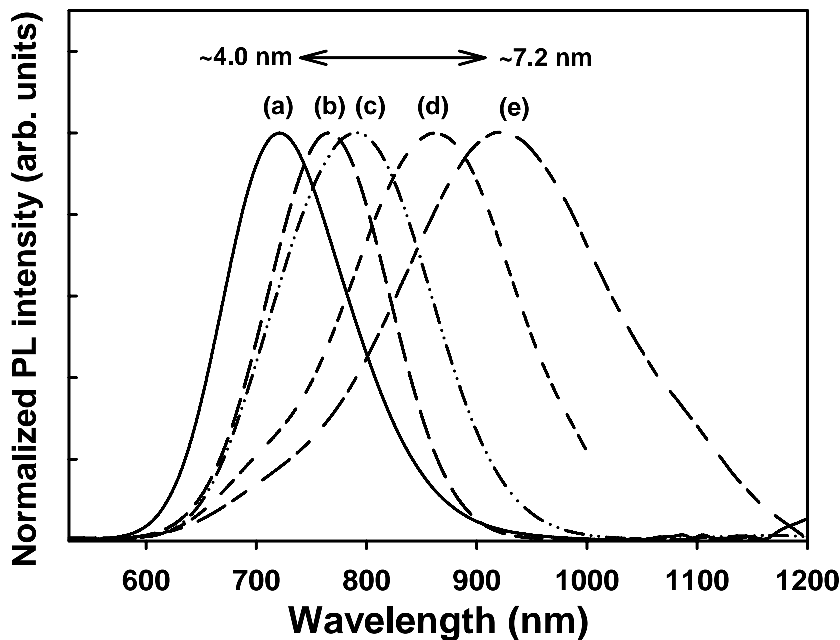

Figure 4.9 Normalized PL spectra for the following samples annealed at 1100 ^{o}C for 20 min: (a) 3×10^{16} ions/cm^2 at 120 keV, (b) 1×10^{17} ions/cm^2 at 100 keV, (c) multiple implantations with 5×10^{15} ions/cm^2 at 20 keV, 1×10^{16} ions/cm^2 at 40 keV, and 2×10^{16} ions/cm^2 at 80 keV, (d) 4×10^{16} at 10 keV, and (e) multiple implantations with 3×10^{15} ions/cm^2 at 1 keV, 8×10^{15} ions/cm^2 at 5 keV, and 4×10^{16} ions/cm^2 at 16 keV.

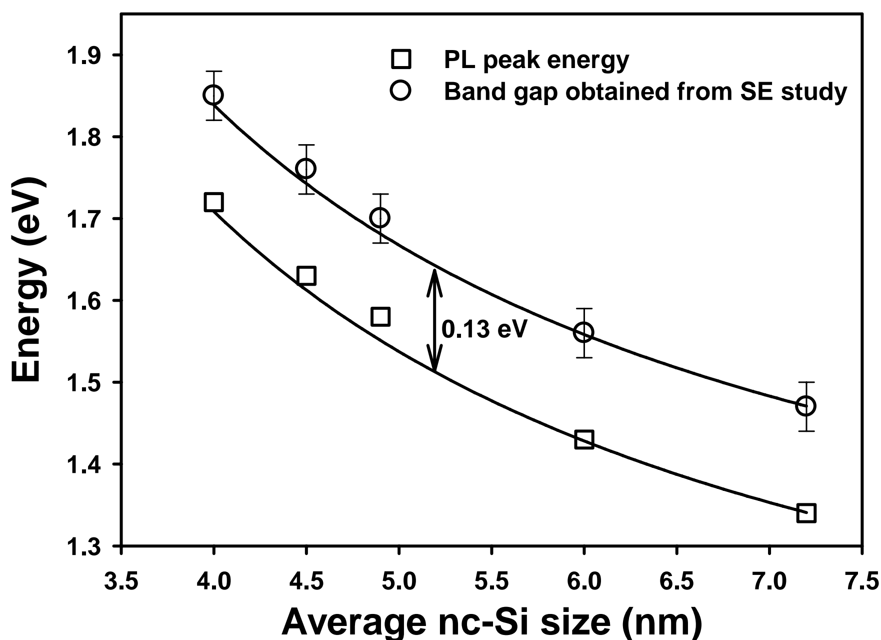

Figure 4.10 Band gap and PL peak energy as functions of nc-Si diameter.

Figure 4.11 shows typical optical-absorption spectra for sample a and d. Absorption spectra must be obtained from the samples fabricated on substrates that are transparent in the wavelength range of interest. Therefore, two samples with different nc-Si sizes fabricated on the fused silica glass are used in the absorbance measurement. A gradual increase of absorbance is observed near the absorption edge towards higher photon energy. However, no obvious blueshift with the decreasing nc-Si size can be found in the absorption spectra as compared with PL spectra. This would be because that the Si nanocrystals are distributed only in a very thin area (<100 nm) close to the surface in the thick fused silica glass (~0.65 mm). Thus, the nc-Si only plays a minor role in the absorption spectra, leading an unobservable size effect of nanocrystals. However, one can see that the absorption of sample d is more significant than that of sample a. This should because that the excess Si concentration of sample d is higher than that of sample a, leading to a larger nanocrystal size and an absorption cross section.

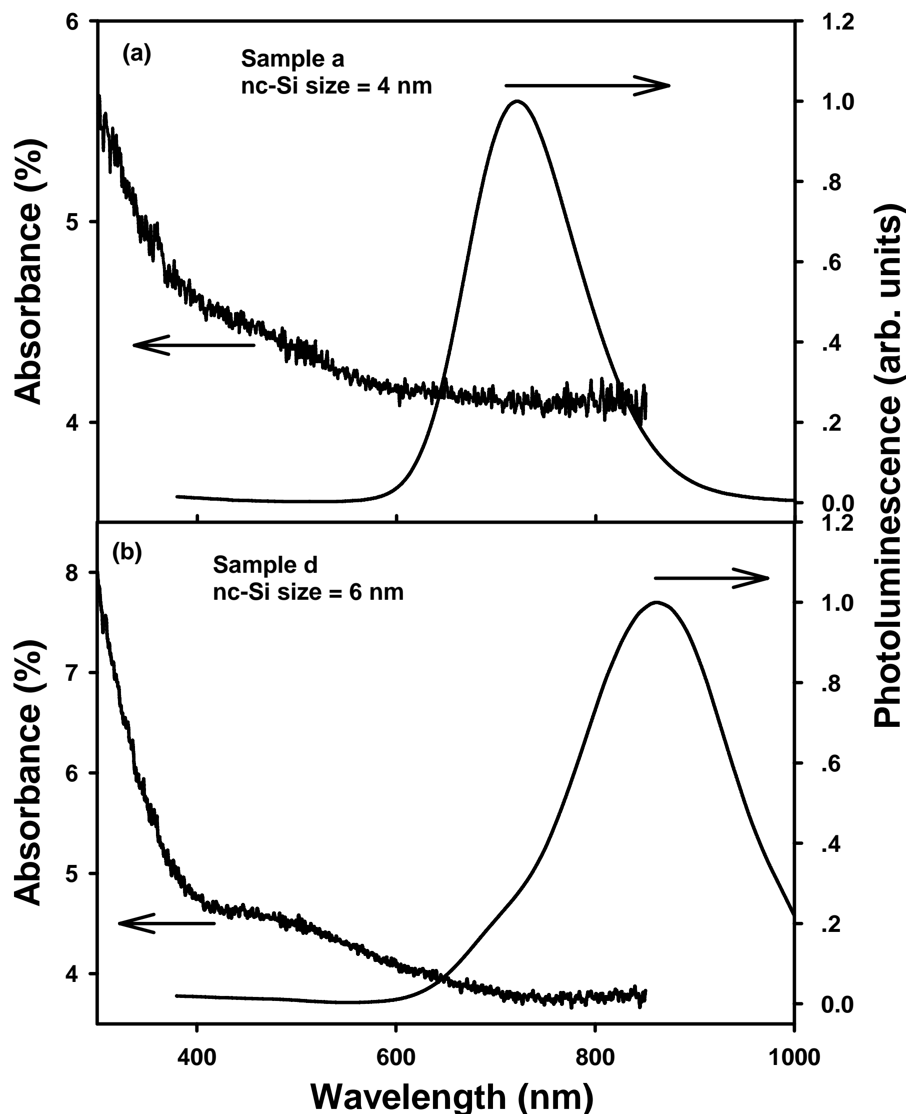

Figure 4.11 Optical-absorption and photoluminescence spectra of Si nanocrystals embedded in SiO_2 for sample a and d. The PL spectra were measured using the sample fabricated on p-type Si substrate, and the absorption spectra were measured using the sample fabricated on fused silica glass.

The different sizes are obtained mainly because of the different concentrations due to the designed implantation recipes. The evolution of the integrated PL intensity versus annealing time for the samples with different excess Si concentration is shown in Fig. 4.12. As can be seen in this figure, the annealing behavior of PL intensity are very similar for all the samples, except for the stronger PL intensities detected from samples with higher excess Si concentrations.

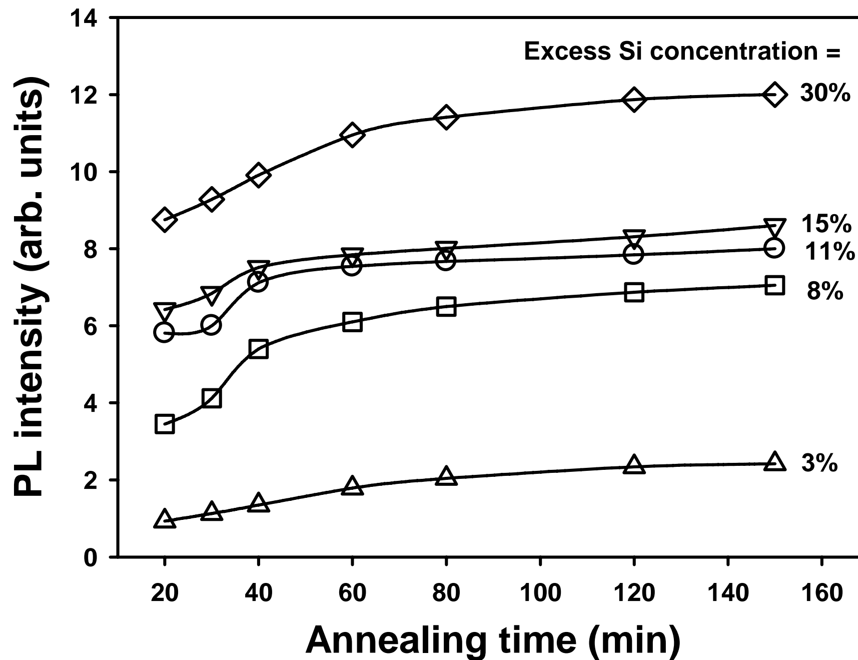

Figure 4.12 Integrated PL intensity as a function of annealing time for the different excess Si volume fractions from 3% to 30%. All the samples are annealed at 1100 ^{o}C in N_2.

It is also interesting to investigate the relationship between the energy position PL peak and the excess Si volume fraction. As shown in Fig. 4.13, the PL peak energy decreases with the increase of excess Si volume fraction. Although the origin of the PL bands for the samples annealed at 1100 ^{o}C is not confirmed whether they are due the quantum confinement of Si nanocrystals, they are indeed related to the size of nc-Si. In addition, the excess Si with a higher concentration would tend to aggregate more easily and form nc-Si with a larger size during the high temperature annealing. Therefore, it is not surprising that the PL peak energy decreases with the increasing excess Si concentration. Figure 4.13 also shows that the samples with higher excess Si concentrations exhibit stronger PL intensities.

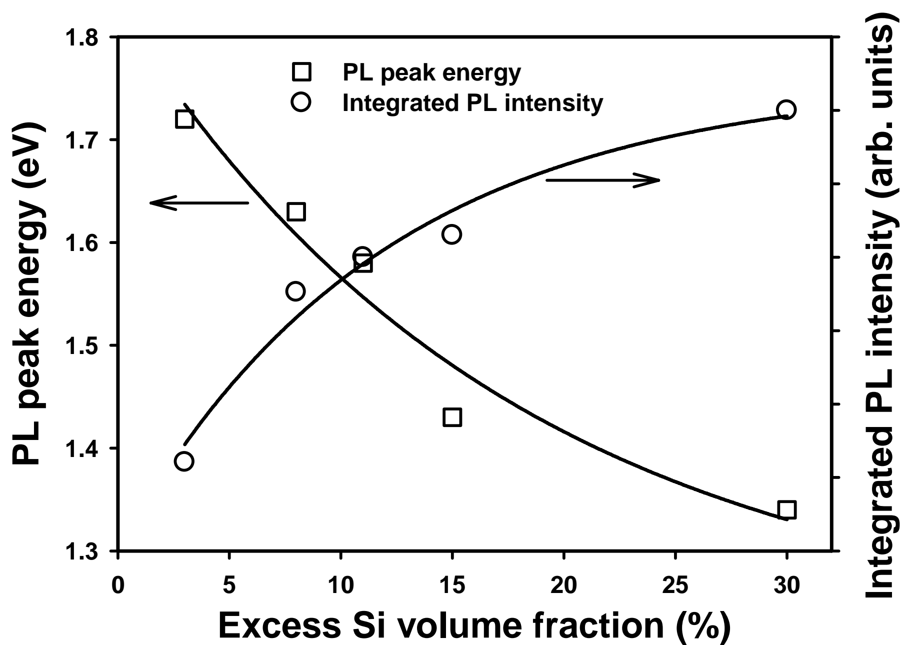

Figure 4.13 PL peak energy and integrated PL intensity as functions of excess Si volume fraction.

Another interesting experimental evidence supporting the existence of strong correlation between nanocrystal size and the PL band for the samples annealed at 1100 ^{o}C is the investigation on the evolution of the full width at half maximum (FWHM) with increasing excess Si concentration, as shown in Fig. 4.14. The increase in the FWHM of the corresponding PL spectrum with the increasing excess Si concentration can be explained with the resulting wider size distribution for the samples with higher excess Si concentrations.

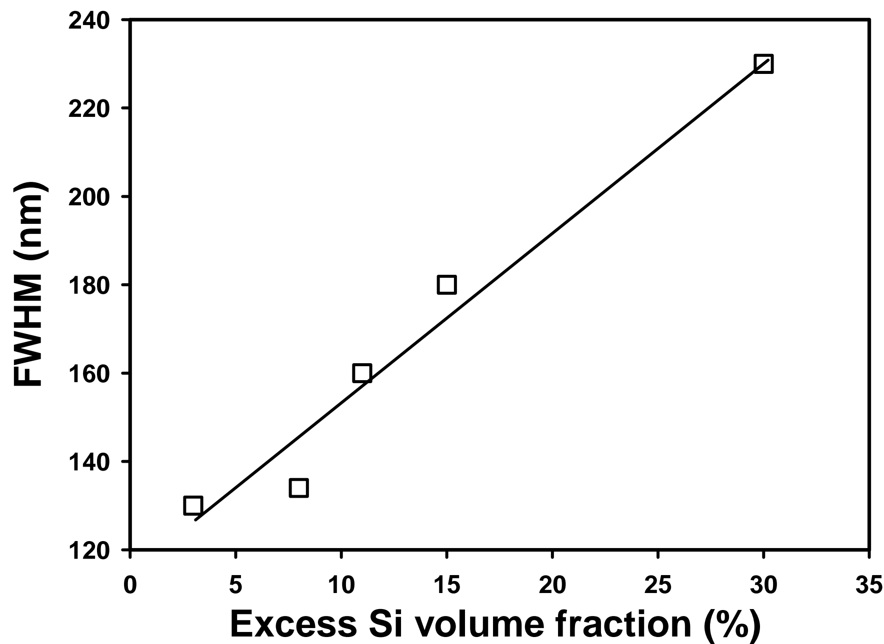

Figure 4.14 Full width at half maximum (FWHM) of the PL peaks as a function of the excess Si concentration for the sample annealed at 1100 ^{o}C.

4.2.4 Conclusion

The band structure of nc-Si embedded in SiO_2 matrix synthesized at different annealing temperatures has been studied with spectroscopy ellipsometry. It is found that the annealing does not change the indirect band structure and the energy gap (~1.76 eV) of the nc-Si. In contrast, the photoluminescence shows a continuous evolution with the annealing. Six PL bands located at ~415, ~460, ~520, ~610, ~760, and ~845 nm are observed depending on the annealing temperature. The annealing at 1100 ^{o}C yields the strongest PL band (i.e., the main PL peak) at ~760 nm (~1.63 eV) with intensity much higher than that of all other PL bands. The influence of excess Si concentration on the properties of PL spectra has been studied. The average nc-Si size evolves with the excess Si concentration in SiO_2 films. Both the band gap energy and the PL peak energy change with the nc-Si size. However, the difference between the PL peak

energy and the energy gap related to the optical transition is always 0.13 ± 0.01 eV, being equal to the Si-O vibration energy. This strongly suggests that the main PL peak is due to the indirect band-to-band transition of the nc-Si assisted by the Si-O vibration at the nc-Si/SiO_2 interface. On the other hand, the ~415-, ~460-, ~520-, and ~610-nm bands are ascribed to the WOB, NOV, E'_{δ} and NBOHC defects, respectively, while the ~845-nm band is proposed to be related to the interfacial luminescent centers.

4.3 PL from Si^+-implanted Si_3N_4 Films

Recently, some research activities have been carried out on the Si-rich Si nitride (SRN) materials, which offer the advantage of lower barrier height for carrier injection and the potential of emitting photons at shorter wavelength compared with that of SiO_2 [246-248]. SRN could be a promising candidate for Si-based full-color light emitting devices. Strong PL emission from red to blue has been demonstrated in SRN materials [247, 248]. In this section, the room temperature PL from Si^+-implanted Si_3N_4 is investigated.

4.3.1 Sample Fabrication and Experiments

Silicon nitride films with the thickness of 120 nm were deposited by low-pressure chemical vapor deposition (LPCVD) on 30-nm-thick SiO_2 thin film thermally grown on Si (100) wafers. A dose of 3.5×10^{16} cm^{-2} Si ions were implanted into the silicon nitride film at the energy of 30 KeV. The maximum

volume fraction of the implanted Si is ~21%, as determined by SRIM calculation. Afterwards, the implanted films were thermally annealed in N_2 ambient for 1 hour at temperatures ranging from 800 to 1100 ^oC. PL spectra were taken with a commercial ACCENT RPM2000 PL system using an excitation laser of 325 nm line with the power of 1 mW. All spectral measurements were performed at room temperature.

4.3.2 Results and Discussions

Broad PL spectra can be detected from the samples with the excitation wavelength of 325 nm at room temperature. Figure 4.15 shows the PL spectra obtained from the Si^+-implanted Si_3N_4 films annealed at different temperatures. The PL spectrum changes significantly with the increasing annealing temperature, indicating that thermal annealing has a significant influence on the PL properties of Si^+-implanted Si_3N_4 film.

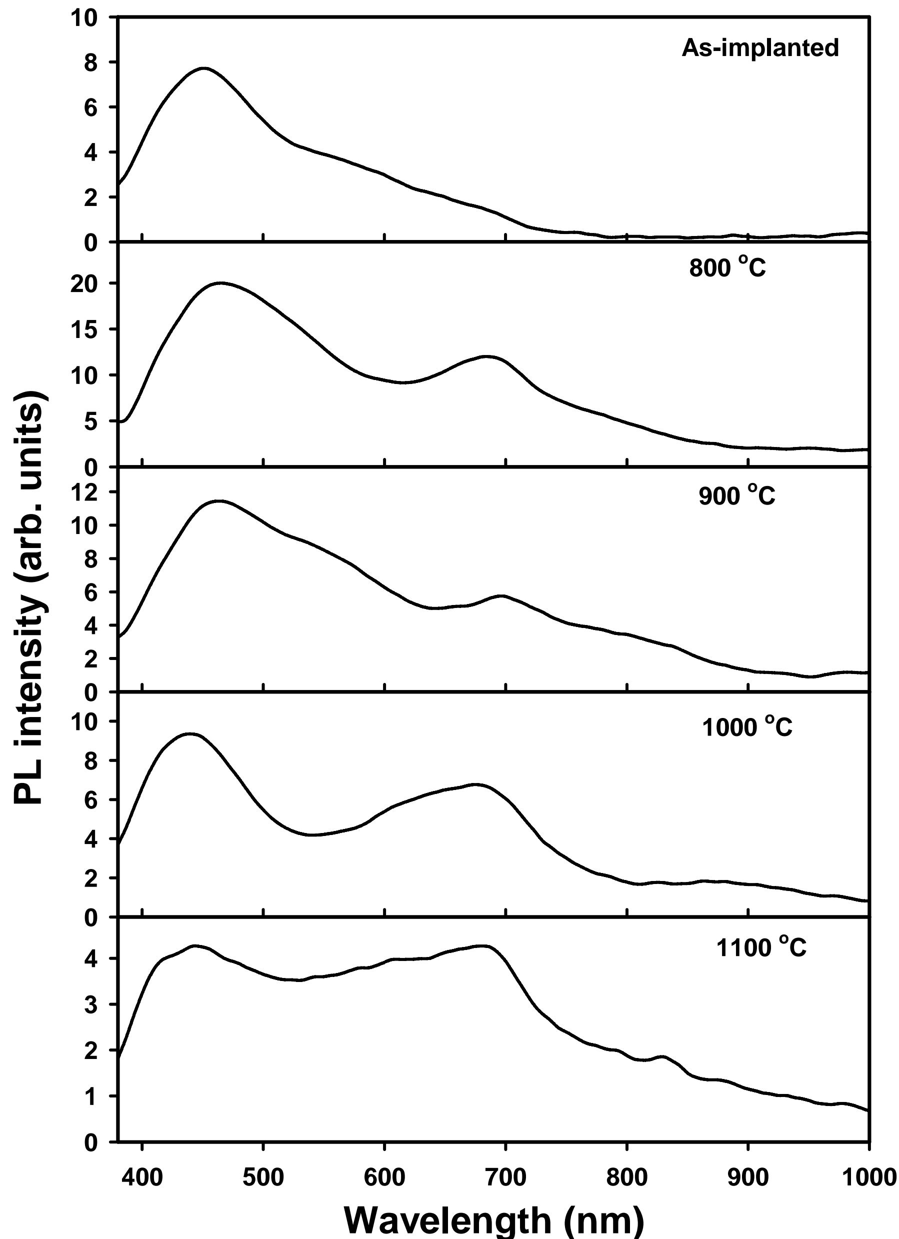

Figure 4.15 PL spectra of Si^{+}-implanted Si_3N_4 films annealed at different temperatures.

In general, the PL spectrum annealed at each temperature mainly consist of a blue-violet PL band peaked at ~435 nm (~2.8 eV) and a red PL band peaked at ~680 nm (~1.8 eV). The blue-violet PL band observed in this study has been demonstrated to be related to the nitrogen dangling bonds [249]. To be specific, it is attributed to the radiative transition between the defect states of the N_4^{+}

level and the bonding Si-Si σ level or between the N_2^0 level and the anti-bonding Si-Si $\sigma*$ level [249]. Unlike the blue-violet PL band, the red PL band is enhanced more significantly by thermal annealing. Although this red light emission has been observed from SRN materials by several studies [246, 247, 249-251], its origin is still controversial. The recombination on the defect states is usually employed to explain this red PL band [247, 249], but some researchers also argued that it is resulted from the quantum confinement of the Si nanocrystals in the host matrix [246, 250, 251].

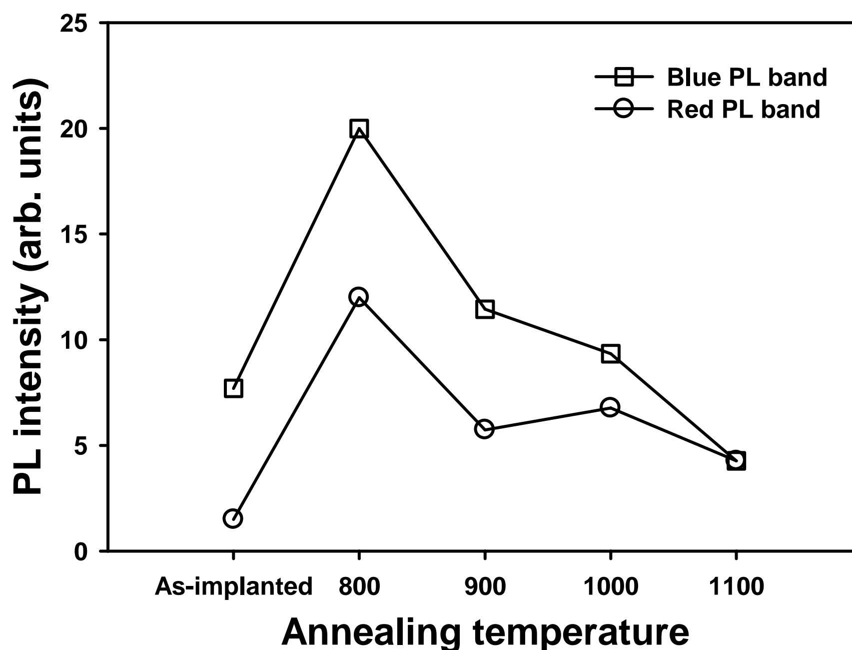

Figure 4.16 Intensity of the blue-violet and red PL band.

Actually, this blue PL band can also be observed from the as-deposited pure Si_3N_4 film, which is not shown in the figure. Although this blue-violet emission is believed to originate from the silicon nitride host matrix, its intensity is also influenced by thermal annealing. As shown in Fig. 4.15, the red PL band can barely be observed in the as-implanted sample, but it is significantly enhanced by the thermal annealing. The defects and the stress introduced by the

implantation can act as non-radiative centers that lead to the absence of the red PL band in the as-implanted sample. The elimination of these non-radiative centers by the annealing at 800 ^{o}C enhances the light emission for both the red and blue-violet PL bands. However, when the annealing temperature is increased, the light emissions from the two bands are quenched gradually in general, as can be seen Fig. 4.16. This quenching behavior in PL is in consistence with the result reported in Ref. [246], where the intensity of the PL from SRN reaches its maximum at the annealing temperature of 700 ^{o}C and then decreases with the increasing annealing temperature. This evolution of the PL intensity with annealing temperature can be interpreted in terms of the non-radiative defects caused by the hydrogen desorption [252]. As shown in Fig. 4.13, for the samples annealed below 1100 ^{o}C, the blue-violet PL band dominates the PL spectrum while the red PL band just appears as its shoulder. Interestingly, when the annealing temperature is increased from 800 ^{o}C to 1100 ^{o}C, the red PL band quenches slower than the blue-violet PL band. At the annealing temperature of 1100 ^{o}C, the intensity of the red PL band is even as strong as that of the blue-violet PL band, as shown in Fig. 4.16. Indeed, from the annealed sample with a much thinner Si^{+}-implanted Si_4N_3 film, the red PL band is the major light emission, because the blue-violet PL band originates from the silicon nitride host matrix, as discussed above. Under different annealing temperature, there is no significant shift of the red PL band, and this fixed PL peak is a characteristic of the defect-related PL. The increased annealing temperature induces the enlargement of the FWHM of the red PL band, which could be attributed to the existence of the green PL (i.e. 515 – 605 nm) arising from the band tail radiative recombination [250]. There are possible

two excitation mechanisms accounting for the red PL band from the Si-implanted silicon nitride samples annealed at different temperature. For the samples annealed at the annealing temperatures below 1100 ^{o}C, the major transition excited by photons may occur between the valence band and the defect states, and then the photon-induced carriers relax to the recombination centers. Another possible excitation transition for the red PL band is only take place at the annealing temperature of 1100 ^{o}C. This transition could originate from the absorption of the stable Si nanocrystals, which are formed via phase separation at the 1100 ^{o}C annealing. After the excitation, the excited carriers transfer to the recombination centers at the surfaces of the nc-Si to emit red light through radiative recombination.

4.3.3 Conclusion

In summary, two PL band are observed from the Si^{+}-implanted Si_3N_4 films. The blue-violet PL band is attributed to the demonstrated to be related to the nitrogen dangling bonds. The Si implantation into the silicon nitride film leads to an enhancement of the red PL band, which needs activation by the thermal annealing. The red PL band is attributed to the radiative recombination on the Si-related defect states. Two excitation mechanisms make contributions to the formation of the red PL band, one of which could be attributed to the formation of Si nanocrystals under the 1100 ^{o}C annealing.

4.4 PL from PECVD-Grown Si rich Si Oxide

Except for the technique of Si ion implantation, PECVD deposition of Si-rich dielectric films followed by high temperature annealing has been regarded as one of the best candidate for the synthesis of luminescent Si nanocrystals embedded in a dielectric matrix. An extraordinary recipe of the mixed gas source containing nitrous oxide (N_2O), ammonia (NH_3), and nomosilane (SiH_4) diluted by nitrogen of hydrogen gas has been frequently used to synthesize SiO_x, SiN_x, and SiO_xN_y films, from which we can form Si nanocrystals after high temperature annealing. In this section, the PL properties from PECVD grown Si-rich SiO_x are investigated.

4.4.1 Sample Fabrication and Experiments

Under a radio frequency (rf) power of 150 W, the Si-rich SiO_x films were grown o a *p*-type Si(100) substrate in a Nextral D200 PECVD system at a chamber pressure of 150 mTorr, in which H_2 fluence was set at 300 sccm while the SiH_4 and N_2O fluences were varied. The N_2O/SiH_4 flow ratio γ was varied between 53.3 and 3. TABLE 4.1 summarizes the flow ratio between N_2O and SiH_4. The substrate temperature was kept at 280 ^oC during the deposition. The RF was set at 150 W for the deposition. The thickness of SiO_x films were within the range from ~180 to ~220 nm by controlling the deposition time. After deposition, the SiO_x films were annealed in a flowing N_2 ambient with the rate of 6 sccm at 1100 ^oC for 1 h in a horizontal furnace.

TABLE 4.1 Summary of sample conditions for the SiO_x films prepared by PECVD.

Sample No.	N_2O (sccm)	SiH_4 (sccm)	Value of y	Value of x	Concentration of nitrogen	PL peak (nm)
SiO_{x1}	400	7.5	53	1.85	7.72%	900
SiO_{x2}	400	10	40	1.78	7.38%	885
SiO_{x3}	400	12.5	32	1.70	6.80%	870
SiO_{x4}	400	15	27	1.58	6.04%	850
SiO_{x5}	400	20	20	1.48	5.27%	835
SiO_{x6}	400	25	16	1.41	4.48%	——
SiO_{x7}	400	30	13	1.37	3.45%	——
SiO_{x8}	400	35	11	1.34	2.75%	——
SiO_{x9}	400	40	10	1.33	2.00%	——
SiO_{x10}	400	45	9	1.33	1.48%	——
SiO_{x11}	400	50	8	1.32	1.05%	——
SiO_{x12}	350	50	7	1.32	0.77%	——
SiO_{x13}	300	50	6	1.32	0.50%	——
SiO_{x14}	250	50	5	1.31	0.30%	——
SiO_{x15}	200	50	4	1.31	0.27%	——
SiO_{x16}	150	50	3	1.31	0.25%	——

The Si concentration of the SiO_x films, which can be estimated by the value of x, has been obtained from x-ray photoemission spectroscopy (XPS) measurement. The XPS experiment was performed by using a Kratos Axis spectrometer with monochromatic Al $K\alpha$ (1486.71 eV) x-ray radiation. The values of y obtained from XPS measurements for all the samples are listed in TABLE 4.1. Actually, the XPS spectra also exhibit another low intensity signal, due to the presence of nitrogen in the SiO_x films. The introduction of nitrogen into SiO_x films is due to the use of N_2O as the gaseous precursor for film deposition. The atomic concentrations of nitrogen in the SiO_x films are also demonstrated in TABLE 4.1. For a clearer demonstration, the dependences of x

value and atomic concentration of nitrogen on the N_2O/SiH_4 flow ratio γ are shown in Fig. 4.17. It is not surprising to found that the x value decreases with the N_2O/SiH_4 flow ratio. Because nitrogen incorporation into the SiO_x films comes from the use of N_2O, the atomic concentration of nitrogen increases with the N_2O/SiH_4 flow ratio, as shown in Fig. 4.17.

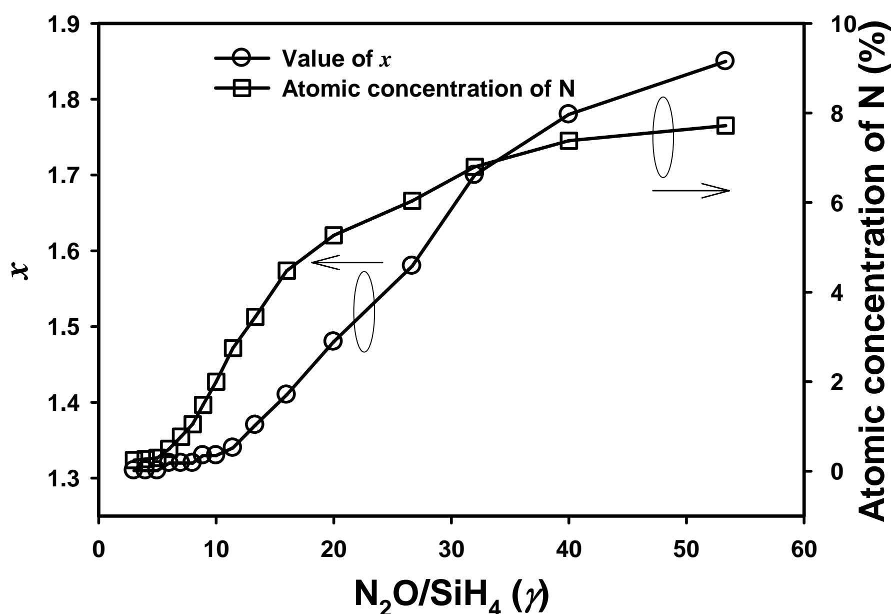

Figure 4.17 The x value and atomic concentration of nitrogen in deposited films as functions of the N_2O/SiH_4 flow ratio γ.

4.4.2 Results and Discussions

PL spectra were taken with a commercial ACCENT RPM2000 PL system using an excitation laser with the wavelength of 325 nm at room temperature. The pump power was 1 mW over a circular area of 2 mm in diameter. Light emission from as-deposited SiOx samples has been found in all cases to consist of very weak signals typically with a very broad and irregular spectrum in the wavelength range from 400 to 950 nm, which will not be discussed in this study. On the other hand, all the samples after the annealing at 1100 ^{o}C exhibit

much stronger room-temperature PL (several orders of magnitude higher than the signals coming from the as-deposited samples). For a clear demonstration, only PL spectra for selected samples after 1100 °C annealing are shown in Fig. 4.18. As can be seen in this figure, not all the annealed PECVD-grown SiOx films exhibit PL at near-infrared region which are commonly believed to be related to the Si nanocrystals embedded in the film. As summarized in TABLE 4.1, the Si nanocrystal related PL can only be observed from the samples with the SiH_4 flow rate equal to or below 20 sccm. In contrast, many oxygen related defects, such as a weak-oxygen-bond (WOB), neutral oxygen vacancy (NOV), and ionized oxygen (O_2^-) centers which have been discussed in Si^+-implanted SiO_2 film in Section 4.2, were also observed in the PECVD-grown SiO_x films, contributing to the significant PL components in the blue-green region [253].

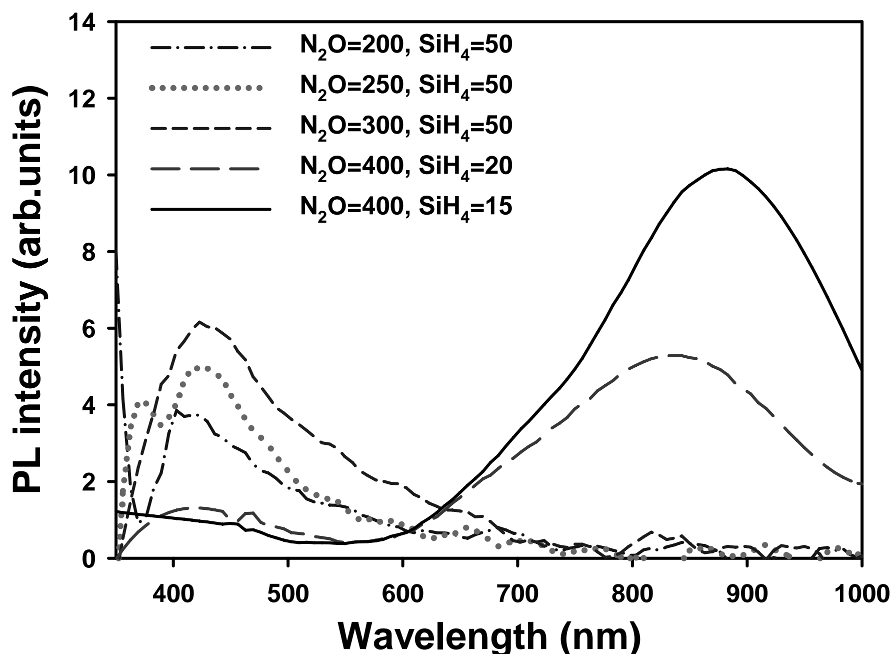

Figure 4.18 Selected PL spectra of PECVD-grown SiO_x films after the annealing at 1100 °C for 1 h.

As shown in Fig. 4.18, the maximum intensity for the near-infrared PL band from the sample with the SiH_4 fluence of 15 sccm is higher than that from the sample with the SiH_4 fluence of 20 sccm. As a matter of fact, it has been confirmed in our study that the near-infrared PL intensity increases with the decreasing flow rate of SiH_4 from 20 to 7.5 sccm if the fluence of N_2O is fixed at 400 sccm. Figure 4.19 shows the normalized PL spectra of PECVD-grown SiO_x films for the samples with the N_2O/SiH_4 flow ratio from 20 to 30, which presents strong near-infrared light emission. As can be seen in this figure, the near-infrared PL peak wavelength increases with the N_2O/SiH_4 flow ratio. This is consistent with the results on the PL of Si^+-implanted SiO_2 films. The redshift of the PL peak with the increasing N_2O/SiH_4 flow ratio should be due to the increase in nanocrystal size with the increasing excess Si concentration. This is in consistence with the PL result of Si^+-implanted SiO_2 films, which has been discussed in Section 4.2. Therefore, it is not surprising that the peak wavelength of Si nanocrystal related PL would decreases with the increasing of x value (i.e., increasing in the excess Si content in SiO_x films). However, the case for the annealed PECVD-grown SiO_x films is different to some extent from that of Si^+-implanted SiO_2 films. The near-infrared PL band only can be observed from the samples fabricated with SiH_4 flow rate equal to or less than 20 sccm. For the samples fabricated with the SiH_4 flow rate larger than 20 sccm, only defect-related PL bands at blue-green region can be observed, as can be seen Fig. 4. 18. This should because that rf power of 150 W used in this study is smaller than the threshold power that is needed to fully decompose SiH_4 with a flow rate larger than 20 sccm into plasma.

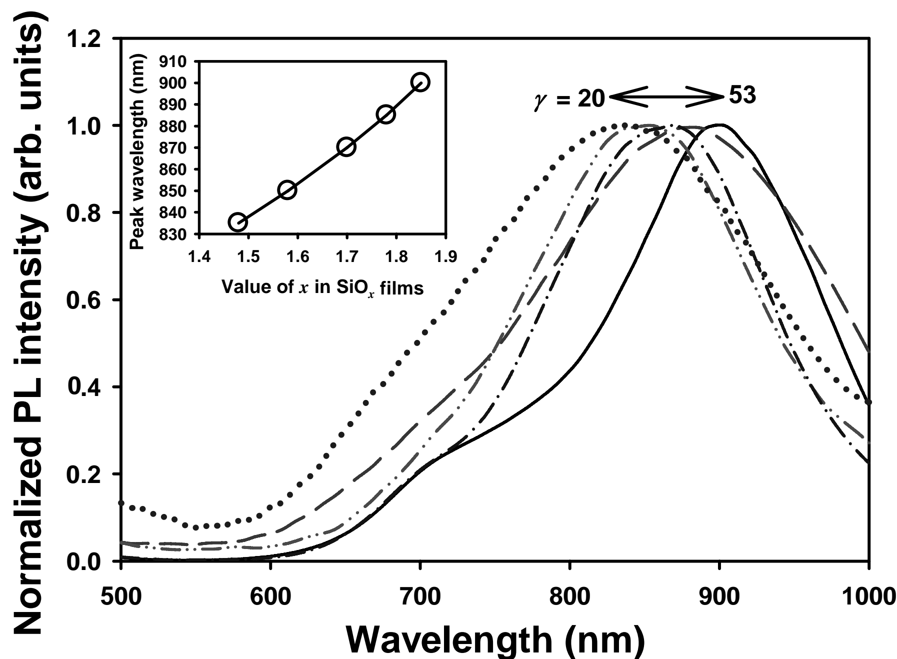

Figure 4.19 Normalized PL spectra of PECVD-grown SiO_x films for the samples with the N_2O/SiH_4 flow ratio from 20 to 30. The inset shows the PL peak wavelength as a function of x value.

4.4.3 Conclusion

In this section, Si nanocrystals embedded in SiO_2 films have been synthesized by PECVD and the subsequent thermal annealing. Strong PL has been observed from the samples. The PL properties from the Si rich SiO_x films fabricated by PECVD have been investigated. The excess Si content in the films has been determined by XPS analysis. Defect-related PL and Si nanocrystal-related PL have been observed dependent on the flow ratio of precursor gases. With the increasing ratio of N_2O/SiH_4, the nanocrystal-related PL peak position has been found to redshift, which should be related to the increasing nanocrystal size resulting from the increasing excess Si content in the Si-rich SiO_x film.

4.5 Summary

In this chapter, PL properties of Si^{+}-implanted dielectric films (i.e., SiO_2 and Si_3N_4) have been investigated. Evolution of PL properties from Si^{+}-implanted SiO_2 films with thermal annealing has been studied. The PL spectrum shows a continuous evolution with the annealing. The annealing at 1100 ^{o}C yields the strongest red PL band, which is related to the formation of Si nanocrystals, with intensity much higher than that of all other PL bands. We attribute the red PL band to the indirect band-to-band transition of the nc-Si assisted by the Si-O vibration at the nc-Si/SiO_2 interface. On the other hand, the 415-, 460-, 520- and 630-nm bands are ascribed to the WOB, NOV, $E_{\sigma}^{'}$ and NBOHC defects, respectively, while the 845-nm band is proposed to be related to the interfacial luminescent centers. The PL peak position of 1100-^{o}C-annealed sample shows a strong dependence on the nanocrystal size. In addition, the PL from Si^{+}-implanted Si_3N_4 films has also been studied. Both blue-violet and red PL band have been observed from Si^{+}-implanted Si_3N_4 films. The influence of thermal annealing on the PL properties from Si^{+}-implanted Si_3N_4 films has also been investigated. In addition, the study on the PL properties of Si rich SiO_x films synthesized by PECVD has carried out also. The effect of flow ratio of precursor gases on the PL properties has been investigated. A similar size effect on the PL peak position of PECVD-grown nc-Si embedded in SiO_2 has been also observed.

CHAPTER 5 ELECTROLUMINESCENCE OF SI NANOCRYSTALS EMBEDDED IN DIELECTRIC FILMS

5.1 Introduction

Not long after the discovery of visible photoluminescence (PL) from porous Si by Canham [12], Koshida *et al.* reported electroluminescence (EL) from porous Si [254]. Si^+-implanted SiO_2 films have been shown to exhibit strong PL emission in the wavelength range from blue-green to near infrared [14, 45, 118, 123, 125, 128, 139]. Recently, visible electroluminescence has also been observed from Si^+-implanted SiO_2 films [138-140, 142, 143, 147-151, 153], and even electrically driven ultraviolet emission from Si^+-implanted SiO_2 films was predicted [148]. In previously reported studies on the light emission properties of Si^+-implanted SiO_2 films, usually medium- or high-energy Si ions were implanted into SiO_2 films with the thickness of hundreds of nanometers. With such a thick SiO_2 film a high voltage (~20 – ~60 V) is required for a measurable EL emission. For practical applications, the thickness of the SiO_2 thin films must be reduced in order to achieve higher carrier injection and lower turn-on voltage for the EL emission. In this study, 30-nm SiO_2 or Si_3N_4 thin films together with low-energy Si ion implantation are used to fabricate the nc-Si light-emitting structure. Different nanocrystal distributions in the SiO_2 films are achieved by varying the implanted Si ion dose and the implantation energy. The influence of nanocrystal distribution on the EL properties of the Si^+-implanted SiO_2 films is investigated. The EL mechanisms are discussed based on the

experimental results. The goal of this work is to fabricate light-emitting devices (LEDs) using a film containing Si nanocrystals as the light emitting layer, which is fully compatible with the mainstream CMOS process.

5.2 EL from Si^+-implanted SiO_2 Films

In this study, visible and infrared (IR) electroluminescence (EL) is observed from the metal-oxide-semiconductor-like (MOS-like) capacitor structure with Si nanocrystals (nc-Si) embedded in the gate oxide fabricated with low-energy ion implantation. The EL spectra are found to consist of four Gaussian-shaped luminescence bands with their peak wavelengths at ~460, ~610, ~740, and ~1260 nm, in which the ~610-nm band is dominant. Samples with different nanocrystal distribution have been fabricated through changing implantation recipes (i.e., the Si ion dose and implantation energy). The influence of nanocrystal distribution on the current transport and EL properties is investigated. It is found that both the current conduction and the EL intensity can be enhanced by increasing the Si ion dose and/or the implantation energy. This study provides much helpful useful information on the fabrication of Si nanocrystal-based light emitting devices (LEDs) with the implantation technique.

5.2.1 Sample Fabrication and Experiments

Various doses of Si ions were implanted into thermally grown 30-nm SiO_2 thin films on *p*-type Si wafers at different implantation energies. For the study of

influence of nc-Si concentration, three samples were fabricated with the Si ion dose of 1×10^{16}, 2×10^{15}, and 3×10^{14} cm^{-2}, respectively, at the implantation energy of 5 keV; and for the study of the influence of nc-Si distribution, the other three samples were fabricated with the Si ion dose of 1×10^{16} cm^{-2} at the implantation energy of 8, 5 and 2 keV, respectively. TABLE 5.1 summarizes the implantation recipes of all the samples under investigation (each sample is denoted with a sample number). After the ion implantation, thermal annealing was conducted at 1000 ^{o}C in N_2 for 1 hour to induce nanocrystallization of excess Si in SiO_2. Afterwards, the backside of the samples was coated with 1-μm Al layer as the back ohmic contact using an electron beam evaporator system. Indium tin oxide (ITO) with a thickness of 130 nm was sputtered onto the surface of the Si^+-implanted SiO_2 film through a hard shadow mask with a pad radius of 1.2 mm. Because of its conductivity and high transparency over the visible to infrared range, the ITO film acts as both the gate electrode and the EL emission window. Figure 5.1(a) shows the schematic cross section of the MOS-like light-emitting structure with the Si^+-implanted SiO_2 as the gate oxide. The cross-sectional transmission electron microscopy (TEM) image confirms the formation of nc-Si embedded in the SiO_2 matrix. As an example, Fig. 5.1(b) shows the TEM image of nc-Si with the size of ~4 nm. The EL measurements were carried out with a PDS-1 photomultiplier tube (PMT) detector together with a monochromator. The measurements were performed at room temperature.

TABLE 5.1 Summary of implantation recipes for the samples in the EL study.

Sample No.	Implantation energy (keV)	Si ion dose (cm^{-2})
5a	5	1×10^{16}
5b	5	2×10^{15}
5c	5	3×10^{14}
8a	8	1×10^{16}
2a	2	1×10^{16}

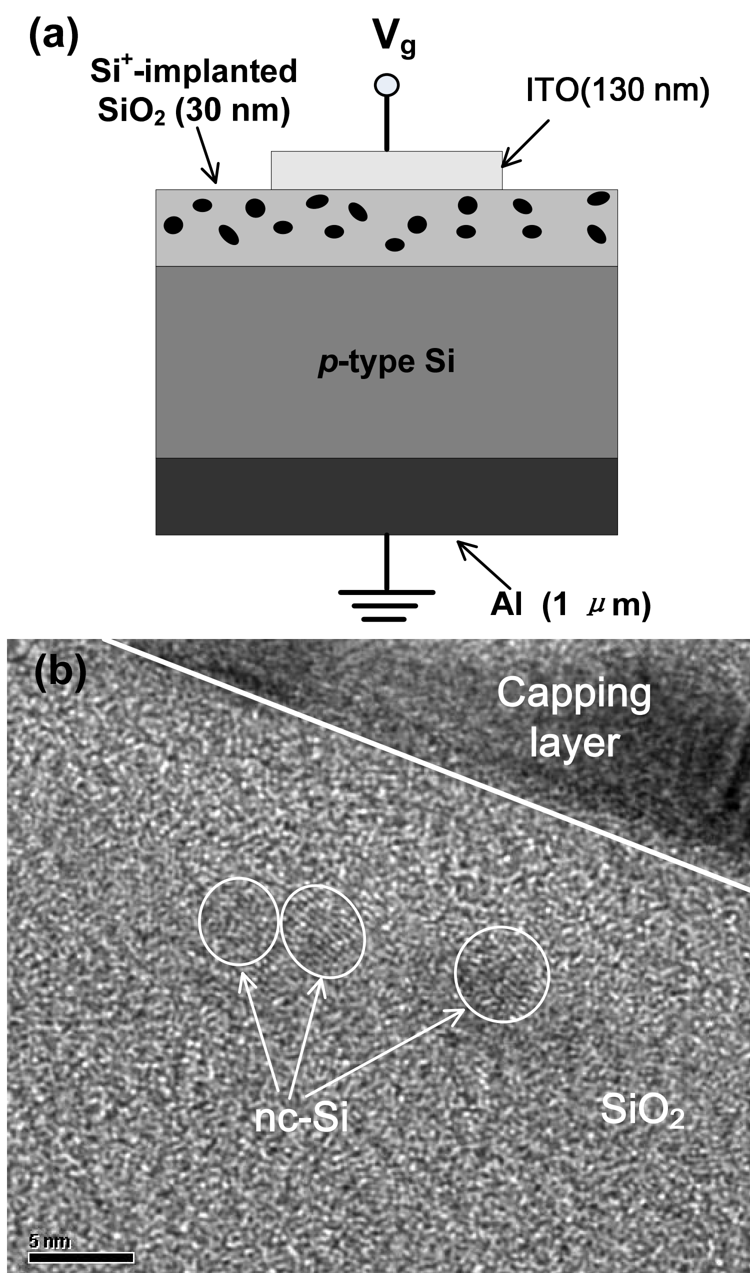

Figure 5.1 (a) Schematic illustration of the device structure; (b) Cross-sectional TEM image of nc-Si embedded in SiO_2 of sample 2a.

5.2.2 SRIM Result and Excess Si Distribution

The implanted Si depth profiles in the SiO_2 films were calculated with Stopping and Range of Ions in Matter (SRIM) simulations. Figure 5.2 shows the calculated depth profiles for the 5 samples. As can be seen in Fig. 5.2(a), for the samples implanted at 5 keV, the excess Si distributes from the oxide surface to the depth of ~23 nm, and the concentration of excess Si reaches its maximum at the depth of ~8 nm. The peak concentrations of excess Si for samples 5a, 5b, and 5c are 1×10^{22} cm^{-3}, 2×10^{21} cm^{-3}, and 3×10^{20} cm^{-3}, respectively. The corresponding peak nc-Si volume fractions are 20%, 4%, and 0.6%, respectively. The depth profiles of excess Si for the samples fabricated at different implanted energies with the same implantation dose (i.e., samples 8a, 5a, and 2a) are presented in Fig. 5.2(b). As shown in this figure, for sample 8a, the excess Si distributes throughout the entire oxide layer with the peak concentration of 5.7×10^{21} cm^{-3} (or the peak nc-Si volume fraction of 11%) located at the depth of ~15 nm from the oxide surface. For sample 2a, the excess Si distributes to the depth of ~15 nm and reaches the peak concentration of 1.7×10^{22} cm^{-3} (the corresponding nc-Si volume fraction is 33%) at the depth of ~4.5 nm.

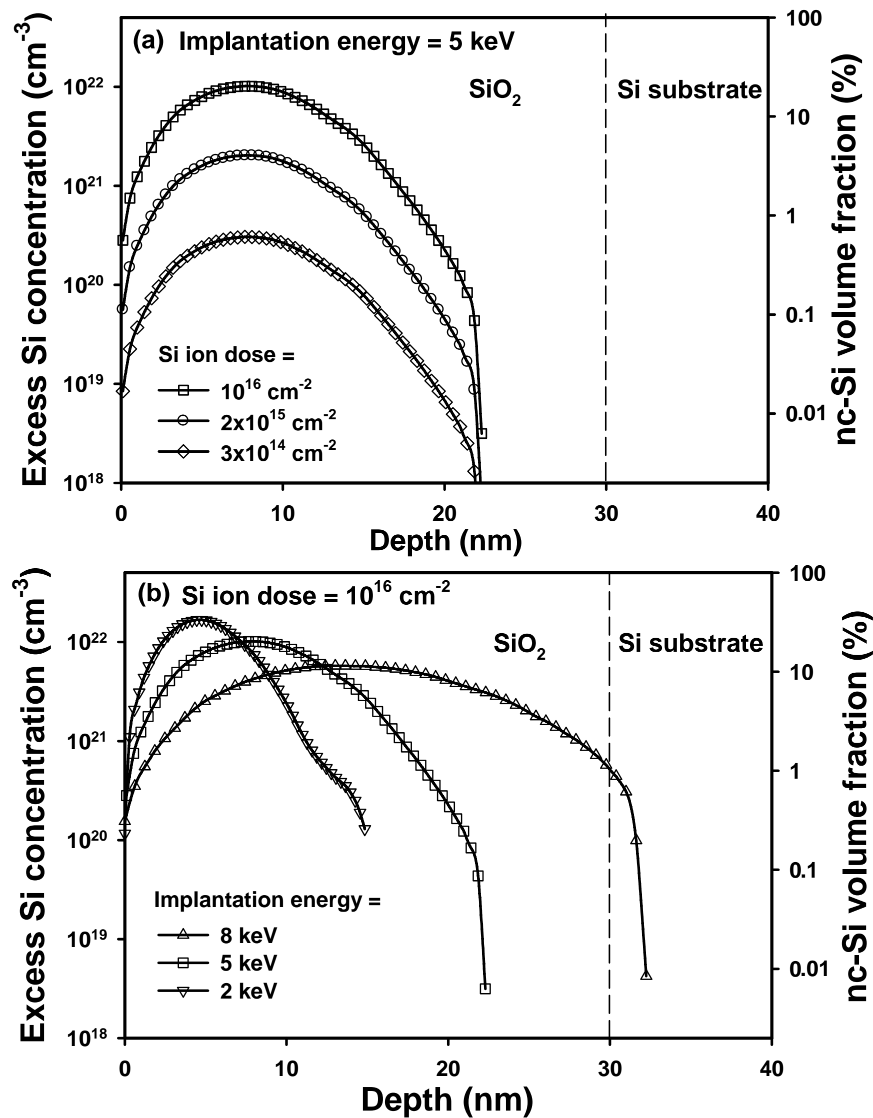

Figure 5.2 Distributions of nc-Si in the gate oxide obtained from SRIM simulations.

5.2.3 EL Spectra

Although it has been presented that annealing at 1000 ^{o}C leads to a wide PL spectrum in Chapter 4, no strong PL from the samples annealed at 1000 ^{o}C was observed in this study. A possible reason is that the film (~30 nm) is too thin (i.e., the excess-Si-distributed region is too narrow) or the concentration of excess Si is too low to produce a strong PL signal. However, visible and

infrared EL can be observed from the MOS-like LED structures when a negative voltage is applied to the ITO gate. No electroluminescence was detected under a positive gate voltage due to the extremely low gate current. When a positive gate voltage is applied, the holes can hardly be provided by the ITO contact, and the electrons are minorities in *p*-type Si substrate. Therefore, a strong EL is difficult to be induced under a positive gate voltage due to the extremely low injection of holes from the positively biased ITO gate and electrons from *p*-type Si substrate. As examples, Fig. 5.3 shows the EL spectra for sample 5a under different gate voltages. As shown in this figure, one can see that the EL intensity increases with the applied gate voltage, but the spectral shape changes little under different gate voltages. The injected current and the integrated EL intensity versus the gate voltage are shown in the inset of Fig. 5.3. The current and integrated EL intensity have a similar dependence on the gate voltage, showing a linear relationship between the integrated EL intensity and the current. Figure 5.4 presents the microphotographs of EL pattern under different voltages for sample 5a. It can be seen that the yellow EL pattern becomes brighter with the increasing gate voltage in accordance with the EL spectra presented in Fig. 5.3.

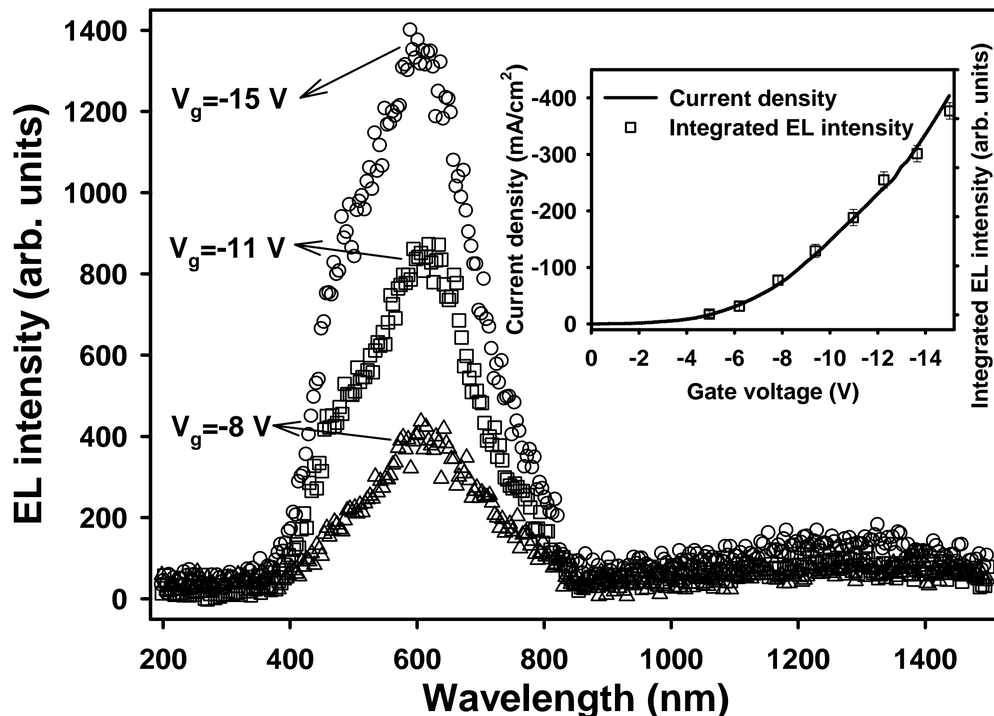

Figure 5.3 EL spectra for sample 5a under the gate voltage of -15, -11, and -8 V, respectively. The inset shows the *I-V* characteristics and the integrated EL intensity as a function of current density.

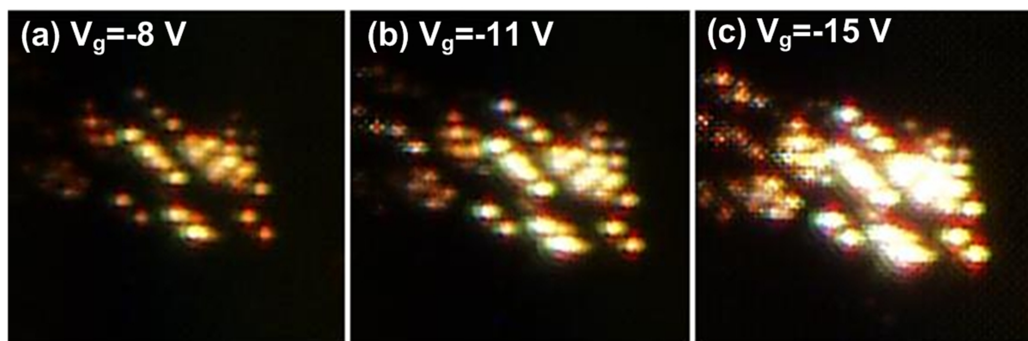

Figure 5.4 Microphotograph of EL patterns under different gate voltages for sample 5a. (a) -8 V, (b) -11 V, and (c) -15 V.

5.2.4 Influence of Implantation Recipe on EL

As these samples have the same implantation energy (i.e., 5 keV), they have the same distribution range of excess Si, namely, the excess Si is distributed from the SiO_2 surface to a depth of ~22 nm in the SiO_2 thin film. This means that there is no excess Si in the oxide in the region from the depth of ~22 nm to the

SiO_2/substrate interface. In other words, there is a tunnel oxide (i.e., the pure SiO_2 region without the excess Si) with the thickness of ~8 nm for all the three samples. The Log-Log plots of *I-V* characteristics for the three samples are also shown in Fig. 5.5. It should be pointed out that in order to simplify the power law formula (see section 5.2.5) for analyzing the current transport, the polarity of gate voltage has been neglected in Fig. 5.5 and 5.6, and only the amplitude of the gate voltage has been used to analyze the current transport. The tunnel current through the pure SiO_2 region and the current conduction in the excess-Si-distributed region play roles in the current transport. However, when the voltage is sufficiently high, the tunneling across the pure oxide is sufficient enough such that the current transport and the light emission are limited only by the conduction in the excess-Si-distributed region. In the EL study, the voltage is at least ~5V to induce measurable EL emission. Therefore, the current conduction in the Si^+-implanted region rules both the EL and the current transport in the voltage range of our interest. The current conduction in the excess-Si-distributed region could be explained with the percolation concept [255]. Similarly to the situation of tunneling paths formed by neutral oxide traps in SiO_2 thin films [255], carriers can be transported through tunneling via the defects, nc-Si, and Si nanoclusters which have been confirmed to co-exist in the Si suboxide films after the annealing at 1000 ^oC [256-262]. With the formation of many conductive percolation paths in the excess-Si distributed region, the conduction of the system is enhanced. This explains why the current conduction increases with the concentration of excess Si as shown in Fig. 5.5. As a result of the increase in the current conduction, more electrons from the ITO gate and more holes from the *p*-type Si substrate are injected into the Si-implanted region,

leading to an increase in the radiative recombination of the injected electrons and holes and thus an increase in the EL intensity. Indeed, as shown in Fig. 5.5, the integrated EL intensity increases with the concentration of excess Si following the same trend of the current conduction.

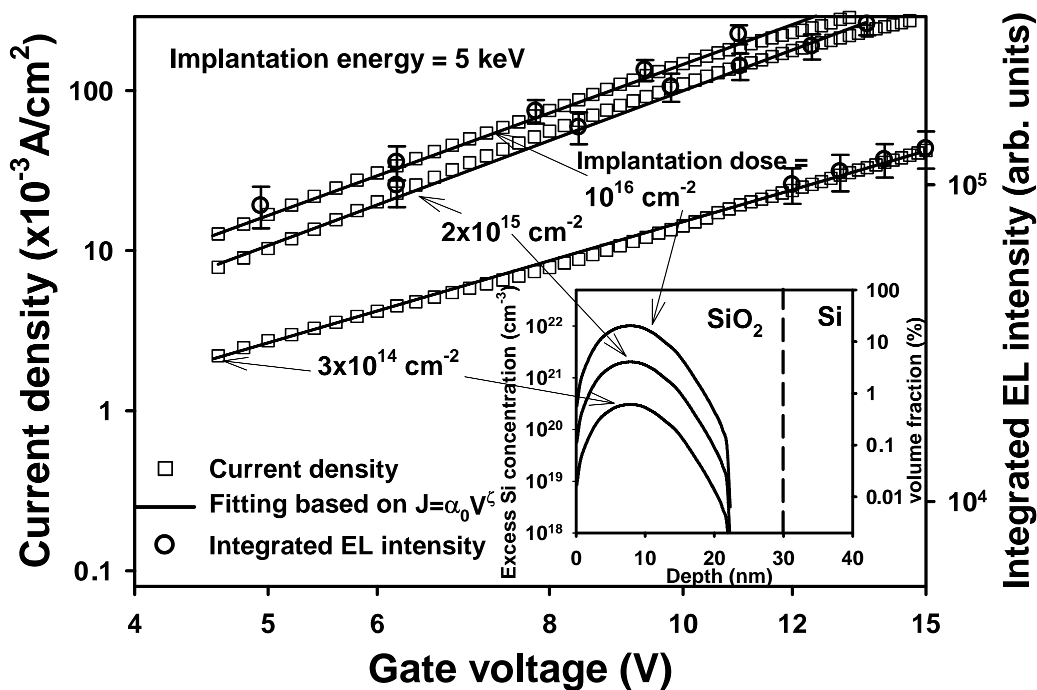

Figure 5.5 Dependence of the current and the integrated EL intensity on the voltage as a function of the implanted Si ion dose (samples 5a, 5b, and 5c). The implantation energy is fixed at 5 keV . The inset shows the concentrations and distributions of the excess Si in the oxide thin film obtained from the SRIM simulations.

On the other hand, to study the influence of the distribution of excess Si, various distributions are achieved by varying the implantation energy. The inset of Fig. 5.6 shows the concentrations of excess Si and distribution profiles for samples 2a, 5a, and 8a which were fabricated at the energies of 2, 5 and 8 keV, respectively, with the fixed Si ion dose of 1×10^{16} cm^{-2}. For sample 2a, the excess Si is distributed from the SiO_2 surface to a depth of ~14 nm in the SiO_2 thin film, forming a tunnel oxide of ~16 nm; for sample 5a, the excess Si is distributed from the SiO_2 surface to a depth of ~22 nm, forming a tunnel oxide

of ~8 nm; and for sample 8a, the excess Si is distributed from the SiO_2 surface until the SiO_2/substrate interface leading to no tunnel oxide formed. As a constant implantation dose is used, the peak concentration of excess Si decreases with the extension of the Si^+-implanted region. With higher implantation energy, the excess-Si-distributed region extends wider while the pure oxide becomes thinner, thus the voltage drop in the excess-Si-distributed region increases for a given applied voltage. Therefore, for a given applied voltage the current will be higher if the conduction in the excess-Si-distributed region plays a dominant role in the current transport. On the other hand, when the excess Si is distributed throughout the entire SiO_2 thin film (i.e., the situation of sample 8a), conductive tunneling paths connecting the substrate to the gate will be formed, leading a large increase in the current conduction. As a result of the two scenarios, the current conduction increases with the implantation energy, as shown in Fig. 5.6. As the EL intensity reflects the transport of the injected carriers, the increase of the current conduction is translated to an increase in the EL intensity with the implantation energy, as shown in Fig. 5.6 also.

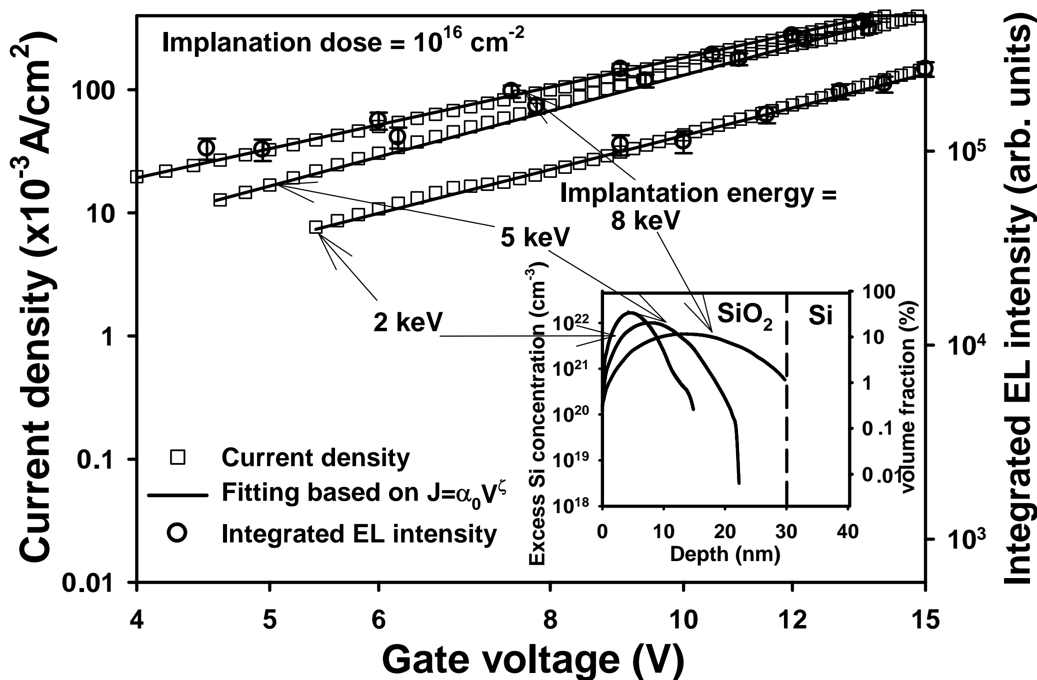

Figure 5.6 Dependence of the current and the integrated EL intensity on the voltage as a function of the implantation energy (samples 2a, 5a, and 8a). The implanted Si ion dose is fixed at 1×10^{16} cm^{-2}. The inset shows the concentrations and distributions of the excess Si in the oxide thin film obtained from the SRIM simulations.

5.2.5 Relationship Between Current Transport and EL

It can be observed from Figs. 5.5 and 5.6 that the *I-V* characteristics for all the samples follow a power law

$$J = \alpha_0 V^{\zeta} \tag{5.1}$$

where J is the current density, V is the applied voltage, α_0 is a coefficient, and ζ is the scaling exponent. The power-law behavior could be explained by a model similar to the one of collective charge transport in arrays of normal-metal quantum dots (QDs) [263]. The values of the two parameters α_0 and ζ obtained from the power-law fittings shown in Figs. 5.5 and 5.6 are presented in Fig. 5.7. As shown in Fig. 5.7, α_0 increases with both the implanted Si ion dose (Fig. 5.7(a)) and the implantation energy (Fig. 5.7(b)). As α_0 reflects the conductance

of the material system, it increases when more tunneling paths are formed with a higher concentration of excess Si or when the Si^+-implanted region extends with higher implantation energy. On the other hand, ζ is found to be in the range of ~2.4 – ~3 for different samples. This is much larger than the values obtained from simulations and experiments of two-dimensional (2D) transport, where ζ ranges from 5/3 to 2.26 [263, 264]. This could suggest that the current conduction in the system of Si^+-implanted SiO_2 thin film is a quasi-3D transport. As shown in Fig. 5.7(a), ζ slightly increases with the Si ion dose; however, as shown in Fig. 5.7(b), ζ decreases with the implantation energy, indicating that the increase in the implantation energy would lead to the evolution towards the 2D transport due to the increase in the lateral spacing between the adjacent defects, Si nanoclusters, or nc-Si.

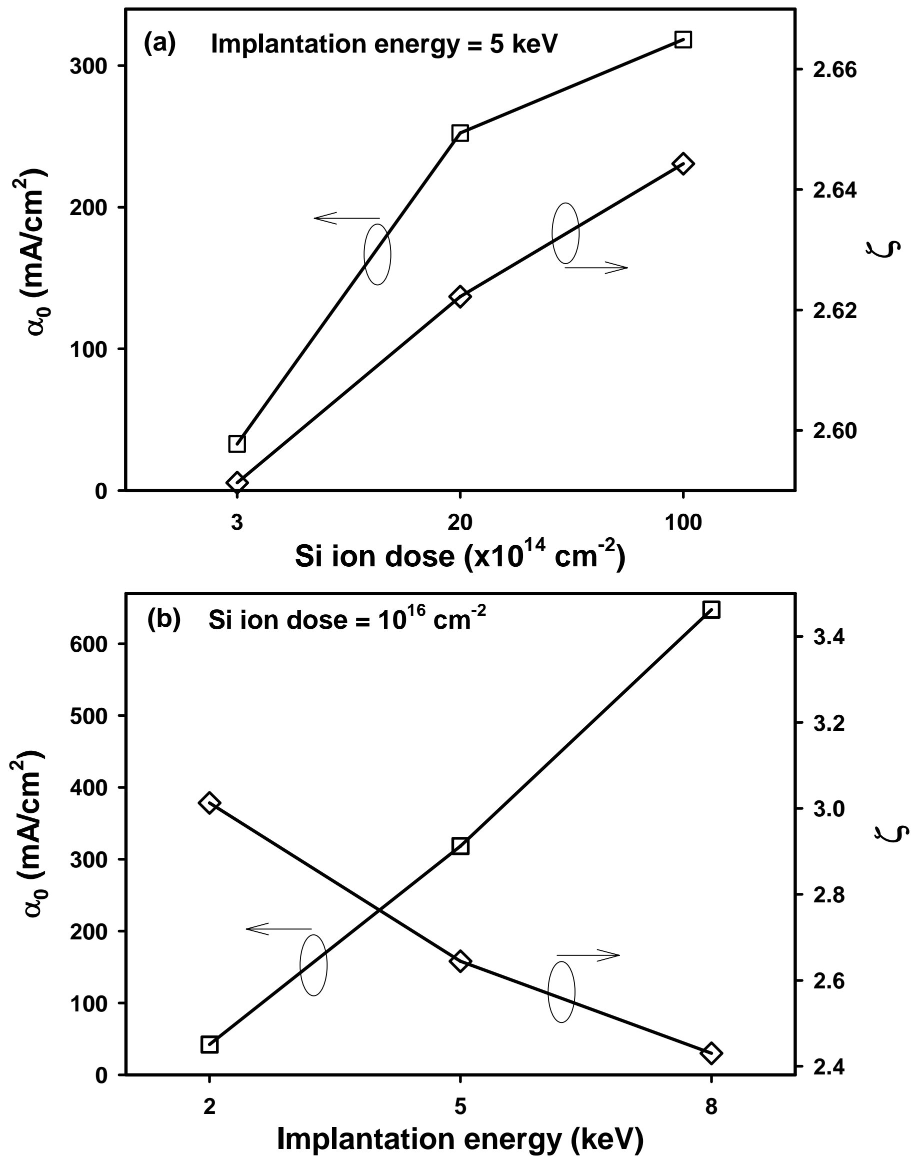

Figure 5.7 α_0 and ζ as functions of implanted Si ion dose (a) or implantation energy (b).

As the EL intensity is proportional to the current, the dependence of the integrated EL intensity on the voltage also follows a power law given by

$$I_{EL} = \alpha_0^{'} V^{\zeta^{'}} \tag{5.2}$$

where I_{EL} is the integrated EL intensity, $\zeta^{'} = \zeta$ within the experimental and fitting errors, and $\alpha_0 / \alpha_0^{'}$ is a constant for all the samples. Obviously, the

dependence of both the $\alpha_0^{'}$ and $\zeta^{'}$ on the concentration and distribution of the excess Si is similar to that of the α_0 and ζ. Therefore, with the knowledge of the influence of the implantation recipe on the α_0 and ζ obtained from the transport study, one can predict the effect of the implantation recipe on the EL intensity, which should be useful in designing nc-Si LEDs synthesized with the ion implantation technique. As an example, the influence of the implantation recipe on the integrated EL intensity, which is obtained from the calculation based on the above power law, is shown in Fig. 5.8. The corresponding experimental result is also included in the figure for comparison. As can be seen in the figure, the calculation is in good agreement with the experiment. It can be also seen in the figure that the EL intensity increases with the implanted Si ion dose and/or the implantation energy.

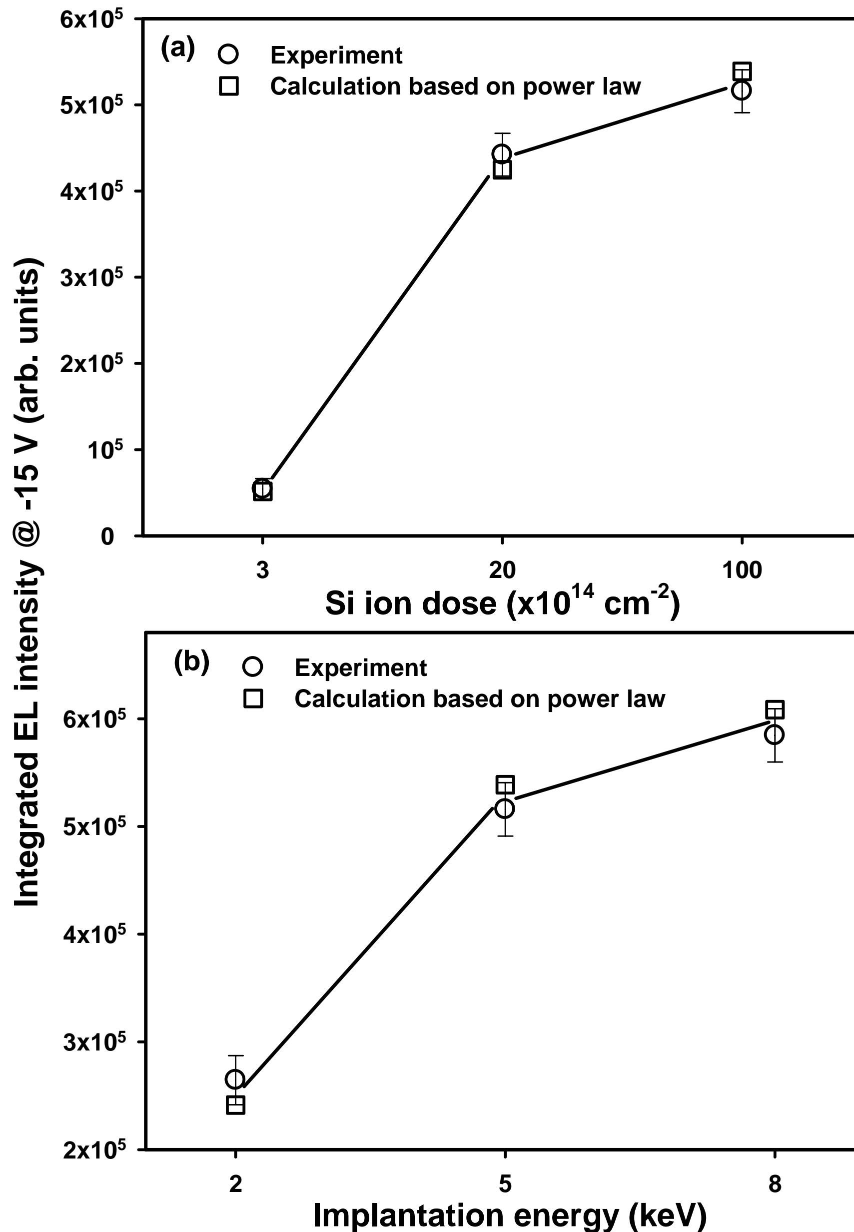

Figure 5.8 Integrated EL intensity under the gate voltage of -15 V as a function of implanted Si ion dose (a) or implantation energy (b). The calculated EL intensity is based on the power law shown in Eq. (5.2).

5.2.6 EL Mechanisms

The EL spectra can be decomposed into 4 Gaussian-shaped EL bands. As an example, the EL spectral decomposition for sample 5a under the gate voltage of -15 V is shown in Fig. 5.9. As can be seen in this figure, the ~610-nm

luminescence band dominates the EL spectrum with two shoulder bands centered at ~460 nm and ~740 nm, respectively. In addition, a luminescence band located at ~1260 nm was observed in the infrared region. Figure 5.10 shows the peak wavelengths of the four EL bands obtained at different gate voltages. It can be seen from the figure that the peak wavelengths change little with the gate voltage. On the other hand, the contribution (in percentage) of each EL band, which is the ratio of the integrated intensity of each EL band to the integrated intensity of the EL spectrum, changes with the gate voltage. Figure 5.11 shows the gate-voltage dependence of the contribution of each EL band for sample 5a. As can be seen in the figure, when the gate voltage increases, the contribution of the dominant EL band (i.e., the ~610-nm band) decreases, while the contributions of the ~460-nm and ~740-nm bands increase but the contribution of the ~1260-nm band shows no change.

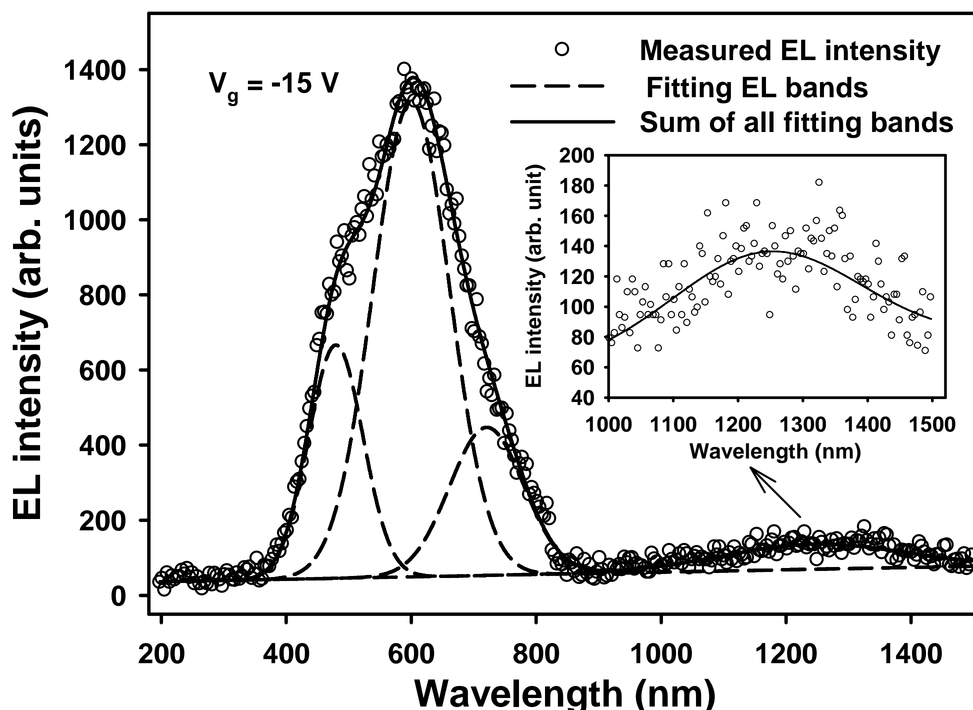

Figure 5.9 Decomposition of the EL spectrum for sample 5a under the gate voltage of -15 V into the following four EL bands: ~460-nm, ~610-nm, ~740-nm, and ~1260-nm bands.

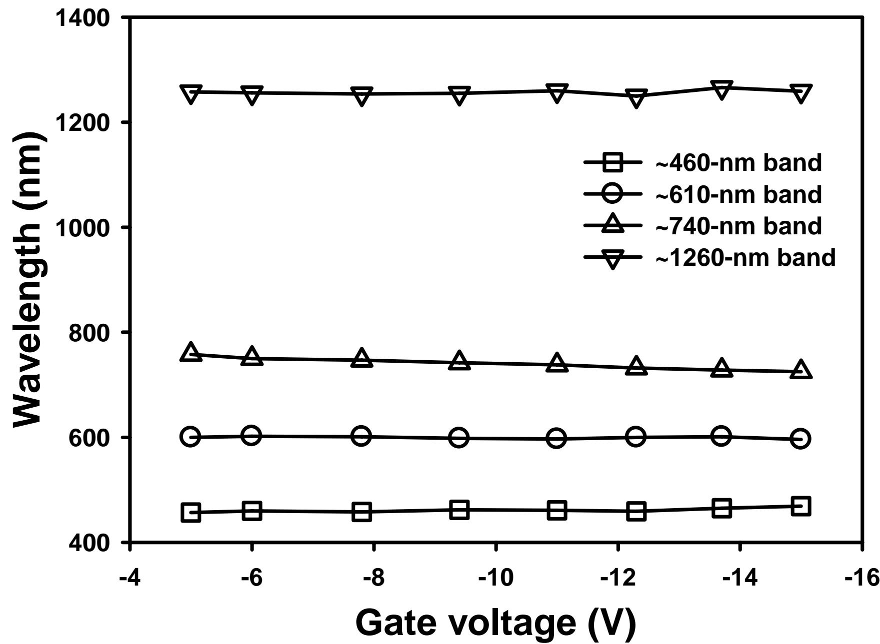

Figure 5.10 Evolution of peak wavelength of the EL spectra with gate voltage for sample 5a.

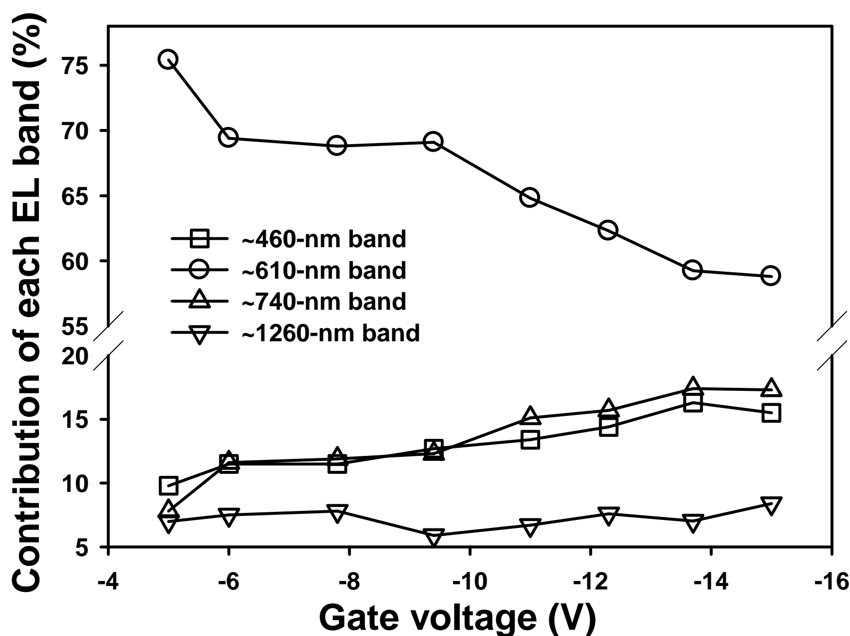

Figure 5.11 Gate-voltage dependence of the contribution of each EL band for sample 5a.

Figure 5.12 shows the EL spectra under the gate voltage of -15 V for the samples fabricated with different implantation doses (i.e., samples 5a, 5b, and 5c). As shown in Fig. 5.12, the integrated EL intensity increases with the implantation dose. Figure 5.13 shows the EL spectra for the samples fabricated

at different implantation energies with the same Si ion dose (i.e., samples 8a, 5a, and 2a). It can be observed that the EL intensity also increases with the implantation energy. The increase in the EL intensity with either the implanted Si ion dose or the implantation energy can be explained by the enhancement in the current conduction of the Si^{+}-implanted oxide, as discussed above.

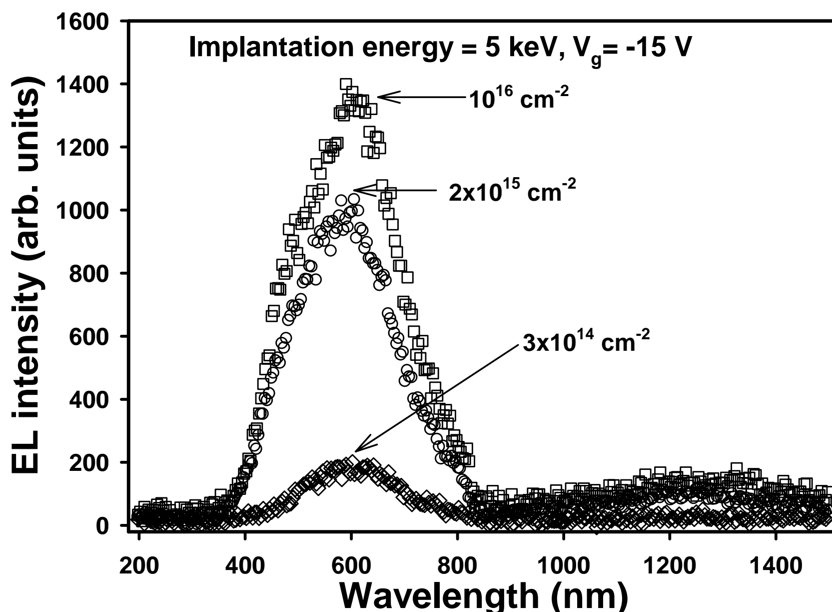

Figure 5.12 Influence of the implanted Si ion dose on the EL spectrum. The EL spectra shown in the figure are from samples 5a, 5b and 5c.

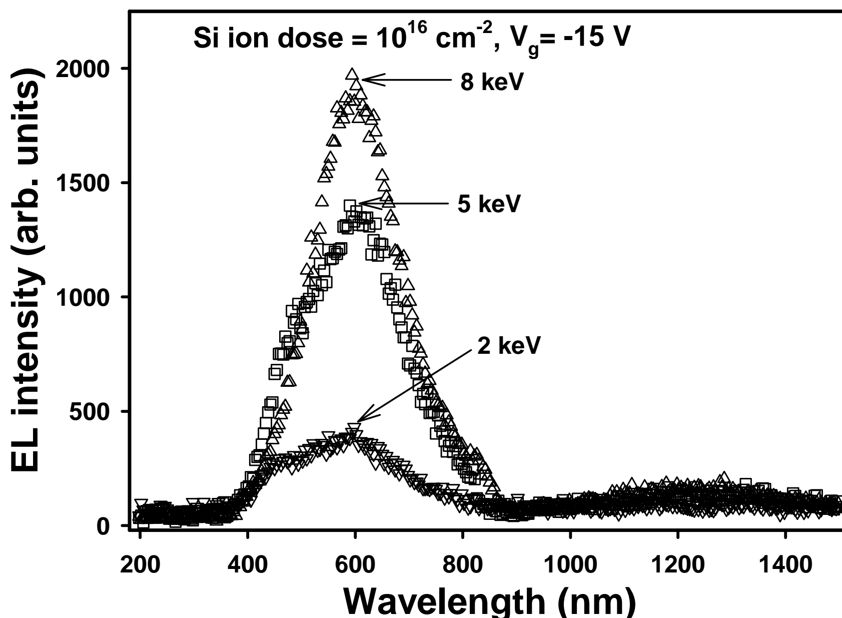

Figure 5.13 Influence of the implantation energy on the EL spectrum. The EL spectra shown in the figure are from samples 8a, 5a and 2a.

Although the integrated EL intensity increases with both the implanted Si ion dose and implantation energy, the contribution of each EL band shows a different picture of its dependence on the implanted Si ion dose and implantation energy. Figure 5.14 shows the contribution of each EL band as a function of the implanted Si ion dose under the gate voltage of -15 V. As shown in Fig. 5.14, for the samples with the same implantation energy (5 keV), the contribution of each EL band is almost independent of the Si ion dose. However, the contribution of each EL band changes with the implantation energy. Figure 5.15 shows the dependence of the contribution of each EL band on the implantation energy for the samples fabricated with the same Si ion dose (10^{16} cm^{-2}). As can be seen in the figure, when the implantation energy increases from 2 keV to 8 keV, the contribution of the ~610-nm band significantly increases from ~ 55% to ~ 61%, the contributions of both the ~740-nm band and the ~1260-nm band show almost no changes, and the contribution of the ~460-nm EL band significantly decreases from ~23% to ~13%.

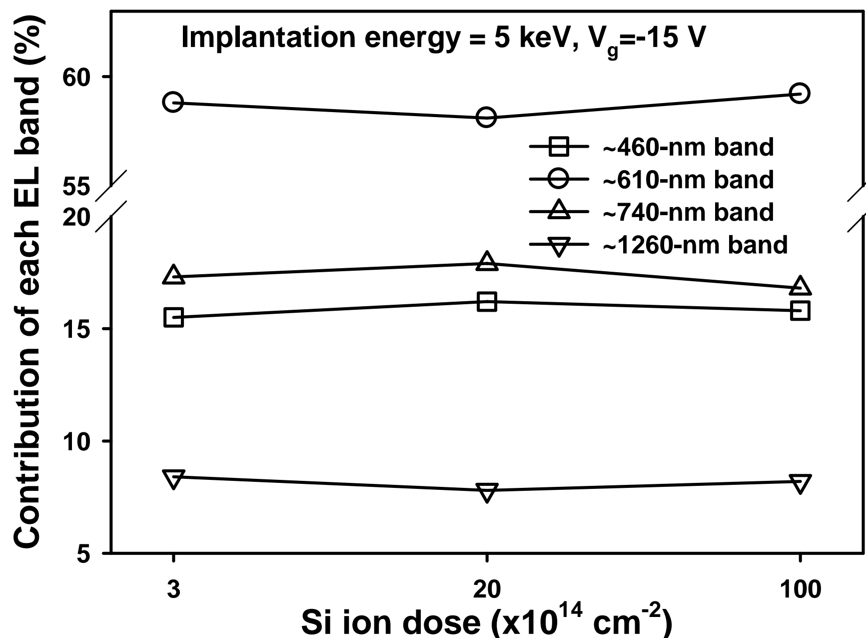

Figure 5.14 Contribution of each EL band as a function of the implanted Si ion dose.

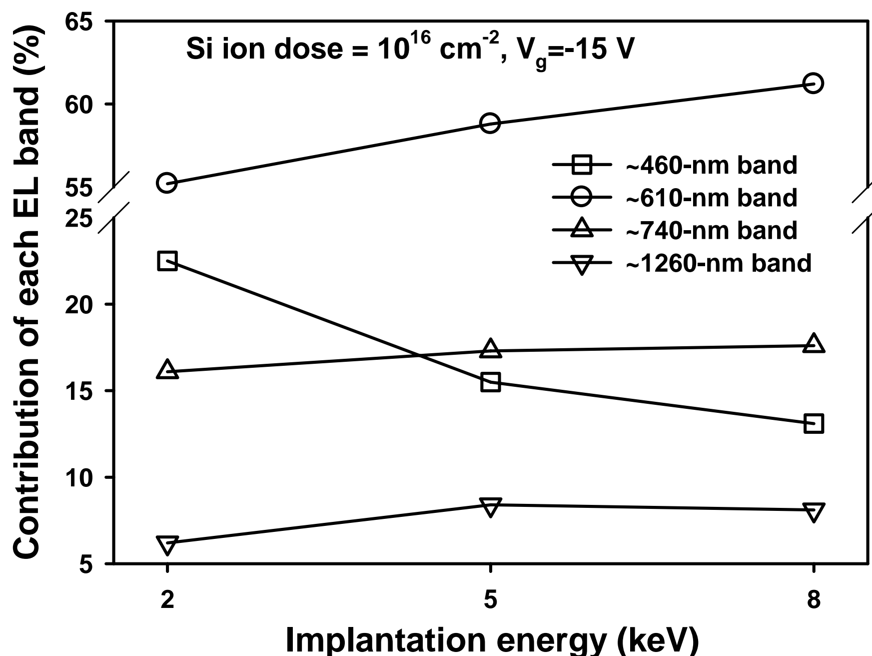

Figure 5.15 Contribution of each EL band as a function of the implantation energy.

The EL bands observed in the present study are very similar to those reported by Song *et al.* [139]. In their study, they also observed the ~460-nm, ~610-nm and ~740-nm EL bands with the ~610-nm band as the dominant one from the Si^+-implanted SiO_2 films. Many kinds of luminescent defects, such as weak-oxygen bond (WOB) (O-O) defects [150, 230], neutral oxygen vacancy (NOV) ($O_3 \equiv \text{Si-Si} \equiv O_3$) [118, 138, 139, 148, 150, 227, 230, 237], non-bridging oxygen hole center (NBOHC) ($O_3 \equiv \text{Si-Si-O} \bullet$) [43, 118, 139, 150, 230, 237], *D* center [118], and *E'* center [14, 53, 118, 123, 139, 150, 230, 265] have been proposed for the mechanisms of luminescence from Si^+-implanted SiO_2 films. Although the origins for the above-mentioned EL bands are still under debate, the following mechanisms are popularly accepted in the literature, and thus our discussions will be also based on these mechanisms. The ~460nm (~2.7 eV) band is ascribed to the NOV defect which was proposed for the EL

band observed from pure silica glass [238] and Si^+-implanted SiO_2 films [118, 138, 139, 148, 150, 227, 230, 237]. It has been known that the NBOHC defects in SiO_2 can emit light at around 2 eV (~610 nm) [43, 118, 139, 150, 230, 234, 237]. Therefore, following Song *et al.* [139], we attribute the ~610-nm band to the NBOHC defects.

As regard to the ~740-nm (~1.7 eV) EL band, first we assume that it is probably due to the existence of nc-Si in the oxide, because there have not been any defects or interface states that can contribute to an emission band around 740 nm in such an extensive literature. As mentioned above, the average diameter of nc-Si formed in the SiO_2 films in this study is ~4 nm. The ~740-nm photoluminescence band was observed which was believed to be due to the formation of nc-Si with a mean size of ~4 nm [237]. Thanks to many previous experimental studies presented in Chapter 3 and 4, and theoretical studies [202], the nc-Si with a diameter of ~4 nm was estimated to have a band gap of ~1.85 eV. The difference between the band gap and the emission energy indicates that the ~740-nm EL band should not originate from the direct band to band transition within the nc-Si. In fact, there are several studies that have demonstrated that the nc-Si with the size larger than ~1 nm still have an indirect band structure in both theoretical [242, 266, 267] and experimental aspects [75, 267, 268]. Therefore, the probability of direct band-to-band transition within the nc-Si is extremely low. It has been found that the energy difference (~0.15 eV) between the band gap and the emission energy is approximately equal to the energy (~0.134 eV) of Si-O vibration with a stretching frequency of 1083 cm^{-1}, implying the importance role of Si-O vibration at the nc-Si/SiO_2 interface in the 740-nm band luminescence. Considering the energy conservation and the

indirect band structure of the nc-Si, we therefore are inclined to believe that the Si-O vibration at the nc-Si/SiO_2 interface provides the mean required for both the energy dissipation due to the energy conservation requirement and the momentum conservation in the EL process. In other words, the ~740-nm band can be attributed to the recombination of carries within the nc-Si assisted by the Si-O vibration at the nc-Si/SiO_2 interface.

As for the infrared EL band center at ~1260 nm, it mostly originates from the Si substrate. In order to confirm whether the virgin oxide and the substrate have any contribution to the observed EL spectra, we measured the EL spectra of the LEDs fabricated with pure thermal grown SiO_2 and SiO_2 films with different implanted elements, such as Ge and Al. Although the EL spectra in the visible range are different, all the samples exhibit infrared EL centered at ~1260 nm. The electrical driven infrared luminescence was also reported by Kulakci *et al.* recently [153]. Although the authors could not determine the peak wavelength of the infrared EL due to the detector limitation, the light emission above 900 nm was indeed observed. In our study, it is noticeable that the photon energy of peak infrared luminescence is ~0.985 V which has a difference of ~0.135 eV as compared to the band gap of bulk crystalline silicon. The energy difference is approximately the same with the Si-O vibration energy (0.134 eV). This observation makes us believe that the infrared EL band centered at ~1260 nm is a result of electron-hole recombination in the accumulation region formed beneath the oxide layer near the interface between the Si substrate and SiO_2. Such recombination is assisted by the Si-O vibration with an energy of ~0.135 eV at the interface between SiO_2 and the Si substrate. In other words, the electron-hole recombination near the interface emits a photon with the energy of

~0.985 eV and a phonon of ~0.135 eV which is actually the Si-O vibration. This mechanism is similar that of the ~740-nm EL band's origin, in which the energy and momentum compensation is provided by the Si-O vibration at the nc-Si/SiO_2 interface.

The excitation of the NOV defect as a luminescence center can be enhanced by a high electric filed in the oxide (E_{ox}) [139, 150, 269]. This agrees with the result shown in Fig. 5.10 that the contribution of the ~460-nm band increases with the applied gate voltage. On the other hand, as discussed early, the nc-Si distributed region extends with increasing the implantation energy, leading to an increase in the gate current. As a result, for a given gate voltage, the voltage drops in the ITO/oxide junction and the oxide/substrate junction increase, and thus the voltage drop in the oxide decreases. Thus the electric field in the oxide decreases weakening the excitation of the NOV defect. Therefore, the contribution of the ~460-nm band decreases with the implantation energy, as shown in Fig. 5.15.

In our experiments, the ~610-nm band always dominates the EL spectra for all the samples, indicating that the excitation energy of the ~610-nm band should be much lower than that of other luminescent defects. The energy distribution of injected carriers can easily satisfy the requirement for the excitation of the NBOHC defects. The excitation of the NBOHC defects becomes saturated at a gate voltage less than 5 V. As the contributions of the ~460-nm band and the ~740-nm band increase with the gate voltage, the contribution of the ~610-nm band decreases with the gate voltage due to the saturation in the excitation of the NBOHC defects (note that the contribution is a relative contribution and the

sum of all the contributions is 100%), as shown in Fig. 5.11. On the other hand, as shown in Fig. 5.15, the contribution of the ~610-nm band increases with the implantation energy. This could suggest that the generation of the NBOHC defects increases with the implantation energy.

As the carrier transport via the nc-Si is enhanced by the electric field in the nc-Si distributed region, the light emission from the nc-Si should increase with the gate voltage. Indeed, the contribution of the ~740-nm band which is attributed to the nc-Si increases with the gate voltage, as shown in Fig. 5.11. In contrast to the contributions of the ~460-nm band and the ~610-nm band which change significantly with the implantation energy, the contribution of the ~740-nm band shows only a small increase with the implantation energy, indicating that the light emission from the nc-Si is not very sensitive to the implantation energy. For all the EL bands, their contributions are insensitive to the implanted Si dose, as shown in Fig. 5.14. This indicates that the increase in the implantation dose does not change the composition of the EL spectra.

Based on the discussions above, the mechanism of the observed four EL bands are illustrated by the band diagram shown in Fig. 5.16. A set of widely accepted values of the work function and the band gap of ITO are used in the band diagram [270, 271].

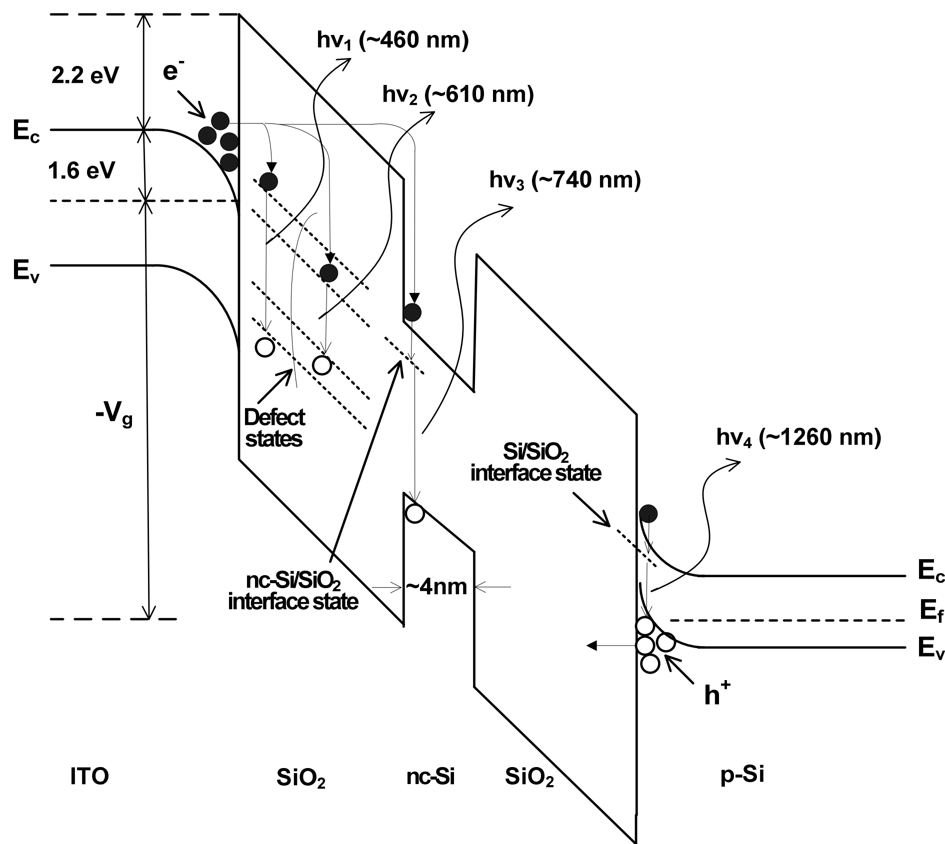

Figure 5.16 Energy band diagram illustrating electroluminescence from the ITO/SiO_2:Si^+/Al capacitor structure. E_c, E_v, and E_f refer to the conduction band, the valence band, and the Fermi level energy, respectively. Energy values are denoted in eV.

5.2.7 Annealing Effect on EL Properties

In the study on the annealing effect on EL properties, sample 5a was taken for the investigation. The sample was annealed at various temperatures for different annealing durations. The annealing experiments were carried out with either a constant annealing time or a constant annealing temperature. For the former case, the annealing time was set at 20 min and the annealing temperature varied from 500 to 1100 ^oC. For the latter case, the annealing temperature was set at 1000 ^oC and the annealing time varied from 20 to 100 min. As-implanted sample is also included in this study. For example, the EL spectra for the

as-implanted sample (Note that the "as-implanted" sample has also experienced some thermal annealing ~250 ^{o}C for ~20 min during the deposition bottom electrode), and the samples annealed at 700 and 1100 ^{o}C are presented in Fig. 5.17. It can be seen that the annealing temperature has little effect on the EL spectral shape while the EL intensity becomes stronger with the increasing annealing temperature. In addition, we found that the annealing time neither had little influence on the EL spectra shape except for the intensity, as shown in Fig. 5.18.

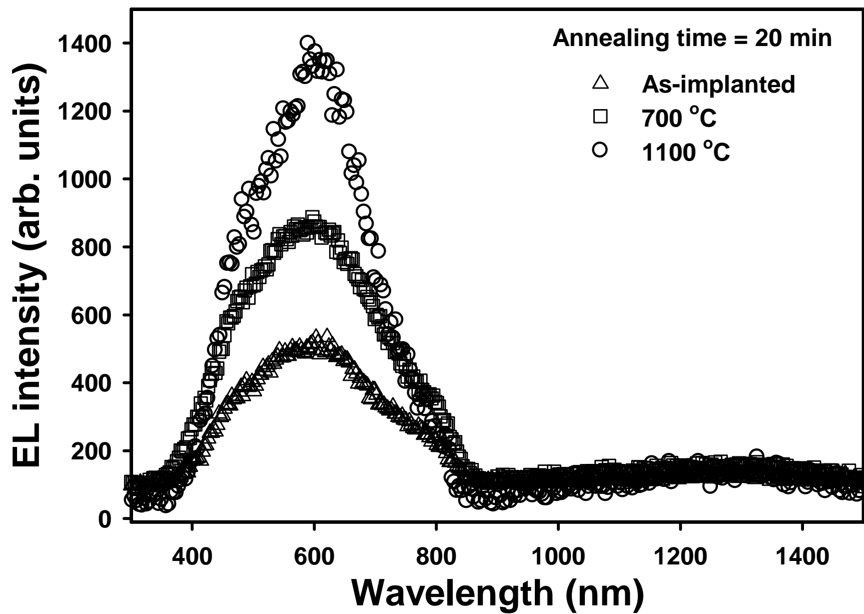

Figure 5.17 EL spectra for the as-implanted sample, and the samples annealed at 700 and 1100 ^{o}C for 20 min.

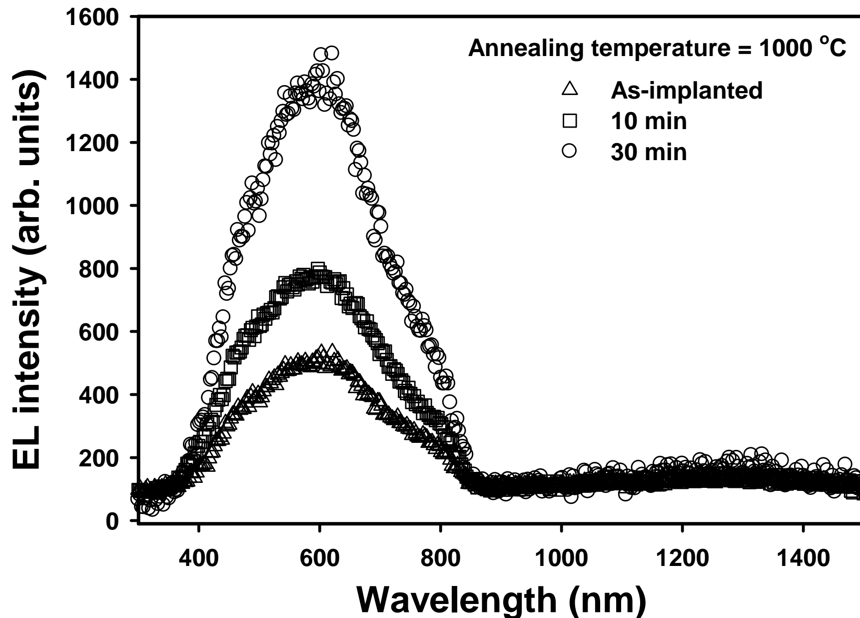

Figure 5.18 EL spectra for the as-implanted sample, and the samples annealed for 10 and 30 min at 1000 ^{o}C.

The effect of annealing conditions on the total EL intensity is further shown in Fig. 5.19 and 5.20. Figure 5.19 presents the integrated EL intensity as a function of annealing temperature. As shown in the figure, the as-implanted sample has the smallest EL intensity, while the integrated EL intensity gradually increases as the annealing temperature increases. When the annealing temperature is higher than 900 ^{o}C, no obvious increase in the EL intensity can be observed, indicating a saturation point of the EL emission. For the case of annealing temperature fixed at 1000 ^{o}C, the integrated EL intensity increases with the annealing time during the first 20 min followed by an almost constant value of the EL intensity for the annealing time longer than 20 min, as shown in Fig. 5.20. The dependence of the integrated EL intensity on both the annealing temperature and annealing time shown in Fig. 5.19 and 5.20 clearly indicates that an annealing at 900 ^{o}C for 20 min is good enough as a higher annealing temperature or a longer annealing time does not increase the EL intensity

significantly. This has an important implication for the fabrication of nc-Si-based LEDs made by Si ion implantation since excess thermal budget must be avoided.

The behavior of EL intensity due to the thermal annealing can be explained by the evolution of the number of trapped Si ions (i.e., excess positive charge) in the oxide with thermal annealing [111]. The electrical properties of the SiO_2 film implanted with Si ions are affected significantly by subsequent annealing. The number of excess positive charge induced by Si ion implantation can be decreased by thermal annealing. In the system of Si^+-implanted SiO_2 films, large number of Si nanocrystals, Si nanoclusters, and defects would form tunneling path in the oxide which greatly enhance the current conduction of the oxide. However, excess charges trapped in the oxide can block some of the tunneling paths, leading to a reduction in the current transport of the oxide as well as the decrease of the total EL emission. In Ref. [111], Ng and the co-workers reported that annealing for 20 min at 900 ^{o}C can remove the most of the trapped ions in the oxide. This is consistent with the result we have shown above that the integrated EL intensity saturates with such an annealing.

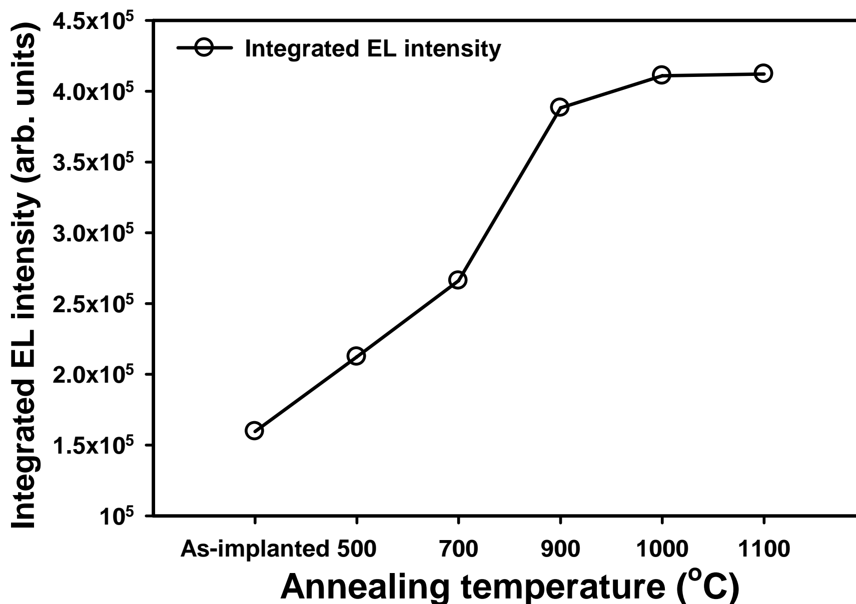

Figure 5.19 Integrated EL intensity as a function of annealing temperature.

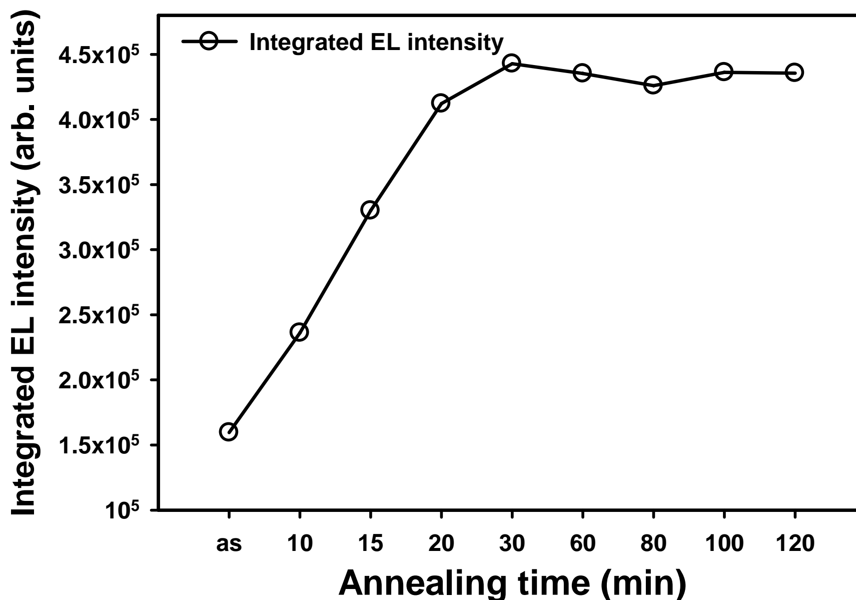

Figure 5.20 Integrated EL intensity as a function of annealing duration.

5.2.8 Comparison between EL and PL

No strong PL was observed from the samples annealed at 1000 °C or 1100 °C which were mentioned in the above section. There are three possible factors that are responsible for the absence of strong PL: (1) this could be attributed to the

PL quenching by the non-radiative defects which are formed in the SiO_2 matrix due to the ion implantation but could not be fully recovered by the annealing at the slightly lower temperature (i.e., 1000 ^{o}C) [261, 262]; (2) the film (~30 nm) is too thin (i.e., the excess-Si-distributed region is too narrow) and the excess Si to produce a strong PL signal; (3) the fraction of excess Si is too low to induce PL signal that is detectable by our PL measurement system. Indeed, as discussed in Chapter 4, a thicker oxide thickness (~1000 nm) with a wide excess-Si-distributed region exhibits a weak PL for the annealing at 1000 ^{o}C, as shown in the Fig. 5.21. Moreover, PL emission is observed from the 30-nm-thick SiO_2 implanted with a higher dose of Si ions (4×10^{16} cm^{-2}) at 16 keV annealed at 1000 ^{o}C, but no PL is observed from the 1000-^{o}C annealed sample.

We look back into the sample fabricated with a thicker oxide (~1000 nm) and implanted with a higher dose (1×10^{17} cm^{-2}) of Si ions at a higher energy (100 keV), whose PL properties has been studied in Chapter 4. PL can be detected from the samples annealed at both 1000 ^{o}C and 1100 ^{o}C, but the PL intensity for the annealing at 1000 ^{o}C is almost 30 times lower than that for the annealing at 1100 ^{o}C, as shown in the Fig. 5.21. The Gaussian-shaped PL spectrum located at ~760 nm for the annealing at 1100 ^{o}C has been proved to be due to the formation of Si nanocrystals. For the annealing at 1000 ^{o}C, the PL spectrum has two clear luminescence bands located at ~610 and ~760 nm, although their intensities are much lower than that of the ~760-nm band of the annealing at 1100 ^{o}C. The existence of the weak ~760-nm PL band for the annealing at 1000 ^{o}C suggests that the 1000-^{o}C annealing can also lead to the formation of Si nanocrystals. However, the non-radiative defects that could not be fully

recovered by the annealing at 1000 °C quench the PL emission, resulting in the ~760 nm band much weaker than that for the annealing at 1100 °C. As regard to the dominance of ~610-nm luminescence band in the EL spectra for both the samples annealed at both 1000 and 1100 °C, it is probably due to the fact that the energy distribution of injected carriers can easily satisfy the requirement of excitation energy for the related luminescent defects while the excitation of nc-Si as an active medium by injected carriers is relatively difficult [139].

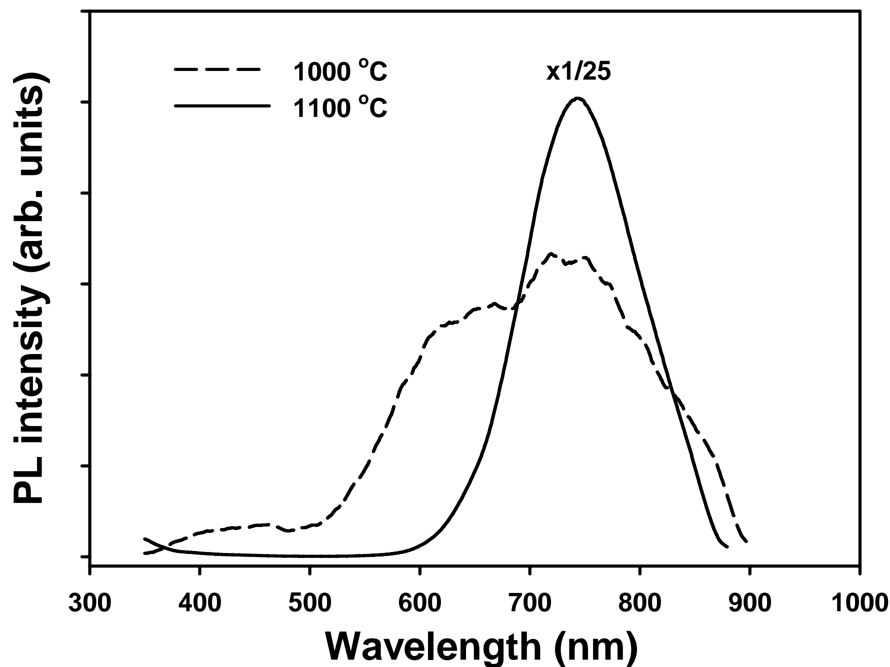

Figure 5.21 PL spectra of the samples with a thicker oxide (~1000 nm) and synthesized with a higher implantation dose (1×10^{17} cm^{-2}) at the energy of 100 keV. The samples were annealed at 1000 °C and 1100 °C for 30 min, respectively.

Moreover, another set of 30-nm-thick samples have been fabricated with the implantation of 4×10^{16} cm^{-2} Si ions at the energy of 10 keV. Both PL and EL can be detected from the samples annealed at 1100 °C, but no PL is observed from the 1000-°C annealed sample. Figure 5.22 shows the normalized PL and EL spectra for the 1100-°C-annealed sample of 30-nm-SiO_2 implanted with

4×10^{16} cm^{-2} Si ions at 10 keV. As can be seen in the figure, the PL and EL spectra present remarkably different traits. Similar to sample 5a, the EL spectrum shown in Fig. 5.22 presents the main peak at ~610 nm which would be related to radiative defects introduced by Si ion implantation. PL shows a Gaussian-shaped spectrum which would be attributed to the formation of Si nanocrystals embedded in the oxide. This proves again that the optical pumping tents to excite nanocrystal-related luminescence but the electrical pumping tends to excite defect-related luminescence instead of nanocrystal-related luminescence.

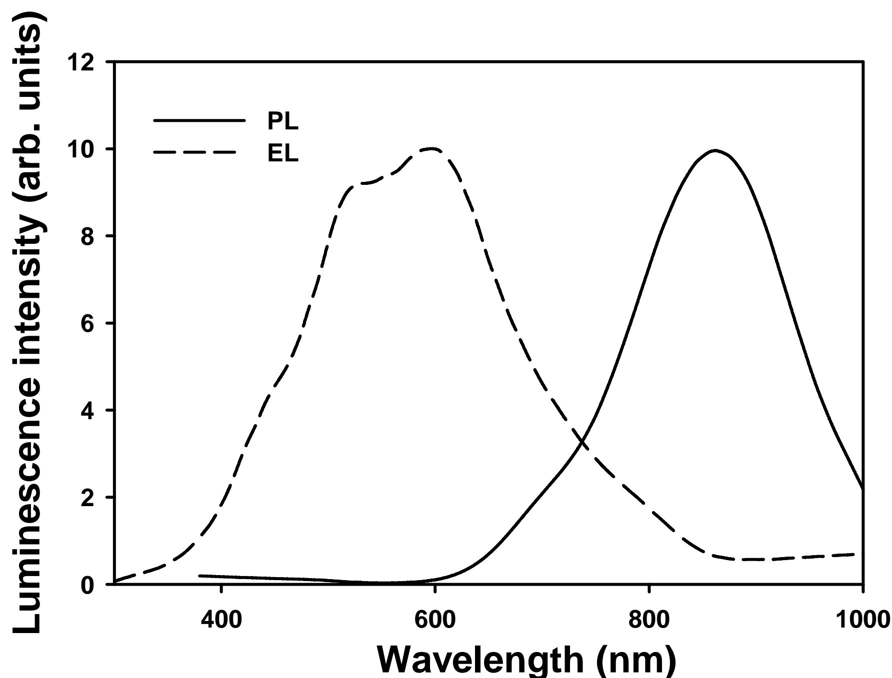

Figure 5.22 PL and EL spectra of the samples implanted with 4×10^{16} cm^{-2} Si ions at the energy of 10 keV. The samples are annealed at 1100 ^{o}C for 1 hour.

5.2.9 Conclusion

In summary, we have presented a study on the EL properties of SiO_2 films embedded with nc-Si synthesized with low energy ion implantation. The MOS-like light-emitting structures are fabricated with various Si ion doses

under different implantation energies. Both visible and infrared electroluminescence has been observed under a negative gate voltage. The influence of nanocrystal distribution on the EL properties has been investigated. It is observed that the EL intensity increases with the Si ion dose and/or the implantation energy, due to the enhanced current transport. Four EL bands peaked at ~460, ~610, ~740, and ~1260 nm have been observed for all the samples. The first two EL bands are ascribed to the NOV and NBOHC defects, respectively. The ~740-nm band is believed to be associated with the formation of the nc-Si embedded in SiO_2. The ~1260-nm EL band is assigned to the electron-hole recombination in the accumulation region in the Si substrate underneath the oxide. The influence of the applied voltage, the implantation dose and implantation energy on the contributions of the EL bands has been investigated.

5.3 EL from Si^+-implanted Si_3N_4 Films

It has been frequently reported that the Si-rich nitride materials have the potential to emit light at short wavelength. In this study, EL properties from Si^+-implanted Si nitride films are investigated. Violet and blue light emission under electrical excitation is observed from the MOS-like capacitor structure with Si nanocrystals embedded in Si_3N_4 films fabricated with Si ion implantation. The influence of thermal annealing on the EL properties of the Si^+-implanted Si nitride film is investigated.

5.3.1 Sample Fabrication and Experiments

30-nm Si nitride films were deposited on a *p*-type Si (100) wafer by LPCVD by standard recipe for stoichiometric composition. The implanted samples were prepared by multi-energy implantation of Si ions into the Si nitride films with the recipe of 4×10^{16} cm^{-2} at 25 keV, 8×10^{15} cm^{-2} at 8 keV, and 3×10^{15} cm^{-2} at 2 keV. This results in a uniformly distributed Si^+-implantation profile inside the Si nitride film in order to enhance the carrier injection. The implantations were carried out at room temperature. Figure 5.23 shows the depth profile of the multi-implanted Si ions calculated with SRIM simulation. As can be seen in this figure, the implanted Si ions are uniformly distributed in the Si nitride film. The concentration of excess Si throughout the nitride film is $\sim1.2\times10^{22}$ cm^{-3}, and the corresponding volume fraction of the implanted Si is ~25%. After implantation, thermal annealing was carried out at 1000 and 1100 ^{o}C under a flowing N_2 gas ambient for 1 h, in order to realize the nanocrystallization of excess Si, activate radiative defects, and eliminate the carrier-trapping centers buried in the nitride. To fabricate the LED structure, a ~200 nm thick Al layer was coated onto the backside of the substrate as the ohmic contact using an electron beam evaporator. On the top of the film, ITO films with the thickness of ~130 nm were onto the surface of the Si^+-implanted nitride films through a hard shadow mask with a pad radius of 1.2 mm. The structure is the same as the MOS-like LED device that has been presented in Section 5.2.1. The EL measurements were carried out with a PDS-1 photomultiplier tube detector together with a monochromator. PL spectra were taken with a commercial ACCENT RPM2000 PL system using an excitation laser of 325 nm line with the power of 1 mW. All spectral measurements were performed at room temperature

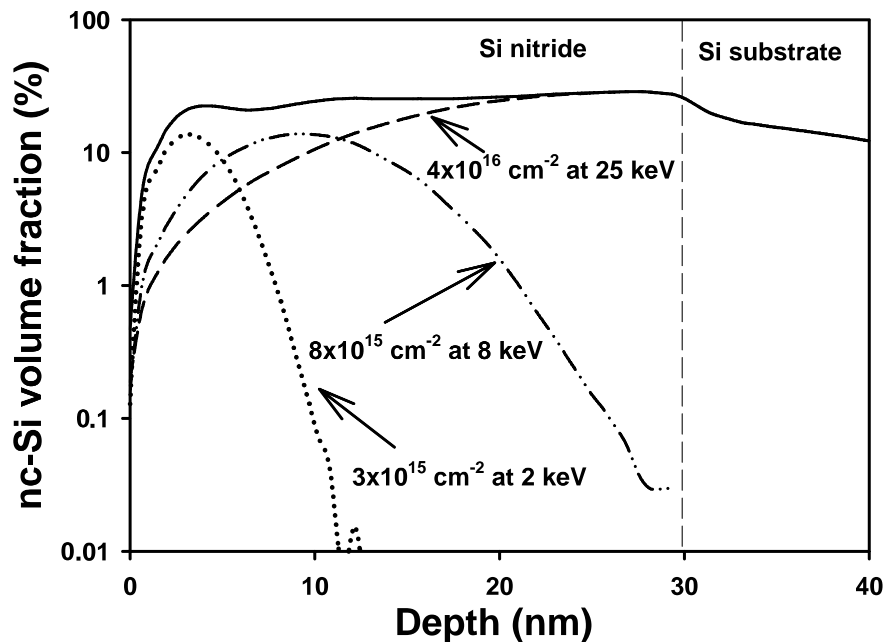

Figure 5.23 Distribution of the implanted Si in the Si nitride film obtained from SRIM simulation.

5.3.2 EL Spectra

Strong visible EL can be observed from the MOS-like LED structure when a negative voltage is applied to the ITO gate. No electroluminescence can be detected under a positive gate voltage due to the insufficient carrier injection. Strong blue light emission can be observed with naked eyes from the top electrode when a negative voltage large enough is applied on the ITO gate. Figure 5.24 shows the EL spectra for the sample annealed at 1100 ^{o}C at different gate voltages. As shown in this figure, one can see that the EL intensity increases with the applied gate voltage, but the spectral shape changes little with the increasing gate voltage. The inset of Fig. 5.24 shows the injected current and the integrated EL intensity as functions of the gate voltage. The gate current and the integrated EL intensity have a similar dependence on the gate voltage when the voltage is large enough to induce a measureable EL, showing a linear

relationship between the integrated EL intensity and the current injection. As can be seen in this figure, a measureable EL is detected when the negative gate voltage is larger than 10 V, while no EL can be observed under a positive gate voltage. Figure 5.25 presents the microphotographs of EL patterns under different voltages for the Si^{+}-implanted Si nitride film annealed at 1100 ^{o}C, whose EL spectra have been presented in Fig. 5.24. It can be seen that the violet EL pattern becomes brighter with the increasing gate voltage, being consistent with the EL spectra shown in Fig. 5.24.

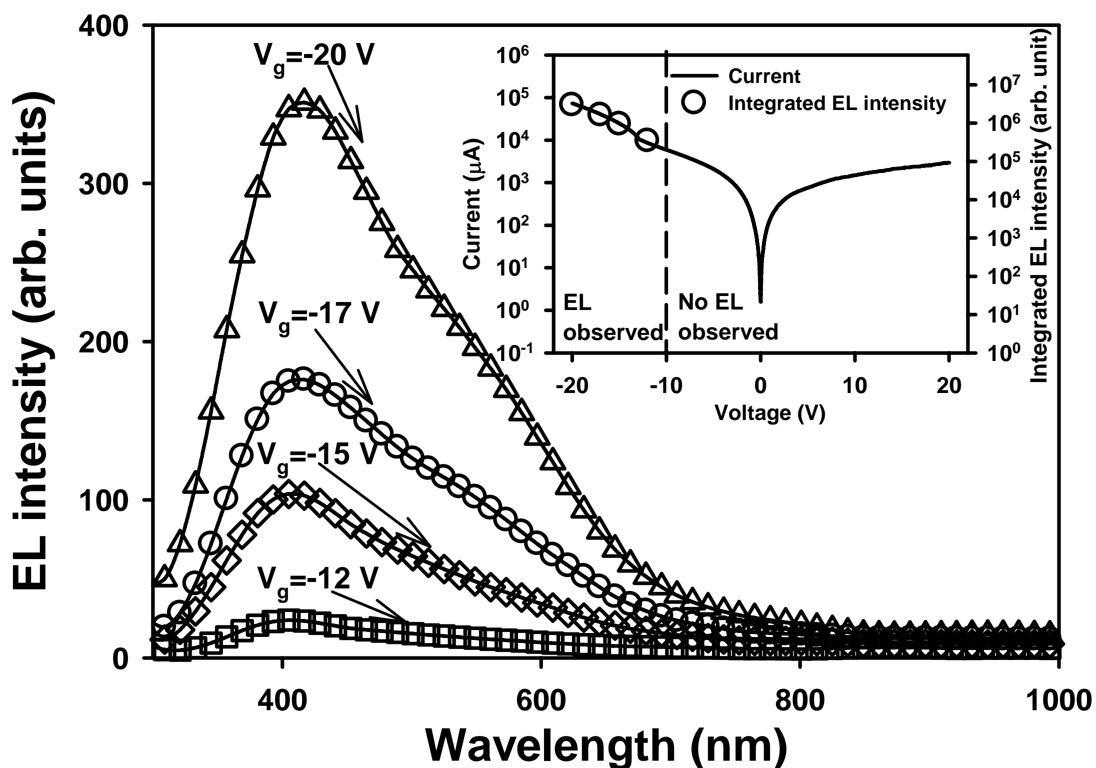

Figure 5.24 EL spectra from the Si^{+}-implanted Si nitride film annealed at 1100 ^{o}C under the gate voltage of -12, -15, and -17, and -20 V, respectively. The inset shows the *I-V* characteristics and the integrated EL intensity as a function of current density.

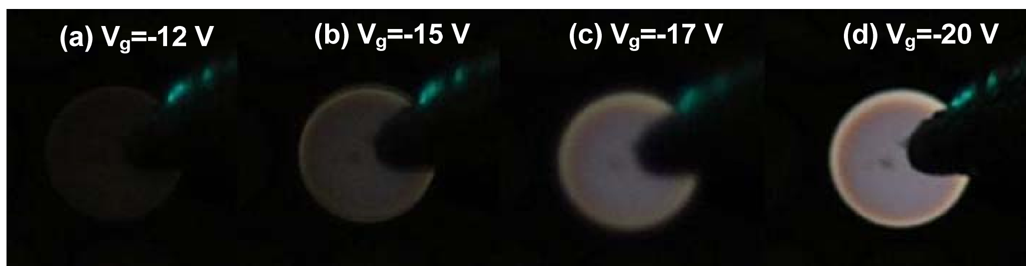

Figure 5.25 Microphotograph of EL patterns under different gate voltages for sample 5a. (a) -12 V, (b) -15 V, (c) -17 V, and (d) -20 V.

5.3.3 Annealing Effect on EL Properties

In Section 5.2.7 on the investigation of the annealing effect on the EL properties of the Si^+-implanted SiO_2 film, it has been found that the thermal annealing only influences the EL intensity of Si^+-implanted SiO_2 films while the spectral shape change little with thermal annealing. However, in the case of Si^+-implanted Si_3N_4 films, it is found that the different annealing temperatures can induce different spectral shapes. For example, Fig. 5.26 shows the EL spectra of the Si^+-implanted Si nitride film annealed at 1000 ^oC under different gate voltages. It can be seen that the EL intensity increases with the applied gate voltage while the spectral shape changes little. By comparing the EL spectra shown in Fig. 5.26 with that of the 1100-^oC-anneald sample which has been shown in Fig. 5.24, one can see that EL spectral shape of the 1000-^oC-annealed sample is different from that of the 1100-^oC-annealed sample and the spectra are much broader than that of the sample annealed at 1100 ^oC. The annealing effect on the EL spectral shape is different from that on the Si^+-implanted SiO_2 films. Figure 5.27 shows the EL spectra for samples annealed at different temperatures under the gate voltage of -20 V. In general, the increasing annealing temperature enhances the EL intensity prominently. As can be seen in this figure, the EL intensity of the 1100-^oC-annealed sample is stronger than that of the

1000-°C-annealed sample and the as-implanted sample by approximately 1 and 2 orders, respectively. Besides the significant increase of EL intensity with thermal annealing, the EL spectral shape evolves significantly with the annealing temperature, as can be seen in Fig. 5.27. Although the EL spectra at different annealing temperatures look so different, each of them can be decomposed into two Gaussian-shaped EL bands peaked at ~435 and ~680 nm, being consistent with the PL spectra obtained from the Si^+-implanted Si nitride films, which have been discussed in Chapter 4. The EL spectrum differs from each other only because the contribution of two EL bands evolves with thermal annealing.

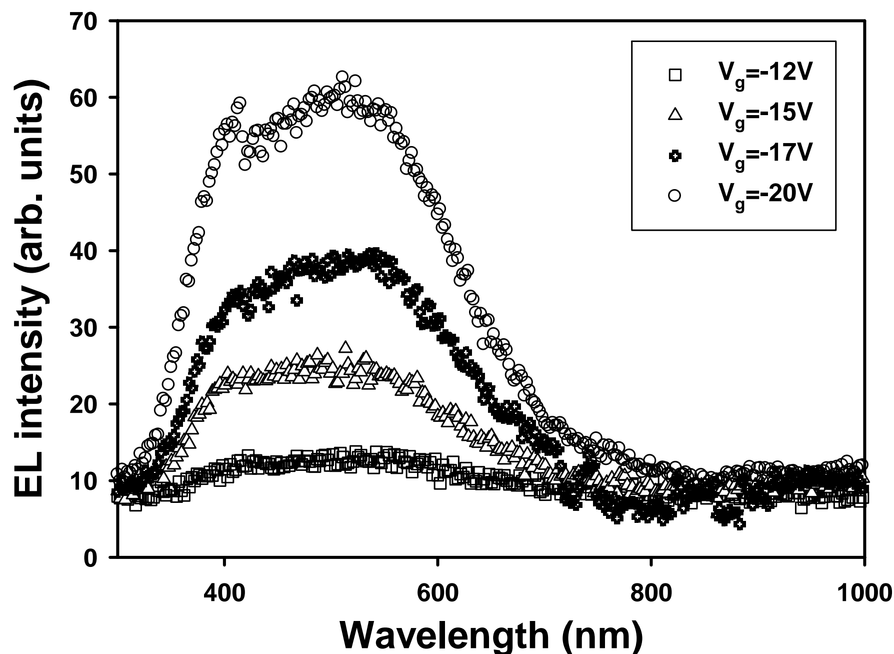

Figure 5.26 EL spectra from the sample of Si^+-implanted Si nitride film annealed at 1000 °C under the gate voltage of -12, -15, and -17, and -20 V, respectively.

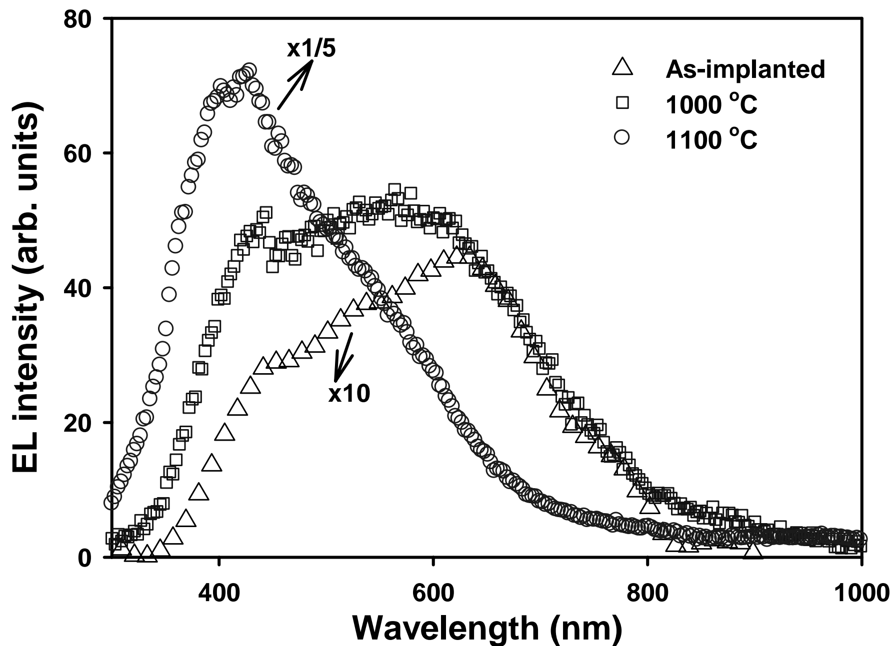

Figure 5.27 EL spectra from the Si^{+}-implanted Si nitride films for the as-implanted sample, and the samples annealed at 1000 °C and 1100 °C for 1 h.

5.3.4 Comparison between EL and PL

It can be seen in Fig. 5.27, the contribution of the blue-violet band to the whole EL spectra increases with the annealing temperature. At the annealing temperature of 1100 °C, the violet-blue emission band dominates the EL spectrum, while the red emission band takes the domination in the EL spectrum of the as-implanted sample. Although the PL spectra are also found to consist of the same two emission bands, they show a different picture in the evolution with thermal annealing. Figure 5.28 shows the comparison between the normalized PL and EL spectra of the Si^{+}-implanted Si nitride. It can be seen that both the PL and EL spectra can be decomposed into a blue-violet and a red emission bands. At the annealing temperature of 1100 °C, the blue-violet emission band makes the major contribution to the EL spectra; but for the as-implanted sample,

the red emission band makes more contribution to the EL spectra. On the contrary, the red PL emission makes much more contribution at the annealing temperature of 1100 ^{o}C; but for the as-implanted sample, the blue-violet emission band makes the major contribution. As discussed in the PL study on Si^{+}-implanted Si nitride in Chapter 4, the short-wavelength light emission is attributed to the recombination through the defects states in the Si nitride band gap. Based on the evolution of EL and PL spectra with thermal annealing, it is reasonable to believe the activation of defects states responsible for the blue-violet emission band is much easier to be realized by carrier injection than by optical pumping. Similarly, one can conclude that the red emission band is much easier to be activated by optical pumping than by electrical excitation.

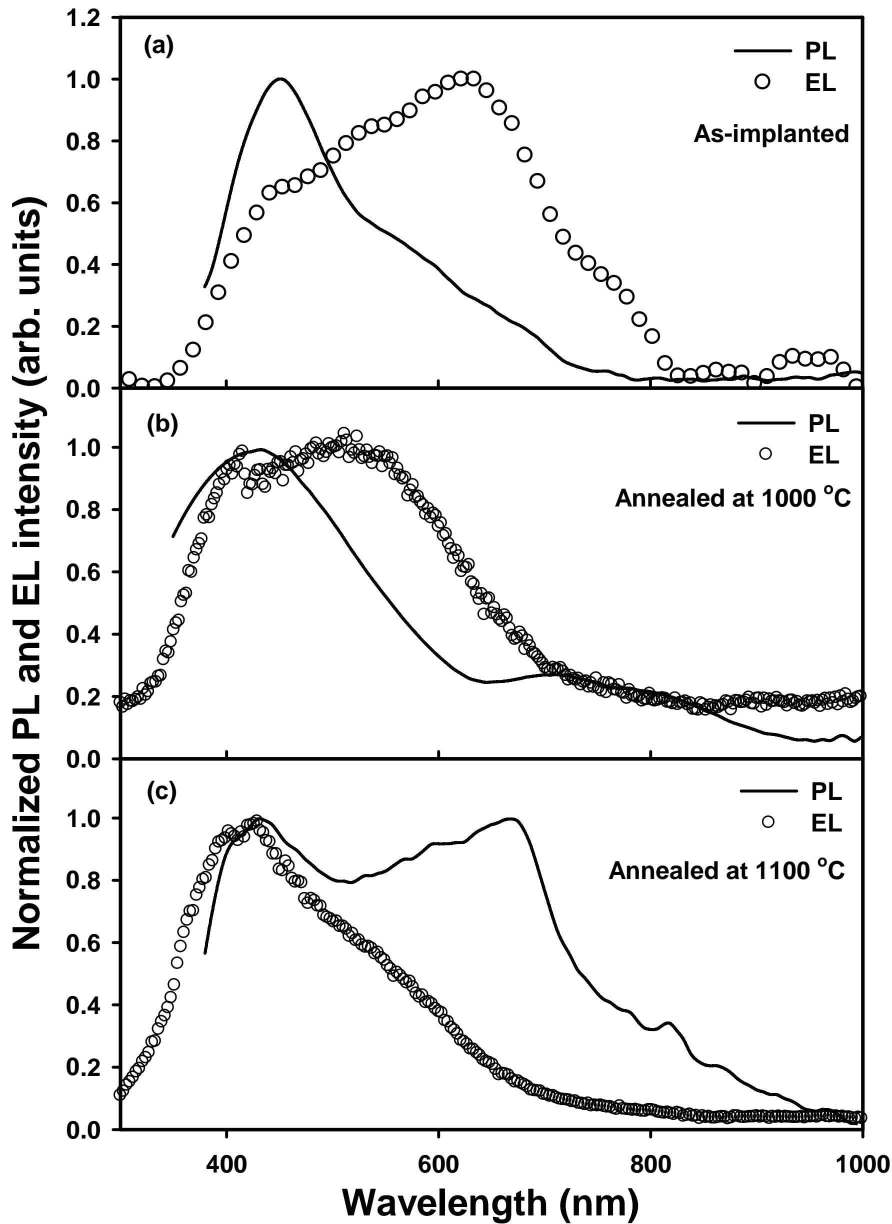

Figure 5.28 Comparison between normalized PL and EL spectra of Si^+-implanted Si nitride films at different annealing temperatures.

5.3.5 Conclusion

In this section, the Si^+-implanted Si nitride films has been demonstrated to emit strong light emission by electrical excitation based on a MOS-like LED structure. The structure has shown the potential for fabricating LEDs that emit light covering the whole visible wavelength range from red to violet. The EL

spectra can be changed by thermal annealing at different temperatures. In addition, the intensity of the light emission has been found to be enhanced by thermal annealing. The activation mechanism of different emission band has been shown to differ from each other. The blue-violet emission band is easier to be activated by carrier injection than by optical pumping, while the activation of the red emission band is much easier to be realized by optical pumping than by electrical excitation.

5.4 Summary

In this chapter, the EL properties of Si nanocrystals embedded in SiO_2 and Si_3N_4 have been investigated. The light emission structures are based on the MOS-like capacitor which shows the potential for fabricating Si nanocrystal-based LEDs. The microphotographs of EL patterns for both Si^+-implanted SiO_2 and Si_3N_4 have been demonstrated. The influence of implantation recipe and the current transport on the EL properties of Si^+-implanted SiO_2 films have been investigated. It is observed that the EL intensity increases with the Si ion dose and/or the implantation energy, due to the enhanced current transport. Thermal annealing has been also found to increase the EL intensity for both Si^+-implanted SiO_2 and Si^+-implanted Si_3N_4. The Si^+-implanted Si nitride films have been demonstrated to emit strong light emission covering the whole visible wavelength range from red to violet depending on the annealing temperature. The EL mechanisms for the Si^+-implanted SiO_2 and Si_3N_4 have been discussed.

CHAPTER 6 ELECTRICAL PROPERTIES OF SI NANOCRYSTALS EMBEDDED IN SIO2 FILMS

6.1 Introduction

While the optical properties and their photonic applications of Si nanocrystals embedded in dielectric films films are intensively investigated, the electrical properties of such structures are receiving increasing research interest due to the potential application in nanocrystal-based non-volatile memory (NVM) devices. The Si nanocrystals embedded in the gate oxide serve as a potential substitute for bulky floating gate in a conventional non-volatile memory cell. The driving force of such memory device structure is derived from the short comings of the electrical erasable programmable read-only memory (EEPROM) where dissipation of heat, charge loss, and switching speed are becoming more critical performance parameters in high-speed electronics [272]. If the floating gate is small enough for the storage of one electron at a time, the mentioned problems will be solved. This leads to the idea of single electron memory devices with quantum floating gate, which employs Si nanocrystal as the charge storage node. Although the effect of single electron tunneling (SET) are most often observed at ultra low temperatures (<77 K) [272], the room temperature SET effect has been frequently observed from Si quantum dot transistors [273, 274]. The single electron charging phenomenon is a manifestation of the Coulomb blockade (CB) effect, which is due to the discrete changes in the charging energy of an-ultra small capacitor [272]. For application in the quantum dot memory devices, a

better understanding of charge trapping and carrier transport in SiO_2 matrix containing Si nanocrystals is thus very necessary. In this chapter, current-voltage (*I-V*), capacitance-voltage (*C-V*), and conductance-voltage (*G-V*) measurements are used to investigate the charge storage and charge transport properties of MOS structures with Si nanocrystals embedded in the gate oxide. The charge mechanisms are investigated with XPS studies.

6.2 Electrical Characterizations

Si nanocrystals have been shown to exhibit charging and discharging effect, which induce the threshold voltage shift due to charge trapping and detrapping using different voltage polarities. For a better understanding in the memory characteristics of the MOS structure with Si nanocrystals embedded in the gate oxide, the investigation on electrical properties (i.e., flatband voltage shift and tunneling current) of the MOS capacitor are indispensible to be explored. In this section, memory effects of nc-Si embedded in SiO_2 thin films synthesized with low energy Si implantation followed by subsequent annealing are investigated by *I-V*, *C-V*, and *G-V* measurements.

6.2.1 Sample Fabrication and Experiments

SiO_2 films were thermally grown to the thickness of 30 nm in dry oxygen at 950 ºC on *n*-type (100) oriented Si wafers. Ion-implantation technique is used to introduce Si ions into SiO_2 thin film. The ion implantation was carried out at 10 keV with a dose of 3×10^{16} cm^{-2}. About one quarter of each of the wafers was not implanted with Si^+ ions where there is only the conventional pure SiO_2 thin

film on the Si substrate. After the implantation, thermal annealing was carried out at 1000 ^{o}C in N_2 ambient for 1 hour to induce nc-Si formation. Figure 6.1 shows the cross-sectional high-resolution TEM image of the nc-Si embedded in the SiO_2 matrix. The size of the nanocrystal is ~4.5 nm in diameter. A 20-nm layer of aluminum was then deposited onto the wafer surface and pattered to define the gate array. The backside of the wafers was coated a layer of aluminum with the thickness of about 1 μm after removing the backside oxide. Finally, metal alloy process was conducted at 425 ºC in N_2 ambient to form ohmic contacts. Current-voltage (*I-V*) measurement was performed with a Keithley 4200 semiconductor characterization system while the capacitance-voltage (*C-V*) and conductance-voltage (*G-V*) measurements were performed at 1 MHz with a HP4284A LCR meter.

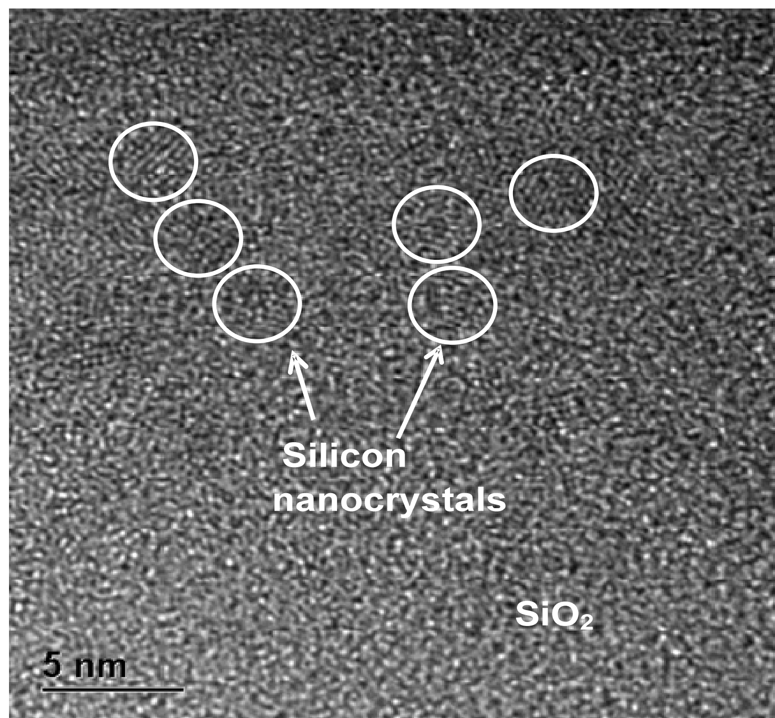

Figure 6.1 TEM image of the nc-Si embedded in a SiO_2 thin film.

6.2.2 Results and Discussion

The *C-V* and *G-V* measurements were carried out simultaneously with a small ac signal (15 mV). As can be seen in Fig. 6.2, during the continuous *C-V* measurement (i.e., the voltage sweeps from -5 V to +5 V and then from +5 V to -5 V), a hysteresis effect can be observed, showing a net electron charging effect during the electrical measurement. In addition, a strong conductance peak close to the flatband voltage is also observed during the *G-V* measurement, indicating the existence of tunneling paths formed by Si nanocrystals and/or defects between the gate and Si substrate [255]. The conductance peak indicates that charge detrapping out from the nanocrystals, resulting in many unblocked tunneling paths which enhance the conductance of the MOS capacitor. The change in the conductance peak (ΔG_{max}) measured before and after the stress is found to vary with the charging voltage. The flatband voltage shift and the ΔG_{max} can be determined simultaneously from the *C-V* and *G-V* measurements.

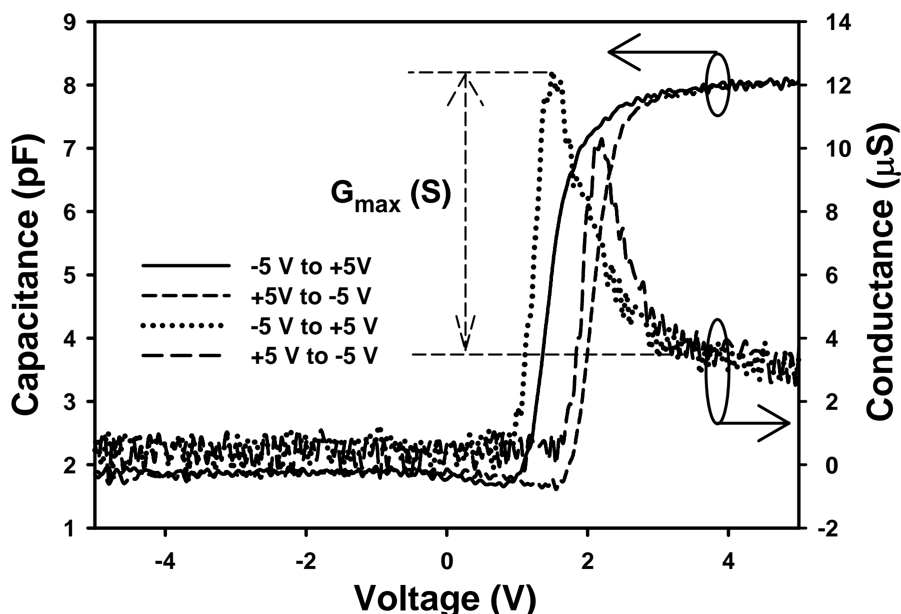

Figure 6.2 *C-V* and *G-V* characteristics for the voltage sweeping from -5 V to +5 V and then from +5 V to – 5V.

Figure 6.3 shows the flatband voltage shift (ΔV_{fb}) as a function of the positive stress voltage for a stress time of 50 s and 70 s. The ΔV_{fb} is the difference in the threshold voltage (V_{fb}) between after stress and before stress. For the positive voltage stress, a negative flatband voltage shift is observed when the stress voltage is larger than ~6 V. The negative flatband voltage shift indicates a net positive charging in the nc-Si. The negative flatband voltage shift could be attributed to the electrons tunneling out from the nc-Si under a high positive gate voltage.

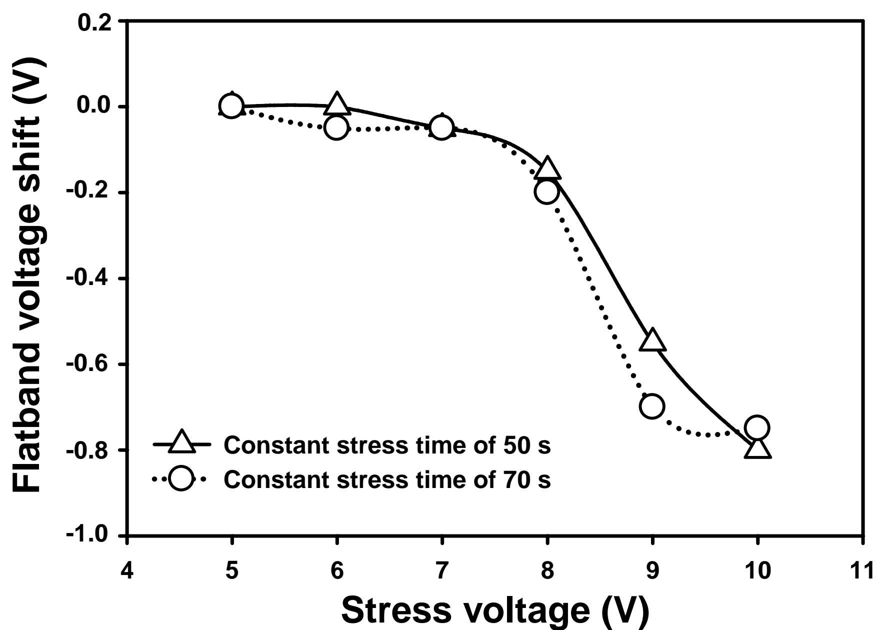

Figure 6.3 Flatband voltage shift as a function of positive stress voltage.

However, for negative voltage stress, a very small flatband voltage fluctuation (0 V to -0.05 V) is observed, as shown in Fig. 6.4. The insignificant change in the flatband voltage should be due to the fact that the nc-Si distributed very near the SiO_2/Si interface can easily communicate with the Si substrate, and thus, there is no significant charging in the gate oxide under a negative gate voltage. Another possible reason is that the gate current is extremely low due to the

insufficient hole injection from the *n*-type Si substrate. Therefore, the charging effect is too insignificant to be reflected in the flatband voltage shift.

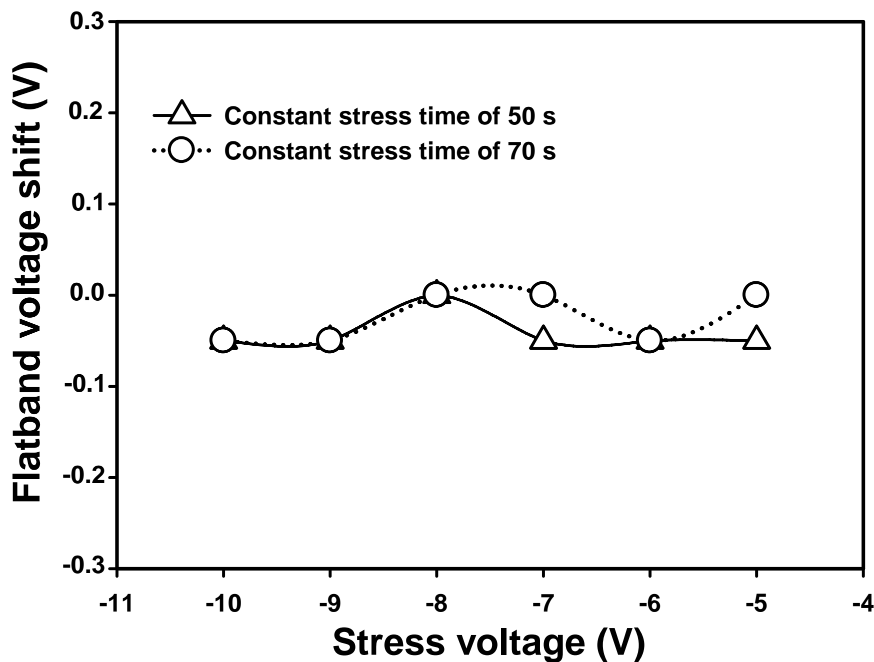

Figure 6.4 Flatband voltage shift as a function of negative stress voltage.

Similarly, the conductance of the film containing Si nanocrystals can be also changed by applying a constant electrical stress. Figure 6.5 shows the change in the conductance peak (ΔG_{max}) after positive voltage stress for 50 s and 70 s. As can be seen in Fig. 6.5, for the positive voltage stress, the ΔG_{max} shows an increase with the increasing stress voltage. The increase in the conductance peak suggests the release of the electrons trapped in the nanocrystals under the influence of a high positive gate voltage. The release of the trapped electrons leads to an increase in the number of neutral nanocrystals. As more neutral nanocrystals contribute to formation of tunneling paths, the conduction peak is enhanced.

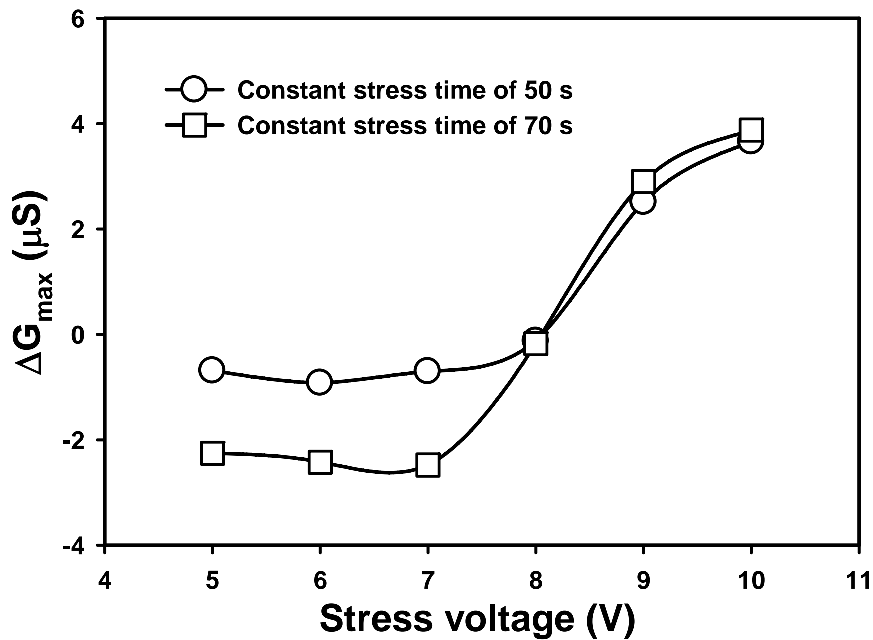

Figure 6.5 Change in conductance peak (G_{max}) as a function of positive stress voltage.

In contrast, as shown in Fig. 6.6, for the negative voltage stress, there are no significant changes in the ΔG_{max}. This is similar to the stress voltage dependence of the flatband voltage shift. This means that no significant charging/discharging in the nc-Si takes place during the application of a negative gate voltage, which is consistent with the insignificant change in the flatband voltage shown in Fig. 6.4. This should be also because the extremely low current when applying a negative stress voltage due to the insufficient hole injection from the *n*-type Si substrate.

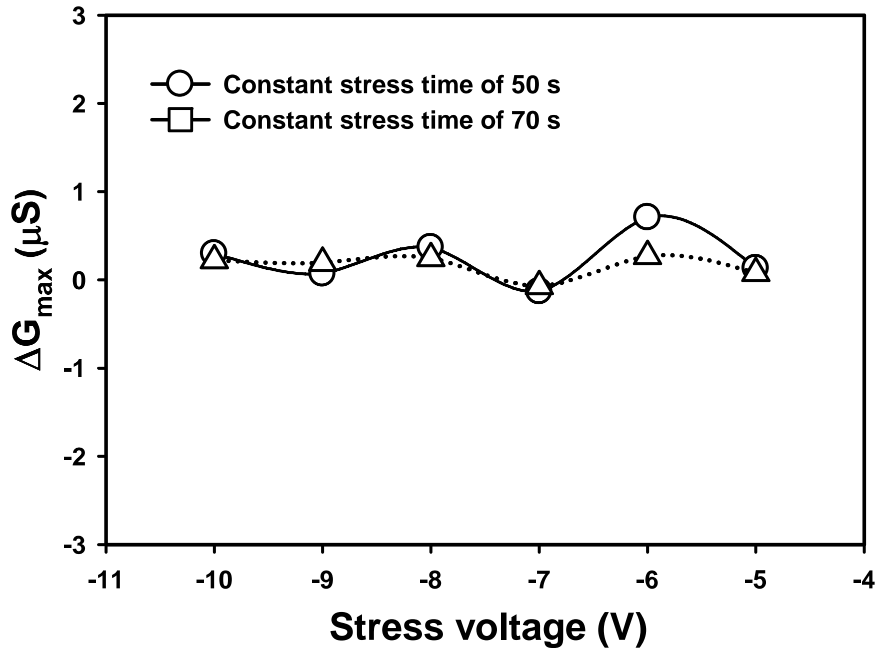

Figure 6.6 Change in conductance peak (G_{max}) as a function of negative stress voltage.

It is also important to examine the flatband voltage shift under a short pulse of charging voltage as the ability to program the device at a fast speed is essential for memory operations. Figure 6.7 shows the flatband voltage shift after a positive voltage stress of 9 V with different stress durations ranging from 1 μs to 10 s. Although the flatband voltage shift is small (-0.05 V to -0.1 V), the negative shifts indicate that there is still some net positive charging in the nc-Si. The shift increases with the stress duration. However, the shift for the duration of 10 s is still much smaller as compared with the shifts shown in Fig. 6.3 for the stress duration of 50 s. The very long charging time is due to the fact that the nc-Si is distributed very near the SiO_2/Si interface and thus is easy to discharge.

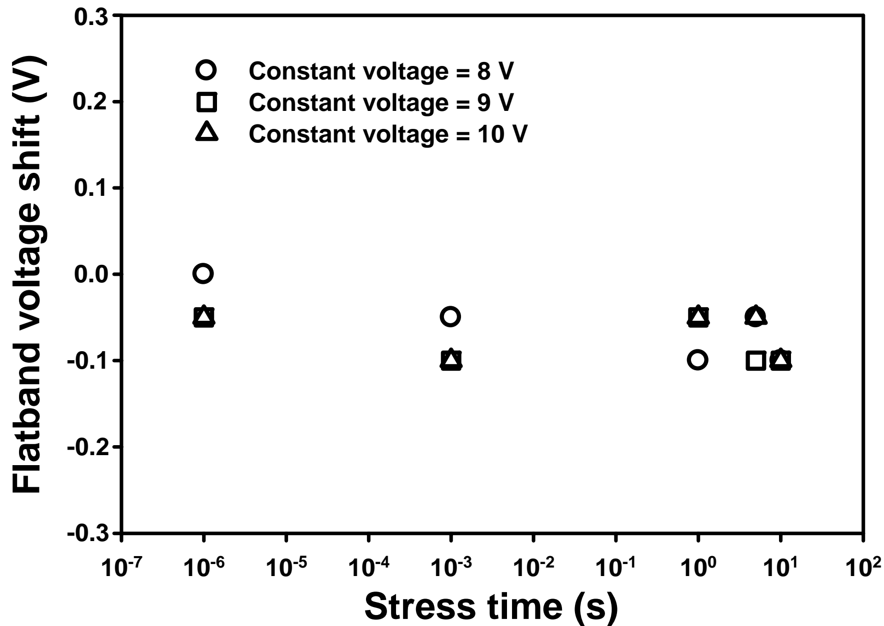

Figure 6.7 Flatband voltage shift as a function of stress time under positive voltage.

Another important observation is that the breakdown of the gate oxide containing nc-Si is reflected in the *G-V* characteristic. Figure 6.8 shows the *G-V* characteristics before and after the positive voltage stress of 14 V for 70 s. Before the stress, there is a normal conductance peak in the *G-V* characteristic, and the *I-V* characteristic is similar to that of a pure SiO_2 film as shown in the inset of Fig. 6.8. However, after the stress, there is a continuous increase in the conductance and the conductance is much larger than that before the stress. Accordingly, there is a drastic increase in the current, and the *I-V* characteristic after stress follows a power law, as shown in the inset of Fig. 6.8. The power-law *I-V* characteristic is a typical behavior of dielectric breakdown of SiO_2 thin film [275]. The conductive breakdown paths lead to a large increase in the conductance and thus the current. It can be concluded from Fig. 6.8 that the change in the *G-V* characteristic is a symptom of the dielectric breakdown.

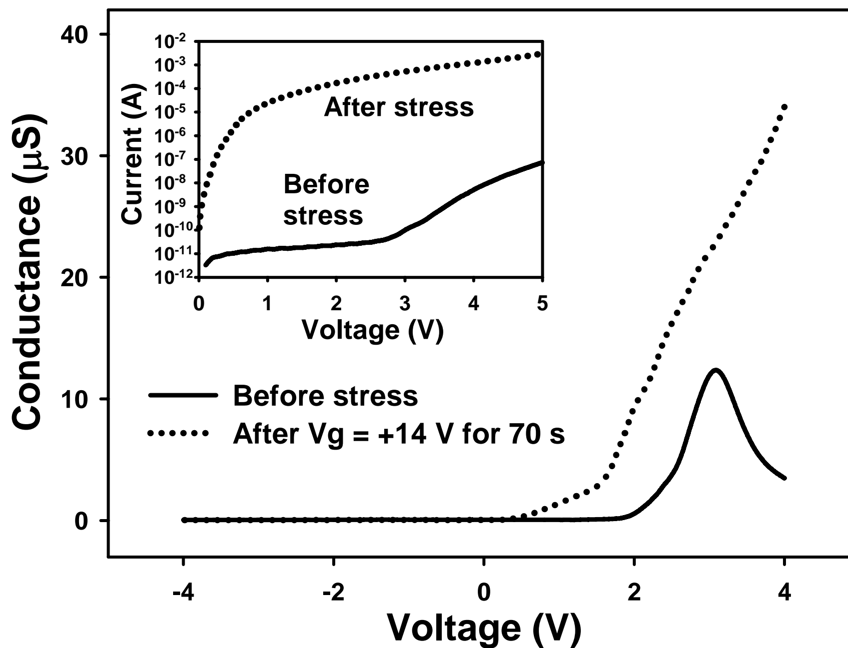

Figure 6.8 *G-V* characteristics before and after dielectric breakdown of the gate oxide containing Si nanocrystals. The breakdown is caused by the positive stress at 14 V for 70 s. The inset shows the corresponding *I-V* characteristics before and after the breakdown.

In contrast to the significant change of the *G-V* curve after dielectric breakdown, the breakdown is not easily observed in the *C-V* characteristic. As shown in Fig. 6.9, the breakdown causes a small shift in the *C-V* characteristic similar to the situation that the MOS capacitor has experienced a normal stress that cannot induce dielectric breakdown. However, it is observed that the accumulation capacitance increases by an observable magnitude after the stress of 14 V for 70 s, as shown in Fig. 6.9. The increase in the accumulation capacitance cannot be observed in a MOS capacitor that has not experienced dielectric breakdown. The enhancement in the accumulation capacitance can be attributed to the increase in the conductance of the gate oxide due to the dielectric breakdown. It can be explained as follows. For a single uncharged nc-Si, it has a capacitance of C_{ncj}, and electrons can tunnel into or off it via the tunneling paths. Its resistance to the gate and the substrate is represented by R_1^j

and R_2^j, respectively. Thus the equivalent circuit of a single uncharged nc-Si can be shown as in left of Fig. 6.10. To relate the nc-Si to an actual capacitance measurement, this equivalent circuit can be converted into a frequency-dependent capacitance $C_p^j(\omega)$ in parallel with a frequency-dependent conductance $G_p^j(\omega)$, as shown in the right of Fig. 6.10, where $C_p^j(\omega) = \frac{C_{nc}^j}{1+[\omega(R_1^j + R_2^j)C_{nc}^j]^2}$ and $G_p^j(\omega) = \frac{(\omega C_{nc}^j)^2 (R_1^j + R_2^j)}{1+[\omega(R_1^j + R_2^j)C_{nc}^j]^2}$. With all the uncharged nc-Si embedded in the SiO_2 matrix taken into account, the total frequency-dependent capacitance $C_p(\omega) = \sum_{j=1}^{N} C_p^j(\omega)$ and the total frequency-dependant conductance $G_p(\omega) = \sum_{j=1}^{N} G_p^j(\omega)$, where N is the number of the uncharged nc-Si in the SiO_2 matrix. Therefore, both the capacitance and conductance of the gate oxide are affected by the charging and discharging in the nc-Si. Before dielectric breakdown, many of the nc-Si are charged up, the resistance (R_1^j and R_2^j) of individual nc-Si could be high due to the blockage of tunneling paths, and thus the total resistance of the gate oxide is high, while the total capacitance $C_p^j(\omega)$ is small. However, after dielectric breakdown when most of the nc-Si are discharged, the resistance (R_1^j and R_2^j) of individual nc-Si could be low due to the existence of tunneling paths which attribute to the significant enhancement of the gate current. Therefore, the low resistance of the nc-Si leads to a high total capacitance $C_p(\omega)$. Thus the increase in the capacitance after dielectric breakdown shown in Fig. 6.9 is just the consequence of the decrease in the resistance shown in the insect in Fig. 6.8.

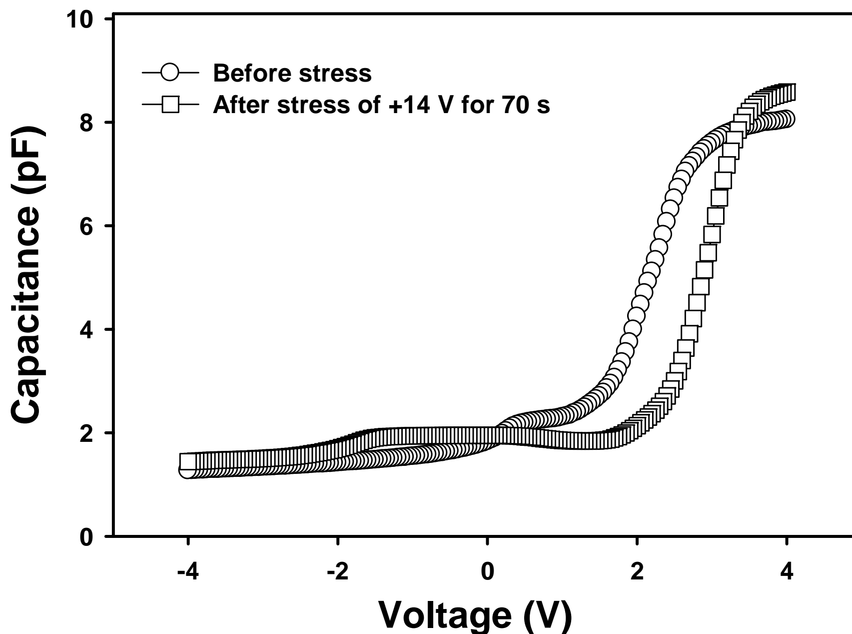

Figure 6.9 *C-V* characteristics before and after dielectric breakdown of the gate oxide containing Si nanocrystals. The breakdown is caused by the positive stress at 14 V for 70 s.

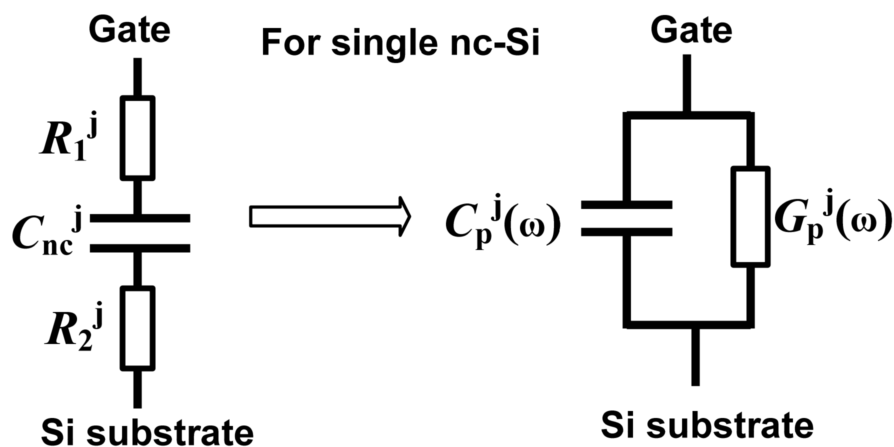

Figure 6.10 Equivalent circuit of a single nc-Si and the conversion to a frequency-dependent capacitance $C_p^j(\omega)$ in parallel with a frequency-dependent conductance $G_p^j(\omega)$.

6.2.3 Conclusion

In conclusion, the electrical properties of nc-Si embedded in SiO_2 have been studied. The relationships between the flatband voltage shift and the change in

the conductance peak (G_{max}) under a positive or negative voltage stress have been investigated. Both the flatband voltage shift and the change in the conductance peak are sensitive to only the positive voltage stress. The influence of stress duration on the flatband voltage shift has been studied. In addition, it has been observed that the dielectric breakdown of the gate oxide containing nc-Si is reflected in the *I-V*, *C-V*, and *G–V* characteristics.

6.3 Charging Mechanism

For the nonvolatile memory application, the nc-Si is normally confined in a narrow layer in the gate dielectric near the substrate. Charging/discharging the nc-Si leads to the flat-band voltage shifts, yielding two distinguishable memory states. There have been many studies on the nc-Si nonvolatile memory devices. However, there are few experimental studies so far on the charging mechanism of the nc-Si/SiO_2 system. It is still in doubt that whether the charging mainly occurs at the nc-Si/SiO_2 interface or inside the nc-Si. In this section, x-ray photoelectron spectroscopy (XPS) experiment is carried out on the system of nc-Si embedded in SiO_2 thin films synthesized by Si ion implantation followed by thermal annealing. During the XPS measurements, x-rays generate the photoelectrons leaving positive charges inside the sample. The C 1s core level is due to the carbon contamination, which exists at the oxide surface. In the system of SiO_2 films embedded with nc-Si, the shift in the C 1s core level can only be induced by the charging effect caused by x-ray irradiation during the XPS measurements. Therefore, the C 1s core level on the surface due to

contamination is used to monitor the charging effect, while the Si 2p peaks are analyzed to obtain the information of the concentrations of the nc-Si (Si^0) and the Si suboxides (Si^{1+}, Si^{2+}, and Si^{3+}) that exist at the nc-Si/SiO_2 interface. By examining the changes of the charging effect and the concentrations of the nc-Si and the Si suboxides with thermal annealing, one may be able to answer the question that whether the nc-Si or the nc-Si/SiO_2 interface plays a dominant role in the charging effect.

6.3.1 Sample Fabrication and Experiments

SiO_2 thin films of 30 nm in thickness were grown on *p*-type Si wafers with (100) orientation by thermal oxidation in dry oxygen at 950 ^oC. Then Si ions were implanted into the SiO_2 films with the dose of 8×10^{16} cm^{-2} at 1 keV. Thermal annealing was carried out in N_2 ambient. For the experiment of annealing temperature, the temperature was varied from 700 to 1100 C° while the annealing time was fixed at 20 min; for the experiment of annealing time, the time was varied from 0 to 100 min while the annealing temperature was kept at 1000 ºC. XPS experiment was performed by using a Kratos AXIS spectrometer with monochromatic Al Kα (1486.71 eV) X-ray radiation. Si 2p spectra were taken to study the changes in the concentrations of five Si oxidation states. C 1s spectra due to the surface carbon contamination were also recorded to monitor the x-ray-induced charging effect in the samples.

6.3.2 Results and Discussion

It has been known that x-ray irradiation can cause charging in both SiO_2/Si system [276] and nc-Si/SiO_2 system [67, 277]. For the system of nc-Si embedded in a SiO_2 matrix, photoemission may leave positive charges in the nc-Si and SiO_2 as well as at the nc-Si/SiO_2 interface, leading to a core-level shift to a higher binding energy. The C 1s core level shift shown in Fig. 6.11 is an indicator of the charging effect. The C 1s core level on pure SiO_2 surface has a shift of ~0.8 eV relative to the C 1s reference, while it shows shifts of ~2.1 eV and ~1.6 eV for the as-implanted sample and the sample annealed at 1100 °C for 20 min, respectively. This indicates that the charging effect is greatly enhanced by the introduction of nc-Si into the SiO_2 matrix. The reduction of the charging effect of the annealed sample is mainly attributed to the reduction of the nc-Si concentration due to the surface oxidation, as discussed later.

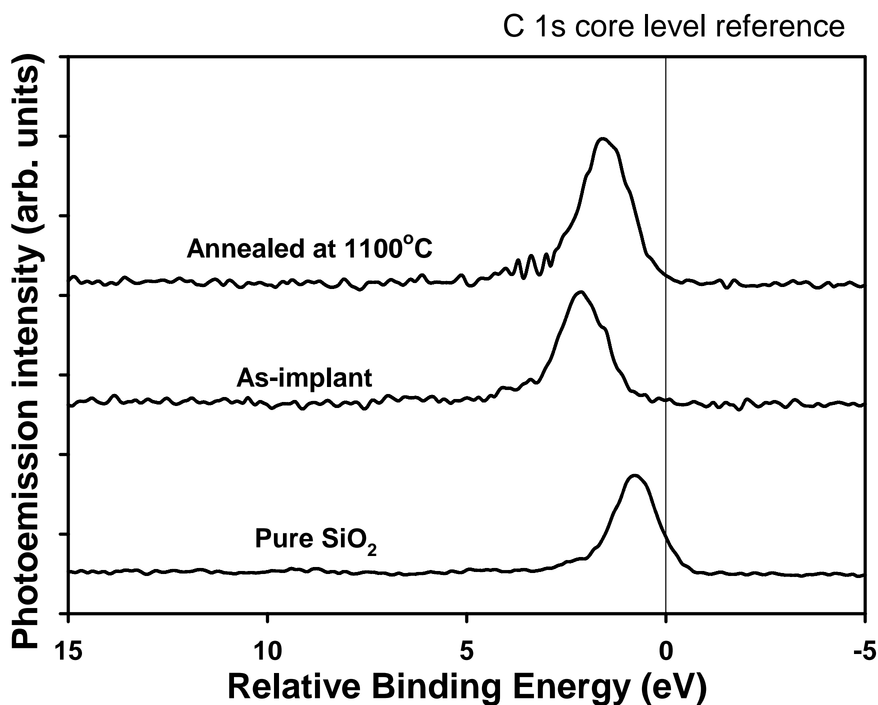

Figure 6.11 C 1s core level shift relative to the reference for the pure SiO_2 sample, the as-implanted sample and the sample annealed at 1100 °C for 20 min.

Figure 6.12(a) and (b) show the XPS Si 2p core level peaks for the as-implanted and the sample annealed at 1100 °C for 20 min, respectively. Five oxidation states Si^{n+} (n = 0, 1, 2, 3, and 4) could exist in the Si-implanted SiO_2 films [67, 277]. Here Si^0 and Si^{4+} correspond to the nc-Si and SiO_2, respectively, while Si^{n+} (n =1, 2, and 3) corresponds to the Si suboxides (Si_2O, SiO and Si_2O_3) which exist at the nc-Si/SiO_2 interface. A curve fitting to the Si 2p core level peaks is carried out by decomposing the spectrum into the Si $2p_{1/2}$ and $2p_{3/2}$ partner lines for the five oxidization states. The spin-orbit splitting is fixed at 0.6eV and the Si $2p_{1/2}$ and $2p_{3/2}$ intensity ratio is set to ½ for all of the five oxidation states [278]. Only the sum of the Si $2p_{1/2}$ and $2p_{3/2}$ partner lines is shown in Fig. 6.12 for a clear presentation. As can be observed in Fig. 6.12, the peak areas of the five oxidation states change with annealing, showing that the concentrations of the five oxidation states vary with the annealing. The relative concentration of each oxidation state can be obtained by calculating the ratio of $\frac{I_{Si^{n+}}}{I_{total}}$ (n= 0, 1, 3, and 4), where $I_{Si^{n+}}$ is the peak area of the oxidation state Si^{n+} and I_{total} is the total area ($=\sum_{i=0}^{4} I_{Si^{n+}}$) of the Si 2p peaks. It can be observed from Fig. 6.12 that after the annealing at 1100°C for 20 min, the SiO_2 (Si^{4+}) concentration increases, while the concentrations of both the Si suboxides (Si^{1+} ,Si^{2+} and Si^{3+}) at the interface and the nc-Si (Si^0) decrease. The reduction of the suboxides is due to the thermal decomposition of the suboxides. The thermal decomposition during the annealing is to form stoichiometric SiO_2 and Si nanocrystals [277]. In other words, the thermal decompositions lead to the growth of both SiO_2 and the nc-Si. However, although the annealing was carried

out in nitrogen gas with purity more than 99.99%, there is some residual oxygen presented in the furnace, and some of the nc-Si is oxidized during the annealing. Therefore, the Si^0 concentration decreases while the Si^{4+} concentration increases after the annealing.

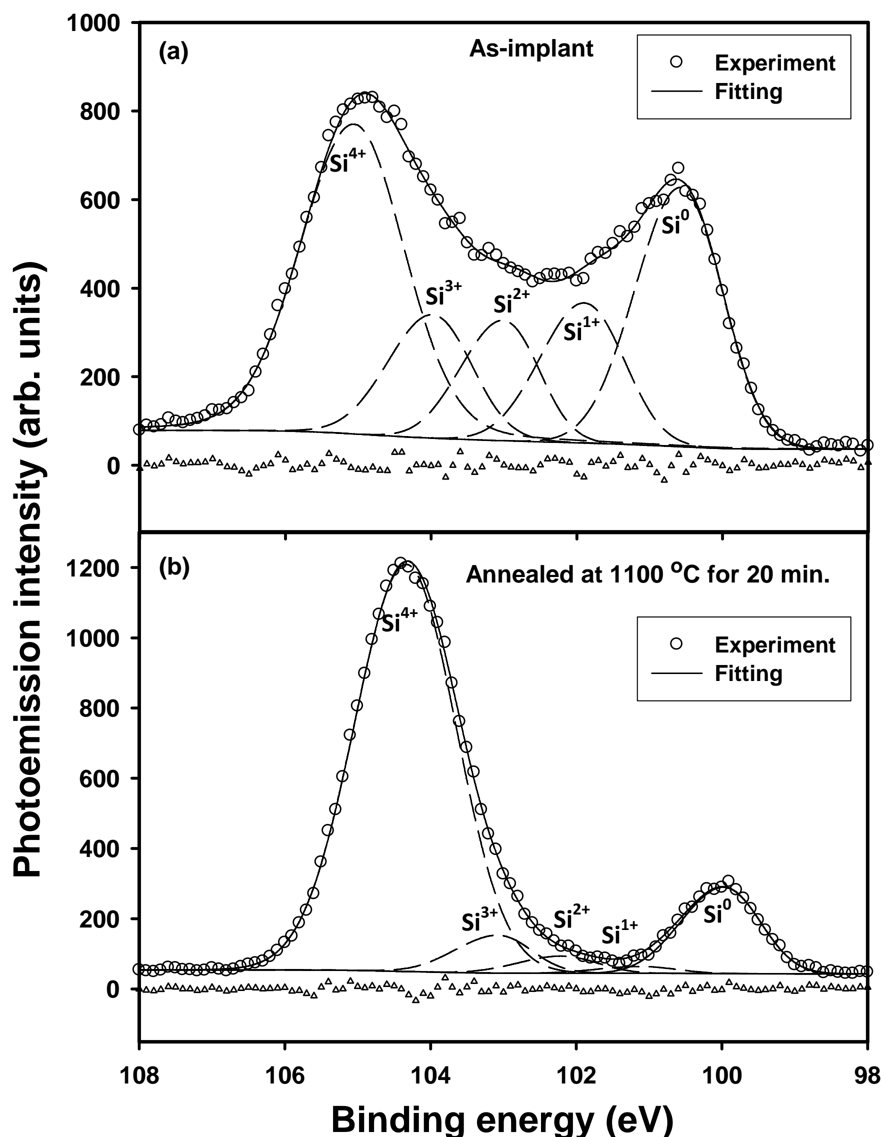

Figure 6.12 The decomposition of Si 2p spectra for the as-implanted sample (a) and the sample annealed at 1100 °C for 20 min (b). The unfilled triangles represent the difference between the measurement and the fitting.

Figure 6.13 (a), (b), and (c) show the C 1s shift, the total concentration ($\frac{\sum_{i=1}^{3} I_{Si}}{I_{total}}$) of the interfacial suboxides, and the nc-Si concentration as a

function of the annealing temperature, respectively. The annealing time is fixed at 20 min. The C 1s shift decreases with annealing temperature, showing that the charging effect is reduced by annealing. However, it should be noted that the reduction of the charging effect is not drastic. For example, the C 1s shift decreases from ~2.1 eV of the as implanted sample to ~1.6 eV of the sample annealed at 1100 °C for 20 min. The shift of 1.6 eV is still much larger than that (0.8 eV) of pure SiO_2 sample, indicating that the system of nc-Si embedded in SiO_2 maintains a good charge storage capability. The total concentration of the interfacial suboxides and the nc-Si concentration both decrease with annealing temperature, as shown in Fig. 13(b) and (c), respectively. The decrease of the total concentration of the interfacial suboxides is attributed to the thermal decomposition of the suboxides, and the decrease of the nc-Si concentration is due to the oxidation of the nanocrystal by the residual oxygen during the annealing, as pointed out early. From a comparison among the annealing-temperature effects on the C 1s shift (Figure 6.13(a)), the total concentration of the interfacial suboxides (Figure 6.13(b)) and the nc-Si concentration (Figure 6.13(c)), one may conclude that the nc-Si plays a more important role in the charging effect than the nc-Si/SiO_2 interface. For example, with a reference to the as-implanted sample, the annealing at 700 °C causes a relative reduction (in percentage) of ~10% in the C 1s shift, ~25% in the nc-Si concentration, and ~55% in the total concentration of the interfacial suboxides. The reduction of the total concentration of the interfacial suboxides is much faster than that of both the C 1s shift and the nc-Si concentration, suggesting that the interface would not play a dominant role in the charging effect.

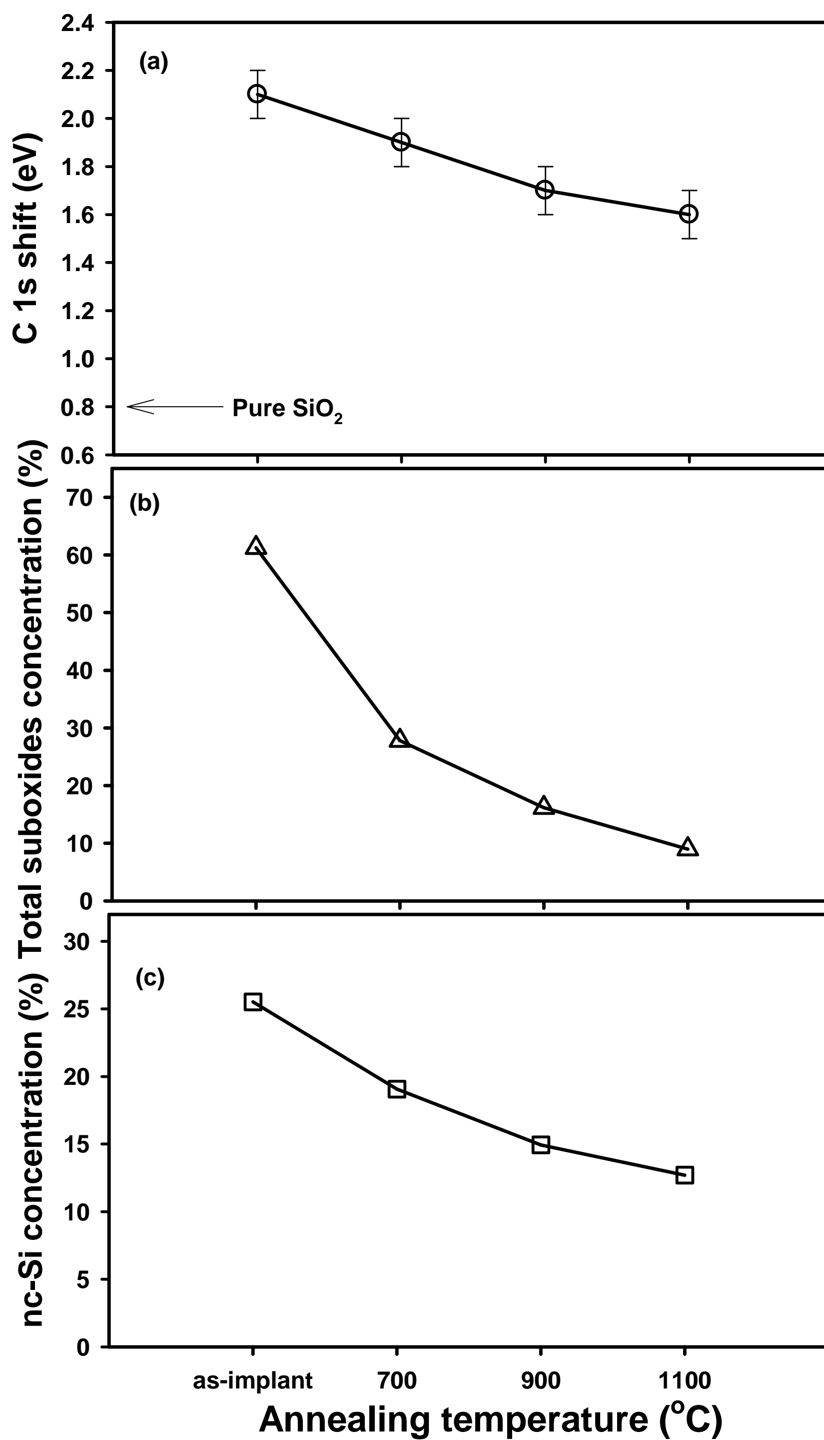

Figure 6.13 Annealing-temperature effect on C 1s core level shift (a), the total concentration of the interfacial suboxides (b) and the nc-Si concentration (c). The annealing duration is fixed at 20 min.

The conclusion that the nc-Si plays a more important role in the charging effect than the nc-Si/SiO_2 interface is further supported by the experiment of

annealing time shown in Fig. 6.14. The experiment was carried out at fixed temperature of 1000°C. As shown in Fig. 6.14(a), the total concentration of the interfacial suboxides is drastically reduced from ~60% for the as-implanted sample to ~10% after the annealing for 20 min and remains unchanged for prolonged annealing. However, as shown in Fig. 6.14(b), the C 1s shift is gently reduced from ~2.1 eV of the as-implanted sample to ~1.6 eV after the annealing for 20 minutes and remains at ~1.8 eV for prolonged annealing. Most importantly, the trend of the C 1s shift with annealing time coincides with that of the nc-Si concentration with annealing time, as shown in Fig. 6.14(b). This strongly suggests that the nc-Si plays a key role in the charging effect.

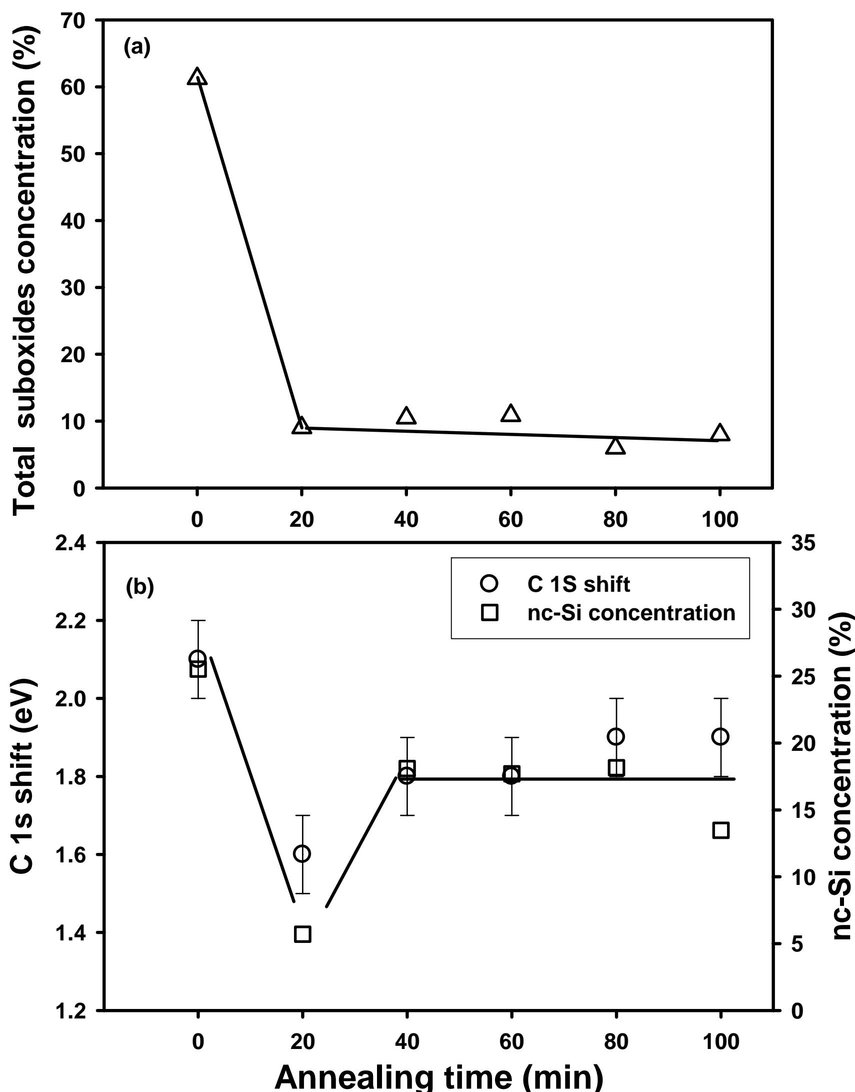

Figure 6.14 (a) The total concentration of the interfacial suboxides as a function of annealing time; and (b) the comparison between the nc-Si concentration and the C 1s core level shift as a function of annealing time. The annealing temperature is fixed at 1000 °C.

6.3.3 Conclusion

In conclusion, the experiments of annealing effects on the C 1s shift, the total concentration of the interfacial suboxides and the nc-Si concentration have been carried out. It is observed that the annealing-caused reduction of the total concentration of the interfacial suboxides is much faster than that of both the C 1s shift and the nc-Si concentration. In addition, the trend of the C 1s shift with

annealing time coincides with that of the nc-Si concentration with annealing time. The results suggest that the nc-Si rather than the nc-Si/SiO_2 interface plays the dominant role in the charging effect in the system of nc-Si embedded in SiO_2.

6.4 Summary

In this chapter, electrical properties of MOS capacitors with Si nanocrystals embedded in the gate oxide synthesized by Si ion implantation have been investigated with *I-V*, *C-V*, and *G-V* characteristics. The influence of stress voltage on the flatband voltage shift and the conductance peak has been studied. The electrical properties of the MOS capacitor after dielectric breakdown have been investigated. In addition, charging mechanism of nc-Si has been investigated by XPS studies. The concentrations of both the nc-Si and the Si suboxides that exist at the nc-Si/SiO_2 interface have been determined as a function of thermal annealing, and the charging effect has been also measured by monitoring the shift of the surface C 1s peak. Si 2p peaks are analyzed to obtain the information of the concentrations of the nc-Si (Si^0) and the Si suboxides (Si^{1+}, Si^{2+}, and Si^{3+}) that exist at the nc-Si/SiO_2 interface. It has been observed that the annealing-caused reduction of the total concentration of the interfacial suboxides is much faster than that of both the C 1s shift and the nc-Si concentration. Furthermore, the trend of the C 1s shift has been found to coincide with that of the nc-Si concentration. The results suggest that the nc-Si, rather than the nc-Si/SiO_2 interface, plays the dominant role in the charging effect.

CHAPTER 7 CONCLUSION AND RECOMMENDATIONS

7.1 Conclusion

This thesis is concerned with the synthesis, characterization, and device application of Si nanocrystals embedded in dielectric films, which have potential applications in Si-based photonic and non-volatile memory devices with the advantage of being fully compatible with modern CMOS technology. Besides the synthesis of the films embedded with Si nanocrystals, investigations on the optical and optoelectronic properties of Si nanocrystals embedded in dielectric matrix have been carried out. This section briefly summarizes the overall work presented in this thesis.

7.1.1 Dielectric Functions

A non-destructive method based on ellipsometric measurements and EMA theory has been developed to experimentally determine the optical constants and dielectric functions of Si nanocrystals isolated in SiO_2 matrix. Bandgap and static dielectric constant of nc-Si are also obtained in the spectroscopic ellipsometry studies thanks to the Forouhi-Bloomer optical dispersion equations. The nc-Si shows a significant reduction in the optical constants and dielectric function as compared to bulk crystalline silicon, being consistent with the first-principle calculation of the optical gap of Si nanocrystals based on

quantum confinement effect. Thermal annealing effect on the bandgap and dielectric functions of nc-Si embedded in a SiO_2 matrix has been investigated also. Annealing results in a small change in the static dielectric constant and a slight increase in the bandgap which can be explained in terms of the size effect. The dielectric functions of densely-stacked nc-Si layer embedded in SiO_2 have been investigated with SE analysis. The results have been compared with the dielectric functions of isolated nc-Si dispersed in SiO_2. In addition, the influence of nanocrystal size on dielectric functions of the nc-Si is investigated with SE. Based on the nc-Si optical constants determined by SE studies, the depth profiling of optical constant of SiO_2 thin films containing Si nanocrystals synthesized by Si ion implantation have been calculated. The result shows that such a structure containing nc-Si in SiO_2 film with a proper nc-Si distribution has a graded optical-constant profile which can offer light-trapping ability and thus the possibility of wave guiding.

7.1.2 PL Properties

Light emission properties of Si nanocrystals embedded in dielectric films have been investigated. Thermal annealing has been found to significantly change the PL spectral shape and enhance the PL intensity from Si^+-implanted SiO_2 films. The annealing at 1100 ^oC yields the strongest PL band which is attributed to the indirect band-to-band transition of the nc-Si assisted by the Si-O vibration at the nc-Si/SiO_2 interface. The PL peak position has been found to redshift with the increasing size of Si nanocrystals. The similar size effect on the PL emission peak has also been found for the PECVD grown SiO_2 embedded with Si

nanocrystals. In addition, the PL properties Si nanocrystals embedded in Si_3N_4 have also been investigated. Short-wavelength light emission has been realized with the Si nitride embedded with nc-Si. The PL mechanisms have been discussed.

7.1.3 EL Properties

Besides the PL properties of Si nanocrystals embedded in dielectric matrix, the EL properties have been investigated systematically. The MOS-like light-emitting structures have been fabricated with various Si ion doses under different implantation energies. Strong EL emission from the structure for both Si^+-implanted SiO_2 and Si_3N_4 has been demonstrated. Thermal annealing effect on the EL properties has been studied. The influence of implantation dose and energy on the EL properties of Si^+-implanted SiO_2 films has been investigated. It is observed that the EL intensity increases with the Si ion dose and/or the implantation energy, due to the enhanced current transport. Using Si nitride as the dielectric matrix to host Si nanocrystals, we have fabricated LEDs that emit light covering the whole visible wavelength range from red to violet. The EL mechanisms have been discussed for both the Si^+-implanted SiO_2 and Si^+-implanted Si_3N_4.

7.1.4 Electrical Properties and Charging Mechanism

For the application in non-volatile memory devices, charging and discharging

effect of Si nanocrystals embedded in the gate oxide of a MOS capacitor have been investigated. *I-V*, *C-V*, and *G-V* characteristics have been studied to investigate the electrical properties of SiO_2 films embedded with Si nanocrystals. The flatband voltage shift and the conductance peak have been found to be affected by both the stress voltage and stress time. The electrical behavior of the MOS capacitor after dielectric breakdown has been investigated by *I-V*, *C-V*, and *G-V* characteristics. It is still under controversial that the charging effect mostly takes place inside the nc-Si or at the nc-Si/SiO_2 interface. This question has been investigated by XPS studies in Chapter 6. The shift of the surface C 1s peak obtained from the XPS spectra has been used to monitor the charging effect. The evolution of the C 1s shift with annealing time has been found to be very similar with that of the nc-Si concentration with annealing time. This is an important indicator that the nc-Si rather than the nc-Si/SiO_2 interface plays the dominant role in the charging effect in the system of nc-Si embedded in SiO_2.

7.2 Recommendations

Working in the silicon nanoscience and nanotechnology, we have progressed quite a bit in the area of Si nanocrystals and their applications in light emitting devices and non-volatile memory devices. However, everyone is doing bits and pieces, and it is not a large comprehensive study. To make the study more complete and comprehensive, the following recommendations are proposed to extend the research on Si nanocrystals.

7.2.1 First-Principle Calculation

First-principle calculation is a useful method to predict optical and electrical properties of nanoscaled materials. Future work should include first-principle calculations to determine the band gap expansion, dielectric suppression of nc-Si. The calculation results should be compared with the experimental results obtained in this work.

7.2.2 Si Nanocrystal Based Laser

An all silicon Raman laser has been proposed and realized by Rong *et al.* [177, 178], which is an important step and breakthrough towards the goal of fabricating inexpensive on-chip light source. However, this laser is operated based on Raman Effect, which makes it difficult to realize efficient electrical pumping. With regard to this point, Si nanocrystals are considered very promising for the realization of an electrically pumped Si laser. There are a lot of scientific and technological problems to be solved before the first demonstration of Si nanocrystal based laser. The first issue is that we need to have a systematic investigation on the optical gain of Si nanocrystals embedded in the dielectric matrix. Another important issue is the structure design of the laser cavity. In order to make a laser, we need to put the optical gain materials in a cavity structure. Distributed Bragg reflector (DBR) is a good candidate for this purpose. The cavity structure design consists of many aspects, such as material selection in the period structure, simulation of reflectivity, understanding the optical loss mechanism of the cavity, and so on.

7.2.3 Memory Devices Based on Si nanocrystals

For memory applications of Si nanocrystals, MOSFETs with gate oxide containing nc-Si in a narrow layer should be fabricated. We need to optimize the implantation recipe to ensure a better device performance. For example, to allow faster memory operation, the tunnel oxide must be reduced without degrading the charge retention characteristics. A possible strategy is the employment of high-K dielectrics as the tunnel oxide [279]. Single electron transistor (SET) should be fabricated for the investigation of single electron tunneling effect. In addition, room temperature and low temperature (i.e., <77 K) electrical experiments should be carried out to under mechanism of charging/discharging effect and current transport in dielectric films embedded with Si nanocrystals.

7.2.4 Photon-Programmed Si nanocrystal Memory

Ge nanocrystals embedded in SiO_2 matrix have been shown to exhibit charging/discharging effect by UV illumination [280]. It is reasonable to expect that Si nanocrystals also have photon-induced charging/discharging effect. Therefore, it can have potential application in a photon programmed Si nanocrystal memory. The charging/discharging effect of Si or Ge nanocrystals induced by optical illumination observed recently is not stable and repeatable, because the charging/discharging effect caused by optical illumination is a random process. The most important issue for the memory operation is that the charging/discharging must be quick and stable enough as the speed is an

important parameter of a memory device. Therefore, the reliability of such an optical memory is a big issue to be addressed.

List of Publications

Journals:

(1) **L. Ding**, T. P. Chen, Y. Liu, C. Y. Ng, and S. Fung, "*Optical properties of silicon nanocrystals embedded in a SiO_2 matrix*", Physics Review B, Vol. **72**, pp. 125419 (2005).

(2) **L. Ding**, T. P. Chen, Y. Liu, C. Y. Ng, Y. C. Liu, and S. Fung, "*Thermal annealing effect and the band gap and dielectric functions of silicon nanocrystals embedded in SiO_2 matrix*", Applied Physics Letters, Vol. **87**, pp. 121903 (2005).

(3) **L. Ding**, T. P. Chen, Y. Liu, C. Y. Ng, and S. Fung, "*An approach to optical-property profiling of a planar-waveguide structure of Si nanocrystals embedded in SiO_2*", Nanotechnology, Vol. **16**, pp. 2657-2660 (2005).

(4) **L. Ding**, T. P. Chen, Y. Liu, and C. Y. Ng, "*Dielectric functions of SiO2 film embedded with Silicon nanocrystals*", Journal of Crystal Growth, Vol. **288**, pp. 87-91 (2006).

(5) **L. Ding**, T. P. Chen, J. I. Wong, M. Yang, Y. Liu, C. Y. Ng, Y. C. Liu, C. H. Tung, A. D. Trigg, and S. Fung, "*Dielectric functions of densely stacked Si nanocrystal layer embedded in SiO_2 thin films*", Applied Physics Letters, Vol. **89**, pp. 251910 (2006).

(6) **L. Ding**, T. P. Chen, M. Yang, J. I. Wong, Y. Liu, S. F. Yu, F. R. Zhu, M. C. Tan, S. Fung. C. H. Tung, and A. D. Trigg, "*Photon-induced conduction modulation in SiO_2 films embedded with Ge nanocrystals*", Applied Physics Letters, Vol. **90**, pp. 103102 (2007).

(7) **L. Ding**, T. P. Chen, Y. Liu, M. Yang, J. I. Wong, K. Y. Liu, F. R. Zhu, and S. Fung, "*The influence of the implantation dose and energy on the electroluminescence of Si^+-implanted amorphous SiO_2 thin films*", Nanotechnology, Vol. **18**, pp. 455306 (2007).

(8) **L. Ding**, T. P. Chen, Y. Liu, M. Yang, J. X. Fang, C. W. Giam, and S. Fung, "*Influence of nanocrystal size on optical properties of Si nanocrystals embedded in SiO_2 synthesized by Si ion implantation*", Journal of Applied Physics, Vol. **101**, pp. 103525 (2007).

(9) **L. Ding,** T. P. Chen, C. Y. Ng, M. Yang, J. I. Wong, F. R. Zhu, M. C. Tan, S. Fung, X. D. Chen, and Y. Huang, "*Evolution of photoluminescence mechanisms of Si^+- implanted SiO_2 films with thermal annealing*", Journal of Nanoscience and Nanotechnology, Vol. **8**, pp. 3555-3560 (2008).

(10) **L. Ding**, T. P. Chen, M. Yang, J. I. Wong, C. H. Cen, Y. Liu, I. P. Hui, F. R. Zhu, and Ampere A. Tseng, "*Relationship between current transport and electroluminescence in the system of Si^+-implanted SiO_2 thin film*", IEEE Transactions on Electron Devices, Under review.

Conferences:

(1) **L. Ding**, T. P. Chen, C.Y. Ng, and Y. Liu, "*Dielectric function of SiO_2 films embedded with silicon nanocrystals with different distributions*", 3rd International Conference on Materials for Advanced Technologies (ICMAT), Singapore (2005).

(2) **L. Ding**, T. P. Chen and Y. Liu, "*Optical Properties of Silicon nanocrystals embedded in SiO_2 Matrix*", 2005 NSTI Nanotechnology Conference and

Trade Show, USA, Proceedings of Nanotech 2005, Vol. 2, pp. 46-49 (2005).

(3) **L. Ding**, T. P. Chen, and C. Q. Sun, "*Dielectric functions of SiO_2 films containing silicon nanocrystals*", 211th Meeting of the Electrochemical Society, USA (2006).

(4) **L. Ding**, T. P. Chen, M. Yang, Y. Liu, Furong Zhu, and Candy Tan, "*Influence of thermal annealing on optical properties of densely stacked Si nanocrystals synthesized with low-energy ion implantation*", 4th International Conference on Materials for Advanced Technologies (ICMAT), Singapore (2007).

(5) **L. Ding**, T. P. Chen, Y. Liu, M. Yang, Furong Zhu, and Candy Tan, "*Random modulations in resistance and capacitance of SiO_2 films embedded with Ge nanocrystals induced by ultraviolet illumination*", 4th International Conference on Materials for Advanced Technologies (ICMAT), Singapore (2007).

(6) **L. Ding**, T. P. Chen, M. Yang, and F. R. Zhu, "Influence of nanocrystal distribution on electroluminescence from Si^+-implanted SiO_2 thin films", 2008 Photonics West, USA, Proceedings of SPIE, Vol 6898, pp. 68980H (2008).

(7) **L. Ding**, T. P. Chen, Y. Liu, and Y. C. Liu, "*A comparative study on the dielectric functions of isolated Si nanocrystals and densely-stacked Si nanocrystal layer embedded in SiO_2 synthesized with Si ion implantation*", 2008 Photonics West, USA, Proceedings of SPIE, Vol 6898, pp. 68980I (2008).

BIBLIOGRAPHY

[1] W. Shockley, "The theory of p-n junctions in semiconductors and p-n junction transistors," *Bell Syst. Tech. J.* vol. **28**, pp. 435-439 (1949).

[2] H. Grimmeiss, "Silicon-germanium—a promise into the future," *Semiconductors* vol. **33**, pp. 939-941 (1999).

[3] L. Pavesi and D. J. Lockwood., *Silicon photonics*. New York: Springer (2004).

[4] A. Cutolo, M. Lodice, P. Spirito, and L. Zeni, "Silicon electro-optic modulator based on a three terminal device integrated in a low-loss single-mode SOI waveguide," *J. Lightwave Technol.* vol. **15**, pp. 505 - 518 (1997).

[5] A. Liu, R. Jones, L. Liao, D. Samara-Rubio, D. Rubin, O. Cohen, R. Nicolaescu, and M. Paniccia, "A high-speed silicon optical modulator based on a metal-oxide-semiconductor capacitor," *Nature* vol. **427**, pp. 615-618 (2004).

[6] C. Z. Zhao, A. H. Chen, E. K. Liu, and G. Z. Li, "Silicon-on-insulator asymmetric optical switch based on total internal reflection," *IEEE Photon. Technol. Lett.* vol. **9**, pp. 1113-1115 (1997).

[7] Y. Liu, E. Liu, G. Li, S. Zhang, J. Luo, F. Zhou, M. Cheng, B. Li, and H. Ge, "Novel silicon waveguide switch based on total internal reflection," *Appl. Phys. Lett.* vol. **64**, pp. 2079-2080 (1994).

[8] M. Ghioni, F. Zappa, V. P. Kesan, and J. Warnock, "A VLSI-compatible high-speed silicon photodetector for optical data link applications," *IEEE Trans. Electron Devices* vol. **43**, pp. 1054 - 1060 (1996).

[9] A. R. Hawkins, W. Wu, P. Abraham, K. Streubel, and J. E. Bowers,

"High gain-bandwidth-product silicon heterointerface photodetector," *Appl. Phys. Lett.* vol. **70**, pp. 303-305 (1997).

[10] R. A. Soref, F. Namavar, N. M. Kalkhoran, and D. M. Koker, "Silicon optical waveguides with buried-CoSi2 cladding layers," *Opt. Lett.* vol. **19**, pp. 1319 (1994).

[11] H. Rong, A. Liu, R. Nicolaescu, M. Paniccia, O. Cohen, and D. Hak, "Raman gain and nonlinear optical absorption measurements in a low-loss silicon waveguide," *Appl. Phys. Lett.* vol. **85**, pp. 2196-2198 (2004).

[12] L. T. Canham, "Silicon quantum wire array fabrication by electrochemical and chemical dissolution of wafers," *Appl. Phys. Lett.* vol. **57**, pp. 1046-1048 (1990).

[13] M. A. Tischler, R. T. Collins, J. H. Stathis, and J. C. Tsang, "Luminescence degradation in porous silicon," *Appl. Phys. Lett.* vol. **60**, pp. 639-641 (1992).

[14] P. Mutti, G. Ghislotti, S. Bertoni, L. Bonoldi, G. F. Cerofolini, L. Meda, E. Grilli, and M. Guzzi, "Room-temperature visible luminescence from silicon nanocrystals in silicon implanted SiO_2 layers," *Appl. Phys. Lett.* vol. **66**, pp. 851-853 (1995).

[15] N.-M. Park, T.-S. Kim, and S.-J. Park, "Band gap engineering of amorphous silicon quantum dots for light-emitting diodes," *Appl. Phys. Lett.* vol. **78**, pp. 2575-2577 (2001).

[16] L. Canham, "Gaining light from silicon," *Nature* vol. **408**, pp. 411-412 (2000).

[17] G. Masini, L. Colace, and G. Assanto, "Si based optoelectronics for

communications," *Mater. Sci. Eng. B* vol. **89**, pp. 2-9 (2002).

[18] N. A. Hill and K. B. Whaley, "Size Dependence of Excitons in Silicon Nanocrystals," *Phys. Rev. Lett.* vol. **75**, pp. 1130-1135 (1995).

[19] P. Carrier, L. J. Lewis, and M. W. C. Dharma-wardana, "Electron confinement and optical enhancement in Si/SiO_2 superlattices," *Phys. Rev. B* vol. **64**, pp. 195330 (2001).

[20] F. Cichos, J. Martin, and C. von Borczyskowski, "Emission intermittency in silicon nanocrystals," *Phys. Rev. B* vol. **70**, pp. 115314 (2004).

[21] K. Leung and K. B. Whaley, "Electron-hole interactions in silicon nanocrystals," *Phys. Rev. B* vol. **56**, pp. 7455-7468 (1997).

[22] G. Ghislotti, B. Nielsen, P. Asoka-Kumar, K. G. Lynn, A. Gambhir, L. F. Di Mauro, and C. E. Bottani, "Effect of different preparation conditions on light emission from silicon implanted SiO_2 layers," *J. Appl. Phys.* vol. **79**, pp. 8660-8663 (1996).

[23] T.-Y. Kim, N.-M. Park, K.-H. Kim, G. Y. Sung, Y.-W. Ok, T.-Y. Seong, and C.-J. Choi, "Quantum confinement effect of silicon nanocrystals in situ grown in silicon nitride films," *Appl. Phys. Lett.* vol. **85**, pp. 5355-5357 (2004).

[24] J. A. Uhlir, "Electrolytic shaping of germanium and silicon," *Bell Syst. Tech. J.* vol. **35**, pp. 333-347 (1956).

[25] M. Fukuda, K. Nakagawa, S. Miyazaki, and M. Hirose, "Resonant tunneling through a self-assembled Si quantum dot," *Appl. Phys. Lett.* vol. **70**, pp. 2291-2293 (1997).

[26] A. Nakajima, Y. Sugita, K. Kawamura, H. Tomita, and N. Yokoyama, "Microstructure and optical absorption properties of Si nanocrystals

fabricated with low-pressure chemical-vapor deposition," *J. Appl. Phys.* vol. **80**, pp. 4006-4011 (1996).

[27] Y. Darma, H. Murakami, and S. Miyazaki, "Formation of nanometer silicon dots with germanium core by highly-selective low-pressure chemical vapor deposition," *Jpn. J. Appl. Phys.* vol. **42**, pp. 4129-4133 (2003).

[28] W. S. Cheong, N. M. Hwang, and D. Y. Yoon, "Observation of nanometer silicon clusters in the hot-filament CVD process," *J. Cryst. Growth* vol. **204**, pp. 52-61 (1999).

[29] E. S. I. S. M. Y. Tatsuro Maeda and I. Kenichi, "Electrical properties of Si nanocrystals embedded in an ultrathin oxide," *Nanotechnology* vol. **10**, pp. 127 (1999).

[30] J. F. Tong, H. L. Hsiao, and H. L. Hwang, "Adjustable emissions from silicon-rich oxide films prepared by plasma-enhanced chemical-vapor deposition," *Appl. Phys. Lett.* vol. **74**, pp. 2316-2318 (1999).

[31] C. S. Yang, C. J. Lin, P. Y. Kuei, S. F. Horng, C. C. H. Hsu, and M. C. Liaw, "Quantum size effects on photoluminescence from Si nanocrystals in PECVD silicon-rich-oxide," *Appl. Surf. Sci.* vol. **113-114**, pp. 116-120 (1997).

[32] Y. Q. Wang, G. L. Kong, W. D. Chen, H. W. Diao, C. Y. Chen, S. B. Zhang, and X. B. Liao, "Getting high-efficiency photoluminescence from Si nanocrystals in SiO_2 matrix," *Appl. Phys. Lett.* vol. **81**, pp. 4174-4176 (2002).

[33] M. Allegrini, C. Ciofi, A. Diligenti, F. Fuso, A. Nannini, V. Pellegrini, and G. Pennelli, "Photoluminescence from ion-beam cosputtered Si/SiO_2

thin films," *Solid State Commun.* vol. **100**, pp. 403-406 (1996).

[34] V. G. Baru, A. P. Chernushich, V. A. Luzanov, G. V. Stepanov, L. Y. Zakharov, K. P. O'Donnell, I. V. Bradley, and N. N. Melnik, "Optical properties of Si nanocrystals prepared by magnetron sputtering," *Appl. Phys. Lett.* vol. **69**, pp. 4148-4150 (1996).

[35] Y. He, L. Bi, J. Y. Feng, and Q. L. Wu, "Properties of Si-rich SiO_2 films by RF magnetron sputtering," *J. Cryst. Growth* vol. **280**, pp. 352-356 (2005).

[36] J. Levoska, M. Tyunina, and S. Leppavuori, "Laser ablation deposition of silicon nanostructures," *Nanostruct. Mater.* vol. **12**, pp. 101-106 (1999).

[37] S. H. Bae, S. Y. Lee, H. Y. Kim, and S. Im, "Luminescence properties of Si nanocrystals fabricated on Si substrate by pulsed laser deposition," *Opt. Mater.* vol. **17**, pp. 87-90 (2001).

[38] C. F. Tan, X. Y. Chen, Y. F. Lu, Y. H. Wu, B. J. Cho, and J. N. Zeng, "Laser annealing of silicon nanocrystal films formed by pulsed-laser deposition," *J. Laser Appl.* vol. **16**, pp. 40-45 (2004).

[39] X. Y. Chen, Y. F. Lu, Y. H. Wu, B. J. Cho, M. H. Liu, D. Y. Dai, and W. D. Song, "Mechanisms of photoluminescence from silicon nanocrystals formed by pulsed-laser deposition in argon and oxygen ambient," *J. Appl. Phys.* vol. **93**, pp. 6311-6319 (2003).

[40] N. Suzuki, T. Makino, Y. Yamada, T. Yoshida, and T. Seto, "Monodispersed, nonagglomerated silicon nanocrystallites," *Appl. Phys. Lett.* vol. **78**, pp. 2043-2045 (2001).

[41] T. Fischer, V. Petrova-Koch, K. Shcheglov, M. S. Brandt, and F. Koch, "Continuously tunable photoluminescence from Si+-implanted and

thermally annealed SiO_2 films," *Thin Solid Films* vol. **276**, pp. 100-103 (1996).

[42] S. Guha, M. D. Pace, D. N. Dunn, and I. L. Singer, "Visible light emission from Si nanocrystals grown by ion implantation and subsequent annealing," *Appl. Phys. Lett.* vol. **70**, pp. 1207-1209 (1997).

[43] T. Muller, K.-H. Heinig, and W. Moller, "Size and location control of Si nanocrystals at ion beam synthesis in thin SiO_2 films," *Appl. Phys. Lett.* vol. **81**, pp. 3049-3051 (2002).

[44] C. Pickering, M. I. J. Beale, D. J. Robbins, P. J. Pearson, and R. Greef, "Optical studies of the structure of porous silicon films formed in p-type degenerate and non-degenerate silicon," *J. Phys. C: Solid State Phys.* vol. **17**, pp. 6535-6552 (1984).

[45] A. R. Wilkinson and R. G. Elliman, "The effect of annealing environment on the luminescence of silicon nanocrystals in silica," *J. Appl. Phys.* vol. **96**, pp. 4018-4020 (2004).

[46] U. Kahler and H. Hofmeister, "Silicon nanocrystallites in buried SiO_x layers via direct wafer bonding," *Appl. Phys. Lett.* vol. **75**, pp. 641-643 (1999).

[47] U. Kahler and H. Hofmeister, "Visible light emission from Si nanocrystalline composites via reactive evaporation of SiO," *Opt. Mater.* vol. **17**, pp. 83-86 (2001).

[48] H. W. Lau, O. K. Tan, Y. Liu, C. Y. Ng, T. P. Chen, K. Pita, and D. Lu, "Defect-induced photoluminescence from tetraethylorthosilicate thin films containing mechanically milled silicon nanocrystals," *J. Appl. Phys.* vol. **97**, pp. 104307 (2005).

[49] K. A. Littau, P. J. Szajowski, A. J. Muller, A. R. Kortan, and L. E. Brus, "A luminescent silicon nanocrystal colloid via a high-temperature aerosol reaction," *J. Phys. Chem.* vol. **97**, pp. 1224-1230 (1993).

[50] M. L. Ostraat, J. W. De Blauwe, M. L. Green, L. D. Bell, H. A. Atwater, and R. C. Flagan, "Ultraclean Two-Stage Aerosol Reactor for Production of Oxide-Passivated Silicon Nanoparticles for Novel Memory Devices," *J. Electrochem. Soc.* vol. **148**, (2001).

[51] M. L. Ostraat, J. W. De Blauwe, M. L. Green, L. D. Bell, M. L. Brongersma, J. Casperson, R. C. Flagan, and H. A. Atwater, "Synthesis and characterization of aerosol silicon nanocrystal nonvolatile floating-gate memory devices," *Appl. Phys. Lett.* vol. **79**, pp. 433-435 (2001).

[52] J. Heitmann, F. Muller, M. Zacharias, and U. Gosele, "Silicon Nanocrystals: Size Matters," *Adv. Mater.* vol. **17**, pp. 795-803 (2005).

[53] A. Nakajima, Y. Sugita, K. Kawamura, H. Tomita, and N. Yokoyama, "Si quantum dot formation with low-pressure chemical vapor deposition," *Jpn. J. Appl. Phys.* vol. **35**, pp. L189-L191 (1996).

[54] Y. Kanemitsu and S. Okamoto, "Phonon structures and Stokes shift in resonantly excited luminescence of silicon nanocrystals," *Phys. Rev. B* vol. **58**, pp. 9652 (1998).

[55] M. Morales, Y. Leconte, R. Rizk, and D. Chateigner, "Structural and microstructural characterization of nanocrystalline silicon thin films obtained by radio-frequency magnetron sputtering," *J. Appl. Phys.* vol. **97**, pp. 034307 (2005).

[56] D. Comedi, O. H. Y. Zalloum, E. A. Irving, J. Wojcik, T. Roschuk, M. J.

Flynn, and P. Mascher, "X-ray-diffraction study of crystalline Si nanocluster formation in annealed silicon-rich silicon oxides," *J. Appl. Phys.* vol. **99**, pp. 023518 (2006).

[57] S. Yerci, U. Serincan, I. Dogan, S. Tokay, M. Genisel, A. Aydinli, and R. Turan, "Formation of silicon nanocrystals in sapphire by ion implantation and the origin of visible photoluminescence," *J. Appl. Phys.* vol. **100**, pp. 074301 (2006).

[58] C. M. Hessel, E. J. Henderson, and J. G. C. Veinot, "An Investigation of the Formation and Growth of Oxide-Embedded Silicon Nanocrystals in Hydrogen Silsesquioxane-Derived Nanocomposites," *J. Phys. Chem. C* vol. **111**, pp. 6956-6961 (2007).

[59] H. R. M. Molinari and M. Vergnat, "Effects of the amorphous-crystalline transition on the luminescence of quantum confined silicon nanoclusters," *Europhys. Lett.* vol. **66**, pp. 674 (2004).

[60] Y. Q. Wang, R. Smirani, and G. G. Ross, "Nanotwinning in Silicon Nanocrystals Produced by Ion Implantation," *Nano Lett.* vol. **4**, pp. 2041-2045 (2004).

[61] D. L. Williamson, "Microstructure of amorphous and microcrystalline Si and SiGe alloys using X-rays and neutrons," *Sol. Energy Mater. Sol. Cells* vol. **78**, pp. 41-84 (2003).

[62] Y. Liu, T. P. Chen, Y. Q. Fu, M. S. Tse, J. H. Hsieh, P. F. Ho, and Y. C. Liu, "A study on Si nanocrystal formation in Si-implanted SiO 2 films by x-ray photoelectron spectroscopy," *J. Phys. D: Appl. Phys.* vol. **36**, pp. L97 (2003).

[63] Y. Liu, T. P. Chen, C. Y. Ng, L. Ding, S. Zhang, Y. Q. Fu, and S. Fung,

"Depth Profiling of Charging Effect of Si Nanocrystals Embedded in SiO_2: A Study of Charge Diffusion among Si Nanocrystals," *J. Phys. Chem. B* vol. **110**, pp. 16499-16502 (2006).

[64] D. Schmeiber, O. Bohme, A. Yfantis, T. Heller, D. R. Batchelor, I. Lundstrom, and A. L. Spetz, "Dipole Moment of Nanoparticles at Interfaces," *Phys. Rev. Lett.* vol. **83**, pp. 380-383 (1999).

[65] K. Borgohain, J. B. Singh, M. V. Rama Rao, T. Shripathi, and S. Mahamuni, "Quantum size effects in CuO nanoparticles," *Phys. Rev. B* vol. **61**, pp. 11093-11096 (2000).

[66] C. Q. Sun, L. K. Pan, Y. Q. Fu, B. K. Tay, and S. Li, "Size Dependence of the 2p-Level Shift of Nanosolid Silicon," *J. Phys. Chem. B* vol. **107**, pp. 5113-5115 (2003).

[67] T. P. Chen, Y. Liu, C. Q. Sun, M. S. Tse, J. H. Hsieh, Y. Q. Fu, Y. C. Liu, and S. Fung, "Core-Level Shift of Si Nanocrystals Embedded in a SiO_2 Matrix," *J. Phys. Chem. B* vol. **108**, pp. 16609-16612 (2004).

[68] V. Mulloni, P. Bellutti, and L. Vanzetti, "XPS and SIMS investigation on the role of nitrogen in Si nanocrystals formation," *Surf. Sci.* vol. **585**, pp. 137-143 (2005).

[69] J. Zi, K. Zhang, and X. Xie, "Comparison of models for Raman spectra of Si nanocrystals," *Phys. Rev. B* vol. **55**, pp. 9263-9266 (1997).

[70] Y. M. Yang, X. L. Wu, L. W. Yang, G. S. Huang, G. G. Siu, and P. K. Chu, "Low-frequency Raman scattering of Ge and Si nanocrystals in silica matrix," *J. Appl. Phys.* vol. **98**, pp. 064303 (2005).

[71] T. Arguirov, T. McHedlidze, M. Kittler, R. Rolver, B. Berghoff, M. Forst, and B. Spangenberg, "Residual stress in Si nanocrystals embedded in a

SiO_2 matrix," *Appl. Phys. Lett.* vol. **89**, pp. 053111 (2006).

[72] H. S. Mavi, S. Prusty, A. K. Shukla, and S. C. Abbi, "Continuous wave laser-induced temperature rise in the thin films of silicon nanocrystals using Raman scattering," *Thin Solid Films* vol. **425**, pp. 90-96 (2003).

[73] S. Biswas, C. Mulcahy, P. Banks, and E. Collart, "Accurate charaterization of dose and shape of ultra low energy arsenic (1 keV and 2 keV) implants by SIMS," *Proc. 14th Int. Conf. Ion Implantation Technology* vol. **1**, pp. 244-247 (2002).

[74] T. P. Chen, Y. Liu, M. S. Tse, O. K. Tan, P. F. Ho, K. Y. Liu, D. Gui, and A. L. K. Tan, "Dielectric functions of Si nanocrystals embedded in a SiO_2 matrix," *Phys. Rev. B* vol. **68**, pp. 153301 (2003).

[75] L. Ding, T. P. Chen, Y. Liu, C. Y. Ng, and S. Fung, "Optical properties of silicon nanocrystals embedded in a SiO_2 matrix," *Phys. Rev. B* vol. **72**, pp. 125419 (2005).

[76] E. S. Marstein, A. E. Gunnas, U. Serincan, R. Turan, A. Olsen, and T. G. Finstad, "Nanocrystal and nanocluster formation and oxidation in annealed Ge-implanted SiO_2 films," *Surf. Coat. Technol.* vol. **158-159**, pp. 544-547 (2002).

[77] C. Y. Ng, T. P. Chen, L. Ding, Y. Liu, M. S. Tse, S. Fung, and Z. L. Dong, "Static dielectric constant of isolated silicon nanocrystals embedded in a SiO_2 thin film," *Appl. Phys. Lett.* vol. **88**, pp. 063103 (2006).

[78] C. Y. Ng, T. P. Chen, L. Ding, M. Yang, J. I. Wong, P. Zhao, X. H. Yang, K. Y. Liu, M. S. Tse, A. D. Trigg, and S. Fung, "Influence of Si nanocrystal distributed in the gate oxide on the MOS capacitance," *IEEE Trans. Electron Devices* vol. **53**, pp. 730-736 (2006).

[79] J. F. Ziegler, J. P. Biersack, and U. Littmark, *The stopping and range of ions in solids*. New York: Pergamon (1985).

[80] Y. Liu, "Characterization of silicon nanocrystals embedded in SiO_2 matrix," in *School of Electrical & Electronic Engineering*. vol. Ph. D Singapore: Nanyang Technological University, 2005.

[81] C. Bonafos, M. Carrada, N. Cherkashin, H. Coffin, D. Chassaing, G. B. Assayag, A. Claverie, T. Muller, K. H. Heinig, M. Perego, M. Fanciulli, P. Dimitrakis, and P. Normand, "Manipulation of two-dimensional arrays of Si nanocrystals embedded in thin SiO_2 layers by low energy ion implantation," *J. Appl. Phys.* vol. **95**, pp. 5696-5702 (2004).

[82] G. B. Assayag, C. Bonafos, M. Carrada, A. Claverie, P. Normand, and D. Tsoukalas, "Transmission electron microscopy measurements of the injection distances in nanocrystal-based memories," *Appl. Phys. Lett.* vol. **82**, pp. 200-202 (2003).

[83] Y. Q. Wang, R. Smirani, G. G. Ross, and F. Schiettekatte, "Ordered coalescence of Si nanocrystals in SiO_2," *Phys. Rev. B* vol. **71**, pp. 161310 (2005).

[84] Y. H. Kwon, C. J. Park, W. C. Lee, D. J. Fu, Y. Shon, T. W. Kang, C. Y. Hong, H. Y. Cho, and K. L. Wang, "Memory effects related to deep levels in metal--oxide--semiconductor structure with nanocrystalline Si," *Appl. Phys. Lett.* vol. **80**, pp. 2502-2504 (2002).

[85] S. S. Kim, K. I. Bang, J. Kwak, and K. S. Lim, "Growth of silicon nanocrystals by low-temperature photo chemical vapor deposition," *Jpn. J. Appl. Phys.* vol. **45**, pp. L46-L49 (2006).

[86] Z. T. Kang, B. Arnold, C. J. Summers, and B. K. Wagner, "Red

luminescence from Si quantum dots embedded in SiOx films grown with controlled stoichiometry," in *Proceedings of SPIE - The International Society for Optical Engineering*, 2005, pp. 1-8.

[87] X. Lu, T. Hanrath, K. P. Johnston, and B. A. Korgel, "Growth of Single Crystal Silicon Nanowires in Supercritical Solution from Tethered Gold Particles on a Silicon Substrate," *Nano Lett.* vol. **3**, pp. 93-99 (2003).

[88] S. N. M. Mestanza, G. O. Dias, J. E. C. Queiroz, I. Doi, J. W. Swart, E. Rodriguez, A. A. R. Neves, and H. Martinho, "Preparation and characterization of silicon nanostructures obtained by ion implantation," in *Proceedings - Electrochemical Society*, 2004, pp. 169-174.

[89] J. Grisolia, C. Dumas, G. Ben Assayag, C. Bonafos, S. Schamm, A. Arbouet, V. Paillard, M. A. F. van den Boogaart, J. Brugger, and P. Normand, "Silicon nanoparticles synthesized in SiO2 pockets by stencil-masked low energy ion implantation and thermal annealing," *Superlattices Microstruct.* vol. **In Press, Corrected Proof**.

[90] G. Binnig, C. F. Quate, and C. Gerber, "Atomic Force Microscope," *Phys. Rev. Lett.* vol. **56**, pp. 930 (1986).

[91] T. van Buuren, L. N. Dinh, L. L. Chase, W. J. Siekhaus, and L. J. Terminello, "Changes in the Electronic Properties of Si Nanocrystals as a Function of Particle Size," *Phys. Rev. Lett.* vol. **80**, pp. 3803 (1998).

[92] Y. Martin, C. C. Williams, and H. K. Wickramasinghe, "Atomic force microscope--force mapping and profiling on a sub 100-[A-ring] scale," *J. Appl. Phys.* vol. **61**, pp. 4723-4729 (1987).

[93] S. Banerjee, M. A. Salem, and S. Oda, "Conducting-tip atomic force microscopy for injection and probing of localized charges in silicon

nanocrystals," *Appl. Phys. Lett.* vol. **83**, pp. 3788-3790 (2003).

[94] S. Decossas, F. Mazen, T. Baron, A. Souifi, and G. Bremond, "Electric measurements by AFM on silicon nanocrystals," *Physica E* vol. **17**, pp. 543-545 (2003).

[95] S. Decossas, F. Mazen, T. Baron, G. Bremond, and A. Souifi, "Atomic force microscopy nanomanipulation of silicon nanocrystals for nanodevice fabrication," *Nanotechnology* vol. **14**, pp. 1272 (2003).

[96] S. Kanjanachuchai, Y. Tsuchiya, K. Usami, and S. Oda, "Nanocrystalline silicon dot displacement using speed-controlled tapping-mode atomic force microscopy," *Microelectron. Eng.* vol. **73-74**, pp. 615-619 (2004).

[97] S. Charvet, R. Madelon, and R. Rizk, "Structural, ellipsometry and photoluminescence spectroscopy studies of silicon nanograins embedded in a silica matrix," *Solid-State Electron.* vol. **45**, pp. 1505-1511 (2001).

[98] D. Amans, S. Callard, A. Gagnaire, J. Joseph, G. Ledoux, and F. Huisken, "Ellipsometric study of silicon nanocrystal optical constants," *J. Appl. Phys.* vol. **93**, pp. 4173-4179 (2003).

[99] K. H. Jun, S. J. Baik, K. S. Lim, H. S. Lee, and J. Y. Lee, "Simulation of ellipsometric spectra from nanocrystalline silicon floating gate structures," *Phys. Rev. B* vol. **67**, pp. 155326 (2003).

[100] A. En Naciri, M. Mansour, L. Johann, J. J. Grob, and C. Eckert, "Correlation between silicon nanocrystalline size effect and spectroscopic ellipsometry responses," *Thin Solid Films* vol. **455-456**, pp. 486-490 (2004).

[101] B. Gallas, C.-C. Kao, C. Defranoux, S. Fisson, G. Vuye, and J. Rivory, "Dielectric function of Si nanocrystals embedded in SiO_2," *Thin Solid*

Films vol. **455-456**, pp. 335-338 (2004).

[102] E. Lioudakis, A. Othonos, G. C. Hadjisavvas, P. C. Kelires, and A. G. Nassiopoulou, "Quantum confinement and interface structure of Si nanocrystals of sizes 3-5 nm embedded in a-SiO_2," *Physica E* vol. **38**, pp. 128-134 (2007).

[103] A. Dutta, Y. Hayafune, and O. Shunri, "Single electron memory devices based on plasma-derived silicon nanocrystals," *Jpn. J. Appl. Phys.* vol. **39**, pp. L855-L857 (2000).

[104] M. A. J. C. Zhenrui Yu and F. Francisco, "Single electron charging in Si nanocrystals embedded in silicon-rich oxide," *Nanotechnology* vol. **14**, pp. 959 (2003).

[105] Y. Liu, T. P. Chen, C. Y. Ng, M. S. Tse, S. Fung, Y. C. Liu, S. Li, and P. Zhao, "Charging Effect on Electrical Characteristics of MOS Structures with Si Nanocrystal Distribution in Gate Oxide," *Electrochem. Solid-State Lett.* vol. **7**, pp. G134-G137 (2004).

[106] C. Y. Ng, T. P. Chen, P. Zhao, L. Ding, Y. Liu, A. A. Tseng, and S. Fung, "Electrical characteristics of Si nanocrystal distributed in a narrow layer in the gate oxide near the gate synthesized with very-low-energy ion beams," *J. Appl. Phys.* vol. **99**, pp. 106105-106103 (2006).

[107] C. Y. Ng, T. P. Chen, L. Ding, and S. Fung, "Memory characteristics of MOSFETs with densely stacked silicon nanocrystal layers in the gate oxide synthesized by low-energy ion beam," *IEEE Electron Device Lett.* vol. **27**, pp. 231-233 (2006).

[108] C. Y. Ng, T. P. Chen, D. Sreeduth, Q. Chen, L. Ding, and A. Du, "Silicon nanocrystal-based non-volatile memory devices," *Thin Solid Films* vol.

504, pp. 25-27 (2006).

[109] E. Kapetanakis, P. Normand, D. Tsoukalas, K. Beltsios, J. Stoemenos, S. Zhang, and J. van den Berg, "Charge storage and interface states effects in Si-nanocrystal memory obtained using low-energy Si^+ implantation and annealing," *Appl. Phys. Lett.* vol. **77**, pp. 3450-3452 (2000).

[110] Y. Kim, K. H. Park, W. C. Choi, T. H. Chung, H. J. Bark, J.-Y. Yi, and J. Jeong, "Charge retention effect in metal-oxide-semiconductor structure containing Si nanocrystals prepared by ion-beam-assisted electron beam deposition," *Mater. Sci. Eng. B* vol. **83**, pp. 145-151 (2001).

[111] C. Y. Ng, T. P. Chen, L. Ding, Q. Chen, Y. Liu, P. Zhao, A. A. Tseng, and S. Fung, "Si ion-induced instability in flatband voltage of Si^+ -implanted gate oxides," *IEEE Trans. Electron Devices* vol. **53**, pp. 1280-1282 (2006).

[112] J. D. Holmes, K. J. Ziegler, R. C. Doty, L. E. Pell, K. P. Johnston, and B. A. Korgel, "Highly Luminescent Silicon Nanocrystals with Discrete Optical Transitions," *J. Am. Chem. Soc.* vol. **123**, pp. 3743-3748 (2001).

[113] S. Guha, "Characterization of Si^+ ion-implanted SiO_2 films and silica glasses," *J. Appl. Phys.* vol. **84**, pp. 5210-5217 (1998).

[114] B. J. Hinds, F. Wang, D. M. Wolfe, C. L. Hinkle, and G. Lucovsky, "Investigation of postoxidation thermal treatments of Si/SiO_2 interface in relationship to the kinetics of amorphous Si suboxide decomposition," in *25th annual conference on the physics and chemistry of semiconductor interfaces*, Salt Lake City, Utah (USA), 1998, pp. 2171-2176.

[115] L. Khriachtchev, M. Rasanen, S. Novikov, and L. Pavesi, "Systematic correlation between Raman spectra, photoluminescence intensity, and

absorption coefficient of silica layers containing Si nanocrystals," *Appl. Phys. Lett.* vol. **85**, pp. 1511-1513 (2004).

[116] V. Y. Timoshenko, L. A. Osminkina, A. I. Efimova, L. A. Golovan, P. K. Kashkarov, D. Kovalev, N. Kunzner, E. Gross, J. Diener, and F. Koch, "Anisotropy of optical absorption in birefringent porous silicon," *Phys. Rev. B* vol. **67**, pp. 113405 (2003).

[117] A. G. Cullis, L. T. Canham, and P. D. J. Calcott, "The structural and luminescence properties of porous silicon," *J. Appl. Phys.* vol. **82**, pp. 909-965 (1997).

[118] H. Z. Song and X. M. Bao, "Visible photoluminescence from silicon-ion-implanted SiO_2 film and its multiple mechanisms," *Phys. Rev. B* vol. **55**, pp. 6988 (1997).

[119] L. N. Dinh, L. L. Chase, M. Balooch, W. J. Siekhaus, and F. Wooten, "Optical properties of passivated Si nanocrystals and SiO_x nanostructures," *Phys. Rev. B* vol. **54**, pp. 5029 (1996).

[120] S. Takeoka, M. Fujii, and S. Hayashi, "Size-dependent photoluminescence from surface-oxidized Si nanocrystals in a weak confinement regime," *Phys. Rev. B* vol. **62**, pp. 16820 (2000).

[121] K. S. Cho, N.-M. Park, T.-Y. Kim, K.-H. Kim, G. Y. Sung, and J. H. Shin, "High efficiency visible electroluminescence from silicon nanocrystals embedded in silicon nitride using a transparent doping layer," *Appl. Phys. Lett.* vol. **86**, pp. 071909 (2005).

[122] J. C. Vial, A. Bsiesy, F. Gaspard, R. Herino, M. Ligeon, F. Muller, R. Romestain, and R. M. Macfarlane, "Mechanisms of visible-light emission from electro-oxidized porous silicon," *Phys. Rev. B* vol. **45**, pp.

14171 (1992).

[123] T. Shimizu-Iwayama, K. Fujita, S. Nakao, K. Saitoh, T. Fujita, and N. Itoh, "Visible photoluminescence in Si^+-implanted silica glass," *J. Appl. Phys.* vol. **75**, pp. 7779-7783 (1994).

[124] S. Cheylan and R. G. Elliman, "Effect of particle size on the photoluminescence from hydrogen passivated Si nanocrystals in SiO_2," *Appl. Phys. Lett.* vol. **78**, pp. 1912-1914 (2001).

[125] M. Lopez, B. Garrido, C. Bonafos, A. Perez-Rodriguez, and J. R. Morante, "Optical and structural characterization of Si nanocrystals ion beam synthesized in SiO_2: correlation between the surface passivation and the photoluminescence emission," *Solid-State Electron.* vol. **45**, pp. 1495-1504 (2001).

[126] M. Zacharias, J. Heitmann, R. Scholz, U. Kahler, M. Schmidt, and J. Blasing, "Size-controlled highly luminescent silicon nanocrystals: A SiO/SiO_2 superlattice approach," *Appl. Phys. Lett.* vol. **80**, pp. 661-663 (2002).

[127] I. Mihalcescu, J. C. Vial, and R. Romestain, "Carrier localization in porous silicon investigated by time-resolved luminescence analysis," *J. Appl. Phys.* vol. **80**, pp. 2404-2411 (1996).

[128] J. Linnros, N. Lalic, A. Galeckas, and V. Grivickas, "Analysis of the stretched exponential photoluminescence decay from nanometer-sized silicon crystals in SiO_2," *J. Appl. Phys.* vol. **86**, pp. 6128-6134 (1999).

[129] C. Delerue, G. Allan, C. Reynaud, O. Guillois, G. Ledoux, and F. Huisken, "Multiexponential photoluminescence decay in indirect-gap semiconductor nanocrystals," *Phys. Rev. B* vol. **73**, pp. 235318-235314

(2006).

[130] B. V. Kamenev and A. G. Nassiopoulou, "Self-trapped excitons in silicon nanocrystals with sizes below 1.5 nm in Si/SiO[sub 2] multilayers," *J. Appl. Phys.* vol. **90**, pp. 5735-5740 (2001).

[131] P. Pellegrino, A. Perez-Rodriguez, B. Garrido, O. Gonzalez-Varona, J. R. Morante, S. Marcinkevicius, A. Galeckas, and J. Linnros, "Time-resolved analysis of the white photoluminescence from SiO[sub 2] films after Si and C coimplantation," *Appl. Phys. Lett.* vol. **84**, pp. 25-27 (2004).

[132] J. V. J.-L. R. R. R. M. J. L. Petr Janda and G. E. Robert, "Modified spontaneous emission of silicon nanocrystals embedded in artificial opals," *J. Phys. D: Appl. Phys.* vol. **40**, pp. 5847 (2007).

[133] M. Fujii, D. Kovalev, B. Goller, S. Minobe, S. Hayashi, and V. Y. Timoshenko, "Time-resolved photoluminescence studies of the energy transfer from excitons confined in Si nanocrystals to oxygen molecules," *Phys. Rev. B* vol. **72**, pp. 165321-165328 (2005).

[134] L. Dal Negro, M. Cazzanelli, N. Daldosso, Z. Gaburro, L. Pavesi, F. Priolo, D. Pacifici, G. Franzo, and F. Iacona, "Stimulated emission in plasma-enhanced chemical vapour deposited silicon nanocrystals," *Physica E* vol. **16**, pp. 297-308 (2003).

[135] K. Toshikiyo, M. Fujii, and S. Hayashi, "Enhanced optical properties of Si nanocrystals in planar microcavity," *Physica E* vol. **17**, pp. 451-452 (2003).

[136] O. Guillois, N. Herlin-Boime, C. Reynaud, G. Ledoux, and F. Huisken, "Photoluminescence decay dynamics of noninteracting silicon nanocrystals," *J. Appl. Phys.* vol. **95**, pp. 3677-3682 (2004).

[137] R. J. Walters, J. Kalkman, A. Polman, H. A. Atwater, and M. J. A. de Dood, "Photoluminescence quantum efficiency of dense silicon nanocrystal ensembles in SiO_2," *Phys. Rev. B* vol. **73**, pp. 132302-132304 (2006).

[138] L. Rebohle, J. von Borany, R. A. Yankov, W. Skorupa, I. E. Tyschenko, H. Frob, and K. Leo, "Strong blue and violet photoluminescence and electroluminescence from germanium-implanted and silicon-implanted silicon-dioxide layers," *Appl. Phys. Lett.* vol. **71**, pp. 2809-2811 (1997).

[139] H.-Z. Song, X.-M. Bao, N.-S. Li, and J.-Y. Zhang, "Relation between electroluminescence and photoluminescence of Si^+-implanted SiO_2," *J. Appl. Phys.* vol. **82**, pp. 4028-4032 (1997).

[140] N. Lalic and J. Linnros, "Light emitting diode structure based on Si nanocrystals formed by implantation into thermal oxide," *J. Lumin.* vol. **80**, pp. 263-267 (1998).

[141] L. Heikkila, T. Kuusela, and H. P. Hedman, "Laser type of spectral narrowing in electroluminescent Si/SiO_2 superlattices prepared by low-pressure chemical vapour deposition," *Superlattices Microstruct.* vol. **26**, pp. 157-169 (1999).

[142] D. Muller, P. Knapek, J. Faure, B. Prevot, J. J. Grob, B. Honerlage, and I. Pelant, "Blue electroluminescence from high dose Si^+ implantation in SiO_2," *Nucl. Instr. Meth. Phys. Res. B* vol. **148**, pp. 997-1001 (1999).

[143] K. Luterova, I. Pelant, J. Valenta, J. L. Rehspringer, D. Muller, J. J. Grob, J. Dian, and B. Honerlage, "Red electroluminescence in Si^+-implanted sol--gel-derived SiO_2 films," *Appl. Phys. Lett.* vol. **77**, pp. 2952-2954 (2000).

[144] J. Valenta, N. Lalic, and J. Linnros, "Electroluminescence microscopy and spectroscopy of silicon nanocrystals in thin SiO_2 layers," *Opt. Mater.* vol. **17**, pp. 45-50 (2001).

[145] G. Franzò, A. Irrera, E. C. Moreira, M. Miritello, F. Iacona, D. Sanfilippo, G. Di Stefano, P. G. Fallica, and F. Priolo, "Electroluminescence of silicon nanocrystals in MOS structures," *Appl. Phys. A* vol. **74**, pp. 1-5 (2002).

[146] J. De la Torre, A. Souifi, M. Lemiti, A. Poncet, C. Busseret, G. Guillot, G. Bremond, O. Gonzalez, B. Garrido, and J. R. Morante, "Optical and electrical transport mechanisms in Si-nanocrystal-based LEDs," *Physica E* vol. **17**, pp. 604-606 (2003).

[147] A. Irrera, D. Pacifici, M. Miritello, G. Franzo, F. Priolo, F. Iacona, D. Sanfilippo, G. Di Stefano, and P. G. Fallica, "Electroluminescence properties of light emitting devices based on silicon nanocrystals," *Physica E* vol. **16**, pp. 395-399 (2003).

[148] T. Matsuda, K. Nishihara, M. Kawabe, H. Iwata, S. Iwatsubo, and T. Ohzone, "Blue electroluminescence from MOS capacitors with Si-implanted SiO_2," *Solid-State Electron.* vol. **48**, pp. 1933-1941 (2004).

[149] A. Irrera, F. Iacona, G. Franzo, S. Boninelli, D. Pacifici, M. Miritello, C. Spinella, D. Sanfilippo, G. Di Stefano, P. G. Fallica, and F. Priolo, "Correlation between electroluminescence and structural properties of Si nanoclusters," *Opt. Mater.* vol. **27**, pp. 1031-1040 (2005).

[150] C. J. Lin and G. R. Lin, "Defect-enhanced visible electroluminescence of multi-energy silicon-implanted silicon dioxide film," *IEEE J. Quantum Electron.* vol. **41**, pp. 441-447 (2005).

[151] A. Fojtik, J. Valenta, T. H. Stuchlikova, J. Stuchlik, I. Pelant, and J. Kocka, "Electroluminescence of silicon nanocrystals in p-i-n diode structures," *Thin Solid Films* vol. **515**, pp. 775-777 (2006).

[152] A. Irrera, F. Iacona, I. Crupi, C. D. Presti, G. Franz, C. Bongiorno, D. Sanfilippo, G. D. Stefano, A. Piana, P. G. Fallica, A. Canino, and F. Priolo, "Electroluminescence and transport properties in amorphous silicon nanostructures," *Nanotechnology* vol. **17**, pp. 1428 (2006).

[153] M. Kulakci, U. Serincan, and R. Turan, "Electroluminescence generated by a metal oxide semiconductor light emitting diode (MOS-LED) with Si nanocrystals embedded in SiO_2 layers by ion implantation," *Semicond. Sci. Technol.* vol. **21**, pp. 1527 (2006).

[154] J. Barreto, M. Peralvarez, J. Antonio Rodriguez, A. Morales, M. Riera, M. Lopez, B. Garrido, L. Lechuga, and C. Dominguez, "Pulsed electroluminescence in silicon nanocrystals-based devices fabricated by PECVD," *Physica E* vol. **38**, pp. 193-196 (2007).

[155] G.-R. Lin, C.-J. Lin, and C.-T. Lin, "Low-plasma and high-temperature PECVD grown silicon-rich SiOx film with enhanced carrier tunneling and light emission," *Nanotechnology* vol. **18**, pp. 395202 (2007).

[156] H. Takagi, H. Ogawa, Y. Yamazaki, A. Ishizaki, and T. Nakagiri, "Quantum size effects on photoluminescence in ultrafine Si particles," *Appl. Phys. Lett.* vol. **56**, pp. 2379-2380 (1990).

[157] P. Deak, M. Rosenbauer, M. Stutzmann, J. Weber, and M. S. Brandt, "Siloxene: Chemical quantum confinement due to oxygen in a silicon matrix," *Phys. Rev. Lett.* vol. **69**, pp. 2531 (1992).

[158] T. K. Sham, D. T. Jiang, I. Coulthard, J. W. Lorimer, X. H. Feng, K. H.

Tan, S. P. Frigo, R. A. Rosenberg, D. C. Houghton, and B. Bryskiewicz, "Origin of luminescence from porous silicon deduced by synchrotron-light-induced optical luminescence," *Nature* vol. **363**, pp. 331-334 (1993).

[159] J. P. Proot, C. Delerue, and G. Allan, "Electronic structure and optical properties of silicon crystallites: Application to porous silicon," *Appl. Phys. Lett.* vol. **61**, pp. 1948-1950 (1992).

[160] S. Guha, S. B. Qadri, R. G. Musket, M. A. Wall, and T. Shimizu-Iwayama, "Characterization of Si nanocrystals grown by annealing SiO_2 films with uniform concentrations of implanted Si," *J. Appl. Phys.* vol. **88**, pp. 3954-3961 (2000).

[161] G. G. Qin, X. S. Liu, S. Y. Ma, J. Lin, G. Q. Yao, X. Y. Lin, and K. X. Lin, "Photoluminescence mechanism for blue-light-emitting porous silicon," *Phys. Rev. B* vol. **55**, pp. 12876 (1997).

[162] A. Y. Kobitski, K. S. Zhuravlev, H. P. Wagner, and D. R. T. Zahn, "Self-trapped exciton recombination in silicon nanocrystals," *Phys. Rev. B* vol. **63**, pp. 115423 (2001).

[163] G. G. Ross, D. Barba, C. Dahmoune, Y. Q. Wang, and F. Martin, "Effect of implanted Si concentration on the Si nanocrystal size and emitted PL spectrum," *Nucl. Instr. Meth. Phys. Res. B* vol. **256**, pp. 211-215 (2007).

[164] M. S. Brandt, H. D. Fuchs, M. Stutzmann, J. Weber, and M. Cardona, "Origin of visible luminescence from 'porous silicon': a new interpretation," *Solid State Commun.* vol. **81**, pp. 307-312 (1992).

[165] L. Pavesi, L. Dal Negro, C. Mazzoleni, G. Franzo, and F. Priolo, "Optical gain in silicon nanocrystals," *Nature* vol. **408**, pp. 440-444 (2000).

[166] L. Dal Negro, L. Pavesi, G. Pucker, G. Franzo, and F. Priolo, "Optical gain in silicon nanocrystals," *Opt. Mater.* vol. **17**, pp. 41-44 (2001).

[167] J. Valenta, I. Pelant, and J. Linnros, "Waveguiding effects in the measurement of optical gain in a layer of Si nanocrystals," *Appl. Phys. Lett.* vol. **81**, pp. 1396-1398 (2002).

[168] L. D. Negro, M. Cazzanelli, B. Danese, L. Pavesi, F. Iacona, G. Franzo, and F. Priolo, "Light amplification in silicon nanocrystals by pump and probe transmission measurements," *J. Appl. Phys.* vol. **96**, pp. 5747-5755 (2004).

[169] J. Valenta, I. Pelant, K. Luterova, R. Tomasiunas, S. Cheylan, R. G. Elliman, J. Linnros, and B. Honerlage, "Active planar optical waveguide made from luminescent silicon nanocrystals," *Appl. Phys. Lett.* vol. **82**, pp. 955-957 (2003).

[170] T. Ostatnicky, J. Valenta, I. Pelant, K. Luterova, R. G. Elliman, S. Cheylan, and B. Honerlage, "Photoluminescence from an active planar optical waveguide made of silicon nanocrystals: dominance of leaky substrate modes in dissipative structures," *Opt. Mater.* vol. **27**, pp. 781-786 (2005).

[171] P. Pellegrino, B. Garrido, C. Garcia, J. Arbiol, J. R. Morante, M. Melchiorri, N. Daldosso, L. Pavesi, E. Scheid, and G. Sarrabayrouse, "Low-loss rib waveguides containing Si nanocrystals embedded in SiO_2," *J. Appl. Phys.* vol. **97**, pp. 074312-074318 (2005).

[172] S. Minissale, T. Gregorkiewicz, M. Forcales, and R. G. Elliman, "On optical activity of Er^{3+} ions in Si-rich SiO_2 waveguides," *Appl. Phys. Lett.* vol. **89**, pp. 171908-171903 (2006).

[173] R. Claps, D. Dimitropoulos, Y. Han, and B. Jalali, "Observation of Raman emission in silicon waveguides at 1.54 μm," *Opt. Express* vol. **10**, pp. 1305-1313 (2002).

[174] R. Claps, D. Dimitropoulos, V. Raghunathan, Y. Han, and B. Jalali, "Observation of stimulated Raman amplification in silicon waveguides," *Opt. Express* vol. **11**, pp. 1731-1739 (2003).

[175] R. Claps, V. Raghunathan, D. Dimitropoulos, and B. Jalali, "Anti-stokes Raman conversion in silicon waveguides," *Opt. Express* vol. **11**, pp. 2862-2872 (2003).

[176] R. L. Espinola, J. I. Dadap, R. M. Osgood Jr, S. J. McNab, and Y. A. Vlasov, "Raman amplification in ultrasmall silicon-on-insulator wire waveguides," *Opt. Express* vol. **12**, pp. 3713-3718 (2004).

[177] H. Rong, R. Jones, A. Liu, O. Cohen, D. Hak, A. Fang, and M. Paniccia, "A continuous-wave Raman silicon laser," *Nature* vol. **433**, pp. 725-728 (2005).

[178] H. Rong, A. Liu, R. Jones, O. Cohen, D. Hak, R. Nicolaescu, A. Fang, and M. Paniccia, "An all-silicon Raman laser," *Nature* vol. **433**, pp. 292-294 (2005).

[179] H. Rong, S. Xu, Y. H. Kuo, V. Sih, O. Cohen, O. Raday, and M. Paniccia, "Low-threshold continuous-wave Raman silicon laser," *Nature Photonics* vol. **1**, pp. 232-237 (2007).

[180] R. J. Walters, G. I. Bourianoff, and H. A. Atwater, "Field-effect electroluminescence in silicon nanocrystals," *Nat. Mater.* vol. **4**, pp. 143-146 (2005).

[181] J. Linnros, "Optoelectronics: Nanocrystals brighten transistors," *Nat.*

Mater. vol. **4**, pp. 117-119 (2005).

[182] M. Peralvarez, C. Garcia, M. Lopez, B. Garrido, J. Barreto, C. Dominguez, and J. A. Rodriguez, "Field effect luminescence from Si nanocrystals obtained by plasma-enhanced chemical vapor deposition," *Appl. Phys. Lett.* vol. **89**, pp. 051112 (2006).

[183] S. Tiwari, F. Rana, K. Chan, H. Hanafi, W. Chan, and D. Buchanan, "Volatile and non-volatile memories in silicon with nano-crystal storage," in *International Electron Devices Meeting*, 1995, pp. 521-524.

[184] F. Rana, S. Tiwari, and D. A. Buchanan, "Self-consistent modeling of accumulation layers and tunneling currents through very thin oxides," *Appl. Phys. Lett.* vol. **69**, pp. 1104-1106 (1996).

[185] S. Tiwari, F. Rana, K. Chan, L. Shi, and H. Hanafi, "Single charge and confinement effects in nano-crystal memories," *Appl. Phys. Lett.* vol. **69**, pp. 1232-1234 (1996).

[186] S. Tiwari, F. Rana, H. Hanafi, A. Hartstein, E. F. Crabbe, and K. Chan, "A silicon nanocrystals based memory," *Appl. Phys. Lett.* vol. **68**, pp. 1377-1379 (1996).

[187] G. Ammendola, V. Ancarani, V. Triolo, M. Bileci, D. Corso, I. Crupi, L. Perniola, C. Gerardi, S. Lombardo, and B. DeSalvo, "Nanocrystal memories for FLASH device applications," *Solid-State Electron.* vol. **48**, pp. 1483-1488 (2004).

[188] R. A. Rao, R. F. Steimle, M. Sadd, C. T. Swift, B. Hradsky, S. Straub, T. Merchant, M. Stoker, S. G. H. Anderson, M. Rossow, J. Yater, B. Acred, K. Harber, E. J. Prinz, B. E. White, and R. Muralidhar, "Silicon nanocrystal based memory devices for NVM and DRAM applications,"

Solid-State Electron. vol. **48**, pp. 1463-1473 (2004).

[189] J. Carreras, B. Garrido, and J. R. Morante, "Improved charge injection in Si nanocrystal non-volatile memories," *Microelectronics and Reliability* vol. **45**, pp. 899-902 (2005).

[190] C. Y. Ng, T. P. Chen, M. Yang, J. B. Yang, L. Ding, C. M. Li, A. Du, and A. Trigg, "Impact of programming mechanisms on the performance and reliability of nonvolatile memory devices based on Si nanocrystals," *IEEE Trans. Electron Devices* vol. **53**, pp. 663-667 (2006).

[191] J. Koh, H. Fujiwara, Y. Lu, C. R. Wronski, and R. W. Collins, "Real time spectroscopic ellipsometry for characterization and optimization of amorphous silicon-based solar cell structures," *Thin Solid Films* vol. **313-314**, pp. 469-473 (1998).

[192] V. Svrcek, A. Slaoui, and J. C. Muller, "Silicon nanocrystals as light converter for solar cells," *Thin Solid Films* vol. **451-452**, pp. 384-388 (2004).

[193] M. H. Wu, R. Mu, A. Ueda, D. O. Henderson, and B. Vlahovic, "Production of silicon quantum dots for photovoltaic applications by picosecond pulsed laser ablation," *Mater. Sci. Eng. B* vol. **116**, pp. 273-277 (2005).

[194] G. Conibeer, M. Green, R. Corkish, Y. Cho, E.-C. Cho, C.-W. Jiang, T. Fangsuwannarak, E. Pink, Y. Huang, T. Puzzer, T. Trupke, B. Richards, A. Shalav, and K.-l. Lin, "Silicon nanostructures for third generation photovoltaic solar cells," *Thin Solid Films* vol. **511-512**, pp. 654-662 (2006).

[195] J. De la Torre, G. Bremond, M. Lemiti, G. Guillot, P. Mur, and N. Buffet,

"Using silicon nanostructures for the improvement of silicon solar cells' efficiency," *Thin Solid Films* vol. **511-512**, pp. 163-166 (2006).

[196] Y. Xu, Z. Hu, H. Diao, Y. Cai, S. Zhang, X. Zeng, H. Hao, X. Liao, E. Fortunato, and R. Martins, "Heterojunction solar cells with n-type nanocrystalline silicon emitters on p-type c-Si wafers," *J. Non-Cryst. Solids* vol. **352**, pp. 1972-1975 (2006).

[197] M. C. Beard, K. P. Knutsen, P. Yu, J. M. Luther, Q. Song, W. K. Metzger, R. J. Ellingson, and A. J. Nozik, "Multiple Exciton Generation in Colloidal Silicon Nanocrystals," *Nano Lett.* vol. **7**, pp. 2506-2512 (2007).

[198] E. C. Cho, M. A. Green, G. Conibeer, D. Song, Y. H. Cho, G. Scardera, S. Huang, S. Park, X. J. Hao, Y. Huang, and L. Van Dao, "Silicon quantum dots in a dielectric matrix for all-silicon tandem solar cells," *Advances in OptoElectronics* vol. **2007**, pp. 69578 (2007).

[199] A. Schuler, M. Python, M. V. del Olmo, and E. de Chambrier, "Quantum dot containing nanocomposite thin films for photoluminescent solar concentrators," *Solar Energy* vol. **81**, pp. 1159-1165 (2007).

[200] D. Song, E.-C. Cho, G. Conibeer, C. Flynn, Y. Huang, and M. A. Green, "Structural, electrical and photovoltaic characterization of Si nanocrystals embedded SiC matrix and Si nanocrystals/c-Si heterojunction devices," *Sol. Energy Mater. Sol. Cells* vol. **92**, pp. 474-481 (2008).

[201] R. F. Steimle, M. Sadd, R. Muralidhar, R. Rao, B. Hradsky, S. Straub, and B. E. White Jr, "Hybrid silicon nanocrystal silicon nitride dynamic random access memory," *IEEE Trans. Nanotechnol.* vol. **2**, pp. 335-340 (2003).

[202] S. Ogut, J. R. Chelikowsky, and S. G. Louie, "Quantum Confinement and Optical Gaps in Si Nanocrystals," *Phys. Rev. Lett.* vol. **79**, pp. 1770-1173 (1997).

[203] C. Bulutay, "Interband, intraband, and excited-state direct photon absorption of silicon and germanium nanocrystals embedded in a wide band-gap lattice," *Phys. Rev. B* vol. **76**, pp. 205321 (2007).

[204] K.-J. Lee, T.-D. Kang, H. Lee, S. H. Hong, S.-H. Choi, T.-Y. Seong, K. J. Kim, and D. W. Moon, "Optical properties of SiO_2/nanocrystalline Si multilayers studied using spectroscopic ellipsometry," *Thin Solid Films* vol. **476**, pp. 196-200 (2005).

[205] L.-W. Wang and A. Zunger, "Dielectric Constants of Silicon Quantum Dots," *Phys. Rev. Lett.* vol. **73**, pp. 1039-1042 (1994).

[206] C. Delerue, G. Allan, and M. Lannoo, "Theoretical aspects of the luminescence of porous silicon," *Phys. Rev. B* vol. **48**, pp. 11024-11036 (1993).

[207] I. Vasiliev, S. Ogut, and J. R. Chelikowsky, "Ab Initio Absorption Spectra and Optical Gaps in Nanocrystalline Silicon," *Phys. Rev. Lett.* vol. **86**, pp. 1813-1816 (2001).

[208] H. C. Weissker, J. Furthmuller, and F. Bechstedt, "Optical properties of Ge and Si nanocrystallites from ab initio calculations. I. Embedded nanocrystallites," *Phys. Rev. B* vol. **65**, pp. 155327 (2002).

[209] H. C. Weissker, J. Furthmuller, and F. Bechstedt, "Optical properties of Ge and Si nanocrystallites from ab initio calculations. II. Hydrogenated nanocrystallites," *Phys. Rev. B* vol. **65**, pp. 155328 (2002).

[210] H. C. Weissker, J. Furthmller, and F. Bechstedt, "Validity of

effective-medium theory for optical properties of embedded nanocrystallites from ab initio supercell calculations," *Phys. Rev. B* vol. **67**, pp. 165322 (2003).

[211] R. M. A. Azzam and N. M. Basharra, *Ellipsometry and Polarized Light*. Amsterdam: North-Holland (1977).

[212] A. R. Forouhi and I. Bloomer, "Optical properties of crystalline semiconductors and dielectrics," *Phys. Rev. B* vol. **38**, pp. 1865 (1988).

[213] U. Rossow, U. Frotscher, C. Pietryga, W. Richter, and D. E. Aspnes, "Interpretation of the dielectric function of porous silicon layers," *Appl. Surf. Sci.* vol. **102**, pp. 413-416 (1996).

[214] H. V. Nguyen, Y. Lu, S. Kim, M. Wakagi, and R. W. Collins, "Optical Properties of Ultrathin Crystalline and Amorphous Silicon Films," *Phys. Rev. Lett.* vol. **74**, pp. 3880-3883 (1995).

[215] J. I. Pankove, *Optical Process in Semiconductors*. New York: Dover (1975).

[216] D. R. Penn, "Wave-Number-Dependent Dielectric Function of Semiconductors," *Phys. Rev.* vol. **128**, pp. 2093-2097 (1962).

[217] L.-W. Wang and A. Zunger, "Pseudopotential calculations of nanoscale CdSe quantum dots," *Phys. Rev. B* vol. **53**, pp. 9579-9582 (1996).

[218] R. Tsu, D. Babic, and J. L. Ioriatti, "Simple model for the dielectric constant of nanoscale silicon particle," *J. Appl. Phys.* vol. **82**, pp. 1327-1329 (1997).

[219] C. Delerue, M. Lannoo, and G. Allan, "Concept of dielectric constant for nanosized systems," *Phys. Rev. B* vol. **68**, pp. 115411 (2003).

[220] B. Garrido, M. Lopez, O. Gonzalez, A. Perez-Rodriguez, J. R. Morante,

and C. Bonafos, "Correlation between structural and optical properties of Si nanocrystals embedded in SiO_2: The mechanism of visible light emission," *Appl. Phys. Lett.* vol. **77**, pp. 3143-3145 (2000).

[221] L. A. Nesbit, "Annealing characteristics of Si-rich SiO_2 films," *Appl. Phys. Lett.* vol. **46**, pp. 38-40 (1985).

[222] A. M. Agarwal and S. T. Dunham, "Consistent quantitative model for the spatial extent of point defect interactions in silicon," *J. Appl. Phys.* vol. **78**, pp. 5313-5319 (1995).

[223] M. Carrada, N. Cherkashin, C. Bonafos, G. Benassayag, D. Chassaing, P. Normand, D. Tsoukalas, V. Soncini, and A. Claverie, "Effect of ion energy and dose on the positioning of 2D-arrays of Si nanocrystals ion beam synthesised in thin SiO_2 layers," *Mater. Sci. Eng. B* vol. **101**, pp. 204-207 (2003).

[224] P. Normand, K. Beltsios, E. Kapetanakis, D. Tsoukalas, T. Travlos, J. Stoemenos, J. Van Den Berg, S. Zhang, C. Vieu, H. Launois, J. Gautier, F. Jourdan, and L. Palun, "Formation of 2-D arrays of semiconductor nanocrystals or semiconductor-rich nanolayers by very low-energy Si or Ge ion implantation in silicon oxide films," *Nucl. Instr. Meth. Phys. Res. B* vol. **178**, pp. 74-77 (2001).

[225] M. V. Wolkin, J. Jorne, P. M. Fauchet, G. Allan, and C. Delerue, "Electronic States and Luminescence in Porous Silicon Quantum Dots: The Role of Oxygen," *Phys. Rev. Lett.* vol. **82**, pp. 197-200 (1999).

[226] F. A. Reboredo, A. Franceschetti, and A. Zunger, "Excitonic transitions and exchange splitting in Si quantum dots," *Appl. Phys. Lett.* vol. **75**, pp. 2972-2974 (1999).

[227] L.-S. Liao, X.-M. Bao, X.-Q. Zheng, N.-S. Li, and N.-B. Min, "Blue luminescence from Si^+-implanted SiO_2 films thermally grown on crystalline silicon," *Appl. Phys. Lett.* vol. **68**, pp. 850-852 (1996).

[228] F. Trani, G. Cantele, D. Ninno, and G. Iadonisi, "Tight-binding calculation of the optical absorption cross section of spherical and ellipsoidal silicon nanocrystals," *Phys. Rev. B* vol. **72**, pp. 075423 (2005).

[229] F. Trani, D. Ninno, and G. Iadonisi, "Role of local fields in the optical properties of silicon nanocrystals using the tight binding approach," *Phys. Rev. B* vol. **75**, pp. 033312 (2007).

[230] C.-J. Lin, C.-K. Lee, E. W.-G. Diau, and G.-R. Lin, "Time-Resolved Photoluminescence Analysis of Multidose Si-Ion-Implanted SiO_2," *J. Electrochem. Soc.* vol. **153**, pp. E25-E32 (2006).

[231] H. Nishikawa, E. Watanabe, D. Ito, M. Takiyama, A. Ieki, and Y. Ohki, "Photoluminescence study of defects in ion-implanted thermal SiO_2 films," *J. Appl. Phys.* vol. **78**, pp. 842-846 (1995).

[232] J. C. Cheang-Wong, A. Oliver, J. Roiz, J. M. Hernandez, L. Rodriguez-Fernandez, J. G. Morales, and A. Crespo-Sosa, "Optical properties of Ir2+-implanted silica glass," *Nucl. Instr. Meth. Phys. Res. B* vol. **175-177**, pp. 490-494 (2001).

[233] H. S. Bae, T. G. Kim, C. N. Whang, S. Im, J. S. Yun, and J. H. Song, "Electroluminescence mechanism in SiOx layers containing radiative centers," *J. Appl. Phys.* vol. **91**, pp. 4078-4081 (2002).

[234] L. Skuja, "Time-resolved low temperature luminescence of non-bridging oxygen hole centers in silica glass," *Solid State Commun.* vol. **84**, pp. 613-616 (1992).

[235] S. Munekuni, T. Yamanaka, Y. Shimogaichi, R. Tohmon, Y. Ohki, K. Nagasawa, and Y. Hama, "Various types of nonbridging oxygen hole center in high-purity silica glass," *J. Appl. Phys.* vol. **68**, pp. 1212-1217 (1990).

[236] T. Bakos, S. N. Rashkeev, and S. T. Pantelides, "The origin of photoluminescence lines in irradiated amorphous SiO_2," *IEEE Transactions on Nuclear Science* vol. **49**, pp. 2713-2717 (2002).

[237] M. Y. Valakh, V. A. Yukhimchuk, V. Y. Bratus, A. A. Konchits, P. L. F. Hemment, and T. Komoda, "Optical and electron paramagnetic resonance study of light-emitting Si^+ ion implanted silicon dioxide layers," *J. Appl. Phys.* vol. **85**, pp. 168-173 (1999).

[238] R. Tohmon, Y. Shimogaichi, H. Mizuno, Y. Ohki, K. Nagasawa, and Y. Hama, "2.7-eV luminescence in as-manufactured high-purity silica glass," *Phys. Rev. Lett.* vol. **62**, pp. 1388-1391 (1989).

[239] H. Nishikawa, R. E. Stahlbush, and J. H. Stathis, "Oxygen-deficient centers and excess Si in buried oxide using photoluminescence spectroscopy," *Phys. Rev. B* vol. **60**, pp. 15910 (1999).

[240] J. H. Stathis and M. A. Kastner, "Photoinduced paramagnetic defects in amorphous silicon dioxide," *Phys. Rev. B* vol. **29**, pp. 7079 (1984).

[241] Y. Kanemitsu, N. Shimizu, T. Komoda, P. L. F. Hemment, and B. J. Sealy, "Photoluminescent spectrum and dynamics of Si^+-ion-implanted and thermally annealed SiO_2 glasses," *Phys. Rev. B* vol. **54**, pp. R14329 (1996).

[242] G. Allan, C. Delerue, and M. Lannoo, "Nature of Luminescent Surface States of Semiconductor Nanocrystallites," *Phys. Rev. Lett.* vol. **76**, pp.

2961-2964 (1996).

[243] K. S. Zhuravlev, A. M. Gilinsky, and A. Y. Kobitsky, "Mechanism of photoluminescence of Si nanocrystals fabricated in a SiO_2 matrix," *Appl. Phys. Lett.* vol. **73**, pp. 2962-2964 (1998).

[244] C. Bonafos, B. Garrido, M. Lopez, A. Romano-Rodriguez, O. Gonzalez-Varona, A. Perez-Rodriguez, J. R. Morante, and R. Rodriguez, "Structural and optical characterization of Mn doped ZnS nanocrystals elaborated by ion implantation in SiO_2," *Nucl. Instr. Meth. Phys. Res. B* vol. **147**, pp. 373-377 (1999).

[245] T. Komoda, J. Kelly, F. Cristiano, A. Nejim, P. L. F. Hemment, K. P. Homewood, R. Gwilliam, J. E. Mynard, and B. J. Sealy, "Visible photoluminescence at room temperature from microcrystalline silicon precipitates in SiO_2 formed by ion implantation," *Nucl. Instr. Meth. Phys. Res. B* vol. **96**, pp. 387-391 (1995).

[246] M. Molinari, H. Rinnert, and M. Vergnat, "Evolution with the annealing treatments of the photoluminescence mechanisms in a-SiN_x:H alloys prepared by reactive evaporation," *J. Appl. Phys.* vol. **101**, pp. 123532 (2007).

[247] L. D. Negro, J. H. Yi, J. Michel, L. C. Kimerling, T. W. F. Chang, V. Sukhovatkin, and E. H. Sargent, "Light emission efficiency and dynamics in silicon-rich silicon nitride films," *Appl. Phys. Lett.* vol. **88**, pp. 233109 (2006).

[248] N.-M. Park, C.-J. Choi, T.-Y. Seong, and S.-J. Park, "Quantum Confinement in Amorphous Silicon Quantum Dots Embedded in Silicon Nitride," *Phys. Rev. Lett.* vol. **86**, pp. 1355-1357 (2001).

[249] S. V. Deshpande, E. Gulari, S. W. Brown, and S. C. Rand, "Optical properties of silicon nitride films deposited by hot filament chemical vapor deposition," *J. Appl. Phys.* vol. **77**, pp. 6534-6541 (1995).

[250] H. L. Hao, L. K. Wu, W. Z. Shen, and H. F. W. Dekkers, "Origin of visible luminescence in hydrogenated amorphous silicon nitride," *Appl. Phys. Lett.* vol. **91**, pp. 201922 (2007).

[251] M. Wang, D. Li, Z. Yuan, D. Yang, and D. Que, "Photoluminescence of Si-rich silicon nitride: Defect-related states and silicon nanoclusters," *Appl. Phys. Lett.* vol. **90**, pp. 131903 (2007).

[252] K. S. Seol, T. Futami, T. Watanabe, Y. Ohki, and M. Takiyama, "Effects of ion implantation and thermal annealing on the photoluminescence in amorphous silicon nitride," *J. Appl. Phys.* vol. **85**, pp. 6746-6750 (1999).

[253] L. Skuja, "Optically active oxygen-deficiency-related centers in amorphous silicon dioxide," *J. Non-Cryst. Solids* vol. **239**, pp. 16-48 (1998).

[254] N. Koshida and H. Koyama, "Visible electroluminescence from porous silicon," *Appl. Phys. Lett.* vol. **60**, pp. 347-349 (1992).

[255] T. P. Chen, M. S. Tse, and X. Zeng, "Snapback behavior of the postbreakdown *I-V* characteristics in ultrathin SiO_2 films," *Appl. Phys. Lett.* vol. **78**, pp. 492-494 (2001).

[256] K. S. Min, K. V. Shcheglov, C. M. Yang, H. A. Atwater, M. L. Brongersma, and A. Polman, "Defect-related versus excitonic visible light emission from ion beam synthesized Si nanocrystals in SiO_2," *Appl. Phys. Lett.* vol. **69**, pp. 2033-2035 (1996).

[257] L. X. Yi, J. Heitmann, R. Scholz, and M. Zacharias, "Si rings, Si clusters,

and Si nanocrystals---different states of ultrathin SiO_2 layers," *Appl. Phys. Lett.* vol. **81**, pp. 4248-4250 (2002).

[258] L. X. Yi, J. Heitmann, R. Scholz, and M. Zacharias, "Phase separation of thin SiO layers in amorphous SiO/SiO 2 superlattices during annealing," *J. Phys.: Condens. Matter* vol. **15**, pp. S2887 (2003).

[259] B. Fazio, M. Vulpio, C. Gerardi, Y. Liao, I. Crupi, S. Lombardo, S. Trusso, and F. Neri, "Residual Crystalline Silicon Phase in Silicon-Rich-Oxide Films Subjected to High Temperature Annealing," *J. Electrochem. Soc.* vol. **149**, pp. G376-G378 (2002).

[260] X. Y. Chen, Y. F. Lu, Y. H. Wu, B. J. Cho, L. J. Tang, D. Lu, and J. R. Dong, "Correlation between optical properties and Si nanocrystal formation of Si-rich Si oxide films prepared by plasma-enhanced chemical vapor deposition," *Appl. Surf. Sci.* vol. **253**, pp. 2718-2726 (2006).

[261] S. Cheylan, N. Langford, and R. G. Elliman, "The effect of ion-irradiation and annealing on the luminescence of Si nanocrystals in SiO_2," *Nucl. Instr. Meth. Phys. Res. B* vol. **166-167**, pp. 851-856 (2000).

[262] B. Garrido, M. Lopez, A. Perez-Rodriguez, C. Garcia, P. Pellegrino, R. Ferr, J. A. Moreno, J. R. Morante, C. Bonafos, M. Carrada, A. Claverie, J. de la Torre, and A. Souifi, "Optical and electrical properties of Si-nanocrystals ion beam synthesized in SiO_2," *Nucl. Instr. Meth. Phys. Res. B* vol. **216**, pp. 213-221 (2004).

[263] A. A. Middleton and N. S. Wingreen, "Collective transport in arrays of small metallic dots," *Phys. Rev. Lett.* vol. **71**, pp. 3198-3201 (1993).

[264] R. Parthasarathy, X.-M. Lin, and H. M. Jaeger, "Electronic Transport in

Metal Nanocrystal Arrays: The Effect of Structural Disorder on Scaling Behavior," *Phys. Rev. Lett.* vol. **87**, pp. 186807 (2001).

[265] T. Shimizu-Iwayama, D. E. Hole, and W. B. Ian, "Mechanism of photoluminescence of Si nanocrystals in SiO 2 fabricated by ion implantation: the role of interactions of nanocrystals and oxygen," *J. Phys.: Condens. Matter* vol. **11**, pp. 6595 (1999).

[266] M. H. Nayfeh, N. Rigakis, and Z. Yamani, "Photoexcitation of Si-Si surface states in nanocrystallites," *Phys. Rev. B* vol. **56**, pp. 2079 (1997).

[267] M. S. Hybertsen, "Absorption and emission of light in nanoscale silicon structures," *Phys. Rev. Lett.* vol. **72**, pp. 1514 (1994).

[268] D. Kovalev, J. Diener, H. Heckler, G. Polisski, N. Kunzner, and F. Koch, "Optical absorption cross sections of Si nanocrystals," *Phys. Rev. B* vol. **61**, pp. 4485 (2000).

[269] P. K. Sahoo, S. Gasiorek, S. Dhar, K. P. Lieb, and P. Schaaf, "Cathodoluminescence and epitaxy after laser annealing of Cs+-irradiated α-quartz," *Appl. Surf. Sci.* vol. **252**, pp. 4477-4480 (2006).

[270] J. Hu, J. Pan, F. Zhu, and H. Gong, "Evidence of nitric-oxide-induced surface band bending of indium tin oxide," *J. Appl. Phys.* vol. **95**, pp. 6273-6276 (2004).

[271] Y. Park, V. Choong, Y. Gao, B. R. Hsieh, and C. W. Tang, "Work function of indium tin oxide transparent conductor measured by photoelectron spectroscopy," *Appl. Phys. Lett.* vol. **68**, pp. 2699-2701 (1996).

[272] H. Grabert and M. H. Devort, *Single charge tunneling: Coulomb blockade phenomena in nanostructures*. New York, Plenum (1992).

[273] L. Zhuang, L. Guo, and S. Y. Chou, "Silicon single-electron quantum-dot transistor switch operating at room temperature," *Appl. Phys. Lett.* vol. **72**, pp. 1205-1207 (1998).

[274] H. Ishikuro, T. Fujii, T. Saraya, G. Hashiguchi, T. Hiramoto, and T. Ikoma, "Coulomb blockade oscillations at room temperature in a Si quantum wire metal-oxide-semiconductor field-effect transistor fabricated by anisotropic etching on a silicon-on-insulator substrate," *Appl. Phys. Lett.* vol. **68**, pp. 3585-3587 (1996).

[275] T. P. Chen, M. S. Tse, X. Zeng, and S. Fung, "On the switching behaviour of post-breakdown conduction in ultra-thin SiO_2 films," *Semicond. Sci. Technol.* vol. **16**, pp. 793-797 (2001).

[276] S. Iwata and A. Ishizaka, "Electron spectroscopic analysis of the SiO_2/Si system and correlation with metal--oxide--semiconductor device characteristics," *J. Appl. Phys.* vol. **79**, pp. 6653-6713 (1996).

[277] Y. Liu, Y. Q. Fu, T. P. Chen, M. S. Tse, S. Fung, J. H. Hsieh, and X. H. Yang, "Depth Profiling of Si Oxidation States in Si-Implanted SiO_2 Films by X-Ray Photoelectron Spectroscopy," *Jpn. J. Appl. Phys.* vol. **42**, pp. L1394-L1396 (2003).

[278] F. J. Himpsel, F. R. McFeely, A. Taleb-Ibrahimi, J. A. Yarmoff, and G. Hollinger, "Microscopic structure of the SiO_2/Si interface," *Phys. Rev. B* vol. **38**, pp. 6084 (1988).

[279] E. Spitale, D. Corso, I. Crupi, S. Lombardo, and C. Gerardi, "Improvement of the P/E window in nanocrystal memories by the use of high-k materials in the control dielectric," *Microelectronics and Reliability* vol. **45**, pp. 895-898 (2005).

[280] L. Ding, T. P. Chen, M. Yang, J. I. Wong, Y. Liu, S. F. Yu, F. R. Zhu, M. C. Tan, S. Fung, C. H. Tung, and A. D. Trigg, "Photon-induced conduction modulation in SiO_2 thin films embedded with Ge nanocrystals," *Appl. Phys. Lett.* vol. **90**, pp. 103102 (2007).